UNIVERSITÀ DEGLI STUDI DI TRIESTE
e
UNIVERSITÀ CA' FOSCARI DI VENEZIA

XXXI CICLO DEL DOTTORATO DI RICERCA IN CHIMICA

Development of electrochemical methods and sensors for the determination of drugs and cancer markers in body fluids and tissues

Settore scientifico-disciplinare: **CHIM/01**

DOTTORANDO / A
GREGORIO BONAZZA

Ph.D. student
Gregorio Bonazza

COORDINATORE
PROF. BARBARA MILANI

Ph.D. program Coordinator
Barbara Milani

SUPERVISORE DI TESI
PROF. SALVATORE DANIELE

Thesis Supervisor
Prof. Salvatore Daniele

ANNO ACCADEMICO 2017/2018

Abstract

Electroanalytical methods and electrochemical sensor systems were developed to deal with so-called therapeutic drug monitoring (TDM) for application in body fluids, or detect specific compounds for early diagnosis of cancer diseases. As for TDM applications, the voltammetric behavior of the anticancer drug irinotecan (CPT-11), its main metabolites and the natural chemical analogous camptothecin (CPT) were investigated in acetonitrile, using glassy carbon (GCE) and platinum electrodes. Based on the voltammetric results, a simple electrochemical method for CPT-11 detection in plasma samples was set-up. The overall procedure included an extraction step of the drug from plasma samples, using acetonitrile as the eluent. Similar electrochemical investigations and analytical protocols were performed/developed for imatinib, an antileukemic drug. In the latter case, ethyl acetate (EtOAc), mixed with acetic and phosphoric acid was employed as solvent. The analytical protocol for the detection of imatinib in plasma samples also included an extraction step. To transfer the methodology to disposable electrode systems, inkjet printed electrodes (IPEs) were investigated. The IPEs were manufactured with relatively cheap materials and printed over flexible PET substrates. The working electrode (WE) and the counter electrode (CE) were made of multiwalled carbon nanotubes (CNTs); the reference electrode (RE) and electrical contacts were made with coalesced silver nanoparticles (AgNPs). UV-curable ink EMD 6415 proved to be promising to guarantee electrical insulation against the rather aggressive media employed in the work for monitoring the drugs. The thesis comprises also the development of innovative investigation approaches and other electrode systems. In particular, the interaction of the irinotecan with a specifically designed peptide was investigated to improve selectivity of the voltammetric methods in TDM applications. To achieve high spatial resolution, the innovative electroanalytical technique scanning electrochemical microscopy (SECM), along with the use of micro- and nana-electrodes was employed. Soft microelectrodes were also fabricated for SECM analysis of not-flat, irregular and soft surfaces. The usefulness of the proposed soft-microelectrodes was assessed for the simultaneous monitoring pH and nitric oxide above a silver band left to corrode in a dilute nitric acid solution. To this purpose, a dual Pt-Au soft probe, modified with active Pt-black and Ir-oxides films, was used. Finally, miniaturized sensors based on single or double barrel microelectrodes, coated with a room temperature ionic liquid layer were also tested for the detection of toxic species in either gaseous or liquid phases.

Index

Chapter 1: Introduction

1.1 Context of the work of the Thesis

Cancer is a generic term which refers to a large group of diseases that can affect any part of the body [1-3]. The common feature of all types of cancer is the rapid and uncontrolled growth of abnormal cells that can spread out to adjoining and distant tissues and organs (metastatic cancer) [1, 4].

Cancer is the second leading cause of death globally, representing roughly 15% of world total deaths in 2014 [4]. Overall mortality rates, however, declined significantly in the past decades, thanks to screening policies and the development of more effective strategies for treatment [5-7]. This fact, along with a global increasing of aged population, is contributing to the rising number (doubled in the last 22 years [4]) of people living with cancer, especially in developed nations (**Fig 1.1**) [8-10].

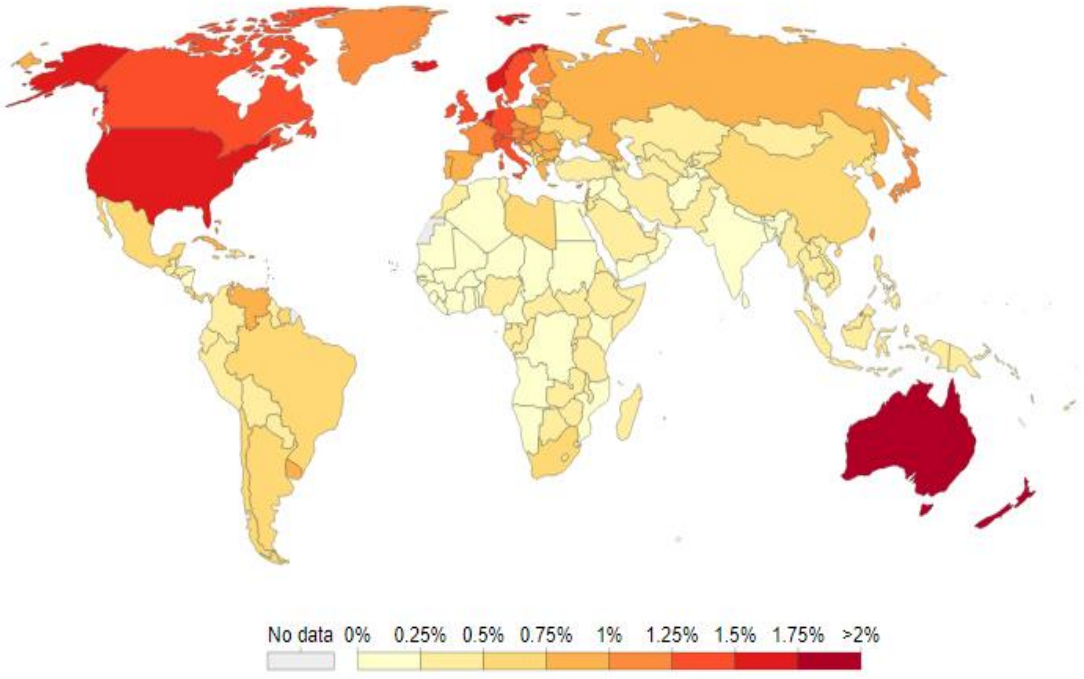

Fig 1.1 - Percentage of whole population living with any kind of cancer (from WHO, 2014 [4]).

This trend has sobering implications for public health policies; the growing demand for cancer care represents a very complex and expensive health burden [8, 11]. In fact, the cost of anticancer treatments increased in recent years [11]. Moreover, current treatments require specific diagnostic and therapeutic strategies and a qualified workforce to implement them [12]. In order to provide equitable access to care in the future, it is urgent to simplify all aspects of clinical treatments, without affecting their effectiveness [12-17].

In the context of oncology, more and more frequently, personalized approaches are adopted. These consist in tailoring the treatments to the individual characteristics of the patients [18-21]. The aim of these approaches is to concentrate preventive or therapeutic actions towards patients who actually need them, avoiding costs and, eventually, toxic effects for those to whom the treatments are not necessary.

To achieve this goal, it is necessary to develop and implement strategies capable of classifying individuals into sub-populations, which differ in their susceptibility to a particular disease or in their response to a specific pharmacological treatment [19, 22]. In the optic of personalized care, extensive use of clinical tests is fundamental to address medical decision. Considering clinical chemistry laboratories, the tests target a wide number of analytes, from biologically important ions (coming from salts and minerals) to small or large organic molecules [23-27, 17].

In recent years, in the field of oncology, small molecules analysis have received particular attention, either in the development of new cancer therapies, or in the research of prognostic or diagnostic markers of diseases [28, 29].

1.2 Cancer and small molecules

In molecular biology, a small molecule is a substance, with molecular weight ≤ 900 Da, which can easily cross a cell membrane, and therefore able of regulating a biological process [30]. This circumstance makes small molecule controls particularly important in the field of oncology, where the metabolic activity of cancer cells is highly altered [28, 30-34]. Controls can be directed towards molecules that are normally produced (e.g., metabolites) or used by the cells (e.g. nutrients) to regulate their activity and, in case of diseases, towards those drugs administered for care. In fact, most of the existing chemotherapeutic drugs are themselves small molecules, acting on intracellular targets [35-37]. A few examples of small molecules of oncologic interest, along with some their characteristics, related to the studies performed in this thesis are given below.

1.2.1 Nutrients and metabolites

a) Glucose flux measurements are particularly suited for understanding some characteristics of diseases and patient's response to drug therapy [40]. Glucose, in fact, can undergo glycolysis to lactate or be shunted through the pentose phosphate pathway to form ribose [40-48]. Glycolysis is important for the production of amino acids, nucleotides and lipids, which are necessary for cells proliferation and vascularization [41]. In cancer cells these processes are

strongly accelerated, and this leads to an increasing energy usage, and consequently to a continuous consumption of energetic substrates, such as carbohydrates. Therefore, glucose monitoring provides a way for understanding of the pathways that are up- or down-regulated and can help to define metabolic phenotypes in disease states [49] or drug responses [50-52].

b) Owing to intensive respiratory CO_2 and acidic metabolites production from glycolisis and citric acid cycle, cancer cells are exposed to larger proton fluxes compared to normal cells; this causes significant pH decrease in the extracellular medium [53-55]. As shown in **Fig 1.2**, different and efficient mechanisms of pH regulation are implemented by the tumor cell to stabilize intracellular pH at a favorable level.

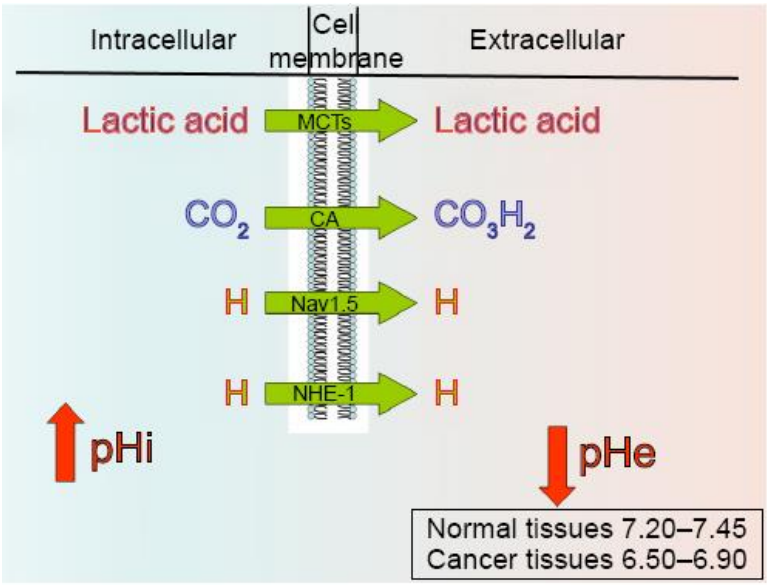

Fig 1.2- Main pH regulators over cell membrane. MCTs: mono-carboxylate transporters, i.e., membrane proteins, which catalyze the proton linked transport of monocarboxylic acids CA: carbonic anhydrase, i.e., a Zn containing enzyme that catalyzes the reversible hydration of CO_2. NHE-1: sodium–proton exchanger-,1 ubiquitous membrane enzyme involved in pH regulation of vertebrate cells. Nav1.5: voltage-gated sodium channel. PHi and PHe refer to intracellular and extracellular typical pH values, respectively. From [56].

The determination of pH levels is useful for exploring the general characteristics of a cancer, in order to improve diagnostics. Moreover, intracellular exchange of H^+ ions determines the ionization state of proteins and, consequently, their activity through key processes for cancer proliferation and metastasis. Therefore, the therapeutic potential of disturbing these sequences by targeting H^+/H^+-equivalent transporters is enormous, since the decrease of proton export from membrane induces apoptosis in cancer cells [55].

c): Anomalous concentration of nitric oxide (NO) and of NO-related species have been detected in various types of cancer [58-60]. NO is a short-lived, endogenously produced gas that acts as a signaling molecule in the body [60]. It is a key molecule in a wide number of physiological

processes. On the other hand, excessive and unregulated NO synthesis is involved under pathological conditions, including cancer. Data from many clinical and experimental studies have demonstrated that the role of NO in the carcinogenic process depends on its concentration: low levels of NO can promote tumor development, whereas its high concentration is toxic for tumor cells [61, 62]. Under normal O_2 levels, NO is produced by the enzyme Nitric Oxide Synthase (NOS) from Arginine (**Fig 1.3**). At low O_2 levels, nitrite is reduced to NO by a variety of reductases, including deoxyhemoglobin (Deoxy-Hb) [63]. Cancer research and oncological practice would benefit from in-tumor (*in situ*) monitoring of NO concentration. It is reported that an increase in the NO concentration in a tumor to roughly more than 1 μM (about a thousand-fold higher than the vasodilation-causing concentrations) would indicate effective treatment and would be a favorable prognostic indicator [63-65].

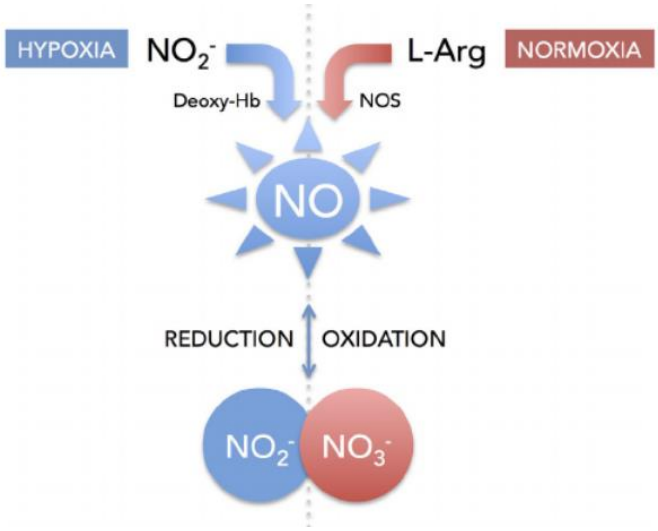

Fig 1.3- Simplified scheme of nitric oxide-nitrite-nitrate physiological pathway. NOS: Nitric Oxide Synthase; Deoxy-Hb: deoxyhemoglobin; L-Arg: L-arginine. From [65].

d) There is considerable experimental evidence that volatile substances in human breath may reflect the presence of neoplasms in the body [42]. The relation of oxygenated compounds, such as ketones and aldehydes, with oxidative stress and tumor-specific tissue composition and metabolism is well established [66]. Straight-chain aldehydes, in particular, have been earmarked as cancer biomarkers. These compounds are produced in the body by lipid peroxidation and are relatively insoluble in blood, so pass quickly into breath and are excreted within minutes of their formation. Sensing aldehydic compounds in gas atmosphere is, therefore, a promising practice for early cancer diagnosis and for monitoring cancer progression or regression [66-68]. However, aldehydes are reactive compounds and tend to decompose or react during the eventual

sample collection and storage. For this reason, conventional analytical techniques have limitations in the analysis of these compounds.

1.2.2 Anticancer drugs

Medical oncology has been introduced as a clinical specialty during 1950s [69]. Before years, treating cancer with drugs was, generally, not considered. The first scientific report regarding remission of a metastatic cancer by means of chemotherapy was in 1953, when methotrexate, an anti-metabolic agent, was employed to treat a choriocarcinoma [70]. From then on, a variety of anticancer drugs have been developed, and on the basis of the mechanism of action, they are classified as "conventional" and "molecularly targeted" drugs [69, 71]. Conventional drugs include alkylating, antimycotic, cytotoxic, hormonal and antimetabolic agents. The therapeutic benefit of conventional drugs is undoubtful. On the other hand, their general toxicity to all proliferating cells, including normal cells, make their clinical use limited [72]. The efforts of recent research are mostly addressed to molecularly targeted drugs, which are able to target selectively cancer cells. These drugs, typically, inhibit key enzymes (that represent the molecular targets) that are involved in cancer cell proliferation [72-74]. As a matter of fact, within the 41 antineoplastic agents approved by U.S. Food and Drug Administration 30 belongs to the class of molecularly targeted drugs [72, 75].

Drugs need to be studied/analyzed either in pharmaceutical formulations or in biological samples [22, 76-78]. In pharmaceutical formulations, analytical methodologies are generally devoted to quality control of bulk, commercialized products and of diluted formulations before administration to patient [76]. Furthermore, they are used to evaluate the stability and compatibility of the drugs with other pharmaceuticals [76]. On the other hand, analysis of drugs in biological samples plays an important role, in prognostics and diagnostics.

1.2.3 Therapeutic Drug Monitoring (TDM) and cancer care

Personalized treatments based on Therapeutic Drug Monitoring (TDM) have recently become object of interest as a medical tool. TDM is the clinical practice devoted to control the concentration of a drug in patient's body fluids at specific time intervals, in order to control and, eventually, modify drug dosage, thus improving efficacy of the treatment, while avoiding side effects [76]. TDM is commonly used to maintain drug concentrations in the vascular system of a patient within a well-established "therapeutic window", which is defined as the concentration

interval in which a pharmacological treatment is effective but not toxic (**Fig 1.4**). TDM is particularly indicated in patients who are either taking multiple drugs or expressing unusual pharmacokinetics as a result of physiological, environmental, or genetic causes [76-84].

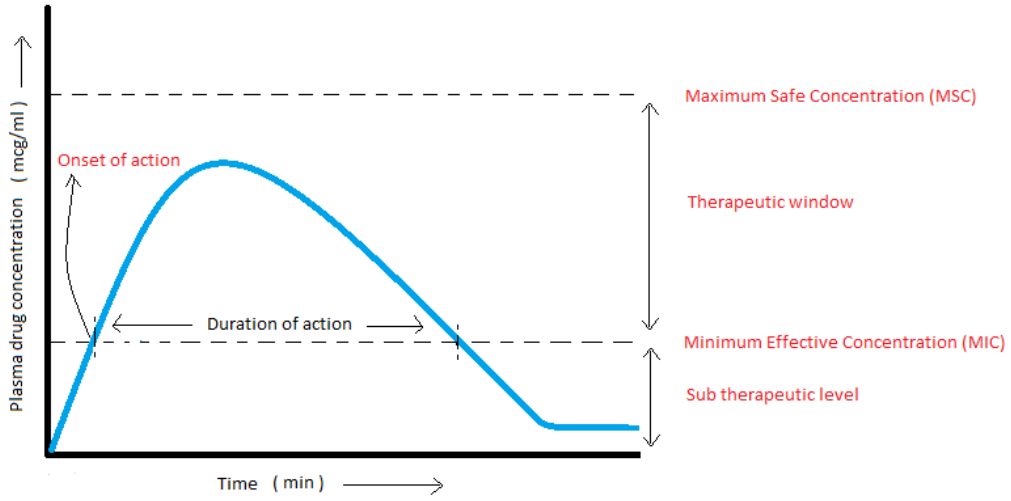

Fig 1.4- concentration versus time diagram of a generic circulating drug after administration

To obtain maximum benefits from TDM, appropriate instrumentation and suitable analytical methodologies are needed. This is a critical aspect for TDM in cancer care, because its implementation requires collection and analysis of a great number of samples from each patient. This fact may, eventually, entail high costs in terms of qualified personnel and very well equipped and organized laboratories.

Mostly used analytical methodologies for the detection of small molecules of clinical interest, including drugs, are based on Liquid Chromatohography (LC, often High Performance Liquid Chromatography (HPLC)), Mass Spectrometry (MS) and a variety of spectroscopic, and hyphenated HPLC-MS, LC-UV-Vis techniques [76, 85-88]. Less commonly, also capillary electrophoresis (CE) coupled with MS or UV detection is used [76, 88]. Typical examples of compounds and matrices investigated using the above mentioned approaches, are shown in **Tables 1.1** and **1.2** for either conventional (Topoisomerase inhibitors) or molecularly targeted drugs (Tyrosin-kinase inhibitors).

Table 1.1

Topoisomerase inhibitors	Matrices	Techniques
Irinotecan	Biological matrices	LC-FD
		LC-MS
		CE-UV-LIF
	Environment	LC-MS
Topotecan	Molecule/ formulations	LC-UV
	Biological matrices	LC-FD
		LC-MS
Etoposide	Molecule/ formulations	LC-UV
		LC-FD
	Biological matrices	LC-UV
		LC-MS
		CE-LIF
		CE-UV
	Environment	LC-MS

Table 1.2

TK inhibitors	Matrices	Techniques
Imatinib	Molecule/ formulations	LC-UV
		CE-UV
	Biological matrices	LC-UV
		LC-MS
		CE-UV
		CE-MS
	Environment	LC-MS
Dasatinib	Molecule/ formulations	LC-UV
		CE-UV
	Biological matrices	LC-UV
		LC-Fluo
		LC-MS
Nilotinib	Molecule/ formulations	LC-UV
	Biological matrices	LC-UV
		LC-MS
Lapatinib	Molecule/ formulations	LC-UV
	Biological matrices	LC-UV
		LC-MS
Erlotinib	Molecule/ formulations	LC-UV
	Biological matrices	LC-UV

Table 1.1 - Existing analytical methods for the detection of some topoisomerase inhibitors. From [76].

Table 1.2 – Existing analytical methods for the detection of some tyrosin-kinase inhibitors. From [76].

The above techniques and relevant analytical methodologies are characterized by high accuracy and sensitivity. Moreover, recent advances coupled to these techniques are continuously being achieved, especially in terms of automation of the analytical and pre-analytical steps [86, 87]. Their main limitations are related to costs, lack of portability of the instruments and long analysis time. Moreover they are usually designed to perform only *ex situ* analysis, while the lifetime of certain potentially diagnostic molecules is typically short, or they are localized on specific zones of the body.

The advent of new personalized approaches to cancer treatment, made the demand for fast and cheap analytical protocols and high throughput analysis to rise [76, 85, 86]. Electrochemical techniques are particularly promising to the latter purposes, and they are able to overcome the above mentioned limitations of HPLC-MS and spectrosopic techniques. In fact, electroanalytical techniques are characterized by high sensitivity, low cost, miniaturisable instrumentation, and measurements can be performed *in situ* even in a single cell [89]. Some examples of

electrochemical techniques, electrodes and methodologies applied to compounds of biological and medical interest are summarized in the following sections.

1.3 Electrochemical methods for the detection of small molecules of oncological interest

Studies related to the determination of antineoplastic drugs and of other small molecules of oncological interest using electrochemical sensors and biosensors, gained prominence in recent years [90]. Despite this, international patent databases revealed no patents currently submitted under this topic, suggesting this is an area to be further explored [90]. Although it is impossible to describe exhaustively the great variety of developed electrochemical devices and methodologies, some general approaches can be distinguished.

1.3.1 Electrochemical sensing by means of specific (bio)-recognition elements

Enzyme based electrochemical sensors exploit the inhibition/promotion of the enzyme activity, induced by the molecules of interest. In this way, electrochemical signals can be related to the analyte concentration [90, 91]. These kinds of sensors possess many advantageous properties, such as high selectivity and sensitivity towards target substrates. However, electrochemical enzyme-based biosensors are subject to interference from compounds present in the sample matrix. In particular, their responses may be affected by signal reduction caused by fouling agents (usually non specifically adsorbed proteins) and interferences from electroactive molecules [92-94]. Moreover, the manufacturing of these sensors is often challenging: enzymes undergo changes in their chemical and physical properties upon immobilization over surfaces, and this may imply unexpected variations in their activity and availability and, therefore, in their reliability [93-94]. Part of these limitations have recently been overcame with the introduction of aptamers [95-103], affimers [104, 105] and other low molecular weight specific recognition elements, such cyclic oligo-peptides [106]. Advantages offered by these compounds include thermal stability, reusability and ease of modification for their immobilization by incorporating reporter molecules (e.g., fluorophores or redox tags) and functional groups [95-108].

Aptamer and affimer based electrochemical sensors proved to be very promising for analysis of pharmaceuticals and other small molecules [96-103]. With aptamer-based sensors, detection in body fluid was achieved for some drug molecule such as cocaine [103] and doxorubicin [108]. The major limitation of these receptors is that their affinity constants towards targets are, in many cases, relatively low (in the tens of μM range) [107].

1.3.2 Electrochemical sensing without specific (bio)-recognition element

Electroanalytical techniques proved to be effective in the determination of pharmaceuticals, antioxidants, neurotransmitters and many other compounds, even in biological matrices [109-118], using electrode systems modified by inorganic, organic and metal-organic films. Selected examples of such kind of sensors are shown in **Table 1.3,** where electrode substrates, modifiers, the specific electroanalytical techniques and limits of detection are summarized.

Active layer	Drug	Electrochemical technique	Limit of detection (mol L^{-1})
($ZnFe_2O_4$/MNPs/IL/CPE) $ZnFe_2O_4$ magnetic nanoparticles/1,3-dipropylimidazolium bromide ionic liquid modified Carbon Paste Electrode	5-fluorouracil	(SWV) Square Wave Voltammetry	7×10^{-8}
(MF/GPE) Mercury film coated graphite pencil electrode	Lomustine	(SWCASV) Square Wave Cathodic Adsorptive Stripping Voltammetry	8.13×10^{-8}
(GMT-MMOF) Microporous metal organic framework for gemcitabine (p-aminothiophenol functionalized gold nanoparticles)	Gemcitabine	(LSV) Linear Sweep Voltammetry	3×10^{-15}
(PDR-PGE) Amino-terminated G4 PAMAM dendrimer modified disposable electrodes	Daunorubicin	(DPV) Differential Pulse Voltammetry	1.28×10^{-7}
(q-MWNTs/GCE) Functionalized multi-walled carbon nanotubes modified glassy carbon electrode	Methotrexate	Ion chromatography with electrochemical detection	0.4×10^{-9}
(2,7-BF/CNPE) 2,7-bis (ferrocenyl ethyl) fluoren-9-one modified carbon nanotube paste electrode	6-thioguanine	DPV	2.2×10^{-8}
(oo-PPY/MWCNT-COOH/GCE) Over-oxidized polypyrrole/multi-walled carbon nanotube composite on glassy carbon electrode	Pemetrexed	(ADSDPV) Adsorptive stripping with Differential Pulse Voltammetry	3.28×10^{-9}
(CD-GNs/GCE) Cyclodextrin-graphene hybrid nanosheets modified glassy carbon electrode	(Doxorubicin) [Methotrexate]	DPV	(0.1×10^{-9}) [2×10^{-8}]
A label-free sensor based on the direct ion transfer at the water/Dichlorohexane micro interface	Daunorubicin	DPV	0.8×10^{-6}
(AuNPs/EN/MWCNTs/AuE) Gold nanoparticles/ ethylenediamine/ multi-wall carbon-nanotubes modified gold electrode	Valrubicin	CV	1.8×10^{-8}
(PLL/GCE) Poly (L-lysine) modified glassy carbon electrode	Methotrexate	SWV	1.7×10^{-9}
(PVC-COOH) Poly (vinyl chloride) carboxylate membrane sensor	Cyclophosphamide and ifosfamide	Potentiometry	Not measured
(AgNPs/GCE) Ag nanoparticles modified glassy carbon electrode	Flutamide	DPV	9.33×10^{-6}
(TAM-MIP) Molecular imprinted sensor for Tamoxifen (o-phenylene-diamine-resorcinol)	Tamoxifen	CV	Not measured
(OMC/PGE) Ordered mesoporous carbon modified pyrolytic graphite electrode	Tirapazamine	DPV	2×10^{-11}
(Polymer-CPE) Polymer film modified carbon paste electrode	Flutamide	DPV	1.8×10^{-7}

Table 1.3 - Selected electrochemical sensors for the detection of anticancer drugs. From [115].

From **Table 1.3** appears that many efforts have been addressed in the development of new materials, able to provide more sensitive and selective response for target classes of analytes [119-123]. These sensors, however, often involve complex preparation procedures, which do not adapt to their mass-production.

1.3.3 Emerging electrochemical approaches for sensing and screening analytes in biological environments

Among the different new electrochemical methodologies developed in the field of sensors for biological and drugs investigations, scanning electrochemical microscopy (SECM) has become a

useful tool to reveal chemical or biochemical events occurring on or in close proximity to a surface. SECM, originated in electroanalytical surface science, has recently attracted increasing attention for biological applications and the study of living organisms [125]. Biological SECM could possibly be employed to quantify the flux of molecules entering or leaving a cell; to probe local electrochemical reactions occurring at or inside a cell; to perform duplicate measurements on both a single cell, or portions of it, or confluent assemblies or tissues [125]. Moreover, SECM measurements combined with other biosensing techniques can conduct and monitor multiple experiments simultaneously on a living object. In the future, Bio-SECM is likely to have a direct impact on the design of drugs and pharmaceutical targets, studying specific metabolites and proteins with high spatial resolution for both single cell and monolayer cultures. Such experiments will provide further insights into some of the unresolved mysteries surrounding life at the molecular and cellular level [125-127].

References

[1] D. Hanahan, R. A. Weinberg, Cell 100 (2000) 57–70.

[2] E. Tranvåg, E. Joakim, O. F. Norheim, T. Ottersen, BMC Cancer 18 (2018) 546-552.

[3] S. H. Hassanpour, M. Dehghani, Journal of Cancer Research and Practice 4 (2017) 127-129.

[4] World Health Organization, World Cancer Report (2014). (http://www.who.int/cancer/publications/WRC_2014/en/)

[5] M.L.G. Janssen-Heijnen, S. Houterman, V.E.P.P. Lemmens, H. Brenner, E. W. Steyerberg, J.W.W. Coebergh, Annals of Oncology 18 (2007) 1408–1413.

[6] A. S. Allegretti, R. I. Thadhani, Nature Reviews Nefrology 14 (2018) 288-290.

[7] G. Lyratzopoulos, Nature Reviews Clinical Oncology 12 (2015) 191-192.

[8] C. Parry, C.E.E. Kent, A.B. Mariotto, C.M. Alfano, J.H. Rowland, Cancer Epidemiology Biomarkers & Prevention 20 (2011) 1996–2005.

[9] P.M. Marcus, N. Pashayan, T.R. Church, V.P. Doria-Rose, M.K. Gould, R.A. Hubbard, M. Marrone, Cancer Epidemiology Biomarkers & Prevention 25 (2016) 1449–1455.

[10] S.M. Phillips, C.M. Alfano, F.M. Perna, R.E. Glasgow, Cancer Epidemiology Biomarkers & Prevention 23 (2014) 687-699.

[11] D. A. Goldstein, J. Clark, Y. Tu, J. Zhang, F. Fang, R. Goldstein, S. M. Stemmer, E. Rosenbaum, Oncotarget 8 (2017) 71548-71555.

[12] G.W. Prager, S. Braga, B. Bystricky, C. Qvortrup, C. Criscitiello, E. Esin, G. S. Sonke, G. A. Martínez, J. Frenel, M. Karamouzis, M. Strijbos, O. Yazici, P. Bossi, S. Banerjee, T. Troiani, A. Eniu, F. Ciardiello, J. Tabernero, C.C. Zielinski, P.G. Casali, F. Cardoso, J. Douillard, S. Jezdic, K. McGregor, G. Bricalli, M. Vyas, A. Ilbawi, ESMO Open 3 (2018) 1-10.

[13] F. Merletti, C. Galassi, T. Spadea, Environmental Health 10 (2011) S7.

[14] A. Bottomley, The Oncologist 7 (2002) 120-125.

[15] P.W. Dickman, P. Auvinen, E.T. Voutilainen, T. Hakulinen, Journal of Epidemiology and Community Health 52 (1998) 727-734.

[16] E. Dolgin, Nature 555 (2018) 26-29.

[17] J. Buttner, Clinica Chimica Acta 232 (1994) 1-9.

[18] H. J. Kushner, Current Trends in Biomedical Engineering & Biosciences 6 (2017) 1-5.

[19] S. Schleidgen, C. Klingler, T. Bertram, W.H. Rogowski, G. Marckmann, BMC Medical Ethics 14 (2013) 1-12.

[20] S. Bates, Drug Discovery Today 15 (2010) 115–120.

[21] E.P. Bottinger, Mount Sinai Journal of Medicine 74 (2007) 15–21.

[22] M.I. Patel, V.S. Periyakoil, D.W. Blayney, D. Moore, A. Nevedal, S. Asch, A. Milstein, T. R. Coker, Journal of Oncology Practice 13 (2017) 291-302.

[23] C.A. Burtis, C.E. Burns, Fundamentals of Clinical Chemistry and Molecular Diagnostics 7th ed (2012) Elsevier.

[24] J.H. Beumer, E. Chu, C. Allegra, Y. Tanigawara, G. Milano, R. Diasio, T.W. Kim, M. Joerger, Clinical Pharmacology & Therapeutics 0 (2018) 1-16.

[25] S. Caroli, G. Zèray, Analytical Techniques for Clinical Chemistry 1st ed (2012) Wiley.

[26] S.P. Storm, Cancer Biology & Medicine 13 (2016) 1-11.

[27] F.H. Wians, Laboratory Medicine 40 (2009) 105–13.

[28] N. Tolliday, P. A. Clemons, P. Ferraiolo, A.N. Koehler, T.A. Lewis, X. Li, S.L. Schreiber, D. S. Gerhard, S. Elias, Journal of Cancer Research 18 (2006) 8935-42.

[29] S. Mehta, A. Shelling, A. Muthukaruppan, A. Lasham, C. Blenkiron, G. Laking, C. Print, Therapeutic Advances in Medical Oncology 2 (2010) 125-48.

[30] N. J. Yang, M. J. Hinner, Methods in Molecular Biology 1266 (2015) 29-53.

[31] B. Sehnert, H. Burkhardt, S. Dübel, R. E. Voll, Journal of Immunological Sciences 1 (2017) 26-32.

[32] K.B. Teuscher, M. Zhang, H. Ji Journal of Medicinal Chemistry 60 (2017) 157-169.

[33] W.A. Weiss, S.S. Taylor, K.M. Shokat, Nature Chemical Biology 3 (2007) 739−744.

[34] S.V. Frye, Nature Chemical Biology 6 (2010) 159−61.

[35] S. Hoelder, P.A. Clarke, P. Workman, Molecular Oncology 6 (2012) 155-76.

[36] D.S. Wishart, Plos One 8 (2012) 1-18.

[37] J.L. Spratlin, N.J. Serkova, E.S. Gail, Clinical Cancer Research 15 (2009) 431-40.

[38] C.M. Metallo, M.G.V. Heiden, Molecular Cell 49 (2013) 388-98.

[39] N. Pavlova, B. C. Thompson, Cell Metabolism 23 (2016) 27–47.

[40] R. Beger, Metabolites 3 (2013) 552–74.

[41] J.L. Griffin, J.P. Shockcor, Nature Reviews Cancer 4 (2004) 551–61.

[42] Y.S. Kim, P. Maruvada, J.A. Milner, Future Oncology 4 (2008) 93–102.

[43] J.L. Spratlin, N.J. Serkova, S.G. Eckhardt, Clinical Cancer Research 15 (2009) 431–40.

[44] T.W. Fan, A.N. Lane, R.M. Higashi, Current Opinion in Molecular Therapy 6 (2004) 584–92.

[45] Y.L. Chung, J.R. Griffiths, Ernst Schering Foundation Symposium 4 (2007) 55–78.

[46] V.M.G. Heiden, Nature Review Drug Discovery 10 (2011) 671–684.

[47] R. Kaddurah-Daouk, B.S. Kristal, R.M. Weinshilboum, Annual Review of Pharmacology and Toxicology 48 (2008) 653–83.

[48] J.K. Nicholson, E. Holmes, I.D. Wilson, Nature Review Microbiology 3 (2005) 431–38.

[49] G.F. Zhang, S. Sadhukhan, G.P. Tochtrop, H. Brunengraber, Journal of Biological Chemistry 286 (2011) 23631–35.

[50] R. Beger, D. Hansen, L. Schnackenberg, B. Cross, J. Fatollahi, F.T. Lagunero, Z. Sarnyai, L. Boros, Metabolomics 5 (2009) 336–345.

[51] L.G. Boros, W.N.P. Lee, M. Cascante, New England Journal of Medicine 347 (2002) 67–68.

[52] L.G. Boros, Metabolomics 1 (2005) 11–15.

[53] K. Kuhne, C. von Neubeck, U. Schwarzenbolz, Z. Yu, B.M. Kessler, J. Pietzsch, L.A. Kunz-Schugart, Journal of Biotechnology 242 (2016) 30-54.

[54] A. Hulikova, R. D. Vaughan-Jones, P. Swietach, Journal of Biological Chemistry 286 (2011) 13815–13826.

[55] M. Damaghi, J.W. Wojtkiviak, R.J. Gillies, Frontiers in Physiology, 4 (2013) 1-10.

[56] T. Koltai, OncoTargets and Theraphy 9 (2016) 6343-6360.

[57] B. Muz, P. de la Puente, F. Azab, A.K. Azab, Hypoxia 83 (2015) 83-92.

[58] G.L. Semenza, Critical Review in Biochemistry and Molecular Biology 35 (2000) 71–103.

[59] C.S. Cabs, J.E. Brenman, K.D. Aldape, D.S. Bredt, M.A. Isrnael, Cancer Reserarch 55 (1995) 727–730.

[60] L.L. Thomson, F.G. Lawton, R.G. Knowles, J.E. Basley, V. Riversomoreno, S. Moncada, Cancer Research 54 (1994) 1352–1354.

[61] K.S. Choudhari, M. Chaudhary, S. Bagde, A.R. Gadbail, V. Joshi World Journal of Surgical Oncology 11 (2013) 118-129.

[62] J. Muntanè, M. de la Mata, World Journal of Hepatology 2 (2010) 337-344.

[63] W. Ratajczak-Wrona, E. Jablonska, B. Antonowicz, D. Dziemianczyk, S.Z. Grabowska, International Journal of Oral Science 5 (2013) 141-145.

[64] A. Heller, Bioanalytical Review 1 (2009) 3-6.

[65] J. Scicinski, B. Oronsky, S. Ning, S. Knox, D. Peehl, M.M. Kim, P. Langecker, G. Fanger, Redox Biology 6 (2015) 1-8.

[66] J. Fuchs, International Journal of Oral Science 5 (2013) 141–145.

[67] D. Poli, M. Goldoni, M. Corradi, O. Acampa, P. Carbognani, E. Internullo, A. Casalini, A. Mutti, Journal of Chromatography B, 878 (2010) 2643-2651.

[68] J. Li, Y. Peng, Y. Liu, W. Li, Y. Jin, Z. Tang, Y. Duan, Clinica Chimica Acta 436 (2014) 59-67.

[69] V.T. DeVita, J. Chu, E. Chuw, Cancer research 68 (2008) 8643-8653.

[70] I.S. Johnson, A.G. Armstrong, M. Gorman, J.P. Burnett, American Association for Cancer Research (1963) 1390-1429.

[71] D.E Gerber, American Family Physician 77 (2008) 311-319.

[72] N. Guichard, D. Guillarme, P. Bonnabrya, S. Fleury-Souverain, Analyst 142 (2017) 2273-2321.

[73] N. Syn, N. Li-Xun, W. Yong, B. Goh, S. Lee, Expert Opinion on Drug Metabolism & Toxicology 12 (2016) 911–922.

[74] M.C. Joshi, Indian Journal of Cancer 44 (2007) 31-35.

[75] Drugs approved by FDA:
https://www.fda.gov/drugs/informationondrugs/approveddrugs/ucm279174.htm

[76] S. Nussbaumer, P. Bonnabry, J. Veuthey, S. Fleury-Souverain, Talanta 85 (2011) 2265-2289.

[77] A. J. Galpin, W. E. Evans, Clinical Chemistry 39 (1993) 2419-2430.

[78] S. Zhou, Y. Gao, W. Jiang, M. Huang, A. Xu, J.W. Paxton, Drug Metabolism Review 35 (2003) 35–98.

[79] P.D Walson, Clinical Chemistry 44 (1998) 415-419.

[80] N. Widmer, C. Bardin, E. Chatelut, A. Paci, J. Beijnen, D. Levéque, G. Veal, A. Astier, Europeam Journal of Cancer 50 (2014) 2020-2036.

[81] M. Enara, MOJ Toxicology 9 (2014) 9-10.

[82] W.E. Evans, M.V. Relling, J.H. Rodman, W.R. Crom, J.M. Boyett, C.H. Pui, New England Journal of Medicine 338 (1998) 499-505.

[83] B. Lennard, Brazilean Journal of Clinical Pharmacology 52 (2001) 75-87.

[84] G. McMahon, Bioanalysis 1 (2009) 508-511.

[85] I.M. Mutton, Chromatographia 47 (1998) 291–298.

[86] P.R. Tiller, L.A. Romanyshyn, U.D. Neue, Analytical and Bioanalytical Chemistry 377 (2003) 788-802.

[87] D.W. Kimmel, G. LeBlanc, M.E. Maschievitz, D.E. Cliffel Analytical Chemistry 84 (2012) 685-707.

[88] J. Powell , E. M. Pijl, Harm Reduction Journal, 14 (2017) 1-13.

[89] T. Malinski, Z. Taha, Nature 358 (1992) 676-678.

[90] M. Labib, E.H. Sargent, S.O. Kelley, Chemical Reviews, 116 (2016) 9001-9090.

[91] E.S. Bucher, E.M. Whigtman, Annual Review of Analytical Chemistry 8 (2015) 239-261.

[92] L. El Harradi, I. Bourais, H. Mohammadi, A. Amine, Sensors 18 (2018) 164-189.

[93] G. Rocchitta, A. Spanu, S. Babudieri, G. Latte, G. Madeddu, G. Galleri, S. Nuvoli, P. Bagella, M. I. Demartis, V. Fiore, R. Manetti, P. A. Serra, Sensors 16 (2016) 780-801.

[94] I.L. Celine, A.B. Justino, A.C. Duarte, T.A.P. Rocha-Santos Trends in Analytical Chemistry 85 (2016) 36-60.

[95] S. Jayasena, Clinical Chemistry 45 (1999) 1628-1633.

[96] C. Tuerk, L. Gold Science 249 (1990) 505–510.

[97] D.M. Tasset, M.F. Kubik, W. Steiner, Journal of Molecular Biology 272 (1997) 688.

[98]J.S. Swensen, J. Xiao, B.S. Ferguson, A.A. Lubin, R.Y. Lai, A. J. Heeger, K.W. Plaxco, H.T. Soh, Journal of the American Chemical Society 131 (2009) 4262–4266.

[99] A. Riuscito, M.C. De Rosa, Frontiers in Chemistry 4 (2016) 1-14.

[100] I. Willner, M. Zayats, Angewandte Chemie 46 (2007) 6408-6418.

[101] S. Song, L. Wang, J. Li, J. Zhao, C. Fan, Trends in Analytical Chemistry 27 (2008) 108-117.

[102] D. Yang, X. Liu, Y. Zhou, Lin Luo, J. Zhang, A. Huang, Q. Mao, X. Chen, L. Tang, Analytical Methods 9 (2017) 1976-1990.

[103] J.S. Swensen, J. Xiao, B.S. Ferguson, A.A. Lubin, R.Y. Lai, A.J. Heeger, K.W. Plaxco, H.T. Soh, Journal of the American Chemical Society 131 (2009) 4262–4266.

[104] P.K. Ferrigno Essays in Biochemistry 60, (2016) 19–25.

[105] A. Johnson, Q. Song, P.K. Ferrigno, P.R. Bueno, J. J. Davis Analytical Chemistry 84 (2012) 6553-6560.

[106] O.A. Farghaly R. S. Abdel Hameed, A. H. Abu-Nawwas, International Journal of Electrochemical Science 9 (2014) 3287-3318.

[107] James M. Carothers, Stephanie C. Oestreich, Jack W. Szostak, Journal of American Chemical Society 128 (2006) 7929-7937.

[108] N. Bahner, P. Reich, D. Frense, M. Menger, K. Schieke, D. Beckmann, Analytical and Bioanalytical Chemistry 410 (2018) 1453-1462.

[109] A. Lesch, F. Cortés-Salazar, M. Prudent, J. Delobel, S. Rastgar, N. Lion, J. Tissot, P. Tacchini, H.H. Girault, Journal of Electroanalytical Chemistry 717 (2014) 61-68.

[110] H. Sakamoto, R. Hatsuda, K. Miyamura, H. Shiraishi, S. Sugiyama, Analytical Sciences 27 (2011) 333-335.

[111] I.N. Jovanovic, S. Komorsky-Lovric, A.L.Vrdoljak, A.R. Popovic, M. Neuberg, Electroanalysis 30 (2018) 336-344.

[112] B. Hatamluyi, F. Lorestani, Z. Es'haghi, Biosensors and Bioelectronics 120 (2018) 22-29.

[113] F. M. Zahed, B. Hatamluyi, F. Lorestani, Z. Es'haghi, Journal of Pharmacheutical and Biomedical Analysis 161 (2018) 12-19.

[114] E.M. Materon, A. Wong, A. Fatibello-Filho, R. Censi Faria, Journal of Electroanalytical Chemistry 827 (2018) 64-72.

[115] D. Lima, G.N. Calaca, A.G. Viana, C.A. Pessoa, Applied Surface Science 427 (2018) 742-753.

[116] E. Orlowska, Inorganic Chemistry 57 (2018) 10702-17.

[117] F. Prieto, M. Rueda, N. Naitlho, M. Vazquez-Gonzalez, M.L. Gonzalez-Rodriguez, A.M. Rabasco, Journal of Electroanalytical Chemistry 815 (2018) 246-254.

[118] N. Arshad, S.I. Farooqi, Applied Biochemistry and Biotechnology (2018) 1-21.

[119] E. Kanat, E. Eksin, B. Karacicek, Y. Erac, A. Erdem, Electroanalysis, 30 (2018) 1566-1574.

[120] E. Eksin, E. Zor, A. Erdem, H. Bingol, Biosensors and Bioelectronics, 92 (2017) 207-214.

[121] P.T. Wilder, D.J. Weber, A. Winstead, S. Parnell, T.V. Hinton, M. Stevenson, D. Giri, S.K. Mandal, Molecular and Cellular Biochemistry, 441 (2018) 151-163.

[122] D. Matyszweska, S. Moczulska, Electrochimica Acta 280 (2018) 229-237.

[123] K. Honeychurch, Separations 3 (2016) 1-29.

[124] J. Marzioch, J. Kieninger, J. A. Sandvik, E. O. Pettersen, Q. Peng, G. Urban, Journal of Physics, 757 (2016) 1-6.

[125] I. Beaulieu, S. Kuss, J. Mauzeroll, Analytical Chemistry 83 (2011) 1485-1492.

[126] F. Conzuelo, A. Schulte, W. Schuhmann, Proceedings of the Royal Society A 474 (2018) 1-24.

[127] S. Kuss, D. Polcari, M. Geissler, D. Brassard, J. Mauzeroll, Proceedings of the National Academy of Sciences 110 (2013) 9249-9254.

2. Objectives of the Thesis

The aim of the research described in this thesis was to investigate and develop various electroanalytical strategies to detect small molecules which are important in the field of cancer care or that reflect the presence of neoplasms in the human body. Among the numerous categories of molecules involved in these processes, here, the interest is devoted to drugs that are administered to patients affected by colorectal cancer or leukaemia, and simple species, such as hydrogen ions (i.e., pH), nitrogen oxides or aldehydes, which are somewhat related to a normal (for healthy) or abnormal (for cancer) activity of human cells.

The aspect concerning the first class of molecules is addressed within the TDM approach, which would require simple, fast and, possibly, inexpensive analytical methods and instrumentations. For these purposes, as mentioned in Introduction, electrochemical techniques are very suited. For these reasons, in recent years, several literature reports have dealt with electrochemical systems for TDM, characterized by high sensitivity, accuracy, and are promising for applications to real samples. Most investigations were devoted at exploring new electrode materials able to enhance the sensitivity, by a catalytic effect, or the selectivity by specific interaction of the drug with the electrode structure or its chemical components. Moreover, in a few examples, it has been shown that some electroactive drugs, or metabolites, could be detected directly in matrices such as urine and serum, spiked on purpose with the investigated compounds. It must be considered, however, that the majority of the electrode systems proposed, though effective, is rather complex to fabricate or to be user friendly. Therefore, a part of this thesis illustrates a strategy, based on the use of commercially available glassy carbon electrodes, coupled with suitable voltammetric techniques and simple extraction/separation pre-analytical procedures, for the detection of target analytes in very complex biological matrices, as plasma.

Specifically, the anticancer drugs, irinotecan and imatinib, have been considered, as they are widely employed for the therapeutic treatment of colorectal cancer or leukaemia, respectively. To establish the most suitable electrode processes allowing their sensitive and reproducible quantification, eventually free from interference, the voltammetric behaviour of the two drugs (and of their metabolites) were investigated in organic solvents. Because in the clinical practice, TDM is typically performed in plasma samples, a pre-analytical procedure was set up using commercially available solid phase extraction (SPE) or simplified liquid extraction (SLE) columns.

In addition to the above procedures, and with the aim of attempting the use of miniaturised electrochemical cells for small volume sample analyses, more innovative detection strategies were also investigated.

One of them was based on the use of inkjet-printed electrodes, coated with multi-walled carbon nanotubes (MWCNTs). These types of electrode systems are generally employed with aqueous solutions, as they are fabricated on substrates made of flexible organic polymers (PET, PEN, polyimide and others). Since organic solvents are required for denaturizing plasma and for the extraction of the drug, a careful study on the stability of the inject-printed sensors in several non-aqueous solvents was performed.

A second approach was based on the use of cyclic peptides for the selective molecular recognition of the drug. This should, in principle, allow increasing selectivity towards the target species, even if measurements are performed directly in the real matrices. Cyclic peptides immobilized onto a substrate can eventually capture the drug and its detection can be performed electrochemically by a scanning probe technique such as SECM. The latter is a powerful technique, which allows investigating chemical phenomena taking place at interfaces with high spatial resolution. Moreover, SECM can also be employed to investigate the successful of the various steps involved in the sensor fabrication.

For the detection of small molecules related to cancer diagnoses, this thesis focused on H^+ changes (i.e., pH changes), nitric oxide (NO) and volatile aldehydes (VA) production. For their detection strategies based on miniaturized soft probes coupled with SECM or micro cell allowing controlling their formation on a substrate or in air atmospheres, respectively, were investigated.

Overview of the Thesis

Chapter 1 presents some general aspects related to cancer diseases, classification of typical drugs employed in therapeutic treatments and the analytical methods generally employed to ascertain their content in body fluids or to establish the concentration of molecules able to diagnose the onset of a tumor.

Chapter 2 reviews theoretical background of mass transport regimes at either conventional and microelectrodes of different geometries. Moreover, diagnostic criteria for elucidating, with cyclic voltammetry, complex electrodes processes, including homogeneous chemical reactions and surface processes are briefly described. Theoretical aspects of the feedback mode of SECM are also given.

Chapter 3 discusses the experimental aspects of the work done. It includes the description of instruments employed, the methods of fabrication of microelectrodes and soft probes, as well as their characterization by voltammetry. The preparation of all solutions and standard procedures used are also presented.

Chapter 4 describes briefly the aim of the work done along with this thesis's overview.

Chapters 5 - 7 are devoted to the results and discussion. In particular:

- ***Chapter 5.1*** examines, comprehensively the voltammetric behaviour of irinotecan, its main metabolites and the co-drugs, 5-fluorouracil (5-FU) and folinic acid (FA), in acetonitrile solutions. Afterward a detailed procedure for the detection of CPT-11 in plasma samples is illustrated, in view of its use in TDM. An example of its application to two real samples collected from oncological patients undergoing the therapeutic treatment is also presented.
- ***Chapter 5.2*** examines the voltammetric behavior of imatinib and its main metabolite N-des-methyl imatinib in acidified ethyl acetate media. The electrochemical information gathered on this drug is then employed to establish an analytical protocol for its detection in plasma samples using and adsorptive stripping voltammetric approach. A fully analytical protocol, involving also an extraction step using ethyl acetate as eluent, is presented. An application is given for TDM in plasma samples collected from oncological patients undergoing the therapeutic treatment.

- ***Chapter 6*** is dedicated to the investigation of the stability in organic solvents of inject-printed electrodes, coated with multi-walled carbon nanotubes (MWCNs), in view of their use for the detection of drugs in plasma samples. An application to the detection of imaninib in ethyl acetate is also discussed. This chapter also includes an investigation concerning the characterization of an electrochemical microprobe, incorporating a room temperature ionic liquid as electrolyte, for sensing volatile aldehydes, such as hexane aldehyde and propionaldehyde, in gaseous phase.
- ***Chapter 7.1*** deals with the preparation of a platform able to immobilize cyclic peptides for the selective molecular recognition of irinotecan. The characterization of the platform system is performed by using scanning electrochemical microscopy and voltammetry. A strategy based on SECM, working in feedback mode, to establish the binding ability of the cyclic peptides with irinotecan is illustrated.
- ***Chapter 7.2*** is devoted to the characterization of dual soft-probes to be used in SECM for monitoring simultaneously pH and nitric oxide formation above a solid substrate. A proof-of-concept on the possibility of imaging these properties with high spatial resolution is illustrated by rastering a dual soft probe above an array of silver microbands subjected to corrosion in a HNO_3 solution.

Chapter 8 summarizes the main conclusions that can be drawn from the preceding chapters and formulates some proposals for future developments/applications of the methodologies/materials employed in the thesis.

Chapter 3: Theory

3.1 Mass transport and diffusion equations for conventional and microelectrodes: potential step experiments.

Most of electrochemical methods rely on mass transport conditions governed by diffusion [1, 2]. Under diffusion controlled conditions, the flux of the electroactive species and consequently the concentration profiles depend on the electrode geometry. Here, the electrode geometry considered are those schematized in **Fig 3.1**.

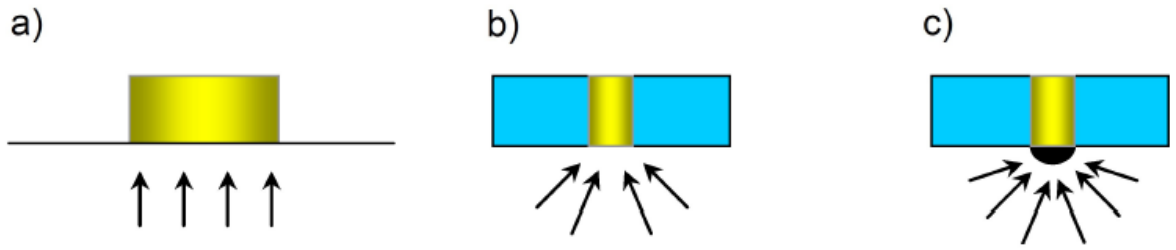

Fig 3.1- **a**) planar electrode; **b**) disk microelectrode embedded in an infinite insulating sheath; **c**) hemispherical microelectrode protruding from an infinite insulating sheath.

3.1.1 Diffusion at a planar electrode in a semi-infinite solution: Potential step experiment

The flux (J) associated with an electrode having is given by the first Fick's law in one-dimension [2]:

$$J\ (x,t) = -D\left[\frac{\partial C(x,t)}{\partial x}\right] \qquad (eq\ 1)$$

where D is the diffusion coefficient (cm^2s^{-1}), x the distance from the electrode surface and t the time. The current i, is given by:

$$i = -nFAJ(x,t) \qquad (eq\ 2)$$

where F is Faraday constant (96500 C mol^{-1}), n the number of electrons, A is the electrode surface. Combination of *eq 1* and *eq 2* provides:

$$i = nFAD\,\frac{\partial C(x,t)}{\partial x} \qquad (eq\ 3)$$

The dependence of concentration over time is given by the solution of the second Fick's law:

$$\frac{\partial C(x,t)}{\partial t} = D_{Ox}\left[\frac{\partial^2 C(x,t)}{\partial x^2}\right] \qquad (eq\ 4)$$

Considering the following reversible electrode process

$$Ox + ne^- \leftrightharpoons Red$$

assuming that only the species *Ox* is initially present in the solution, and that a sufficiently high negative potential is applied to the electrode, such that the concentration of *Ox* species at the electrode surface is equal to zero the solution of *eq 4*, under proper boundary conditions, provides the concentration profiles of the species in the solution. For *Ox*, the following equation holds:

$$C(x,t) = C_{Ox} erf\left[\frac{x}{2\sqrt{D_{Ox}t}}\right] \qquad (eq\ 5)$$

Fig. 3.2 comprises several plots for different values of the pulse time.

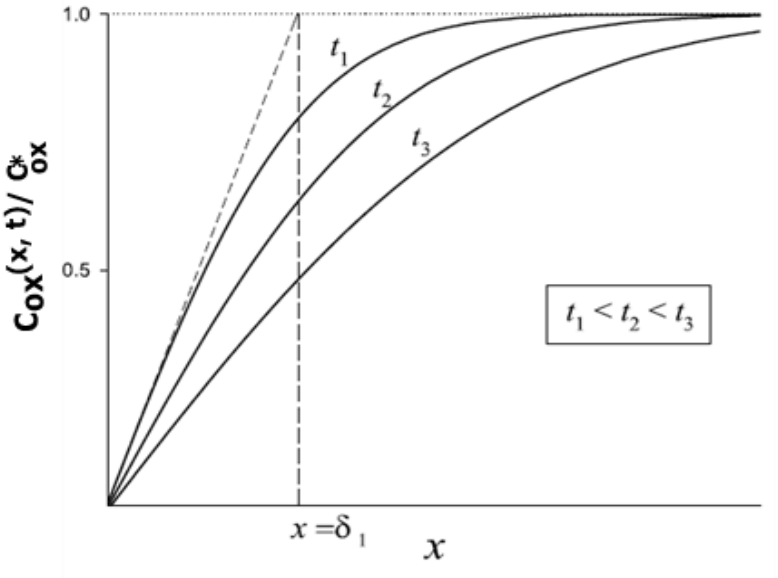

Fig 3.2-Concentration profiles at different pulse times for the species *Ox*. From [2].

As is evident, the *Ox* concentration increases with the distance from a zero value to the value in the bulk of the solution. This distance is the diffusion layer (δ), which, for a generic species *i*, can be calculated by

$$\delta_i = \sqrt{\pi D_{Ox} t} \qquad (eq\ 6)$$

Considering the flux at the electrode surface and *eq 3*, the following relationship is obtained:

$$\frac{i}{nFA} = D_{Ox}\left[\frac{\partial C_{Ox}(x,t)}{\partial x}\right] \qquad (eq\ 7)$$

After considering *eq 5*, Cottrell equation is obtained [1, 2].

$$i = \frac{nFAD_{Ox}^{1/2}\, C_{Ox}^{b}}{\pi^{1/2} t^{1/2}} \qquad (eq\ 8)$$

where C^b_{Ox} is the concentration of *Ox* in the bulk solution and the other symbols have their usual meaning. A typical current/time response is shown in **Fig 3.3** (black line).

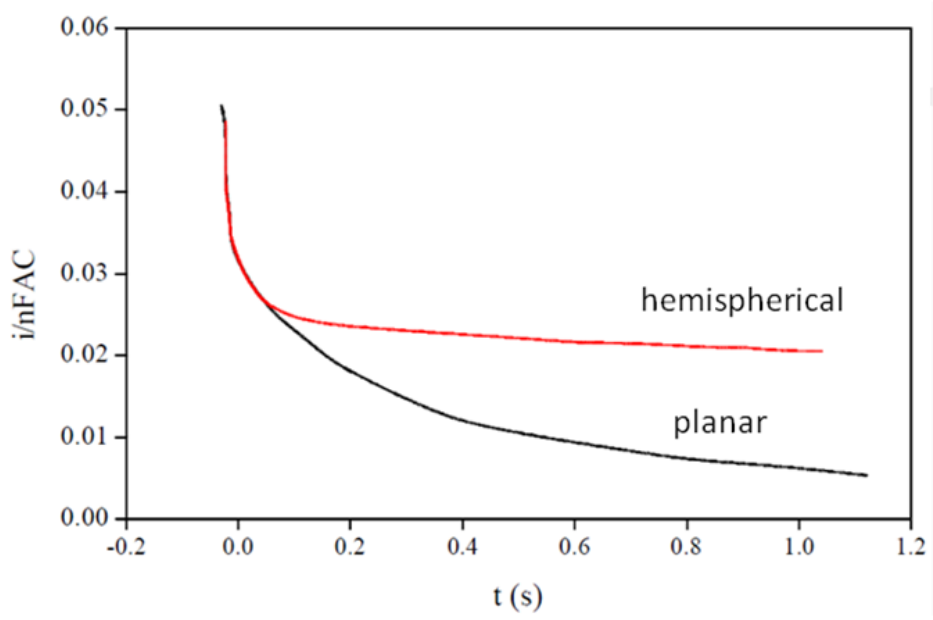

Fig 3.3-Current vs time response in a chronoamperometric experiment for electrodes with different geometry: planar (black line) and hemispherical (red line). From [2]

3.1.2 Semi-infinite spherical diffusion (the case of a hemispherical microelectrode)

Applying the potential step experiment to a hemispherical electrode, the second Fick's law in spherical coordinates becomes [2]:

$$\frac{\partial C_{Ox}(r,t)}{\partial t} = D_{Ox}\left[\frac{\partial^2 C_{Ox}(r,t)}{\partial r^2} + \frac{2}{r}\frac{\partial C_{Ox}(r,t)}{\partial r}\right] \qquad (eq\ 9)$$

where r is the radial distance from the electrode center, and the other symbols have their usual meaning.

The solution of *eq 9* allows obtaining the concentration profiles; the solution of the first Fick's law and considering its relationship with the current intensity, provides the following relation [2]:

$$i = \frac{nFAD_{Ox}^{1/2} C_{Ox}^b}{\pi^{1/2} t^{1/2}} + \frac{nFAD_{Ox} C_{Ox}^b}{r_0} \qquad (eq\ 10)$$

where r_0 is the electrode radius.

It is evident that for t→0 *eq 10* is identical to the Cottrell equation (*eq 8*). For t → ∞ (or in the case of an electrode with very small radius r_0), *eq 10* becomes:

$$i = 2\pi nFD_{Ox}C_{Ox}^b r_0 \qquad (eq\ 11)$$

that is a steady-state current. **Fig 3.3** (black curve) shows the current-time profile for a hemispherical electrode. It is evident that this profile differs from that observed for a planar electrode because of the achievement of a steady state at relatively long times.

3.1.2.1 Diffusion at a microdisk electrode

Diffusion to a microdisk is complicated theoretically, as it occurs radially, with respect to axis of symmetry, and normal to the plane of the electrode (**Fig 3.3**). The second Fick's law for the *Ox* species needs to be written in cylindrical coordinates [1, 2].

$$\frac{\partial C_{Ox}}{\partial t} = D_{Ox}\left[\frac{\partial^2 C_{Ox}}{\partial r^2} + \frac{1}{r}\frac{\partial C_{Ox}}{\partial r} + \frac{\partial^2 C_{Ox}}{\partial z^2}\right] \qquad (eq\ 12)$$

Where *r* is the radial direction with the origin at the center of the disk, and *z* is the direction perpendicular to the electrode surface (**Fig 3.4**).

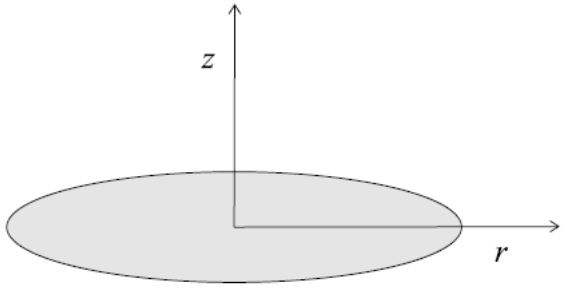

Fig 3.4-Coordinates for a microdisk electrode

The solution of *eq 12* is very complex. Approximate numerical solutions have been provided to predict with good accuracy the current / time responses for this electrode geometry [1, 3-8]. Among them, that proposed by Shoup and Szabo (*eq 15*) [4] covers the entire range of time in a single relationship as a function of the adimensional parameter τ

$$i(\tau) = \frac{4nFAD_{Ox}C_{Ox}^{b}}{\pi a} f(\tau) \qquad (eq\ 13)$$

where $f(\tau)$ is given by

$$f(\tau) = 0.7854 + 0.8862\tau^{1/2} + 0.2146\, e^{-0.7823\tau^{-1/2}} \qquad (eq\ 14)$$

and

$$\tau = \frac{4D_{Ox}t}{a^2} \qquad (eq\ 15)$$

where *a* is the radius of the microdisk.

For $t \rightarrow 0$, *eq 13* is reduced to the Cottrell equation; while for $t \rightarrow \infty$, *eq 13* becomes

$$i = i_{ss} = 4nFD_{Ox}C_{Ox}^{b}a \qquad (eq\ 16)$$

3.2 Voltammetric techniques

Diffusion equations for voltammetric techniques are similar to those considered in section 2.1 and depend on whether planar or spherical diffusion applies. The boundary conditions to solve the second Fick's law vary according to the specific wave-form and process considered. In what follows a summary of the wave-forms, of typical voltammetric responses, as well as of important potential and current parameters expected from the various techniques employed in the thesis is given.

3.2.1 Cyclic Voltammetry

The wave form of cyclic voltammetry (CV) is shown in **Fig 3.5**. The voltage from an initial value E_i is swept linearly up to a potential E_f, at which the scan direction is reversed and then swept back to E_i.

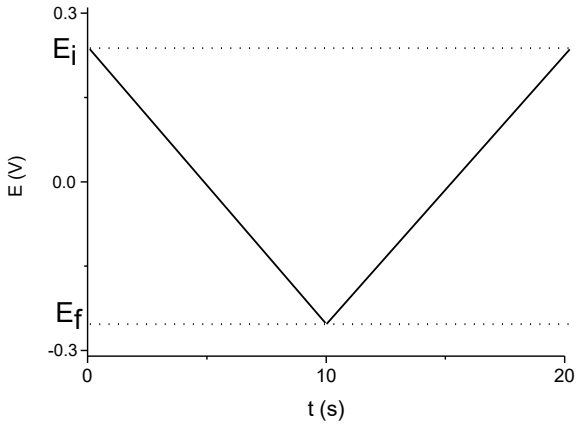

Fig 3.5- Wave form applied to the working electrode in a typical Cyclic voltammetry experiment.

For conventional electrodes, where planar diffusion applies, a typical CV response for a reversible reduction process is shown in **Fig 3.6.**

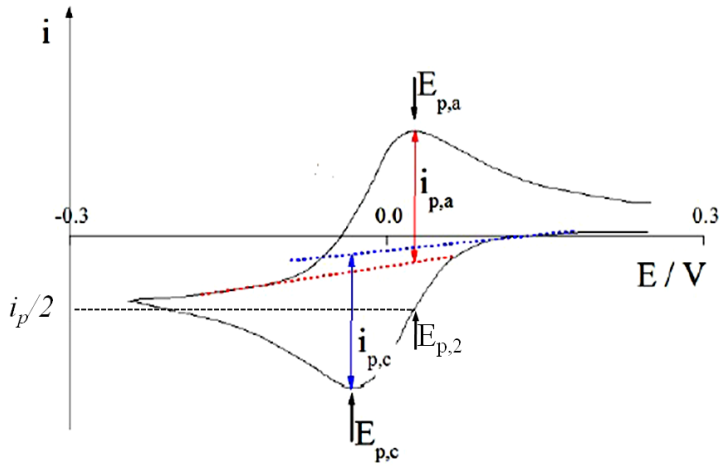

Fig 3.6-Cyclic voltammogram predicted for a one electron, reversible reduction process at a conventional electrode.

Important parameters are: the cathodic ($E_{p,c}$) end anodic peak ($E_{p,a}$) potentials; the cathodic ($i_{p,c}$) and anodic (i_{pa}) peak currents. The analysis of these parameters as the scan rate varies allows establishing the nature of the electrode process and, in particular, the reversibility of the heterogeneous charge transfer. The maximum current of the forward peak for a reversible reduction process (**Fig 3.6**) is expressed by the Randles-Sevcick equation (at 25°C) [1, 2]:

$$i_p = 2.69x10^5 n^{3/2} A D_{Ox}^{1/2} C_{Ox}^b v^{1/2} \qquad (eq\ 17)$$

where v is the scan rate and the other symbols have their usual meaning, as described in the previous sections.

Peak potential ($E_{p,c}$) is independent from scan rate, and can be expressed by the relation [2]

$$E_p = E_{1/2} - 1.109\frac{RT}{nF} \qquad (eq\ 18)$$

peak potentials separation is:

$$\Delta E = E_{p,c} - E_{p,a} = \frac{59}{n}\ mV \qquad (eq\ 19)$$

regardless of scan rate.

The ratio of peak currents is equal to one, regardless of scan rate.

$$\frac{i_{p,c}}{i_{p,a}} = 1 \qquad (eq\ 20)$$

According to (*eq 17*), the peak current is proportional to the square root of the scan rate.

Another useful parameter for to assess reversibility or redox processes is $|E_p - E_{p/2}|$, where $E_{p/2}$ is the potential at $i_p/2$ (**Fig 3.6**). For a reversible process this difference is 56/n mV, where n is the number of electron exchanged.

In the case where the electron transfer is slow, considerably different voltammetric pictures are obtained, as shown in **Fig 3.7** (lines b, c).

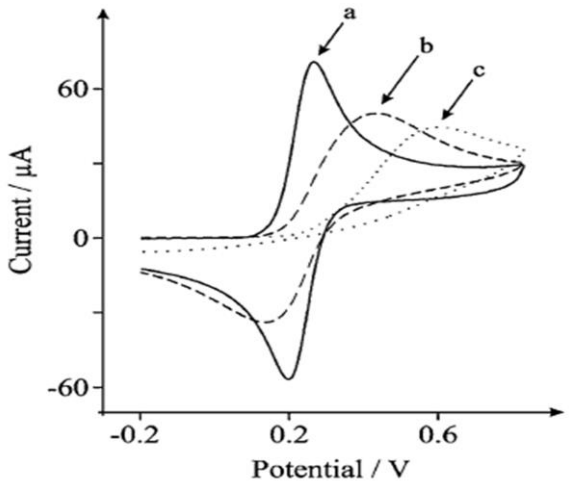

Fig 3.7- Cyclic voltammograms for reversible (**a**), quasi-reversible (**b**) and fully irreversible (**c**) electron transfer. From [1].

The maximum peak current for irreversible electron transfer (**Fig 3.7,** line c), is given (at 25°C) by

$$i_p = 2.99x10^5 \alpha^{1/2} A D_{Ox}^{1/2} C_{Ox}^b \nu^{1/2} \qquad (eq\ 21)$$

where α is the transfer coefficient and the other symbols have their usual meaning. Also in this case, the peak current is proportional to the square root of the scan rate.

Peak potential is function of scan rate. It can be expressed by the following relation:

$$E_p = E^0 - \frac{RT}{\alpha F}\left[0.780 + ln\left(\frac{D_{Ox}^{1/2}}{k^0}\right) + ln\left(\frac{\alpha F \nu}{RT}\right)^{1/2}\right] \qquad (eq\ 22)$$

The parameter $|E_p - E_{p/2}|$ is provided by the following equation

$$|E_p - E_{p/2}| = \frac{1.857RT}{\alpha F} = \frac{47.7}{\alpha}\ mV \qquad (eq\ 23)$$

peak potentials separation increases with scan rate [2].

In the case of micro disk electrodes, due to the complexity of the mathematical treatments, again only approximate relationships have been derived. The shape of the voltammograms depends on

the scan rate employed. At sufficiently high scan rates, planar diffusion applies [2], and therefore the CV has a shape as that recorded for a conventional sized electrode (**Fig 3.6**). At sufficiently low scan rates, instead, radial diffusion applies and the shape of the CV is sigmoidal, with no hysteresis on scan reversal (**Fig 3.8**). Therefore, the CV is under steady-state and the current plateau can be predicted by *eq 16* [2, 8].

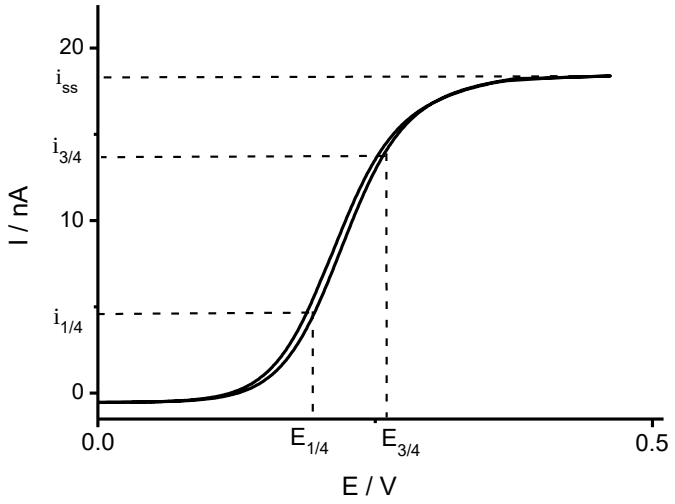

Fig 3.8 - Cyclic voltammograms of 5 mM of Ferrocene recorded at a Pt (Ø = 25 µm) microelectrode at 5 mV/s.

It is possible to characterize reversibility at microelectrodes by the difference $|E_{3/4} - E_{1/4}|$ that is called Tomeš parameter. The potentials $E_{3/4}$ and $E_{1/4}$ are those for which $i = 3i_{ss}/4$ and $i = i_{ss}/4$, respectively (**Fig 3.8**). Value of Tomeš parameter of 59/n mV corresponds to a reversible process.

Transition from typical steady state to peak shaped voltammograms can be obtained by increasing the scan rate, as is displayed in **Fig 3.9**.

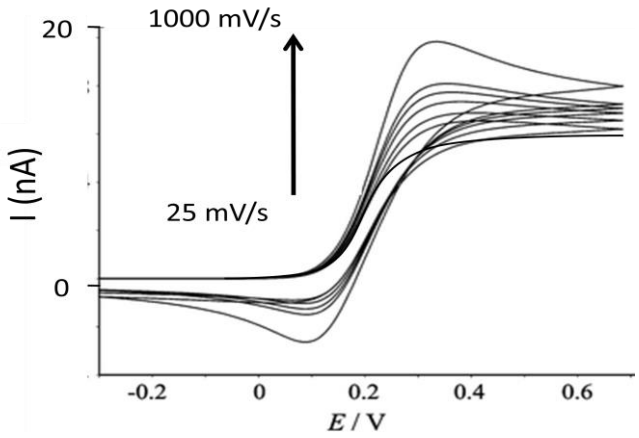

Fig 3.9 - Cyclic voltammograms of Ferrocene recorded at a Pt (Ø = 25 µm) microelectrode at increasing scan rates (form 0.025 to 1 V/s).

The current maximum at the different scan rates can be predicted with sufficiently accuracy (the error is <0.23%) using equation *eq 24*, derived by simulations a function of the dimensionless parameter *p* [8, 9]:

$$\frac{i_p}{4nFCDa} = 0.34\exp(-0.66p) + 0.66 - 0.13\exp\left(\frac{11}{3}\right) + 0.351p \qquad (eq\ 24)$$

Where *p* is:

$$p = \left(\frac{nFa^2v}{RTD}\right) \qquad (eq\ 25)$$

and other symbols have their usual meaning.

The planar contribution to the steady-state current can be accounted for by the parameter *p*, as is shown in **Table 3.1** for a range of values [9].

P	% planar diffusion
0.6	10
0.33	5
0.21	3
0.076	1

Table 3.1: some values of p parameter and correspondent planar diffusion contribution (%)

3.2.2 Differential Pulse Voltammetry

Differential Pulse Voltammetry (DPV) is a technique that employs a particular potential modulation to discriminate between Faradaic to capacitive currents, thus increasing sensitivity [2, 10, 11]. A typical wave-form is displayed in **Fig 3.10A**. It is composed by a series of regular voltage pulses superimposed on a staircase. Two current samples are taken during each step time, the first immediately before the pulse, the second late in the pulse just before pulse end. A DPV response is given by the difference of the two sampled currents against the base potential of the staircase (**Fig 3.10B**).

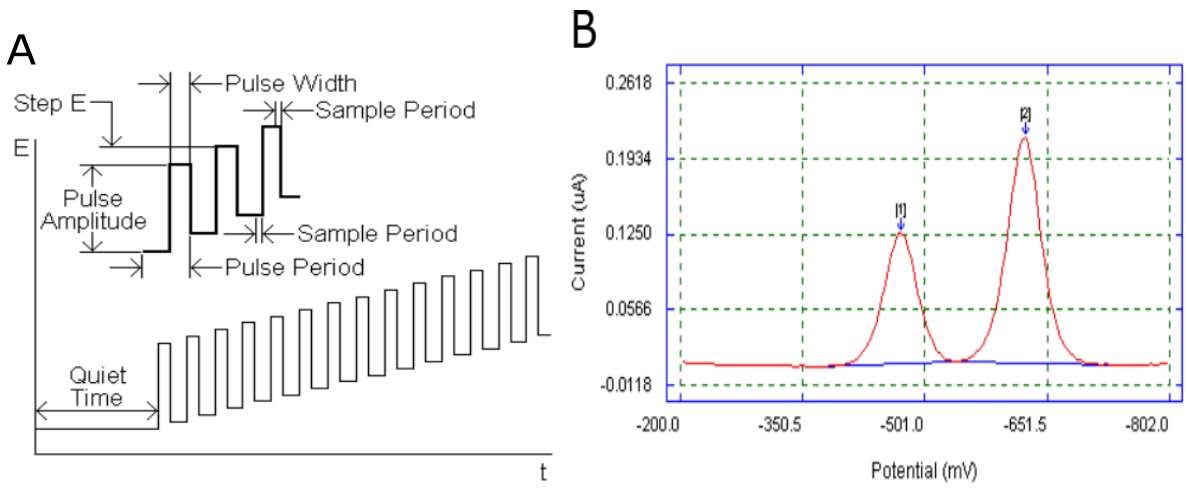

Fig 3.10- (A) differential pulse voltammetry waveform. (**B**) Typical differential pulse voltammogram of two analytes. From [11].

Besides being useful to eliminate the capacitive current, DPV is convenient for resolving the voltammetric signals due to two (or more) species with close half-wave potentials, producing easily quantifiable peak shaped responses (**Fig 3.10B**) [11].

3.2.3 Thin layer Voltammetry

Thin layer voltammetry is carried out under conditions where a thin layer of electrolytic solution is contained between the electrode and the electrochemical cell wall, generally at a distance of less than few tens of microns (thus comparable with diffusion layer thickness) [2].

The consequence of this cell configuration implies that the phenomena related to the mass transport of *Ox* and *Red* are practically absent and that the concentration of *Ox* and *Red* at each potential is uniform in the considered solution layer.

A thin cell behavior makes the principles of the electrode processes to radically differ from those seen previously (section 3.2.1). Considering a condition in which a potential scan is applied, the shape of the voltammograms takes forms as those shown in **Fig 3.11**, for a linear sweep (**Fig. 3.11A**), or for a cyclic voltammetry (**Fig 3.11B**).

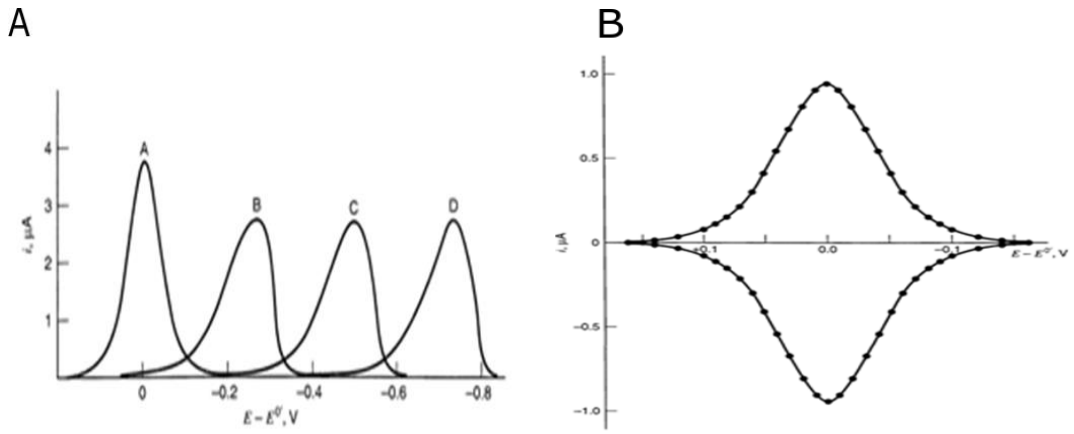

Fig 3.11- (**A)** linear sweep voltammograms corresponding to processes with decreasing value (from A to D) of heterogeneous rate constant; (**B**) cyclic voltammogram of a reversible, monoelectronic process recorded in a thin layer cell. From [2].

The peak current ($i_{p,c}$) of the forward scan is given by:

$$i_p = \frac{n^2 F^2 V \nu C_{Ox}^*}{4RT} \qquad (eq\ 26)$$

where *V* is the volume of electrolyte solution involved and other symbols have their usual meaning. From this equation it is observed that the peak current is directly proportional to the concentration of the analyte and to the scan rate. Therefore, a rapid diagnostic criterion for determining whether a voltammetric wave has a thin layer behavior is to verify that the peak current is linearly dependent on *v*. On the other hand, the area under the peak corresponds to the charge (Q) involved in the electrolysis of the analyte present in the thin layer. Therefore, on the basis of Faraday's law, it corresponds to the number of moles of the electrolyzed analyte, obtainable from the well known equation:

$$Q = nFN_0 \qquad (eq\ 27)$$

where N_0 is the number of moles of the species undergoing oxidation or reduction.

For an irreversible process, the current and the potentials of the peaks depend not only on the parameters seen above, but also on the transfer coefficient α and on the charge transfer constant k_0.

In particular, i_{pc} is given by:

$$i_{p,c} = \frac{\alpha F^2 V \nu C_{Ox}^*}{2.718RT} \qquad (eq\ 28)$$

and the peak potential ($E_{p,c}$) is given by:

$$E_{p,c} = E^{0\prime} + \frac{RT}{\alpha F}\ln\left(\frac{RTK^0}{\alpha FV\nu}\right) \qquad (eq\ 29)$$

where the symbols have their usual meaning. From *eq 28* it can be observed that also in this case the $i_{p,c}$ linearly depends on both concentration and scan rate. As for E_{pc}, it is displaced with respect to the value of the formal (or standard) potential E_0 of an amount which depends on both α and k_0. The area of the peak, even in these conditions, corresponds to the number of moles of electrolyzed substance.

3.2.4 Voltammetry of chemical species adsorbed on the electrode surface

The theory for voltammetric responses of a reversible *Ox* + ne $\rightleftharpoons$ *Red* process, in which both *Ox* and *Red* can give adsorption phenomena, follows straightforward same theory developed for a thin layer cell.

The shape of voltammograms, however, depends on the following circumstances:

-1) both *Ox* and *Red* are electro-active.

-2) only *Ox* or *Red* are adsorbed.

-3) the electrode process is reversible or non-reversible.

For case 1) and when the electrode process is reversible, the CVs have the shapes as those shown in **Fig 3.12**.

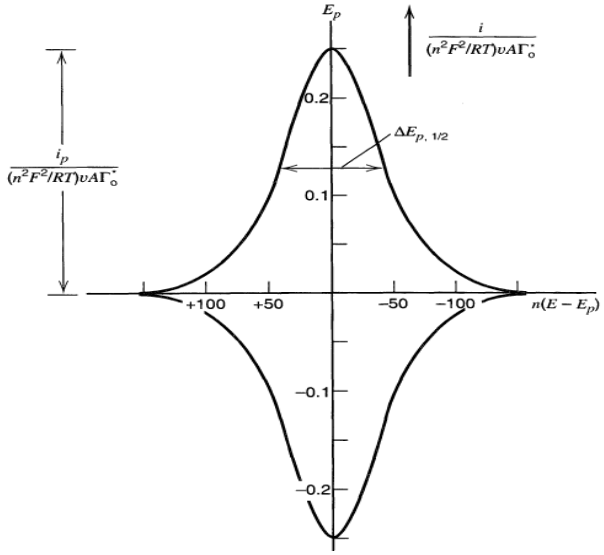

Fig 3.12-Theoretical cyclic voltammetric curve for reduction and subsequent reoxidation of adsorbed *Ox*. From [2].

I_p and E_p are given by the following equations:

$$i_p = \frac{n^2F^2}{4RT}\nu A\Gamma_{ox}^* \qquad (eq\ 30)$$

$$E_p = E^{0\prime} - \frac{RT}{nF}\ln\left(\frac{b_{Ox}}{b_{red}}\right) \qquad (eq\ 31)$$

where (Γ_o *) corresponds to the amount of *Ox* at saturation of the surface, while b_{Ox} and b_{Red} are two parameters that account for both to the type of adsorption isotherm that characterizes the species of the redox couple and to the surface fraction covered by *Ox* and *Red* [2].

From *eq 30* it is evident that, also in this case, i_p is proportional to the scan rate and to the amount of species adsorbed on the electrode surface. The area under the peak is related to the charge required to reduce the layer of material adsorbed on the electrode surface, and it is therefore given by:

$$Q = nFA\ (\Gamma\ *) \qquad (eq\ 32)$$

The peak observed in the reverse scan is the mirror image of the process obtained in the forward scan.

For an ideally reversible process, assuming that the adsorption follows the Langmuir isotherm, the anodic and cathodic peak potentials are identical ($E_{p,a} = E_{p,c}$).

Moreover, the total width at half height of either the cathodic and anodic peaks, $\Delta E_{p,1/2}$, is given by:

$$\Delta E_{p,1/2} = 3.53\frac{RT}{nF} = \frac{90.6}{n}\ mV \qquad (eq\ 33)$$

For adsorption processes which do not follow case 1) and the electrode process is irreversible, the current potential profile is given by.

$$I_p = FAk'\Gamma_{ox}^{*}exp\left[\left(\frac{RT}{\alpha F}\right)\left(\frac{k'}{v}\right)\right] \qquad (eq\ 34)$$

For these processes, the parameters i_p, E_p and $\Delta E_{p,1/2}$ are provided by the following equations:

$$i_p = \frac{\alpha F^2 A v \Gamma_O^{*}}{2.718RT} \qquad (eq\ 35)$$

$$E_p = E^{0\prime} + \frac{RT}{\alpha F}\ln\left(\frac{RT\,k^0}{\alpha F\,v}\right) \qquad (eq\ 36)$$

$$\Delta E_{p,1/2} = 2.44\left(\frac{RT}{\alpha F}\right) = \frac{62.5}{\alpha}mV \qquad (eq\ 37)$$

For irreversible processes, the shape of the peak becomes less symmetrical, as shown, for example, in **Fig 3.13** [2, 12].

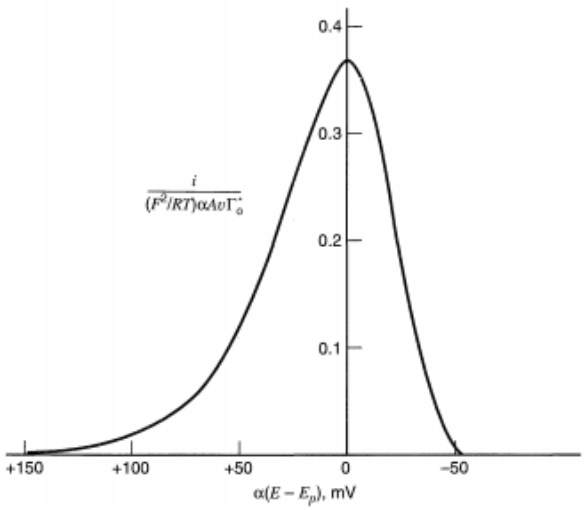

Fig 3.13- Theoretical voltammogram of an irreversible adsorption electrode process. From [2].

3.2.5 Adsorptive Stripping Voltammetry

The adsorptive stripping voltammetry (AdSV) is a variant of voltammetric stripping techniques. It is based on the pre-concentration of the analyte on the electrode surface by adsorption, followed by the scanning of the potential in the cathodic or anodic direction, with consequent reduction or oxidation of the analyte [2, 12].

The technique includes two steps (**Fig 3.14**): accumulation of the analyte (or of an analyte's product) on the surface of the working electrode by electrolysis; re-dissolution (stripping) of the adsorbed species by applying a voltammetric technique.

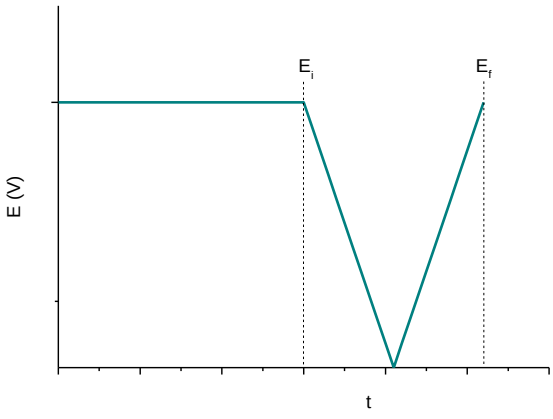

Fig 3.14- wave form imposed in a typical AdSV experiment. From [2].

AdSV is very sensitive, since the adsorption takes place on the flat electrode surface, therefore all the deposited material is immediately available for reduction or oxidation. In addition to sensitivity, the main advantage of the technique is its applicability to a wide number of

compounds. However, deviations to the linearity of the response may occur due to the surface saturation. Because of its characteristics, AdSV suffers from interference due to the competitive absorption of other substances that may be present in the sample [12].

3.3 Scanning Electrochemical Microscopy

Scanning electrochemical microscopy (SECM) is a technique that allows performing chemical and electrochemical investigations on surfaces of various kinds and to the interface of solid / liquid, liquid / liquid and liquid / gas systems. This technique is based on the controlled movement of a microelectrode close to the surface under investigation, as is schematized in **Fig 3.15** [2, 13].

The measured signal corresponds, typically, to the Faradaic current associated with the oxidation / reduction of a redox mediator, i.e., an electroactive species in solution that can interact with the surface of the sample in various ways [13]. One of the fundamental aspects of SECM is that the current signal is reproducibly perturbed on the basis of the distance between the sample surface and the microelectrode. This perturbation is related to the fact that the sample surface may hinder the transport of species towards the electrode (**Fig 3.15b**), or may behave as a local source of electroactive species (**Fig 3.15c**) [13].

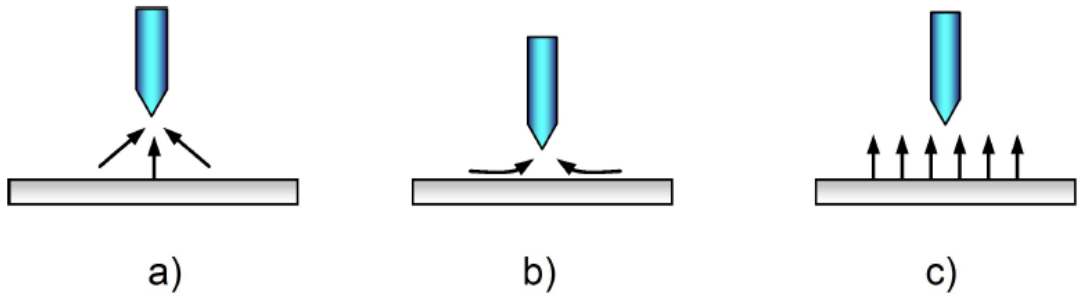

Fig 3.15 - Effect of approaching of the SECM probe to the target surface on the diffusion of the electroactive species.

A typical SECM apparatus is shown in **Fig 3.16**. It consists of an electrochemical cell equipped with three electrodes (microelectrode, counter electrode and reference electrode), a bipotentiostat for controlling the potential applied to the microelectrode (working electrode) and/or to the substrate (if it is a conductor) and a micropositioner. The substrate investigated is usually placed on the bottom of the cell and the electrolyte solution contains a redox mediator, i.e., an electroactive species of known electrochemistry, whose response at the microelectrode allows characterizing the substrate properties.

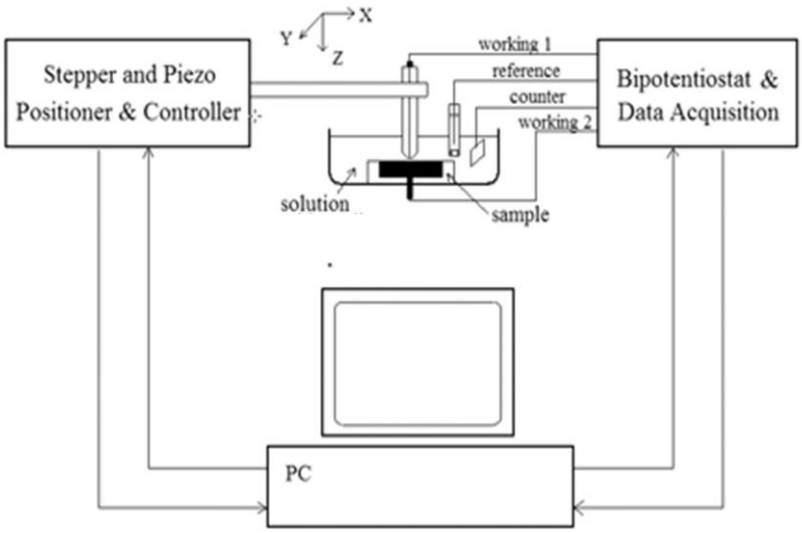

Fig 3.16 - Scheme of a typical SECM setup.

3.3.1 Modes of operation

There are many operation modes of SECM, and their classification derives from the way the tip is moved/kept above the substrate or on the interaction of the redox mediator with both microelectrode and substrate. In the following, SECM operational modes employed in the present thesis are briefly illustrated.

In the feedback mode the microelectrode is perpendicularly moved away from, or approached to the substrate (**Fig 3.17**). In this way, it is possible to investigate the features of the sample surface by recording the so called approach curves.

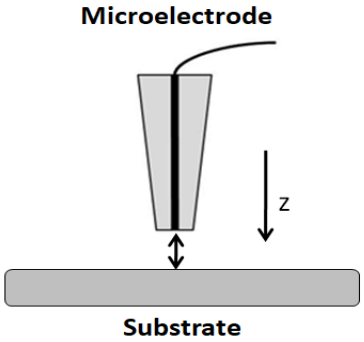

Fig 3.17 – Feedback mode

In the scanning mode the microelectrode is placed at a fixed distance above the substrate and it is translated parallel to the surface in a two or one dimension along the surface (**Fig 3.18**). The plot of current as a function of the spatial coordinates allows imaging the investigated surface in terms of either topography and chemical reactivity.

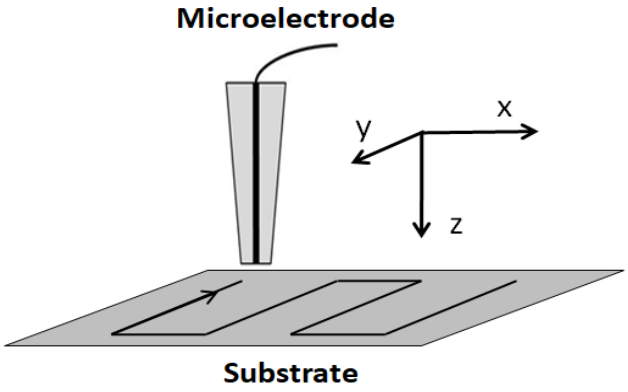

Fig 3.18 - Scanning mode

The generation/collection mode can be distinguished in tip generation/substrate collection (TG/SC) and substrate generation/tip collection (SG/TC). In TG/SC the tip generates an electroactive species that diffuses across the tip-substrate gap and eventually reacts with the substrate (see **Fig 3.19A**). In the SG/TC an electroactive species is generated at the substrate surface and it is collected at the tip (**Fig 3.19 B**).

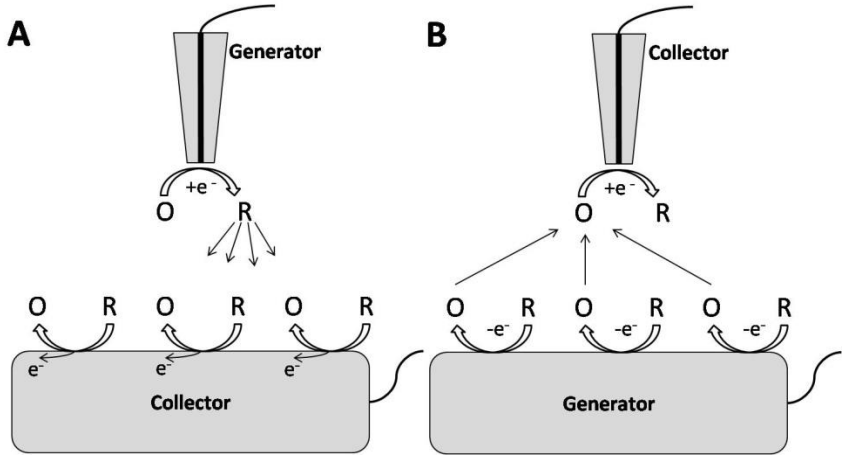

Fig 3.19 – Generation-Collection mode. **A**) TG/SC, the species generated at the tip is collected at the substrate. **B**) SG/TC, the species generated at the substrate is collected at the tip.

3.3.2 SECM probes

In most of the SECM applications, the microelectrodes are disk shaped. Therefore, main characteristics of SECM probes of such geometry are described as it follows.

RG parameter

SECM spatial resolution depends primarily on the microelectrode size and the RG parameter; the latter is defined as :

$$RG = \frac{R}{a} \qquad \textit{(eq 38)}$$

where *R* is the overall radius of the electrode tip, which includes both the insulating sheath and the metal disk (**Fig 3.20**); *a* is the radius of the microdisk.

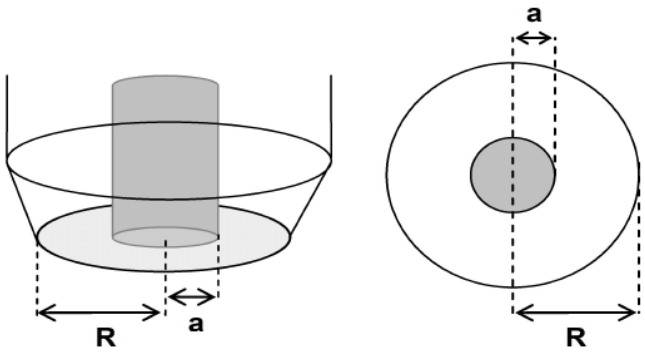

Fig 3.20-Scheme of a SECM tip showing the parameters *R* and *a* for RG determination.

3.3.3 Feedback Mode

The steady state current at a microelectrode is affected by the presence of a substrate when the distance between the microelectrode and the substrate is less than the thickness of the diffusion layer that grows at the microelectrode surface [13]. In fact, when the SECM tip is far from the substrate (**Fig 3.21A**), the application of a suitable potential produces a steady state current (predicted by *eq 16*, see page 33). When the tip is brought very near the substrate surface, the current is perturbed by two effects. If the surface is not conducting (or inactive), the substrate blocks diffusion of the redox mediator towards the microelectrode (**Fig 3.21B**) and the current decreases [13]. This phenomenon is called “negative feedback”. If the substrate is conducting (or active) and is able to regenerate the redox mediator (**Fig 3.21C)**, the result is a larger flux of the redox mediator and the current increases [13]. This phenomenon is called “positive feedback”. Therefore, in either cases, the current at the SECM tip is a function of its distance.

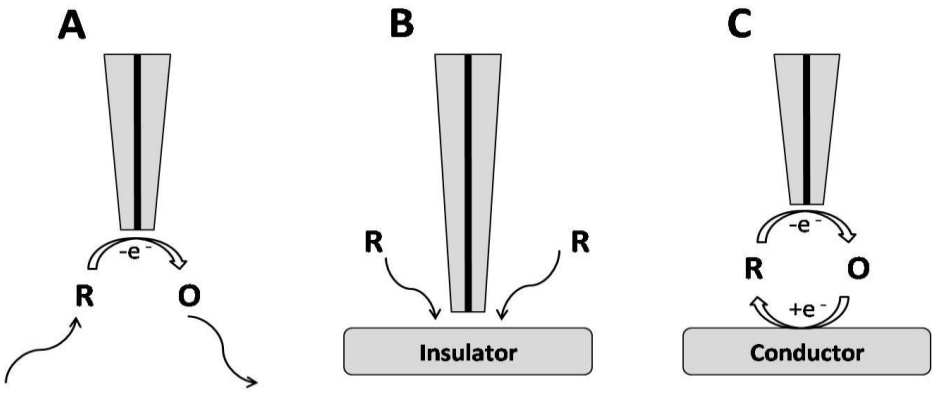

Fig 3.21 - Feedback mode: **A**) the tip is in the bulk of the solution containing the redox mediator; **B**) Negative feedback; **C**) Positive feedback.

3.3.3.1 Approach Curves

The feedback effects are, in general, visualized by plots of the normalized current $(i/L) = i_M/i_{L\infty}$ as a function of the normalized tip-substrate distance, $L = d/a$. These plots are called *approach curves* and allows establishing the microelectrode position with respect to the sample surface under investigation. Theoretical approach curves have been derived for several electrode geometries using digital simulations and numerical approaches [13-15].

For a microdisk, *eq 39* has been proposed to account for the negative feedback effects:

$$\frac{i_M}{i_{L,\infty}} = \frac{1}{K_1^N + \frac{K_2^N}{L} + K_3^N . \; e^{\frac{K_4^N}{L}}} \qquad (eq\ 39)$$

where K_1^N, K_2^N, $K_3^N$and K_4^N are constants, which depend on the *RG* parameter [13]. Typical approach curves calculated by *eq 39* as a function of *L*, are displayed in **Fig 3.22**.

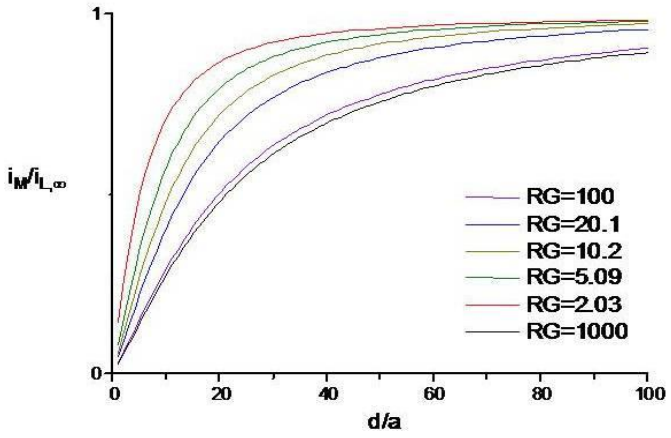

Fig 3.22: Theoretical approach curves in negative feedback conditions obtained for different RG values. From [13].

It is evident that for large *d* values (*i.e.*, long microelectrode to substrate distances), *RG* has no influence. For small *d* values, the slope is affected by *RG* and, in particular, it becomes higher as *RG* decreases. This indicates a higher sensitivity (i.e., higher spatial resolution) of the probe in the *z* direction.

For positive feedback effects, the following *eq 40* has been proposed:

$$\frac{i_M}{i_{L,\infty}} = K_1^P + \frac{K_2^P}{L} + K_3^P .\ e^{\frac{K_4^N}{L}} \qquad \textit{(eq 40)}$$

Where, again, K_1^P, K_2^P, $K_3^P$and K_4^P are constants, which depend on RG [15] (**Fig 3.23)**.

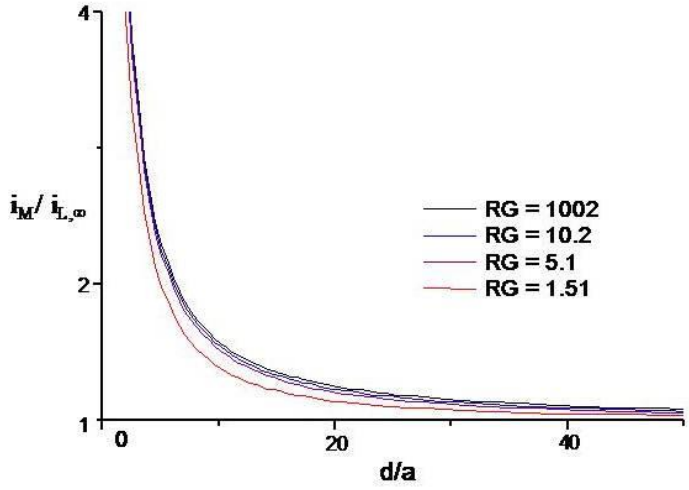

Fig. 3.23-Theoretical approach curves in positive feedback conditions obtained for different RG values. From [13].

As it is evident, in this case, *RG* is relatively unimportant in determining the shape of the approach curve. In fact, either for large or small *L* values, the response of the microelectrode is, respectively, little or much influenced by the presence of the substrate, regardless of the *RG* value.

The approach curves, apart from they use to establish the tip to substrate distances, they play an important role in the characterization of microelectrodes to define both *R* and *a*, and, consequently, *RG* parameters. For the latter purpose, fitting of experimental and theoretical approach curves is performed (see above).

3.3.4 Applications of SECM

SECM has been exploited in a large number of applications, too numerous to be recalled here, so this section will consider a selection of studies where the unique properties of SECM have been harnessed.

a-SECM as a tool for imaging chemical information:

One of the most striking examples of the concept of scanning electrochemical imaging with a redox mediator is the mapping of precursor sites for pitting on metal and metal oxide layers [16,17]. In these studies it was demonstrated the ability of the technique to image a localized chemical process, as for instance the breakdown in the passivation of the oxide layer, before the onset of corrosion; to image a variety of interfacial reactions including biological and chemical processes [18-22]. Recently the imaging capability was demonstrated on a large scale with the use of flexible tip arrays [23, 24].

b-SECM as tool to provide variable mass transfer conditions:

In many studies the SECM is operated in a direction normal to the substrate simply to vary the rate of mass transport. Far away the tip operates as an independent microelectrode and its steady state mass transfer coefficient, $k_{m,\infty}$, is determined by the tip geometry. Thus, k_m can be finely tuned to values below $k_{m,\infty}$ when approaching an inert substrate (hindered diffusion) or to values above $k_{m,\infty}$ when approaching a conducting substrate (positive feedback). Therefore, SECM can be operated as a tool providing a variable steady state mass transfer coefficient, akin to the rotating disc electrode but without the inherent problems of hydrodynamically controlled systems [25].

c-SECM as a tool to investigate lateral charge transfer:

The technique has been used in several studies to probe how charges propagate at the surface of the substrate to sustain the charge transfer process between the substrate and the redox mediator [26]. For instance, lateral charge propagation along ultrathin polyaniline layers (mono and multilayers) was investigated and from these measurements, accurate SECM methodology to extract the conductivity of thin films from feedback measurements [27].

References

[1] R.G. Compton, E. La Borda, K.R. Ward, Understanding Voltammetry, Imperial College Press, Singapore (2014).

[2] A.J. Bard, L.R. Faulkner, Electrochemical Methods, Wiley, New York (2001).

[3] I. Lavagnini, P. Pastore, F. Magno, Journal of Electroanalytical Chemistry 333 (1992) 1-10 S.
[4] D. Shoup, A.Szabo, Journal of Electroanalytical Chemistry 140 (1982) 237-408.

[5] K. Aoki, K. Akimoto, K. Tokuda, H. Matsuda, J. Osteryoung, Journal of Electrtoanalytical Chemistry

[6] C.G. Zoski, Handbook of Electrochemistry, Elsevier (2007).

[7] M. Fleishmann, S. Pons, D.R. Rolison, P.P. Schmidt, Ultramicroelectrodes, Datatech (1987).

[8] S. Daniele, C. Bragato, Environmental Analysis by Electrochemical Sensors and Biosensors, Springer Science+Business Media, New York (2014).

[9] K. Stulik, C. Amatore, K. Holub, V. Marecek, W. Kutner, Pure and Applied Chemistry 72 (2000) 1483-1492.

[10] J.B. Flato, Analytical Chemistry 44 (1972) 75A.

[11] D.A.C Brownson, C.E. Banks, The handbook of grapheme electrochemistry, Chapter 2, Springer (2014).

[12] C. Batchelor-McAuley, E. Kätelhön, E.O. Barnes, R.G Compton, E. Laborda, A. Molina, Chemistry Open 4 (2015) 224-60.

[13] A.J. Bard, M.V. Mirkin, Scanning Electrochemical Microscopy, M. Dekker, New York, (2001).

[14] G. Linsday, G. Denuault, S. Daniele, E. De Faveri, Analytical Chemistry 79 (2007) 2952-2956.

[15] M.V. Mirkin, F. Ren, F.F. Fan, A.J. Bard, Journal of Electroanalytical Chemistry 328 (1992) 47.

[16] R.M. Souto, Y. Gonzales-Garcia, D. Battistel, S. Daniele, Chemistry-A European Journal 18 (2012) 230-236.

[17] R.M. Souto, Y. Gonzales-Garcia, D. Battistel, S. Daniele, Corrosion Science 55 (2012) 401-406.

[18] G. Wittstock, W. Schuhmann, Analytical Chemistry 69 (1997) 5059-5066.

[19] C.A. Zhao, G. Wittstock, Analytical Chemistry 76 (2004) 3145-3154.

[20] M. Zhang, A. Becue, M. Prudent, C. Champod, H.H. Girault, Chemistry Communications 37 (2007) 3948-3950.

[21] M.Q. Zhang, H.H. Girault, Electrochemistry Communications 9 (2007) 1778-1782.

[22] M. Zhang, H.H. Girault, Analyst 134 (2009) 25-30.

[23] F. Cortes-Salazar, M. Trauble, F. Li, J.M. Busnel, A.L. Gassner, M. Hojeij, G. Wittstock H.H. Girault, Analytical Chemistry 81 (2009) 6889-6896.

[24] F. Cortés-Salazar, D. Momotenko, H.H. Girault, A. Lesch, G. Wittstock, Analytical Chemistry 83 (2011) 1493-1499.

[25] A.J. Bard, Scanning Electrochemical Microscopy. In Scanning Electrochemical Microscopy, 2nd ed.; Bard, A. J.; Mirkin, M. V., Eds. CRC Press: Boca Raton, 2012; p 660.

[26] D. Mandler, P.R. Unwin, Journal of Physical Chemistry B 107 (2013) 407-410.

[27] A.L. Whitworth, D. Mandler, P.R. Unwin, Physical Chemistry Chemiscal Physycs 7 (2005) 356-365.

Chapter 4: Experimental

4.1 Chemicals and materials

- Solvents

Acetonitrile (CH_3CN anhydrous, 99.9%), dimethylsulfoxide (DMSO, anhydrous, ≥ 99.9%), isopropanol, were purchased from Sigma Aldrich. Ethyl acetate (EtOAc, ≥ 99.9%) was from Fischer Chemicals, Methanol, LC-MS Grade, was from VWR International, Ethanol, LC-MS grade, was from FLUKA.

- Supporting electrolytes

Tetrabutylammonium hexafluorophosphate ($TBAPF_6$), tetrabutylammonium perchlorate ($TBAClO_4$), potassium chloride (KCl), potassium nitrate (KNO_3), 1-Ethyl-3-methylimidazolium tris(pentafluoroethyl)trifluorophosphate (MIM-TPT) were from Sigma Aldrich.

- Buffers

Phosphate buffered saline (PBS, tablets), 2-(N-Morpholino)ethanesulfonic acid hemisodium salt (MES buffer) were from Sigma Aldrich.

- Drugs and related metabolites

7-ethyl-10[4-(piperidino)-1piperidino]-carbonyloxycamptothecin hydrochloride, (irinotecan hydrochloride, CPT-11HCl), 7-ethyl-10-hydroxycamptothecin (SN-38), 4-[(4-Methyl-1-piperazinyl)methyl]-N-(4-methyl-3-{[4-(3-pyridinyl)-2-pyrimidinyl]amino}phenyl)benzamide **(**Imatinib or IMA),N-[4-methyl-3-[(4-pyridin-3-ylpyrimidin-2-yl)amino]phenyl]-4-(piperazin-1-ylmethyl)benzamide (N-desmethyl imatinib or Des-imatinib), all at purity≥ 98 %, were purchased from Sigma Aldrich. 7-Ethyl-10-hydroxy-camptothecin glucoronide (SN-38G), 7-ethyl-10-[4-N-(5-aminopentanoicacid)-1-piperidino]carbonyloxycamptothecin (APC), 7-ethyl-10-[4-(1-piperidino)-1-amino]-carbonyloxycamptothecin (NPC), camptotechin (CPT), N-(4-{[(2-Amino-5-formyl-4-oxo-1,4,5,6,7,8-hexahydro-6pteridinyl)methyl]amino}benzoyl) glutamic acid **(**folinic acid, or FA) were from Toronto research chemicals, Canada. 5-Fluoro-2,4(1H,3H)-pyrimidinedione **(**5- Fluoruracil, or 5-FU) was from Tocris Bioscience.

- Other chemicals

Triethylamine (TEA), triethylammonium chloride (TrEAHCl), tetraethylammonium chloride (TEACl), tetrabutylammonium hydroxide (TBAOH), tris(β-diketonato)ruthenium(III) ($Ru(acac)_3$),iso-quinoline, Sulfo-N-hydroxysuccynimmide (NHS), 1-Ethyl-3-(3-

dimethylaminopropyl)carbodiimide hydrochloride (EDCHCl), mercaptoottanoic acid (MOA), mercaptoundecanoic acid (MUA), sodium nitrite ($NaNO_2$), 1-butyl-3-methylimidazolium bis(trifluoromethyl-sulfonyl)imide [BMIM][NTF_2], 1-butyl-3-methylimidazolium hydrogen sulphate [BMIM][HSO_4], Hexanaldehyde, propanaldehyde and 2,6,10,15,19,23-hexamethyl-2,6,10,14,18,22-tetracosahexaene (squalene), potassium exachloroiridate ($K_3[IrCl_6]$), ferrocene (Fc), ferrocene-methanol (Fc-MeOH), hexammineruthenium trichloride ($[Ru(NH_3)_6]Cl_3$), and nitric acid (HNO_3) were from Sigma Aldrich (Merk). Sodium tetraborate decahydrate ($Na_2B_4O_7 \cdot 10H_2O$) and acetic acid (CH_3COOH) were from Carlo Erba Reagenti. Sulfuric acid (H_2SO_4) was from J.T. Baker, hydrogen peroxide from Elchive, phosphoric acid (H_3PO_4) from Rudipont. Cyclic peptide having sequence NH_2-Lys-Gly-Gly-Gly-Cys-His-Lys-Thr-Arg-Phe-Trp-Lys-Trp-Trp-Arg-Cys-COOH (cyclic peptide HK) was purchased from Espikem s.r.l. N_2 was from SIAD (≥ 99.99% pure) and was employed to purge the solutions when required.

Polyethylene terephtalate (PET) was from FOLEX (UK), UV-curable dielectric inks EMD 6415 and EMD 6200, silver nanoparticles ink EMD 5603 were from Sun Chemical, carbon nanotubes ink BSI.B12212 (CNTs ink) was from Brewer Science, gold-coated glass slides (1.1 X 1.1 cm, gold plates) were from Arrandee. Platinum, Gold, carbon (graphitic) fibers and polyimide (Kapton) tapes were from Goodfellow, UK.

- Materials for Solid Phase Extraction (SPE) and for Simplified Liquid Extraction (SLE)

Strata XL, Polymeric Reversed Phase SPE columns (SX columns, 1 mL). These columns are filled with a large particle, reversed phase functionalized polymeric sorbent which gives strong retention of neutral, acidic, or basic compounds under aggressive, high organic wash conditions. This sorbent relies on 3 mechanisms of retention: π-π bonding, hydrogen bonding (dipole-dipole interactions), and hydrophobic interaction. The large particle format is ideal for processing large volumes or viscous samples.

Novum Simplified Liquid Extraction columns (SLE columns, 1 cc) are filled with a synthetic material (patent pending). Both columns were purchased from Phenomenex (USA).

4.2 Preparation of specific synthetic solutions, handling and storage of reagents, analytes and collection of plasma samples

Stock solutions of CPT-11HCl, APC, NPC, SN-38, SN-38G, in the concentration range 0.5 mM - 5 mM, were prepared in pure CH_3CN or in DMSO; they were stored at 4°C and used within ten days after their preparation.

Stock solutions of IMA and Des-IMA, in the concentration range 0.1 - 1 mM, were prepared in EtOAc or in DMSO. They were stored at 4°C and used within ten days after their preparation.

Plasma samples, collected from either healthy volunteers or patients undergoing chemotherapeutic treatment, were from the IRCCS Centro di Riferimento Oncologico di Aviano, Italy. Plasma samples, stored at -20°C, were de-frosted slowly in ice bath for 1 h prior to analysis; this was done especially to prevent the conversion of the target drugs into other metabolites.

EDCHCl and NHS were stored at + 4° C in well sealed packages. Stock solutions were stored at 4° C, and used within 2 days from preparation. Peptide HK (powder) were stored in a well sealed package at -18 °C; stock solutions of peptide HK were prepared in PBS and were stored at -18 °C.

100 mL stock solutions of the medium employed for studying the voltammetric behavior of imatinib was prepared by mixing 85 mL of EtOAc, 7 mL of H_3PO_4 (85% aqueous solution), 5.5 mL CH_3COOH (glacial) and Milli-Q water to volume. This mixture was stirred to achieve homogeneous phase (no phase separation could be observed under naked eyes observations). The composition of this solution was optimized by trial and error attempt, up to obtain reproducible voltammetric responses (*vide infra*, chapter 5.2). For the sake of simplicity, this mixture will be identified as EtOAc-AM (Ethyl acetate Acidic Mixture) in the following sections.

4.3 Electrodes and instrumentation

Generally, voltammetric investigations and detection of irinotecan and imatinib were performed in a three-electrode cell. The working electrodes were either a glassy carbon disk (GCE) (Ø = 3 mm) or a Pt disk (Ø = 3 mm). A silver wire and a platinum spiral were employed as quasi-reference (AgQR) and counter electrode, respectively. The AgQR was employed to avoid contamination of the acetonitrile solutions with chloride ions leaching from the classical Ag/AgCl (KCl saturated) reference electrode. The GC and Pt conventional electrodes were

mechanically polished with diamond suspensions (0.1 μm diameter) placed over a Buehler microcloth, and then rinsed with milliQ water and acetonitrile or ethyl acetate.
To prepare micro and nano-electrodes, borosilicate glass and quartz capillaries, from Sutter Instruments were employed.
For the above experiments a CHI 920 C bipotentiostat (CH Instruments) was employed.

Voltammetric experiments conducted using inkjet printed electrodes were carried out using a MultiEmStat potentiostat (EmStat3, Palmsens).
Voltammetric and chronoamperometric measurements conducted with Electrochemical microprobes (EMP) were performed by a 430A CHI electrochemical analyzer (CH Instruments, Austin, TX, USA), driven by the relevant 2.07 software.

SECM experiments involving the use of single glass-sealed platinum micro or nano-electrode were performed using a SECM CHI 920 C workstation (CH Instruments). The apparatus included: a digital function generator, a bipotentiostat, a high resolution data acquisition circuit and a three axis positioning device. The latter included either three stepper motors and a closed loop piezoelectric system. SECM experiments performed using soft probes were carried out using a customized SECM setup running under SECMx software (University of Oldenburg, Germany), comprising a CompactStat (Ivium Technologies) and an electronic sample tilt table (Zaber Technologies). The soft probes were used as working electrodes and a three-electrode configuration was completed by using an Ag/AgCl reference electrode and a platinum wire as counter electrode. Analysis of SECM approach curves or 1D or 2D plots were carried out using MIRA software (University of Oldenburg, Germany).

Non-electrochemical instrumentation

Glass-sealed platinum micro- and nano-electrodes were fabricated using a Laser Puller Sutter 2000.
An intralux 4000 optical microscope and a laser scanning microscope Keyence VK 8700 (Keyence, Osaka, Japan) were used for visualization and optical examination of microelectrodes and inkjet printed patterns.
A homemade aluminium cage containing four UV lamps (30 W, from Philips) was used for photocuring of the dielectric inks.

4.3.1 Platinum black preparation

Platinum Black deposits (Pt-Bs) were prepared by electrodeposition of platinum onto the smooth platinum microdisks from a 50% hexachloroplatinic acid aqueous solution. Platinum deposition was carried out under potentiostatic conditions at -0.6 V vs PtPRe. The amount of Pt deposited was controlled from the current/potential profiles recorded during the plating step.

Geometric areas (A_g) were determined, before and after deposits formation, measuring the steady state current of 1 mM FcMeOH and using *eq 16* of Chapter 3 to calculate the microdisk electrode radius, then the corresponding area. **Fig 4.1A** shows typical cyclic voltammograms thus obtained, with a Pt-B (red line in **Fig 4.1A**) and that corresponding smooth Pt microdisk before Pt deposition (black line in **Fig 4.1A**). The electrochemical active surface areas of the Pt-Bs were evaluated by cyclic voltammetry in a 0.5 M H_2SO_4 aqueous solution, and exploiting the hydrogen UPD process [2]. **Fig 4.1B** shows typical cyclic voltammograms obtained at 200 mVs^{-1} over the potential range -0.3 – -0.7 V vs PtPRe, with a Pt-B (red line in **Fig 4.1B**) and that of the corresponding smooth Pt microdisk before platinum deposition (black line in **Fig 4.1B**). At both types of microelectrodes the typical voltammetric pattern expected for polycrystalline platinum is observed.

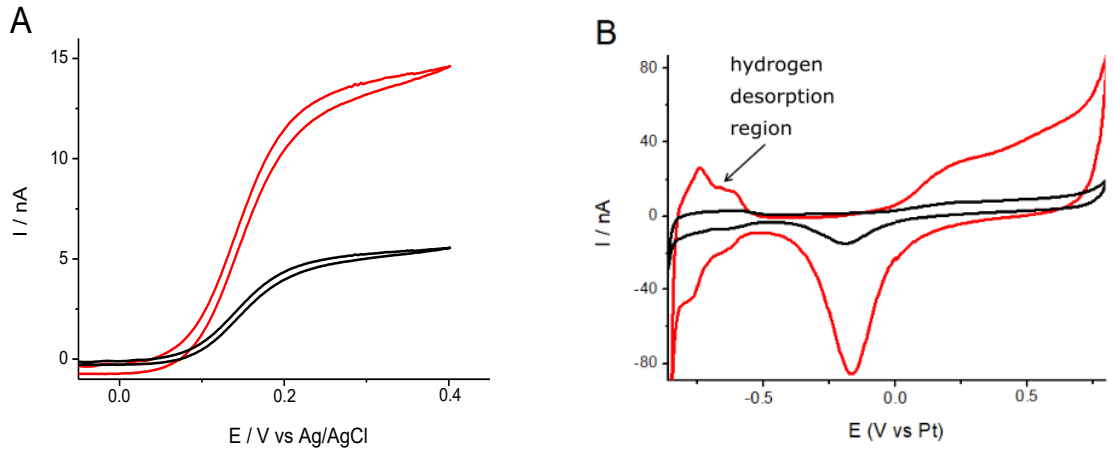

Fig 4.1- (**A**) Cyclic voltammogram recorded at a Ø = 25 µm Pt microelectrode in 1 mM FcMeOH, 0.1 M KNO_3 solution before (black line) and after (red line) platinum black deposition. Scan rate: 20 mVs^{-1}. (**B**) Cyclic voltammogram (lasts of 15 cycles) recorded at Pt microelectrode in 0.5 M H_2SO_4 before (black line) and after (red line) platinum black deposition. Scan rate: 200 mVs^{-1}

The larger current involved at the Pt-B is clearly due to the enhanced effective surface area, upon Pt deposition. From the hydrogen adsorption/desorption charge involved in the potential range -0.4 – -0.7 V vs PtPRe (**Fig 4.1**) (after the subtraction of the double layer charge, and assuming a monolayer of hydrogen corresponds to an adsorption of 210 $\mu C/cm^2$ [3]), the real surface areas

of the Pt-Bs, and, for comparison, those of the corresponding smooth microdisks, were evaluated. These surface area values were divided for the corresponding geometric area to produce the RF value**,** which increased from 3.1 to 28.2 before and after platinum black deposition.

4.3.2 Iridium oxide (IrO_x) preparation

The electrodeposition of thin layer films of iridium oxide onto the gold microelectrode surface was carried out by using a two-step procedure, which was adapted from literature protocols [4, 5]. The first step involved the electrodeposition of an IrO_2 film at constant potential of 0.8 V vs. Ag/AgCl (sat. KCl) for 600 s (**Fig 4.2A**). The overall reaction occurring for the iridium oxide formation is described by *Eq. 1* [6].

$$[Ir(COO)_2(OH)_4]^{2-}_{aq} \rightarrow IrO_2 + CO_2 + 2H_2O + 2e^- \qquad \textit{(Eq. 1)}$$

In the second step, the coated gold microelectrode was cycled consecutively for at least five cycles over the potential window from 0 to 0.8 V at 100 mVs^{-1} either to increase the amount of IrO_x deposited or to form the mixed Ir(IV)/Ir(III) oxides system, which is sensitive to pH changes [7]. **Fig 4.2B** shows a voltammogram recorded with an IrO_x-coated gold microelectrode 0.5 V in a 0.1 M $HPO_4^{2-}/H_2PO_4^-$ (pH 7). As is evident an anodic peak corresponding to the oxidation of Ir(III) to Ir(IV) and a cathodic one due to the inverse process, typical for surface confined species, are observed. This behaviour agrees with previous reports [8].

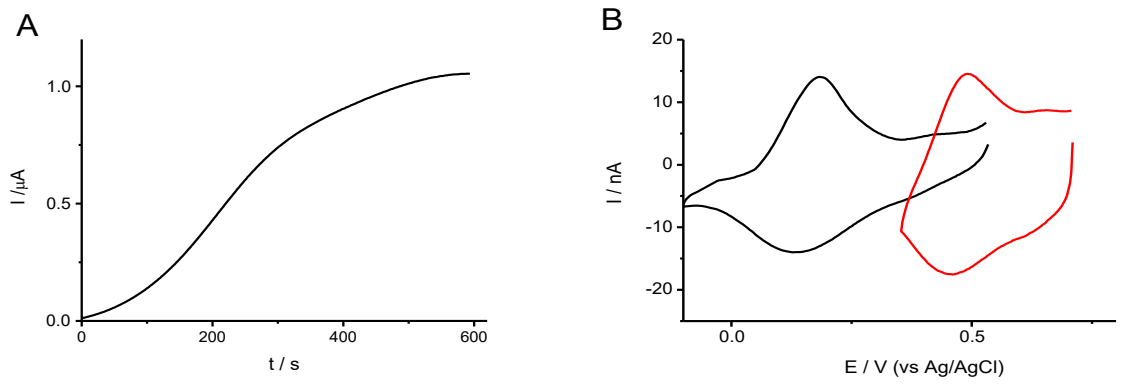

Fig 4.2 – (**A**) chronoamperometry recorded at Au microelectrode that was held at +0.8 Vvs Ag/AgCl in the deposition solution. (**B**) Cyclic voltammograms of an IrOx film recorded in a pH = 7 PBS solution (black line) and in a pH = 1.9 H_3PO_4 solution (red line), at 50 mVs^{-1}.

4.3.3 Fabrication of micrometer and sub-micrometer glass-sealed electrodes

Platinum microdisk electrodes were prepared by sealing Pt wires having Ø = 25 µm within borosilicate glass capillaries, using a P-2000 Laser Puller as described in detail elsewhere [9, 10]. In short, About 1.5 cm of a platinum wire was inserted inside a borosilicate glass capillary, of 0.58 mm (i.d.), 1.0 mm (o.d.) and 10 cm length Fig.1.3 (steps 1 and 2). In order to avoid the formation of bubbles, the two ends of the capillary were connected to a vacuum pump, for the entire length of the sealing procedure (**Fig 4.3**, step 3). The capillary tube, within the melting zone, was cut by a small circular saw, thus obtaining two tips containing the electrode material. The sealing quality and the continuity of the wire were checked by an optical microscope. The electric contact between the platinum fiber and the external circuit was realized with a copper wire soldered by means of indium flakes (optical image in **Fig 4.3**).

The active surface of the microelectrodes was exposed mechanically by using emery paper (Buehler, Illinois, U.S.A.) of decreasing grain size and alumina suspensions in water from 1 down to 0.05 µm. The microelectrodes were afterward characterized by cyclic voltammetry (CV) at low scan rates and SECM to evaluate the actual radius of the microelectrodes and the overall tip radius to the electrode radius ratio, RG, respectively, as described below.

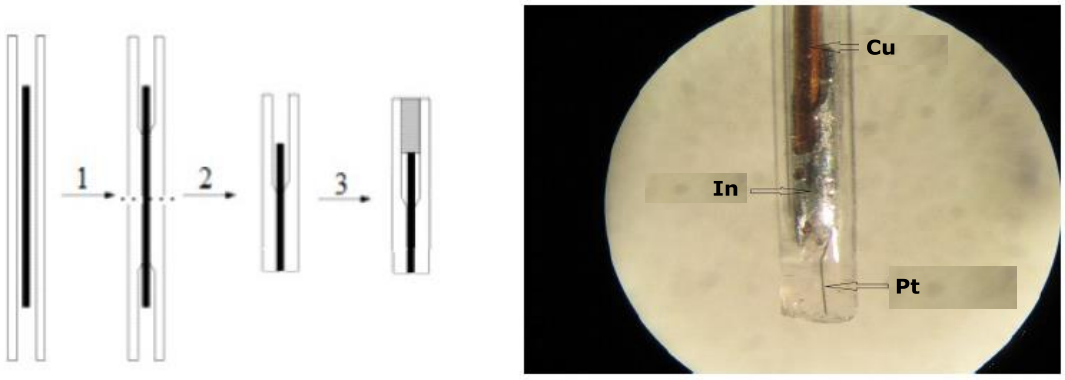

Fig 4.3 - **left**: schematic representation of the manufacturing of a microelectrode (1: sealing of the wire within glass. 2: separation of the sealed part. 3: electric contact fabrication). **Right**: microscope imageof a microelectrode before mechanical polishing.

Pt nanoelectrodes (down to Ø = 300 nm) were obtained by using a procedure reported in the literature [10]. In short, a Pt wire 12.5 µm radius was inserted into a quartz glass capillary and gently heated using the laser puller while applying vacuum to the two ends of the capillary as described above. This causes the glass capillary to collapse concentrically and thus to tightly

enclose the micrometric wire within the capillary. In a second step, more heat is applied and the two ends of the capillary are strongly pulled apart whereas both the glass sheath and the metal wire reduce their dimensions to yield two nearly identical nanoelectrodes (**Fig 4.4)**.

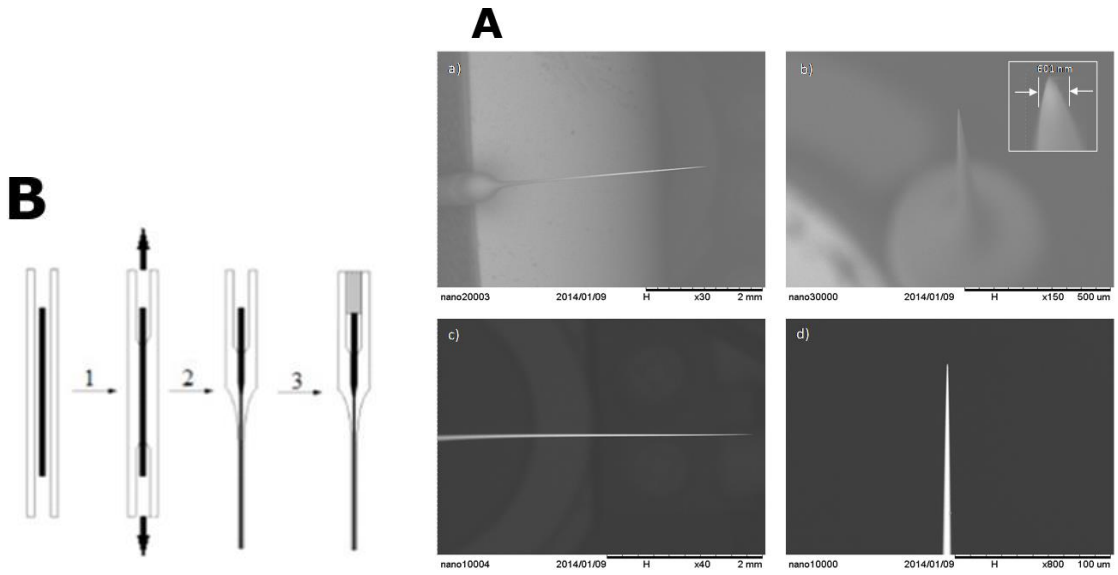

Fig 4.4 - (A) SEM images of a nanoelectrode. (**B) -** schematic representation of the manufacturing of a microelectrode (1: sealing of the wire within glass. 2: separation of the sealed part. 3: electric contact fabrication).

Micro and nano-electrodes were mechanically polished with gradually graded abrasive paper and alumina powder (0.3 µm) suspended in MilliQ water over Buheler polishing cloth.

4.3.4 Electrochemical characterization of the micro- and nano-electrodes

The micro and nano-electrodes were characterized electrochemically to establish their size, the irregular functioning and for SECM experiments the *RG* parameter. The radii were determined measuring the steady-state current by voltammetry, using 1 mM of Ferrocene in 0.1 M $TBAPF_6$, CH_3CN solution. **Fig 4.5** shows typical cyclic voltammograms obtained at 10 mVs^{-1}. The electrode radius was obtained using the experimental diffusion limiting current and *eq 17* (*D* of Fc is equal to 2.2 $x10^{-5}$ cm^2 s^{-1} [11]).

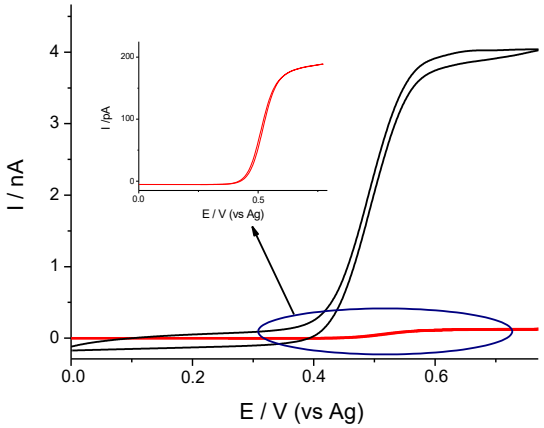

Fig 4.5 - Cyclic voltammograms recorded in a 1 mM Fc, 0.1 M $TBAPF_6$ CH_3CN solution of: 13.0 µm radius Pt disk electrode (black line), 0.41 µm radius Pt disk electrode (red line). 10 mVs^{-1}.

The Tomeš criterion was used to verify their regular behavior. In all cases a value of 56 (± 1) mV was obtained, in agreement with the occurrence of fully reversible process.

The RG parameter was obtained by SECM measurements in either 1 mM $[Ru(NH_3)_6]Cl_3$, 0.1 M KCl aqueous solutions, or in 1 mM Fc, 0.1 M $TBAPF_6$ CH_3CN solutions. Approach curves were recorded either over a conducting (**Fig 4.6A**) or insulating (**Fig 4.6B**) substrate; the experimental curves were then fitted with the theoretical ones to obtain the closest RG parameter. The micro- and nano-electrodes employed in this thesis had RG values ranging from about 3 and 8.

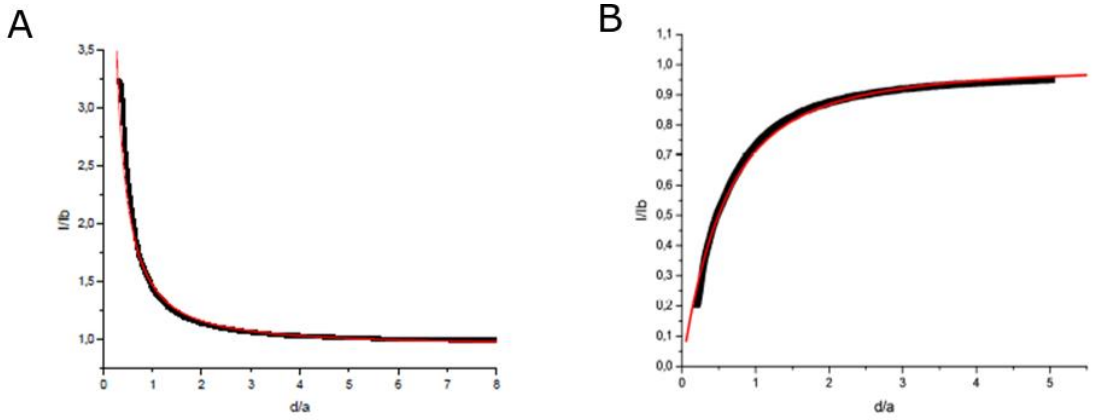

Fig 4.6 –experimental (black lines) and theoretical (red lines) approach curves corresponding to a positive feedback (**A**) and negative feedback (**B**) for a SECM tip with an RG = 3.10.

4.3.5 Fabrication of the electrochemical microprobe (EMP) for head-space measurements

The electrochemical microprobe (EMP) was fabricated according to a procedure reported in detail elsewhere [11]. In brief, two platinum fibers of 25 and 300 µm diameter were sealed into a theta glass pipette to obtain a two-electrode cell (**Fig 4.7**).

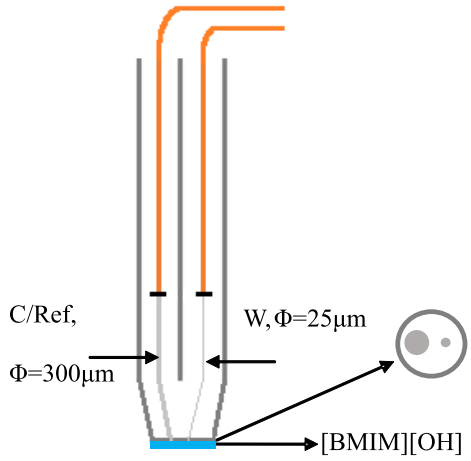

Fig 4.7 – Scheme of the EMP

The smallest disk was used as working electrode and the biggest as counter/pseudo-reference electrode. Before use, the entire tip surface was mechanically polished with aqueous suspensions of graded alumina powder of different sizes (1, 0.3 and 0.05 µm) supported on a polishing microcloth (Buehler, Düsseldorf, Germany). The effective electrode radii of the microdisks were determined electrochemically by steady-state voltammetry, as described elsewhere above for other microelectrode.

4.4 Manufacturing of inkjet printed electrodes and electrochemical cells

Inkjet printed electrodes and patterns were prepared on 0.18 mm-thick PET foils by a multilayer inkjet printing process [12]. A drop-on-demand Ceradrop 3000 X-Series printer, equipped with a movable UV-lamp, was used. Ink EMD 5603 and ink BSI.B12212 (4 or 5 layers) were printed firstly. The insulating UV curable ink EMD 6415 was printed immediately exposed to UV-light for avoiding excessive droplet spreading, which would affect the resolution of the printed path. Specific printing parameters such as jetting frequency, waveform, voltage, cartridge and substrate temperature, and cleaning cycles were previously adjusted for optimum printing performance of each ink. The printing apparatus was controlled by a LabView (National Instruments) software.

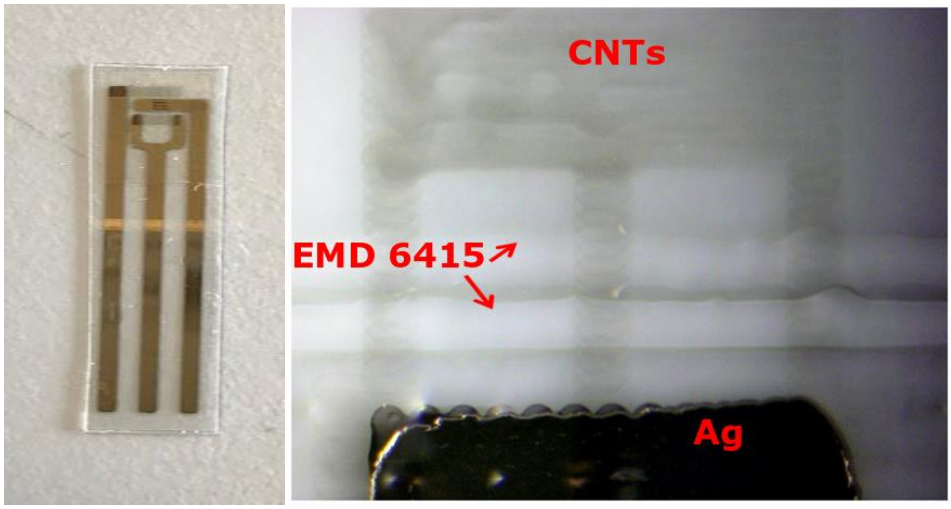

Fig 4.8 –Microscope image of an inkjet printed sensor (**left**) and of an inkjet printed electrode (**right**). CNTs: carbon nanotubes, working electrode. EMD 6415: insulating ink. Ag is the electric contact.

4.5 Preparation of Self Assembled Monolayers (SAM) of thiols on gold plates

Gold plates were removed from package and immersed in EtOH, for glue residues removal from their bottom. They were then immersed again in fresh EtOH and dried under N_2 stream. The dried plates were immersed in the piraña solution (See **4.5 a**)) for 3 minutes, accurately rinsed with Milli-Q water then rinsed and soaked in EtOH for at least 10 min. The plates were then placed in the thiol solution (See **4.5 b**)) and left to react for 24 h. Finally, they were rinsed with pure EtOH and preserved in desiccators, under N_2 or Ar atmosphere.

4.5 a) Preparation of Piraña solution

Piraña solution (careful: strong acid and oxidizer) was prepared mixing 3 mL of H_2SO_4 (96%) with 1 mL of H_2O_2 solution (30 %). The solution was allowed to cool to room temperature before the use.

4.5 b) Preparation of the thiol solution

The thiol solution was prepared by adding 1 mM of the desired thiol to a de-aerated EtOH solution, enriched with 50 mM of CCl_3COOH; during the SAM formation, the thiol solution was kept in a dark, dry environment [13].

4.6 SAM functionalization with cyclic peptides

The MUA-modified gold plates were soaked in 10 mL of a 0.05 M MES buffer (pH = 6.2), which was previously amended with 0.5 M NaCl (the pH was adjusted by addition of HCl). A solution of 2 mM EDCHCl and 5 mM of NHS was prepared and then immediately added to the MES buffer, to avoid degradation of the reagents. After 10 minutes, gold plates were removed from the solution and dried under N_2 stream. PBS (pH = 7.5) containing 0.1 mg/mL cyclic oligo-peptide was added over each plate by drop casting (200 µL over each plate); the plates were then left for 3 h into a N_2 filled desiccator and finally rinsed with fresh PBS and Milli-Q water [14].

References

[1] R. Kang, Journal of Imaging Science and Technology (1991) 179–188.

[2] A. Kicela, S. Daniele, Talanta 68 (2006) 1632-1639.

[3] W.H. Reinmuth, Analytical Chemistry 32 (1960) 1509-1512.

[4] D. O. Wipf, F. Ge, T. W. Spaine, J. E. Baur, Analytical Chemistry 72 (2000) 4921 – 4927.

[5] H.A. Elsen, C.F. Monson, M. Majda, Journal of Electrochemical Society (2009) 156, F1.

[6] E. Bitziou, D. O'Hare, B.A. Patel, Analytical Chemistry 80 (2008) 8733– 8740.

[7] E.E.D.M. El-Giar, D.O. Wipf, Journal of Electroanalytical Chemistry 609 (2007) 147– 154.

[8] I. G. Casella, M. Contursi, R. Toniolo, Journal of Electroanalytical Chemistry 736 (2015) 147– 152.

[9] D. Battistel, F. Baldi, M. Gallo, C. Faleri, S. Daniele, Talanta 132 (2015) 294-300.

[10] M. Etienne, A. Schulte, W. Schuhmann, Electrochemistry Communications 6 (2004) 288–293.

[11] Y.E. Wang, I.Rogers, R. G.Compton, Journal of Electroanalytical Chemistry 648 (2010) 15-19.

[12] S. Magdassi, The Chemistry of Inkjet Printing, World Scientific Publishing 1 (2010).

[13] J. C. Love, L.A. Estroff, J.K. Kriebel, M.G. Nuzzo, G.M. Whitesides, Chemical Reviews 105 (2005) 1103-70.

[14] G.T. Hermanson, Bioconjugate Techniques, Elsevier, 3rd edition (2008).

Results and Discussion

Chapter 5 – Irinotecan and imatinib

5.1 Irinotecan and its detection in plasma samples

5.1.1 Irinotecan, its metabolites and co-drugs

Irinotecan (CPT-11) is a cytotoxic pro-drug currently used in several chemotherapy regimens [1-5]. It is activated by the enzyme liver-carboxylesterase (CE) to provide (SN-38) [5], which is a potent topoisomerase I inhibitor [6-8] (**Scheme 5.1)**. CPT-11 is also subject to extensive metabolic conversion by other enzyme systems providing several products such as (APC) and (NPC). The latter, in turn, can be hydrolysed by CE to release SN-38 [7-8], which, by further enzymatic conversion, provides SN-38G (**Scheme 5.1**) [7-8].

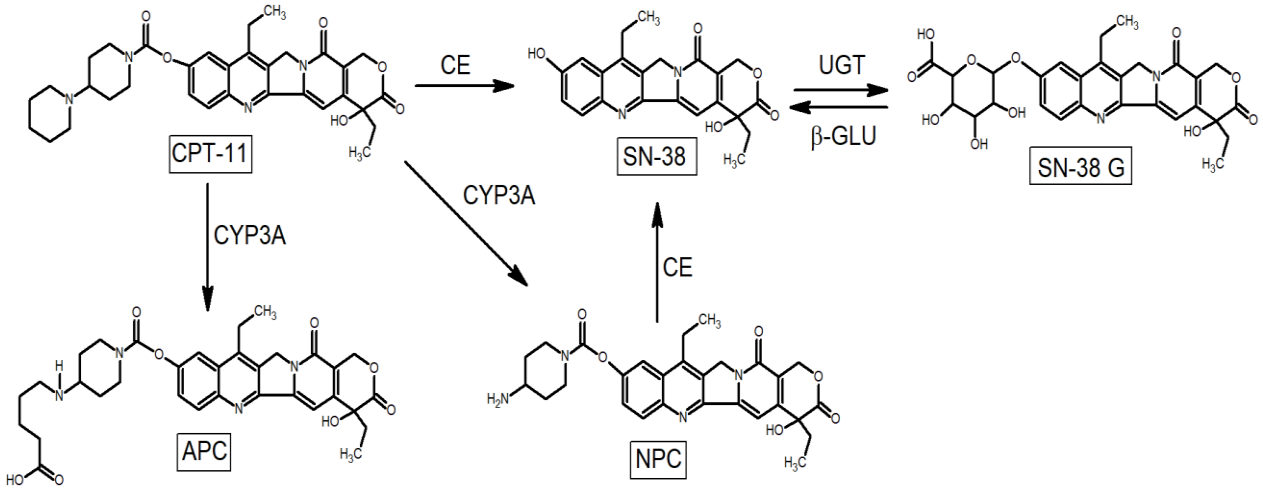

Scheme 5.1-Metabolic pathway of CPT-11, according to [5,7,8]. CYP3A: cytochrome P 450 isoform 3A; CE: Carboxylesterase; UGT: Glucoronosyltransferase; β-GLU: β-Glucoronidase

Because of its complex metabolic pathway, any analytical methodology devised for CPT-11 detection in body fluids, has to face with possible interference due to the various metabolites, which share the skeleton structure of the plant alkaloid camptothecin (CPT) with CPT-11 (**Scheme 5.2B**) [9]. In addition, it must be considered that in clinical regimens, CPT-11 is administered as irinotecan hydrochloride (CPT-11HCl) [8] (**Scheme 5.2A**), whose analytical characteristics may be different from that of CPT-11 in its neutral amine form; furthermore,

depending on the specific regimen, CPT-11HCl is administered in combination with co-drugs, such as 5-fluorouracil (5-FU) and folinic acid (FA), as is the case, in the FOLFIRI regimen [10, 11] (specifically considered in this thesis).

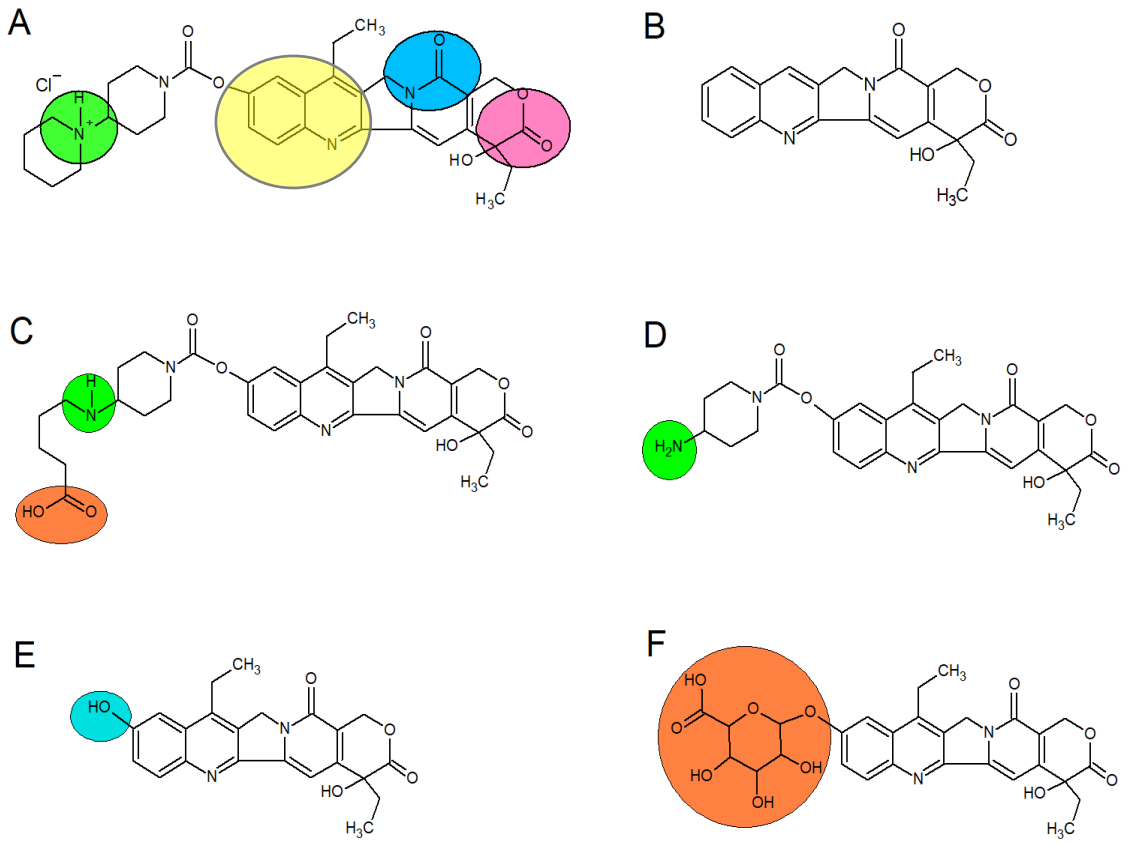

Scheme 5.2-Structural formulas of the investigated compounds. **A)**: CPT-11HCl; **B)**: CPT; **C)**: APC; **D)**: NPC; **E)**:SN-38; **F)**: SN-38G

5.1.1.2 Issues related to the detection of irinotecan in body fluids

To date, most of analytical protocols developed for the detection of irinotecan are based on fluorescence [12, 13] and hyphenated HPLC-MS and HPLC-fluorescence methods [14-20]. As mentioned in **Chapter 1**, the latter approaches, though accurate, suffer from disadvantages related to costs, portability of the instruments, long time analysis, while measurements require centralized and well-equipped laboratories, as well as qualified personnel. Moreover, they are not very suited for controlling and personalizing drug dosages on the basis of a TDM approach [21]. Recently, electrochemical methods have gathered significant interest in TDM [22-27], especially for applications to a variety of neurological drugs, neurotransmitters [23] and other therapeutic drugs [24-27]. Instead, TDM in oncology is not a fully developed clinical practice yet, rather it is very limited or even absent. In addition, focusing on irinotecan, there are only a

few reports dealing with its electrochemistry and/or quantification by electrochemical techniques [28-32]. Most of them refer to investigations performed in aqueous media [28-31], and only a recent article has reported on the electrochemistry of CPT-11HCl (and CPT-11) in acetonitrile, and the aim was to establish the sites involved in the oxidation processes of the molecule [32]. As for the CPT-11 metabolites, to the best of our knowledge, no report exists on their electrochemical behaviour neither in aqueous nor in organic media.

Broader information on the electrochemistry of CPT-11 and CPT-11HCl in organic solvents can be useful, for developing suitable electroanalytical protocols for their detection. In fact, organic solvents are normally employed in clinical protocols to either denature proteins or extract the target analyte from biofluids [17, 33]. On the other hand, knowledge on the electrochemical behaviour of the above-mentioned CPT-11 metabolites, which could strongly interfere in the CPT-11 detection, is also required. In addition, the redox behaviour of the different compounds can be useful to provide valuable insights in the activity or stability of the molecules in biological media, upon injection or removal of electrons from the molecules.

Considering the above scenario, in the first part of this section, it is examined, comprehensively the voltammetric behaviour of: CPT-11 in its neutral and hydrochloride form, its main metabolites (SN-38, SN-38G, APC, NPC), for comparison the natural chemical analogous of CPT-11, camptothecin (CPT, **Scheme 5.2B**), the co-drugs 5-fluorouracil (5-FU) and folinic acid (FA) in acetonitrile solutions. The latter solvent has been chosen as it provided strong advantages with respect to aqueous solutions. Firstly, the wide electrochemical window of CH_3CN allowed a clear discrimination of the voltammetric patterns for all compounds involved in this study. Secondly, CH_3CN is also used as a solvent of election in common analytical methodologies, such as HPLC-MS, for the treatment of biofluids to extract and analyse drug molecules [17]. The general voltammetric investigation has been performed using glassy carbon and platinum electrodes. The latter has been actually employed to investigate specifically the cathodic region and to ascertain the involvement in the electrode processes of acidic moieties present in the structure of the various compounds.

In the second part of this section, a detailed procedure for the detection of CPT-11 in plasma samples is illustrated, in view of its use in TDM. It must be remarked that for the latter purpose, apart from the above mentioned complex CPT-11's pharmacokinetics (Scheme 5.1) and interferences, other factors have to be considered. In fact CPT-11 has a narrow therapeutic window. Moreover, plasma proteins bind CPT-11 to a considerable extent (> 60-70%) [38] and this may lead to problems related to recovery of the drug from the real matrix. Therefore,

because of the above additional complications, it is likely that preliminary steps, involving denaturation of proteins and extraction of irinotecan from the matrix, are required before performing the voltammetric analysis. As is illustrated later in the next sections, the preliminary steps were performed by using commercially available solid phase extraction (SPE) columns.

5.1.2 Voltammetric behaviour of irinotecan, of its metabolites, of 5-fluorouracil and folinic acid (FA) in acetonitrile

5.1.2.1 Voltammetric behaviour of CPT-11HCl/CPT-11 and CPT

Fig 5.2 shows typical cyclic voltammograms recorded at 200 mVs^{-1}at the GCE in 0.5 mM CPT-11HCl solutions. The CVs were generally run starting from 0 V *vs.* AgQR up to the solvent discharge, which occurred beyond about -2 and +2 V, respectively (**Fig 5.2A**, black line). As it can be seen, a rather complex CV pattern is observed in both negative and positive potential regions, showing a series of peaks and redox processes, most of them with no associated peaks in the reverse scan. When the scan was initially performed directly in the positive direction, the main difference observed in the CV was the lack of the small and broad peaks located at about +0.7 and +1 V (see **Fig 5.2B**), which are instead observed when the sweep was initially scanned in the negative direction (see details in inset of **5.2A**). In particular, the processes at +0.7 V and +1 V appeared when the scan direction was reversed after the second main cathodic peak at -1.605 V (R_4, described later in the text) and the main cathodic peak at -1.195 V (R_2, described later in the text), respectively (**Fig 5.3**).

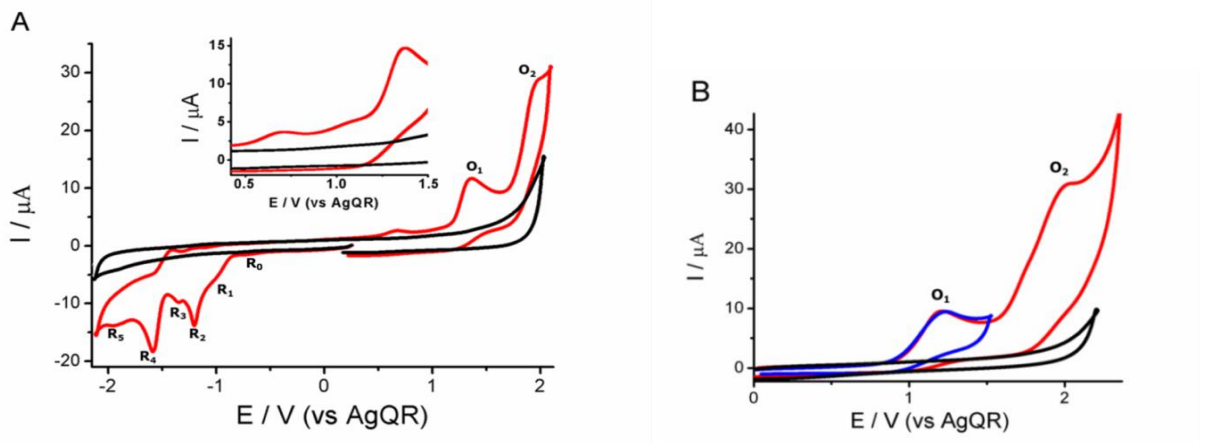

Fig 5.2A-Cyclic voltammograms recorded in a 0.5 mM CPT-11HCl (red lines) + 0.1 M $TBAPF_6/CH_3CN$ solution at a GCE.A) Potential region explored between -2.1 and +2.1 V *vs.*AgQR; initial scan in the negative direction; background (black line). Inset: enlargement of the anodic potential region up to +1.5 V. **Fig 5.2B**: Direct scan in the positive potential region between 0 and +2.5V(red line) and +1.5 V (blue line) *vs.*AgQR. Scan rate: 200 mVs^{-1}.

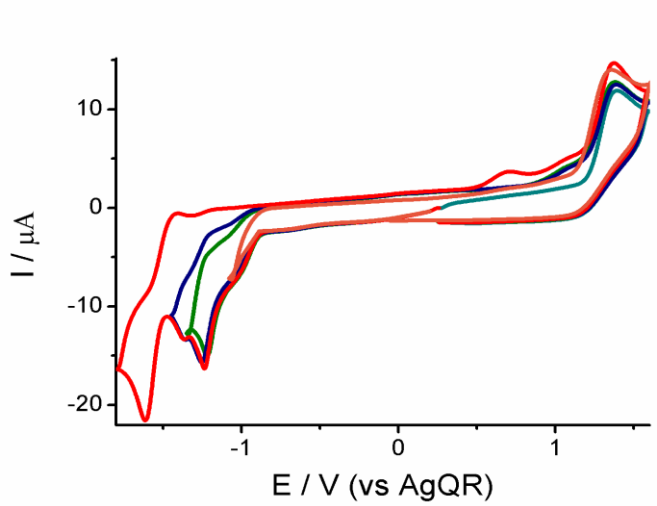

Fig 5.3-Cyclic voltammogramsrecorded in a 0.5 mM CPT-11HCl, 0.1 M $TBAPF_6/CH_3CN$ solution at a GCE and scan reversal at different potentials as indicated by the different colors. Scan rate: 200 mVs^{-1}.

Fig 5.4 shows typical CVs recorded at 200 mVs^{-1} at the GCE in 0.5 mM CPT solutions. As it is evident, most voltammetric features are similar to those displayed in **Fig 5.2** for CPT-11HCl. Similarly, the CV recorded by scanning the potential directly in the positive region was somewhat simpler (**Fig 5.4B**), because of the lack of the peaks located at potentials lower than +1.2 V.

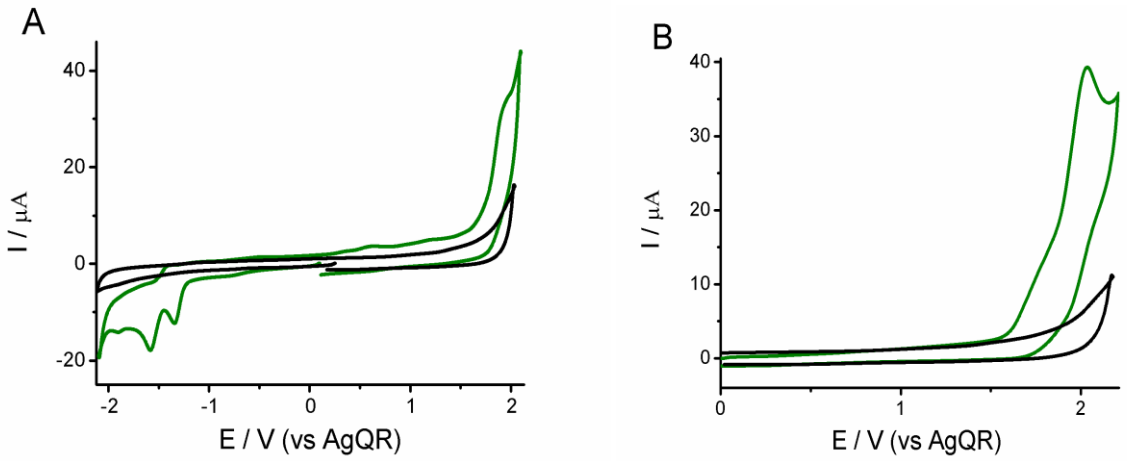

Fig 5.4 - Cyclic voltammograms recorded in a 0.5 mM CPT + 0.1 M $TBAPF_6/CH_3CN$ solution at a GCE (green line); background (black line). **(A)** Initial scan in the negative direction over the potential region between -2.1 and +2.1 V *vs.* AgQR.**(B)** Initial scan in the positive direction over the potential region between 0 and +2.2 V *vs.* AgQR. Scan rate: 200 mVs^{-1}.

To get more insights on the various processes involved and for sake of simplicity in the presentation of the results, the voltammetric behaviour of the compounds was examined in the region of positive and negative potentials, separately.

5.1.2.1.1 Cathodic potential region

In the forward scan (**Fig 5.5**, black line), CPT-11HCl displayed five reduction processes. The first reduction wave, located at -1.005 V (R_1), was followed by a cathodic peak at -1.195 V (R_2), and by a small peak at-1.340 V (R_3). A fourth peak appeared at-1.605 V (R_4),followed by a small broad peak at-1.920 V (R_5). For the sake of discussion, we also noticed an undefined and very weak redox process at about -0.650 V (R_0), which could be due to some impurities present in the solvent or in the reagents employed. In the reverse scan, an oxidation peak at -1.465 V, associated to the second main reduction process (R_4), was observed (peak potentials separation was equal to 140 mV, at 200 mV s^{-1}). Instead, no significant oxidation peaks were recorded upon reversal of the scan direction soon after the less negative reduction peaks R_2 and R_3 (**Fig 5.5**, with blue, green and orange lines).

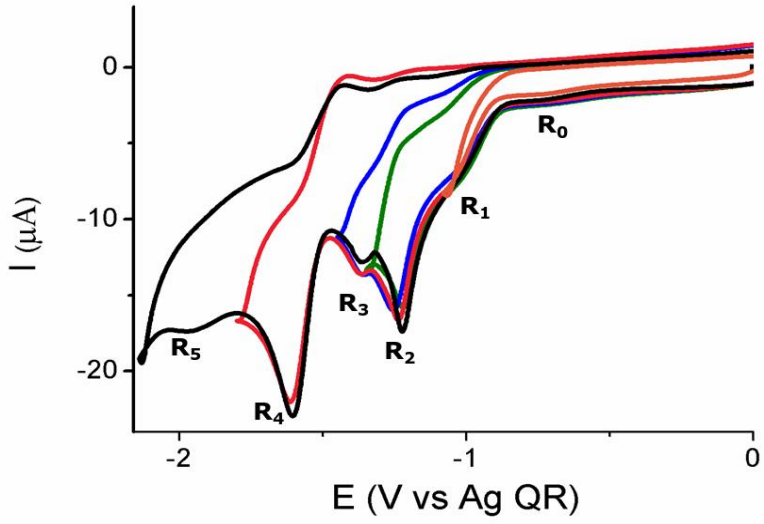

Fig 5.5- Cyclic voltammograms recorded in a 0.5 mM CPT-11HCl +0.1 M $TBAPF_6/CH_3CN$ solution at a GCE. Initial scan in the negative direction and scan reversal at different potentials as indicated by the different colors. Scan rate: 200 mVs^{-1}.

Table 5.1 –Peak potential values of the main processes recorded at a GCE in 0.5 mM each of the investigated compounds. They were obtained from CVs recorded at 200 mV/s and referred against AgQR.

Compound	$E_{p,c}^{1}$ (±0.015)/V	$E_{p,c}^{2}$ (±0.015)/V	$E_{p,c}^{3}$ (±0.015)/V	$E_{p,c}^{4}$(±0.015)/V	$E_{p,a}^{1}$(±0.015)/V	$E_{p,a}^{2}$(±0.015)/V	$E_{p,a}^{3}$ (±0.015)/V
CPT-11 HCl	-1.195	-1.340	-1.605	-1.920	-	+ 1.330	+ 1.980
CPT-11 *	-	-1.350	-1.480	-1.920	+ 0.980	+ 1.370	-
CPT	-	-1.365	-1.600	-1.910	-	-	+ 1.980
APC**	c.a. -1.180	-1.340	-1.610	-1.920	+ 1.240	-	+ 1.960
NPC	-	-1.350	-1.600	-1.920	+ 1.340	-	+ 1.980
SN-38 ***	-	-1.340	-1.640	-1,980	+ 1.380	-	+ 1.970
SN-38 G	-	-1.360	-1.605	-1.950	-	-	+ 1.960
TEAHCl	-1.210	-	-	-	-	+ 1.350	-
TEA****	-	-	-	-	+ 0.940	+ 1.380	-
TEA	-	-	-	-	+ 0.960	-	-

$E_{p,c}^{1}$, $E_{p,c}^{2}$, $E_{p,}c^{3}$refer, respectively, to: the first main cathodic peak assigned to the reduction of the protonated tertiary ammine or acidic moieties; the second cathodic peak assigned to the reduction of the 2-pyridone ring; the third cathodic peak assigned to the reduction of the lactone ring. $E_{p,c}^{4}$refers to the fourth cathodic peak. $E_{p,a}^{1}$, $E_{p,a}^{2}$, $E_{p,a}^{3}$, refer, respectively, to: the first anodic peak assigned to the oxidation of the various amine ends; thepeak due to the oxidation of Cl^{-} ions; thepeak due to the oxidation of the 2-pyridone ring.

*Obtained by addition of sodium borate to the CPT-11HCl acetonitrile solutions.

**Recorded in APC solution at 20 mV/s.

*** Recorded after 6 min from the preparation of the solution

*** *Obtained by addition of sodium borate to the TEAHCl acetonitrile solution

Measurements performed at different scan rates (over the range 20 – 200 mV s^{-1}) or at different concentrations (over the range 0.1 – 0.5 mM) did not lead to substantial changes to the above picture (**Fig 5.6**). Because of the difficulty to evaluate the peak current associated to each process, the analysis of the voltammetric parameters, as a function of scan rate or concentration, was performed with respect to peak potentials. It was found that all processes retained essentially the same potential values (within ± 15 mV experimental error) regardless of both scan rate and CPT-11HCl concentration.

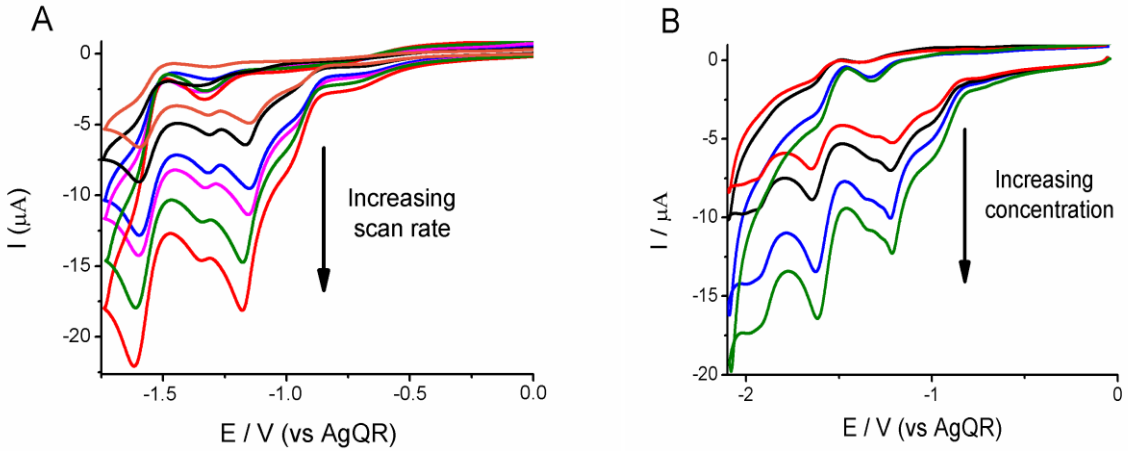

Fig 5.6-Cyclic voltammograms recorded at a GCEforCPT-11HCl + 0.1 M $TBAPF_6/CH_3CN$ solution: (**A**) 0.5 mM CPT-11HCl and different scan rates (20, 30, 50, 80, 100, 150, 200 mV/s), as indicated;(**B**) CPT-11HCl at different concentrations (0.1, 0.2, 0.4, 0.5 mM) at 200 mV/s.

Considering the results reported in [32], where, however, only linear sweep voltammograms were considered, R_2along with R_1, and R_3 were assigned to the reduction of the protonated tertiary amine (see green highlight in **Scheme 5.2A**), and to the reduction of the 2-pyridone ring of the irinotecan structure (see blue highlight in **Scheme 5.2A**), respectively. Confirmatory experiments performed in this work, described later in detail, agree with this view.

As for R_4 at -1.605 V, for which no information was provided in [32], it could involve either the products formed in the previous electrode processes or other chemical moieties of the irinotecan structure, particularly the lactone or quinoline rings (**Scheme 5.2A**, highlighted in magenta and yellow, respectively). The involvement of the lactone ring in the reduction process at -1.605 V was assumed to be likely, considering that similar CV patterns were reported in the literature for the reduction of a series of mono- and di-substituted n-alkyl esters in acetonitrile [39,40] and for camptothecin (model compound for CPT-11, **Scheme 5.2B**) in aqueous media [41]. In these articles, a reduction process involving the formation of a sufficiently stable carbonyl radical of the various lactone forms, further reduced at more negative potentials, was hypothesized as a likely reaction path [39-41]. We believe that the same mechanism applies for CPT-11HCl, and therefore the peak at -1.605V is assigned to the formation of a carbonyl radical, which is further

reduced at -1.920 V. On the other hand, the involvement of the quinoline moiety, over the above potential region, was ruled out, as CVs performed in solutions containing pure iso-quinoline, as model compound, did not provide processes matching those observed for CPT-11HCl up to about -1.8 V (**Fig 5.7**). Instead, the reduction of iso-quinoline [42] occurred over the same potential region of the peak R_5 of CPT-11HCl, i.e., at -1.920 V (**Fig 5.7**, blue line). However, the intensity of the latter process was too small to be assigned to the reduction of iso-quinoline [42].

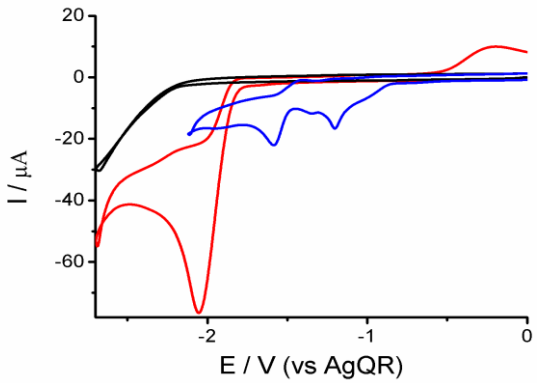

Fig 5.7 - Comparison between the cyclic voltammograms recorded at a GCE in 0.1 M $TBAPF_6/CH_3CN$ solutions containing 0.5 mM CPT-11HCl (blue line) and 0.5 mM iso-quinoline (red line). Black line refers to the background. Scan rate: 200 mV/s.

Returning to the first two reduction steps (i.e., R_1 and R_2), the involvement of the protonated amine moiety was assessed by performing CVs in CPT-11HCl solutions at a Pt disk electrode, which displays catalytic activity towards the reduction of acidic species [43-46]. In fact, at the Pt electrode a reduction peak at -0.580 V, overlapping the undefined process R_0 when employing GCE (**Fig 5.5 and 5.6**), and an associated small oxidation peak at -0.290 V, upon scan reversal, were recorded (**Fig 5.8**, red and blue lines). This behaviour is typical for reduction of weak acids to hydrogen, as conceivably is the case of the protonated tertiary amine of CPT-11HCl [30].

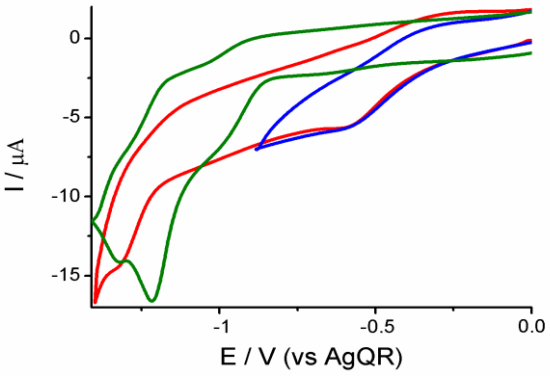

Fig 5.8 - Cyclic voltammograms recorded in a 0.5 mM CPT-11HCl + 0.1 M $TBAPF_6/CH_3CN$ solution at a GCE (green) and Pt(red and blue lines and at different reversal potentials) electrodes. Scan rate: 200 mV/s.

A series of CVs performed using both GC and Pt electrodes in acetonitrile solutions containing the model compound triethylammonium chloride (a weak acid with *pKa ~18* in CH_3CN [47, 48]) provided similar voltammetric patterns (**Fig 5.9**). In particular, an irreversible broad reduction peak at -1.2 V, i.e., close to that of CPT-11HCl, with no associated anodic peak, was recorded at the GCE (**Fig 5.9A**, blue line), while a couple of cathodic (at -0.610 V) and anodic (at -0.310 V) peaks was recorded at the Pt electrode (**Fig 5.9A**, red line), which is congruent with the direct reduction of weak acids to hydrogen [45-48]. A further check was also performed to verify whether the reduction peak system R_1-R_2 could be due to HCl coming from dissociation of CPT-11HCl. Measurements performed in an acetonitrile solution containing 0.5 mM HCl yielded an irreversible peak at -0.930 V at the GCE (**Fig 5.9B)**, and a cathodic-anodic system centred at -0.107 V at the Pt electrode. These less negative potential values, obtained at both types of electrodes, exclude that HCl is involved in the R_1-R_2 peaks. This also agrees with circumstance that HCl is an acid stronger (*pKa* = 1.6 [49]) than the protonated tertiary amines of both CPT-11HCl and triethylammonium chloride.

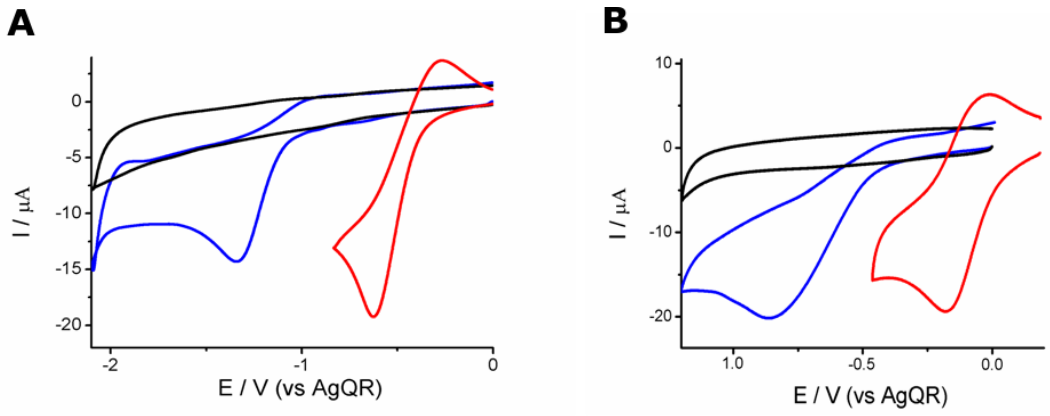

Fig 5.9 -Cyclic voltammograms recordedat a Pt (red lines) and GCE (blue lines) electrode in a 0.1 M $TBAPF_6/CH_3CN$ solution containing: (**A**) 0.5 mM TrEAHCl, (**B**) 0.5 mMHCl.Black line refers to background. Scan rate: 200 mV/s.

A series of measurements was also performed with the GCE in CPT-11HCl containing acetonitrile solutions at which either one equivalent of TBAOH or an excess of $Na_2B_4O_7$ was added to compensate the proton level, thus obtaining the CPT-11 species. Under these conditions, R_1 and R_2 disappeared (**Fig 5.10**, red line), while the peak at -1.350 V, assigned to the reduction of 2-pyridone ring, was well developed, yet with no associated peak upon scan reversal (**Fig 5.10**, pink line).

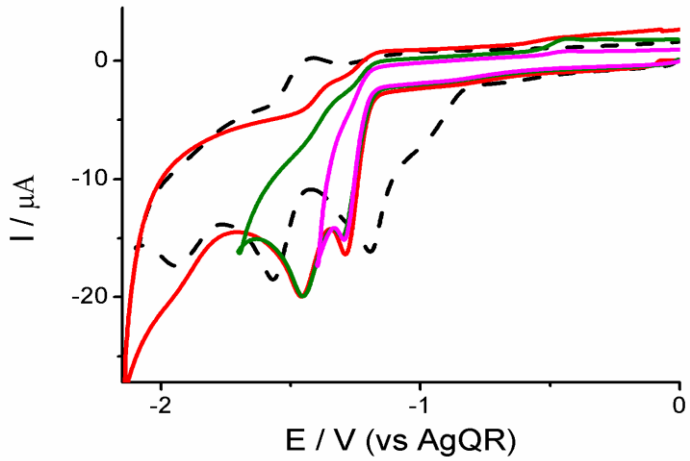

Fig 5.10-Comparison between cyclic voltammograms recorded in a 0.5 mM CPT-11HCl + 0.1 M $TBAPF_6/CH_3CN$ solution at a GCE without (dashed black line) and with 0.73 mM$Na_2B_4O_7$(red line). Initial scan in the negative direction and scan reversal at different potentials as indicated by the green and pink lines. Scan rate: 200 mVs^{-1}.

For the latter process, the analysis of peak current against the square root of scan rate (over the range 10-200 mV s^{-1}, **Fig 5.11**) provided a linear trend (correlation coefficient 0.992), while the peak width (i.e., $E_p - E_{p/2}$, [50]) was equal to 63 (± 2) mV, regardless of scan rate, consistent with the occurrence of an appreciably fast one-electron, diffusion-controlled, chemically irreversible reduction process [50]. This result also fully agrees with that reported in [32].

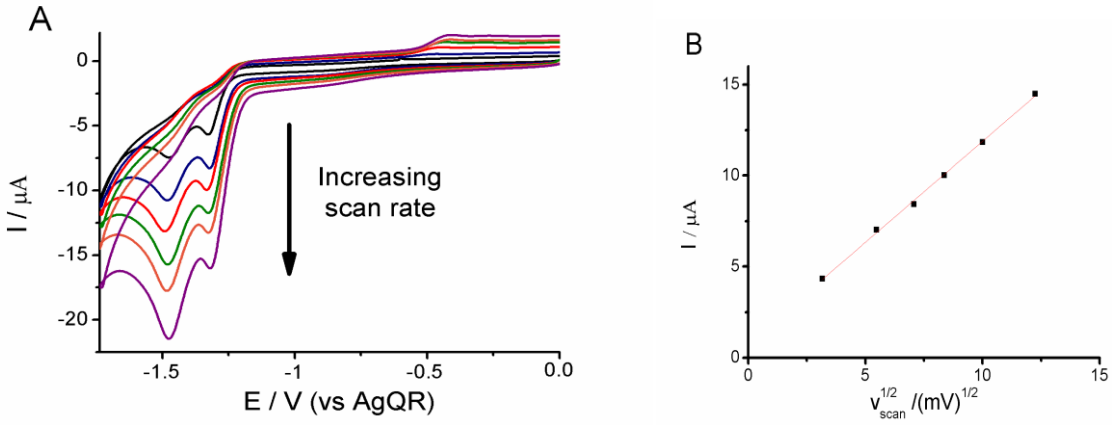

Fig 5.11- (**A**) Cyclic voltammograms recorded in a 0.5 mM CPT-11HCl + 0.1 M $TBAPF_6$ + 0.73 mM $Na_2B_4O_7$ in CH_3CN solution at a GCE at different scan rates (10, 30, 50, 80, 100, 150 mV/s). (**B**) Plot of peak current against square root of scan rate for the first peak**.**

Moreover, the occurrence of a one-electron process was also assessed by comparison of the peak current at -1.350 V with that obtained at the same GCE in acetonitrile solutions containing 0.5 mM of $Ru(acac)_3$, which is known to undergo a one-electron reduction process [51]. In fact, peak currents, which differed no more than 10%, were obtained.

In the basified CPT-11HCl solution, the second main peak was still present (**Fig 5.10**,red and green lines), though it occurred at less negative potentials, while the associated anodic peak in

the backward scan was much less developed. This behaviour can be explained considering that the lactone ring of CPT-11, in basic media, reversibly converts into a carboxylate form [7]. Moreover, the small amount of water added with the basifying agent can, in part, favour a follow-up chemical reaction (i.e., *EC* process [51]) involving the carbonyl radical formed in the reduction process.

The scenarios hypothesized above for the assignment of the peaks were supported from measurements performed in solutions of CPT, which shares with CPT-11HClthe structures of 2-pyridone,quinoline and lactone rings (**Scheme 5.2A,B**). **Fig 5.12** compares typical CVs obtained at the GCE for acetonitrile solutions containing 0.5 mM of CPT and CPT-11HCleach. As is evident, apart from the lack of R_1 and R_2, attributed to the protonated tertiary amine of CPT-11HCl (see above), the two voltammograms display the same number of peaks occurring, within experimental errors, at identical potentials (**Table 5.1**).

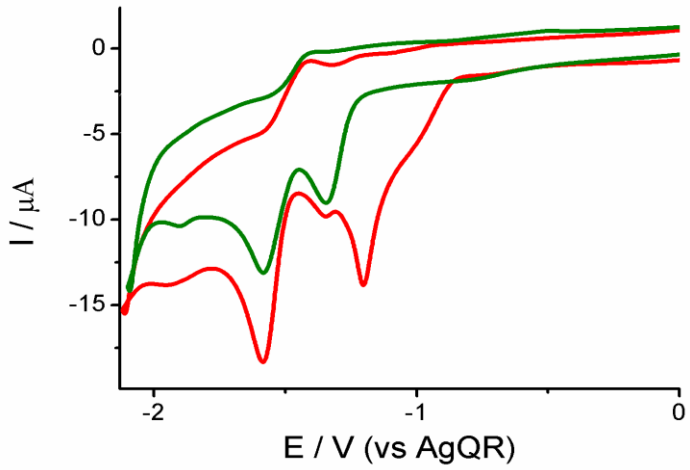

Fig 5.12- Comparison between cyclic voltammograms recorded in a 0.5 mM CPT-11HCl (red line) and 0.5 mM CPT (green line) in 0.1 M $TBAPF_6/CH_3CN$ solution at a GCE. Initial scan in the negative direction. Scan rate: 100 mVs^{-1}.

Moreover, the CVs of CPT-11HCl and CPT, recorded in acetonitrile containing sodium borate (where CPT-11HCl is in the neutral form CPT-11), displayed almost identical features (**Fig 5.13**).

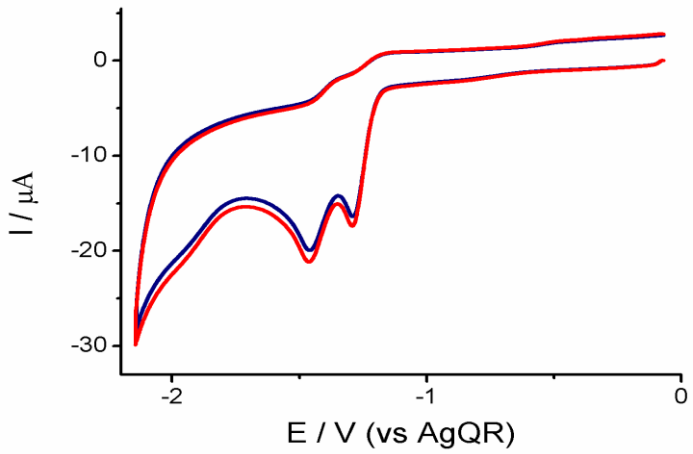

Fig 5.13 Cyclic voltammograms recordedat a GCE in 0.1 M $TBAPF_6$ + 0.73 mM$Na_2B_4O_7$ in CH_3CN solutions containing 0.5 mM CPT (blue line) and 0.5 mM CPT-11HCl (red line). Scan rate: 200 mV/s.

5.1.2.1.2 Anodic potential region

A typical CV recorded in 0.5 mM CPT-11HCl solution at 0.2 V s^{-1}at the GCE, scanning the potential directly in the positive region up to the onset of the background discharge, is shown in **Fig 5.1B** (red line). Two main processes at +1.330 V (O_1) and +1.980 V (O_2) (potential are also given in **Table 5.1**) are observed with no associated return peaks upon scan reversal either from O_2 (red line) or O_1 (orange line). This picture agrees with that reported in [30], where, again, only the linear sweep voltammogram was displayed. In the latter work, the two processes (occurring at about +0.8 V and +1.5 V, respectively, *vs.* Ag/Ag^+, 0.1 M $AgNO_3$in CH_3CN [30]) were assigned to the oxidation of Cl^- and the 2-pyridone ring of the CPT-11HCl, respectively. The involvement of these species in the two anodic peaks, recorded here against the AgQR, was confirmed by comparing the CV of CPT-11HCl with those of TEAHCl and TEACl (for Cl^-), and with that of CPT, the latter lacking the protonated tertiary amine end (for the 2-pyridone ring). Indeed, all CPT-11HCl, TrEAHCl and TEACl displayed an oxidation peak at about +1.3 V (**Fig 5.14A**). CV patterns of CPT-11HCl and CPT were also compared, and the latter one showed only the anodic process O_2, given that no Cl^- can be oxidized (**Fig 5.14B**).

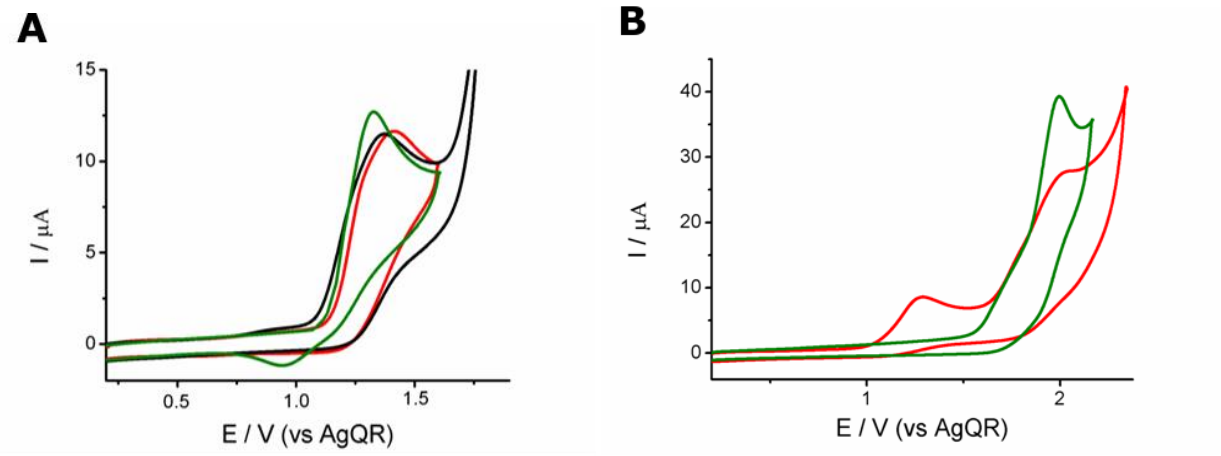

Fig5.14- (A) Cyclic voltammograms recorded at a GCE in 0.1 M $TBAPF_6CH_3CN$ solutions containing: 0.5 mM CPT-11 HCl (black line), 0.5 mM TrEAHCl (red line) and 0.5 mMTEACl (green line). (**B**) Cyclic voltammograms recorded at a GCE in 0.1 M $TBAPF_6/CH_3CN$ solutions containing 0.5 mM CPT-11HCl (red line), 0.5 mM CPT (green line). Initial scan positive direction. Scan rate: 200 mV/s.

The above results also suggest that the protonated tertiary amine of both CPT-11HCl and TrEAHCl are not electroactive over the potential window examined. Instead, their base form can provide oxidation processes, in accordance with the general electrochemical behaviour of aliphatic amines in organic solvents [52-54]. This was confirmed from a series of CV measurements performed in CPT-11HCl and TrEAHCl acetonitrile solutions basified with sodium borate (to compensate the proton level), as well as on an authentic sample of triethylamine. As shown in **Fig 5.15**, triethylamine gives rise to a single irreversible process (O_3) at +0.960 (± 0.010) V (Fig. 6A), while both CPT-11HCl and TrEAHCl (**Figs 5.15 B**, and **Fig 5.15 C**, respectively) provide two distinct oxidation processes, the first of which occurs at +0.980 (± 0.010) V, i.e., very close to that of triethylamine; the location of second peak, assigned to the oxidation of chloride ions, remains unchanged.

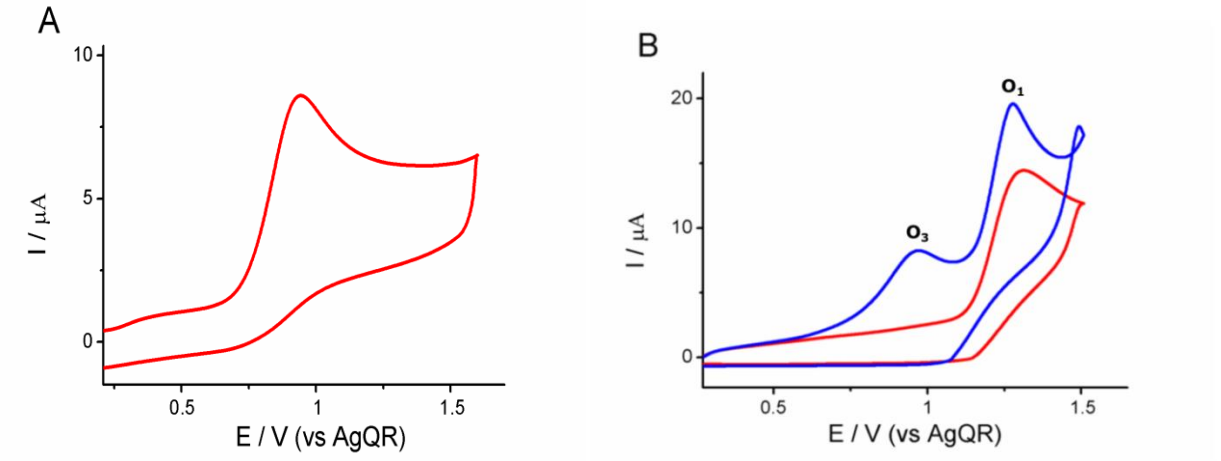

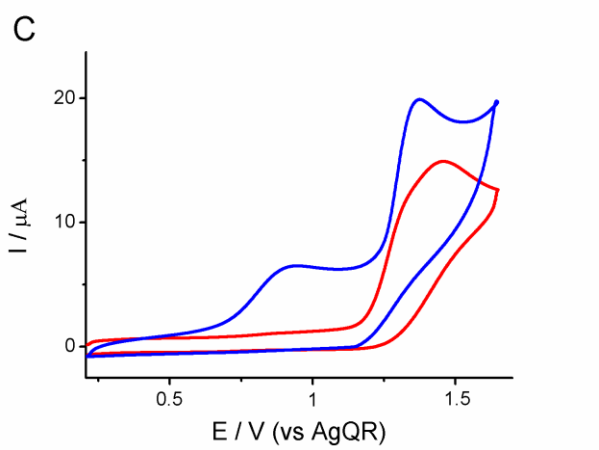

Fig5.15-Comparison between cyclic voltammograms recorded ata GCE in 0.1 M $TBAPF_6/CH_3CN$ solutions containing: (**A**) 0.5 mM triethylamine; (**B**) 0.5 mM CPT-11HCl; (**C**) 0.5 mMTrEAHCl. Red and blue lines refer to the above solutions without and with 0.73 mM$Na_2B_4O_7$, respectively. Initial scan in the positive direction. Scan rate: 100 mVs^{-1}.

According to the literature, the oxidation process of simple aliphatic amines shows in CV (over the same range of scan rates employed here) a single irreversible peak. The overall mechanism is rather complex, and the first stage involves an EC process, with the formation of a radical cation followed by a fast deprotonation to provide a radical, which can also react with the electrode surface [52-54]. Moreover, the heterogeneous electron transfer is rather slow. The general shapes of the above examined compounds are consistent with this interpretation. In particular, the kinetic control by the heterogeneous electron transfer is confirmed by the values of peak width (i.e., $E_{p,a} - E_{p,a/2}$ [43]) found here, which, at 200 mVs^{-1}, were 130 (± 4) mV, 120 (± 4) and 99 (± 2) mV for CPT-11HCl, TrEAHCl and triethylamine, respectively. These values are in good agreement with those reported in the literature for the oxidation of a series of tertiary amines in acetonitrile [32,54].

Based on the latter findings and considering again the backward scans of the CVs shown in **Fig 5.3**, we can confidently state that, in the CPT-11HCl solutions, the peak at about +1 V, appearing upon reversal the scan from the main cathodic peak at about -1.2 V (i.e., after the reduction of the protonated tertiary amine), involves the oxidation of the tertiary amine. On the other hand, the peak at about +0.7 V, which is seen for both CPT-11HCl and CPT (see **Fig 5.2**), is conceivably due to a non-identified product arising from the reduction of the lactone ring at about -1.6 V.

5.1.2.2 Voltammetric behaviour of the CPT-11' metabolites.

Fig 5.16 displays the CVs recorded for each metabolite in 0.1 mM acetonitrile solutions over the potential window covering the most important processes described in the previous sections for CPT-11HCl. **Table 5.1** summarizes the potential values of the main peaks observed. Similarities and differences in the voltammetric pattern with respect to those recorded for CPT-11HCl, CPT-11 (the latter obtained after the addition of sodium borate) and CPT will be illustrated for each metabolite in the following sections.

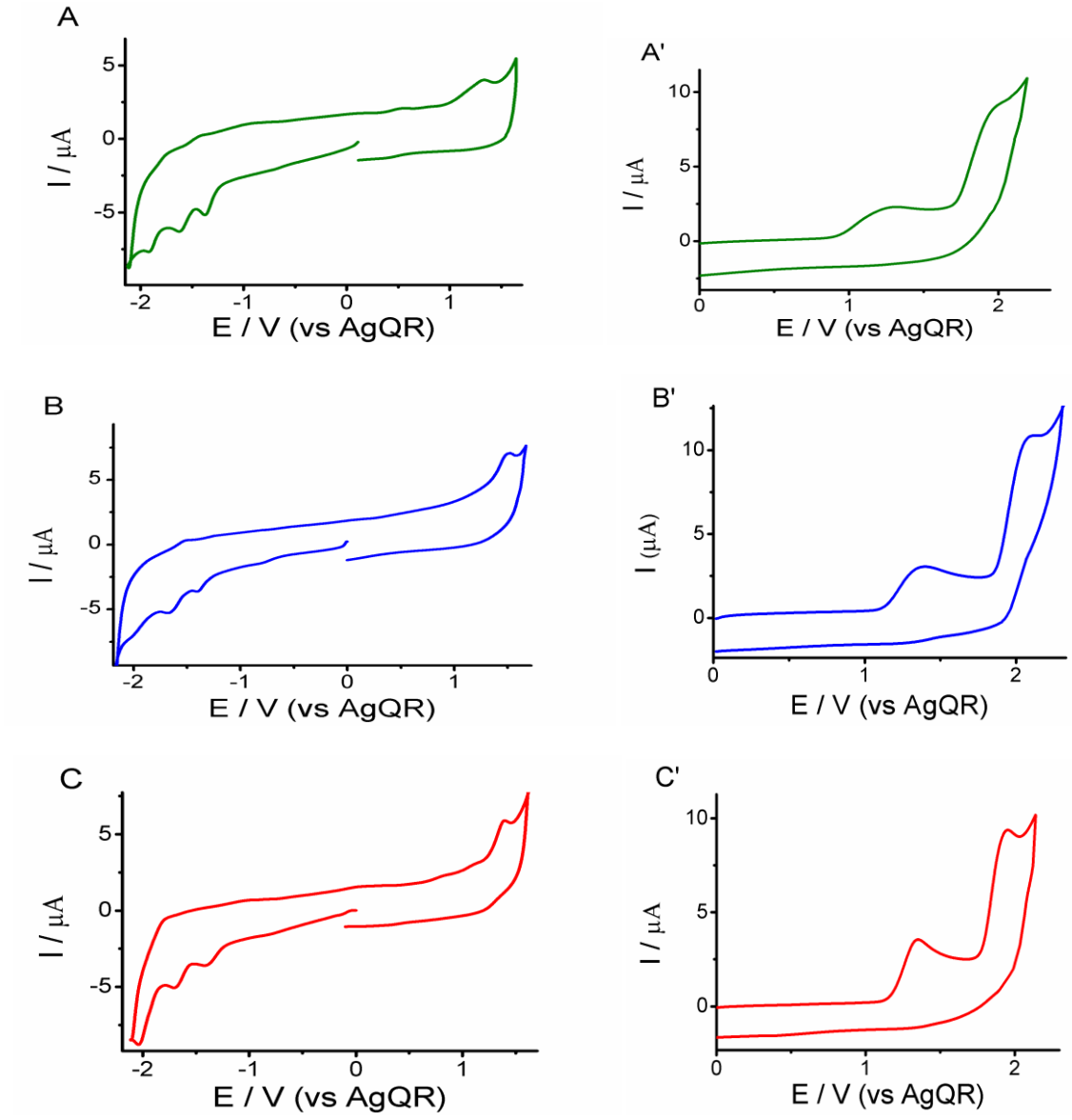

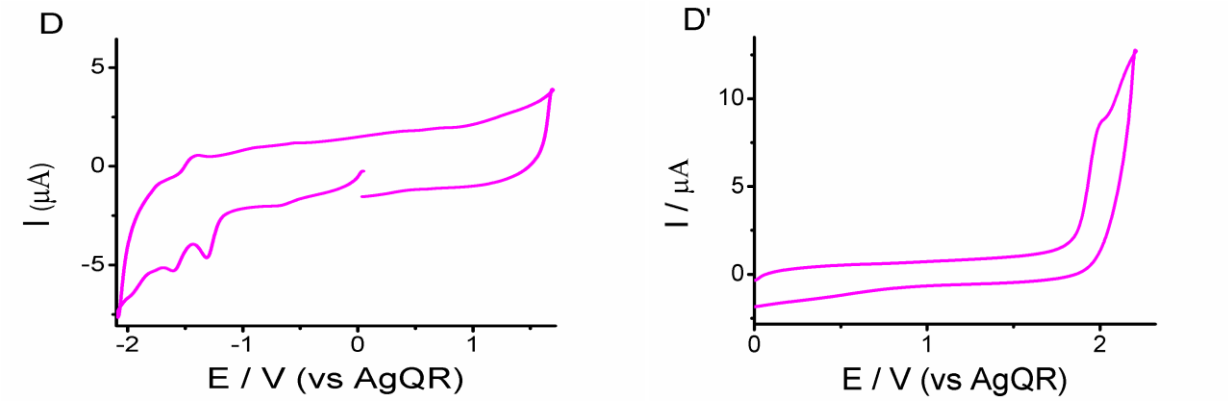

Fig 5.16- Cyclic voltammogramsrecorded at a GCEin 0.1 M $TBAPF_6/CH_3CN$ solutions containing 0.1 mM of:(**A**) – (**A'**) APC;(**B**) – (**B'**) NPC;(**C**) – (**C'**) SN-38;(**D**) - (**D'**) SN-38G. Scan rate: 200 mVs^{-1}. Capital letters without and with superscript refer to the initial scan direction towards the negative and positive potentials, respectively.

5.1.2.2.1 Voltammetric behaviour of APC

Fig 5.16A-A' shows typical CVs recorded at 200 mV s^{-1} for APC. In the negative potential region (**Fig 5.16A**) the recorded processes take place at the same potentials as those observed for CPT-11 (Table 1), attributed to the 2-pyridone and lactone rings (**Fig 5.17**, for direct comparison of CVs). Measurements performed at different scan rates provided, essentially, the same picture as long as scan rates higher than 50 mV s^{-1} were employed. At lower scan rates, a new composite process, resembling that attributed to the reduction of the protonated amine end of CPT-11HCl, appeared (see **Fig 5.17B**) over the potential region between about -0.9 to -1.1 V). This process can be attributed to the reduction of an acidic moiety present in APC; considering the structure of the molecule, the acidic moiety responsible of the electrode process could be formed through arelatively slow intra hydrogen-bonding equilibrium between the carboxylic acid (**Scheme 5.2C** highlighted in red) and the secondary amine (**Scheme 5.2C** highlighted in green) ends [54, 55].

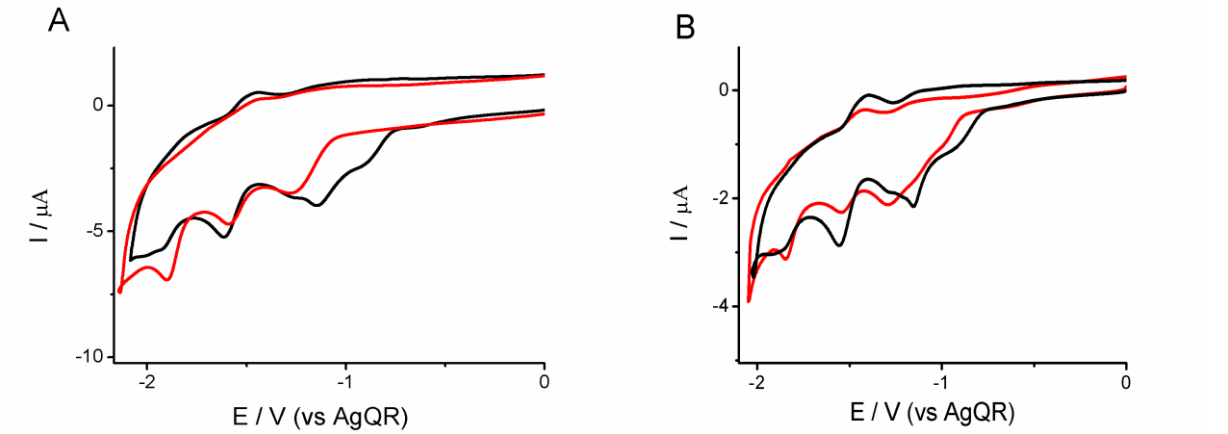

Fig 5.17 - Comparison between cyclic voltammograms recorded at a GCE in a 0.1 M $TBAPF_6/CH_3CN$ solution containing 0.1mM APC (red lines) and 0.1 mM CPT-11HCl (black lines). Scan rate: (**A**) 200 mV/s; (**B**) 20 mV/s.

The direct reduction of the carboxylic acid at the GCE could also be possible. However, it must be considered that aliphatic acids in acetonitrile are characterized by a very low dissociation constant (for instance, for acetic acid *pKa* = 23.51 was reported [47]) and therefore one would expect to observe a reduction wave at potential much more negative than that obtained for the protonated tertiary amine of CPT-11HCl [40]. CVs performed at Pt electrodes, whose catalytic ability can be exploited towards the hydrogen evolution reaction, confirmed that also for APC, a rather drown-out response, shifted towards less negative potential values with respect to that observed at the GCE, could be recorded (**Fig 5.18**, green line). The peak potential difference between cathodic and anodic peak was 290 mV, similar to that of CPT-11HCl (**Table 5.2**), also in this case in agreement with the reduction of a rather weak acid [43-45]. In the direct anodic scan, a drown-out oxidation process at +1.240V (peak width 135 mV, at 200 mVs^{-1}), followed by a second larger peak at 1.960 V were observed (**Fig 5.16A'**). The latter occurred at the same potential as those recorded for CPT-11 and CPT and can be assigned to the oxidation of the 2-pyridone ring (O_2). The peak at +1.240 V is conceivably due to the oxidation of the secondary amine end (**Scheme 5.2C**) [52-54]. In fact, the higher potential required, compared to that due for the oxidation of the tertiary amine of CPT-11 (O_3 in **Table 5.1**), is congruent with the general behaviour of alkyl amines, whose difficulty to be oxidized follows the order: tertiary < secondary < primary [52-54]. The mechanism involved should be similar to that mentioned above for the tertiary amine ($E_{p,a} - E_{p,a/2}$was 135 mV, at 200 mVs^{-1}), in agreement with literature reports for secondary amines [53, 54].

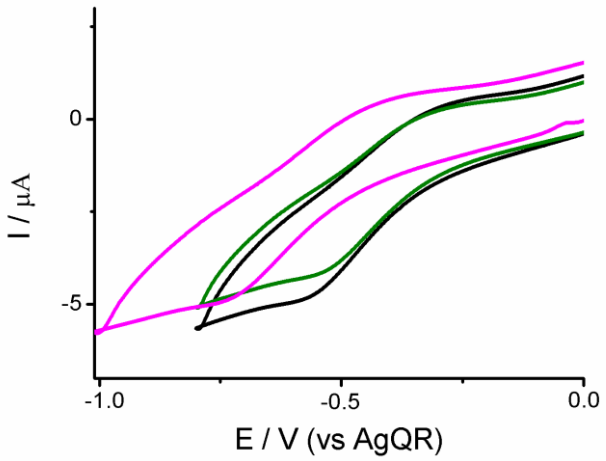

Fig 5.18 - Comparison among cyclic voltammograms recorded at a Pt electrode in 0.1 M $TBAPF_6/CH_3CN$ solution containing: 0.1 mMCPT-11 HCl (black line), 0.1 mM APC (green line), SN-38 G (pink line). Scan rate 200 mV/s

Table 5.2: Peak potentials (vs AgQR) recorded at a Pt electrode in 0.1 mM solutions of the indicated compounds in CH_3CN + 0.1 M $TBAPF_6$ solutions.

Compound	$E_{p,c}$/ V	$E_{p,a}$ / V	$E_{p,c}$– $E_{p,a}$ / V
CPT-11HCl	-0.58	-0.29	0.29
TrEAHCl	-0.61	-0.31	0.30
HCl	-0.19	-0.025	0.16
APC	-0.57	-0.28	0.29
SN-38 G	-0.89	-0.51	0.37

5.1.2.2.2 Voltammetric behaviour of NPC

Fig 5.16B-B' shows typical CVs recorded at 200 mV s^{-1} for NPC. In the negative potential region (**Fig 5.16B**), again, the recorded processes take place at the same potentials as those observed for CPT (**Table 5.1** and **Fig 5.19** for direct comparison of CVs) and can therefore be attributed to the 2-pyridone and lactone rings. Measurements performed at different scan rates did not show any change with respect to the above picture, which is congruent with the fact that the NPC structure does not contain easily reducible acidic moieties.

The CV recorded in the anodic region (**Fig 5.16B'**) displays two peaks at +1.340 V and +1.980 V (O_3 and O_2, respectively in **Table 5.1**). The latter is due to the oxidation of 2-pyridone ring, as for CPT (**Fig 5.19B** for direct comparison of CVs). The first peak (at +1.340V) is assigned to the oxidation of the primary amine end (see Scheme 2D highlighted in green), and the higher potential observed, compared with those required for both CPT-11 and APC (seeO_3peak potential values for CPT-11, APC and NPC in **Table 5.1**), follows the expected oxidability trend of alkyl amines mentioned above. Also, for the primary amine end of NPC, an EC mechanism with characteristics of slow electron transfer, similar to those seen for the tertiary and secondary amine ends, probably applies ($E_{p,a} - E_{p,a/2}$ at 200 mVs^{-1} was 135 mV).

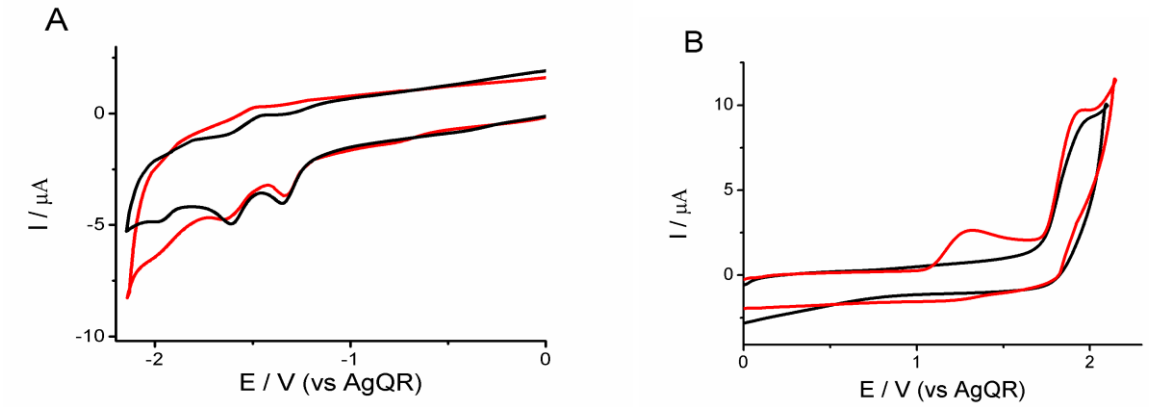

Fig 5.19 - Comparison between cyclic voltammograms recorded at a GCE in 0.1 M $TBAPF_6/CH_3CN$ solutions containing 0.1 mM NPC (red line) and 0.1 mM CPT (black line). (**A**) Negative and (**B**) positive potential regions. Scan rate: 200 mV/s**.**

5.1.2.2.3 Voltammetric behaviour of SN-38

The structure of SN-38 is essentially the same as that of CPT, apart from the presence in the quinoline moiety of the hydroxyl group (**Scheme 5.2E**, highlighted in blue). However, SN-38 in acetonitrile, at room temperature, proved to be rather unstable, and CVs recorded at different times (i.e., within a few minutes) changed substantially from one measurement to another. **Fig 5.16C-C'** shows typical CVs recorded after about 5-6 min from the preparation of the solution. In the negative potential zone, three peaks are observed, of which, the two occurring at less negative potentials almost coincide with those recorded for CPT (**Table 5.1**). Therefore, these peaks can be assigned to the 2-pyridone and lactone moieties. The third peak of SN-38, at -1.980 V, is about 60 mV more negative (**Table 5.1**) and of higher intensity than that of the corresponding one of CPT. Moreover, the peak height increased with elapsing time (**Fig 5.20A**), while, simultaneously, the two less negative peaks broadened and finally overlapped (**Fig 5.20**, green line). This indicated that undesired reactions occurred in the bulk solution.

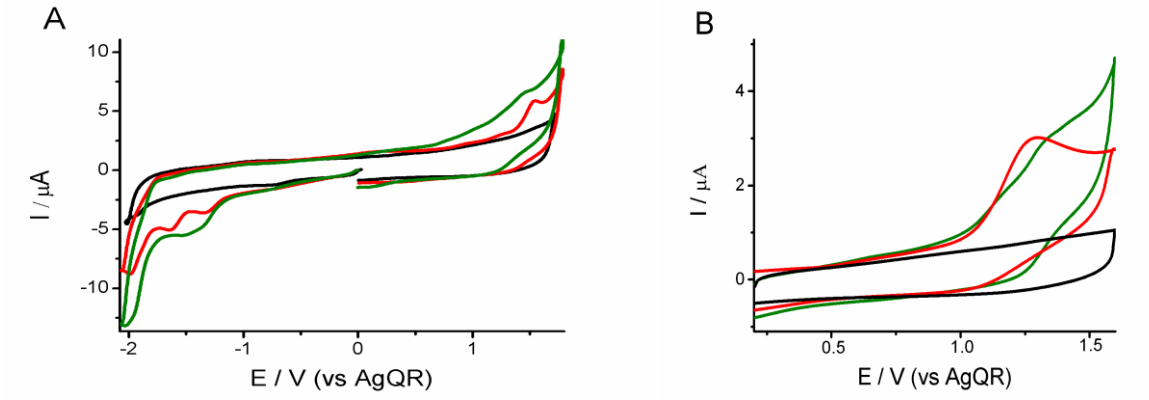

Fig 5.20- Cyclic voltammograms recorded at a GCE in a 0.1 M $TBAPF_6/CH_3CN$ solutioncontaining 0.1mM SN-38**.** (**A**) Direct negative potential scans at various times after the preparation of the solution: 5 (red line) and 35 (green line) min; background (black line). (**B**) direct anodic scan at various times 5 (red line) and 35 (green line) min. Scan rate: 200 mV/s.

The low stability of SN-38 affected also the voltammetric behaviour in the positive potential region. The CV recorded after about 5-6 minutes displayed two peaks (**Fig 5.17C'**), the one occurring at more positive potentials, matched, as expected, that attributed to the oxidation of 2-pyridone ring. The peak recorded at the less positive potentials changed with time (**Fig 5.20**), and this was concurrently with the changes of the CV features observed in the negative potential region. This oxidation peak can be attributed to oxidation of hydroxyl group at quinoline moiety [56]. This was confirmed by its absence in the CV in **Fig 5.16D** (see below). However, it is worth to highlight that, even after SN-38 degraded to a stable form, no process was recorded over the potential region in which the oxidation of the tertiary amine of CPT-11 occurred. No further investigation on SN-38 was performed to establish the identity of the final degradation products.

5.1.2.2.4 Voltammetric behaviour of SN-38G

SN38-G proved to be much more stable than the parent compound from which it is derived by the enzymatic reaction [7]. The molecule contains the glucoronide moiety (**Scheme 5.2F** highlighted in red), which probably imparts stability to the metabolite. Typical CVs recorded in a 0.1 mM SN-38G acetonitrile solution are shown in **Fig 5.16D-D'**. In the negative potential region three peaks occurring at potentials close to that of CPT are observed (**Table 5.1** and **Fig 5.21** for direct comparison of the CVs). The glucoronide moiety actually contains a carboxylic group, which could be directly reduced to hydrogen. However, as discussed in section 5.1.2.1, the aliphatic carboxylic acids in acetonitrile are characterized by very low dissociation constants [47] and therefore the relevant reduction processes at the GCE might occur beyond the potential window explored. This result in part confirms the circumstance outlined above for the carboxylic acid moieties of APC, which should not be directly reduced over the negative potential explored. However, at the Pt electrode in the negative potential region, also SN-38G provided a rather drown-out cathodic-anodic peak system, which is shifted to more negative potentials and with a larger anodic-cathodic peak separation (**Fig 5.18**, purple line) with respect to those recorded for both CPT-11HCl and APC, in agreement with the involvement of a weaker acidic species [43, 47, 57].

In the positive potential region, SN-38G provided only an oxidation peak, whose potential matched that of CPT, and therefore assigned to the 2-pyridone ring (**Fig 5.21B**).

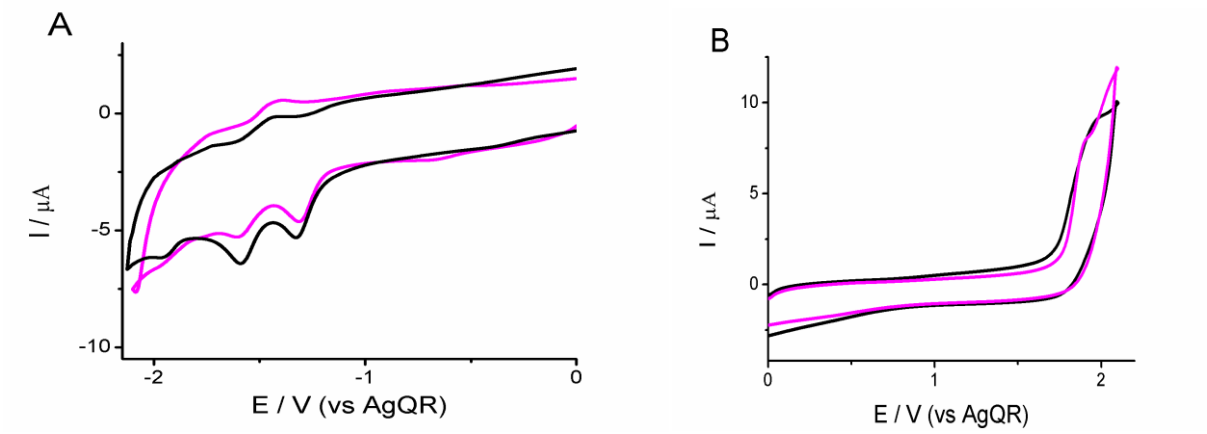

Fig 5.21 - Comparison between cyclic voltammograms recorded at a GCE in 0.1 M $TBAPF_6/CH_3CN$ solutions containing 0.1 mM SN-38G (magenta line), and 0.1 mM CPT (black line). (**A**) negative and (**B**) positive potential region. Scan rate 200 mV/s**.**

5.1.2.3 Voltammetric behaviour of CPT-11 and its metabolites in the presence of sodium borate.

The results presented in the previous sections clearly indicate that the voltammetric patterns of CPT-11 or CPT-11HCl are very similar to those of their metabolites. However, considering peak potential values shown in **Table 5.1**, it appears that in the anodic region the tertiary amine end of CPT-11 (as can be obtained from CPT-11HCl after compensation of the proton level with an excess of sodium borate) provided an oxidation peak over a potential region almost free from interferences. To further confirm this view, the voltammetric behaviour at the GCE of all metabolites was examined in acetonitrile solutions containing sodium borate. **Fig 5.22A,B** shows the CVs thus obtained. As it can be observed, while in the negative potential region all metabolites provide peaks that strongly overlap with those of CPT-11, in the positive region, the oxidation peak attributed to the amine end of CPT-11 is completely separated from the others, including that due to the oxidation of Cl^- coming from the use of the injectable CPT-11HCl solution.

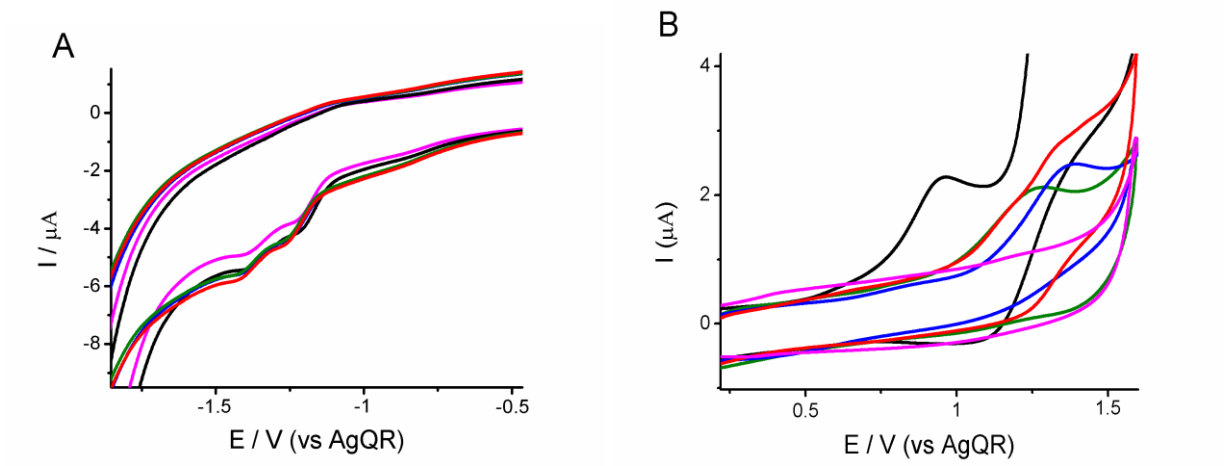

Fig 5.22- Cyclic voltammograms recorded at a GCE in 0.1 M $TBAPF_6/CH_3CN$ and 0.73 mM$Na_2B_4O_7$ solutions containing 0.1 mM of: CPT-11HCl (black); APC (green); NPC (blue); SN-38(red); SN38-G(magenta). (**A**) Negative potential region; (**B**) positive potential region. Scan rate: 200 mVs^{-1}

5.1.2.4 Voltammetric behaviour of 5-FU and FA.

From the results discussed above for CPT-11 and CPT-11' metabolites, it is evident that the anodic potential zone is the most useful for the detection of irinotecan. Therefore the voltammetric behavior of the co-drugs 5-FU and FA was briefly investigated in acetonitrile-borate buffer solutions (i.e., the same medium, where no interference due to CPT-11' metabolites occurs), with the aim to establish whether or not they eventually provide responses which could overlap with that due to the oxidation of the tertiary amine of CPT-11.

The chemical structure of 5-FU, FA and folinic acid (FoA) are displayed in **Scheme 5.3**:

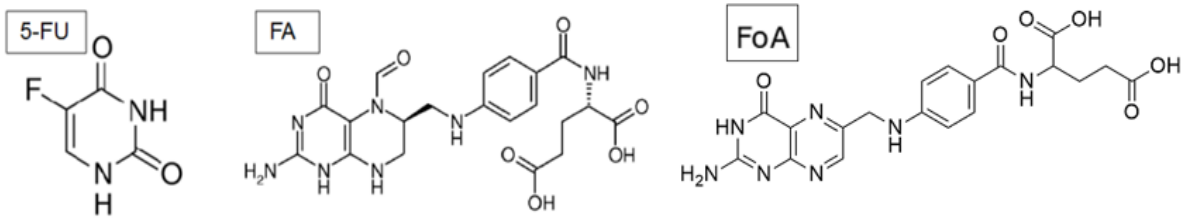

Scheme 5.3 - Structures of 5-Fluorouracil (5-FU) and Folinic Acid (FA), Folic acid (FoA)

Both 5-FU and FA are water soluble. In the literature, the voltammetric behavior of 5-FU in aqueous media was reported and a mechanism involving the oxidation of the amidic moiety in an irreversible one electron process was proposed [58, 59]. No information exists for 5-FU in non-aqueous media. As for FA, no voltammetric investigation has been previously reported neither in

aqueous or non-aqueous media. Voltammetry of folic acid (**Scheme 5.3**), which share with FA a similar skeleton structure, has been reported in the literature [62-66]. It is therefore likely that the voltammetric behavior of FA is similar to that of folic acid.

Typical CVs recorded in basified CH_3CN solutions containing 80 µM of 5-FU or 40 µM of FA are displayed in **Fig 5.34A** and **Fig 5.34B**, respectively.

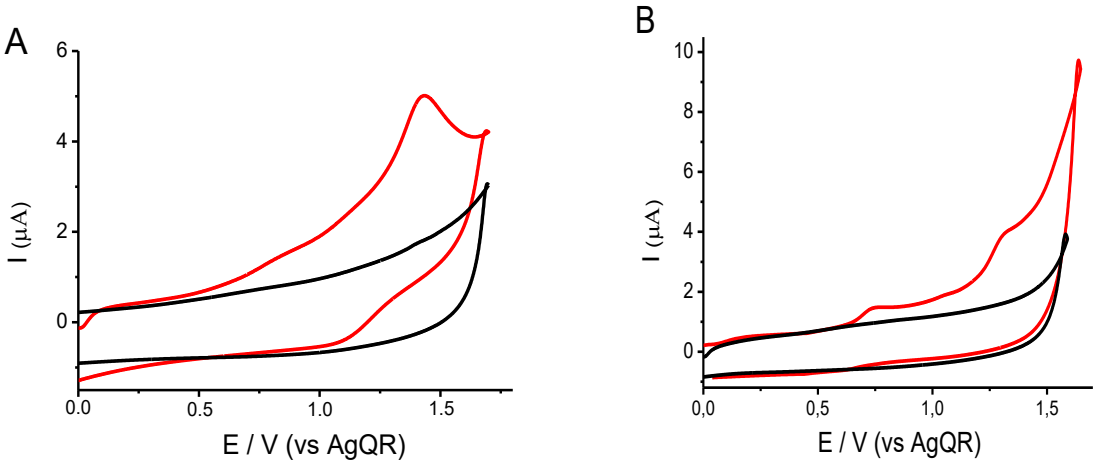

Fig 5.34- CVs of 80 µM of 5-FU (**A,** red line) and of 40 µM of FA (**B,** red line) recorded in 0.1 M $TBAPF_6/CH_3CN$ + 0.73 mM $Na_2B_4O_7$ solutions. Black lines are backgrounds. 200 mV/s.

As is evident, 5-FU shows two irreversible broad peaks at about + 0.8 and + 1.35 V vs. AgQR. The main peak at 1.35 V is conceivably ascribable to the same amide group involved in the oxidation process applying in aqueous media [58-61]. Since the peak position for this process depends on pH [59, 60], the small peak at 0.8 can be due to a small amount of a deprotonated form of 5-FU formed by acid-base equilibria.

As for FA, considering the mechanism reported in the literature for FoA [62-65], it is likely that the main peak recorded at about 1.35 V *vs.* AgQR in CH_3CN can be due to the oxidation of the secondary amine at C9-N10 position [63].

No further investigation was performed to elucidate the mechanisms applying for both 5-FU and FA in acetonitrile. In the next sections, the discussion is limited to the interference arising from the presence of the two co-drugs on the oxidation process of tertiary amine of CPT-11.

5.1.3 Detection of CPT-11 in synthetic solutions by cyclic voltammetry and differential pulse voltammetry

As stated in the previous section,the process at about + 0.98 V, obtained 0.1 M $TBAPF_6/CH_3CN$ solution amended with 0.73 mM of $Na_2B_4O_7$, could be exploited to detect CPT-11, provided that a linear dependence exists between peak current against concentration. This was assessed in preliminary measurements performed in acetonitrile solutions basified with sodium borate and containing CPT-11HCl at different concentrations (over the range 0.02 – 0.2 mM) using CV, at 100 mVs^{-1}. A series of CVs along with relevant calibration plot are shown in **Fig 5.23**. Under these conditions, peak current (*I*) against concentration ($C_{CPT\text{-}11HCl}$) yielded a straight line and the linear regression analysis of experimental data provided: $I\ (\mu A) = 27\ C_{CPT\text{-}11HCl}\ (mM) + 0.08$ with a correlation coefficient of 0.994. The reproducibility was within 3% from three replicates, The detection limits were determined according to the IUPAC [67] achieving a value of 5.5 µM.

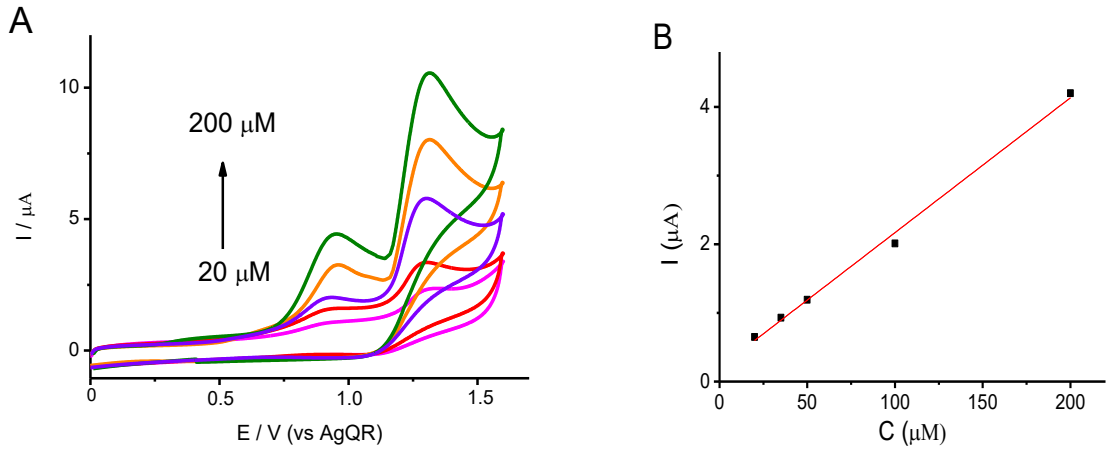

Fig 5.23- Cyclic voltammograms (**A**) and relevant calibration plot (**B**) of 20, 35, 50, 100, 200 µM CPT-11 HCl in CH_3CN, 0.1 M $TBAPF_6$ amended with 0.73 mM of $Na_2B_4O_7$. Scan rate: 50 mVs^{-1}.

To increase the sensitivity, and thus achieving lower detection limits, which are needed for TDM applications of CPT-11 [68] measurements were also performed by using differential pulse voltammetry (DPV). A series of preliminarily measurements was performed in a 4 µM CPT-11HCl solution to optimize DPV parameters, which resulted to the following pulse height 0.05 V; potential increment 4 mV; pulse width 0.2 s; pulse period 0.5 s. These were used in all quantification procedures involving CPT-11 (or CPT-11HCl).

Typical DPVs recorded at different concentrations of CPT-11HCl in CH_3CN solutions without and with sodium borate, are displayed in **Fig 5.24**. As expected, in the absence of borate buffer, only the peak due to the oxidation of chloride ion was recorded (**Fig 5.24A**), whose current intensity depended linearly on CPT-11HCl concentration (see inset in **Fig 5.24A)**. In the

presence of borate both peaks due to chloride and tertiary amine were found (**Fig 5.24B**) and current intensities were proportional to CPT-11HCl concentration (see insets in **Fig 5.24B**).

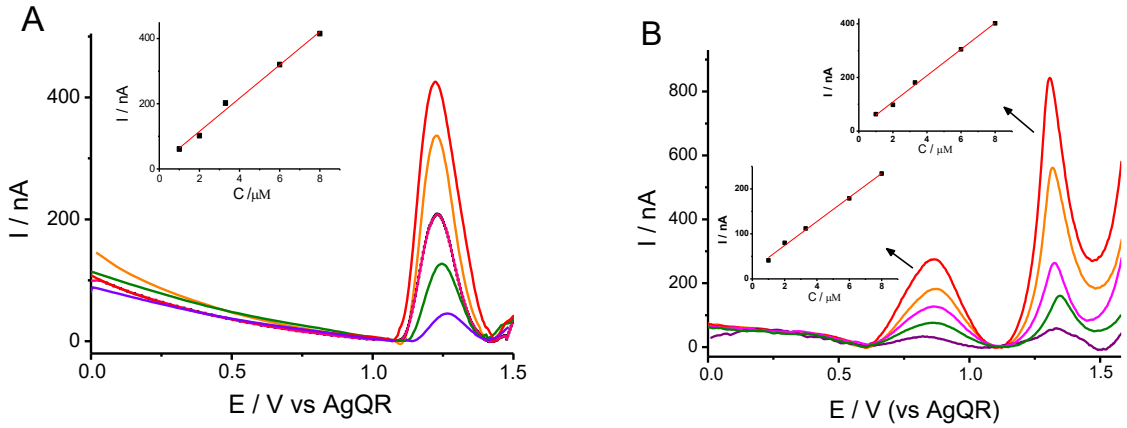

Fig 5.24 -DPVs of CPT-11 HCl at 1, 2, 3.3, 6, 8 µM in CH_3CN, 0.1 M $TBAPF_6$ solutions without (**A**) and with (**B**) 0.73 mM of $Na_2B_4O_7$. Voltammograms are baseline subtracted respect to the first peak.

Fig 5.25 shows a series of DPVs and relevant calibration plot obtained over a wider CPT-11HCl concentration range (i.e., 0.25 – 9 µM). In this case, the linear regression analysis of experimental data provided: $I\ (\mu A) = 0.0326\ C_{CPT\text{-}11HCl}\ (\mu M) + 0.006$ with a correlation coefficient of 0.994. The reproducibility was within 3% from three replicates and the detection limit was 0.11 µM.

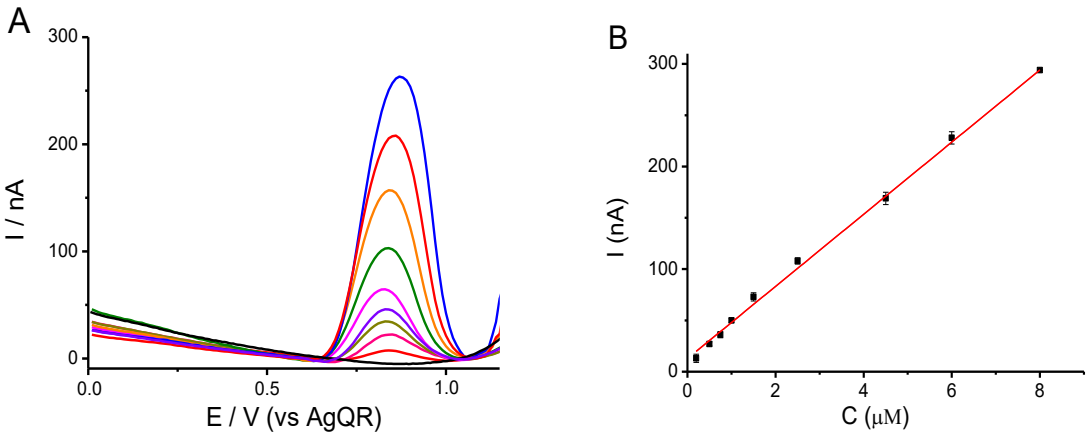

Fig 5.25- (**A**) DPVs of different concentrations of CPT-11HCl recorded in CH_3CN, 0.1 M $TBAPF_6$, 0.73 mM of $Na_2B_4O_7$ solutions (synthetic solutions). (**B**) Relevant calibration plot; error bars refer to ± 2SD from 3 replicates.

5.1.4 Interferences from co-therapeutics

The interference due to 5-FU and FA was investigated in detail, as in the FOLFIRI regimen their concentrations can be up to 10 and 3 times, respectively, higher than that CPT-11HCl. Thus, considering the voltammetric behavior of the three compounds described in the previous section,

their presence in the plasma matrix can represent a consistent source of interferences and consequently of errors in the CPT-11 evaluation.

This investigation was performed only using DPV, and typical voltammograms obtained for the co-drugs in CH_3CN-borate buffer solutions are displayed in **Fig 5.26.** As is evident, major interference on the CPT-11 oxidation process arises from the presence of FA (**Fig 5.26B**), because of the peak at about 0.74 V. 5-FU (**Fig 5.26A**) provides only an increment of the background current over the potential range 0.5 – 0.9 V.

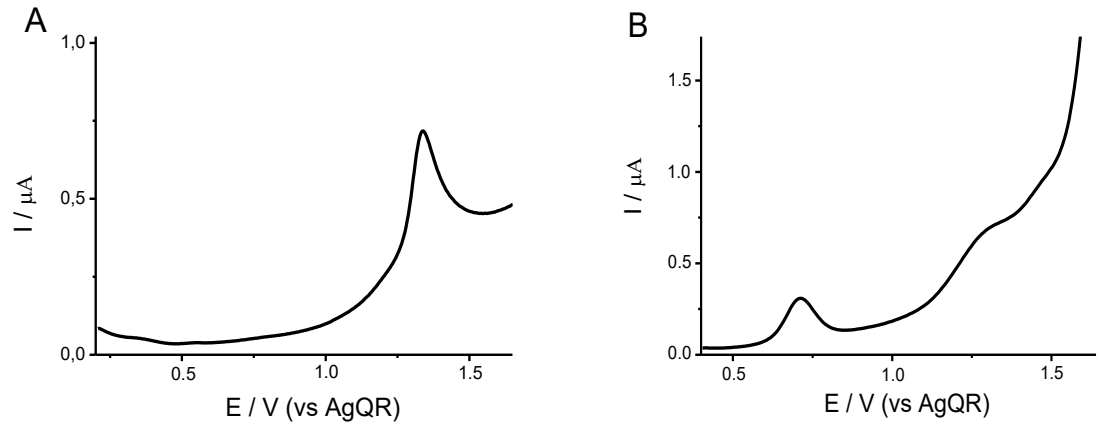

Fig 5.26-(A) DPV of 12 µM of 5-FU recorded in CH_3CN, 0.1 M $TBAPF_6$, amended with 0.73 mM of $Na_2B_4O_7$. (**B**) DPV of 10µM of FA recorded in CH_3CN, 0.1 M $TBAPF_6$ amended with 0.73 mM of $Na_2B_4O_7$.

To better visualize the interference due to the co-drugs, series of measurements were performed in CH_3CN-sodium borate solutions containing, initially, 2.5 µM CPT-11HCl (**Fig 5.27, black line**) to which increasing amounts of 5-FU (**Fig 5.27A**) and FA (**Fig 5.26B**) were added.

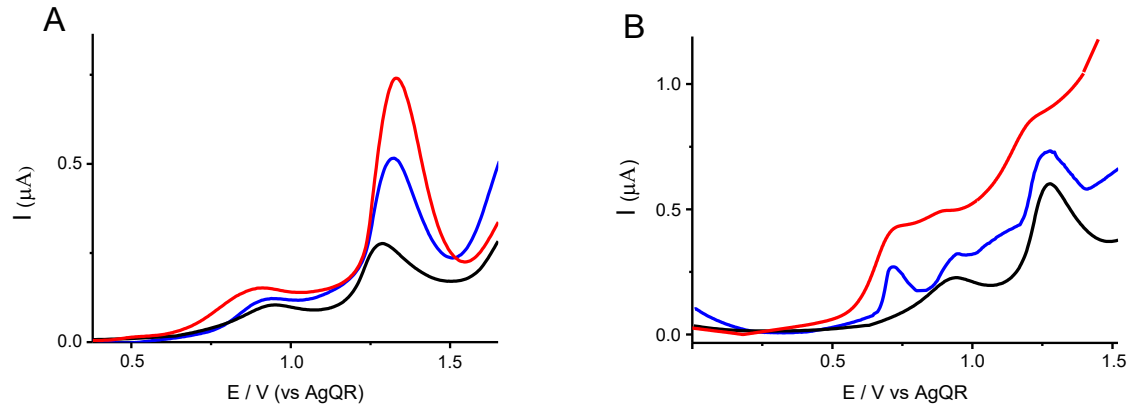

Fig 5.27- (**A**) DPV of 2.5 µM CPT-11 HCl (black line) in CH_3CN, 0.05 M $TBAPF_6$ amended with 0.73 mM of $Na_2B_4O_7$; after the addition of 6 µM 5-FU (blue) and 12 µM 5-FU (red). (**B**) DPV of 2.5 µM CPT-11HCl in CH_3CN, 0.05 M $TBAPF_6$ amended with 0.73 mM of $Na_2B_4O_7$ (black line); after the addition of 4 µM FA (blue) and 10 µM FA (red).

From **Fig 5.27**, it is clear that the main process due to 5-FU overlaps with that due chloride, its presence, however lead to an increase of the oxidation process of the tertiary amine of CPT-11. Instead the processes due to FA completely overlap those of CPT-11HCl. Thus, to avoid the latter interference, a pre-treatment procedure would be required (see in the next sections).

5.1.5 Detection of CPT-11 in plasma samples

The application of DPV for the detection of CPT-11 in plasma samples was firstly performed directly in the real matrix spiked with known amounts of CPT-11HCl. Typically, 200 µL of plasma was spiked with different concentrations of CPT-11HCl and then diluted with 800 µL of CH_3CN containing 0.05 M of $TBAPF_6$ and 0.73 mM of $Na_2B_4O_7$. **Fig 5.28** shows the voltammogram obtained in the un-spiked plasma sample (black curve) and those recorded after addition of CPT-11HCl (blue and red curves). As is evident, in the un-spiked plasma sample, processes due to some endogenous compounds (such as, ascorbic or uric acid) are evident, which prevent a clear discrimination of the peak due to the tertiary amine of CPT-11, even at 5 µM levels (**Fig 5.28** red curve), which are however too high for TDM application.

Considering the latter result and those discussed in the previous section, it appears that a separation/extraction step of the analyte of interest is required before the voltammetric detection of CPT-11. This aspect is addressed in the next section.

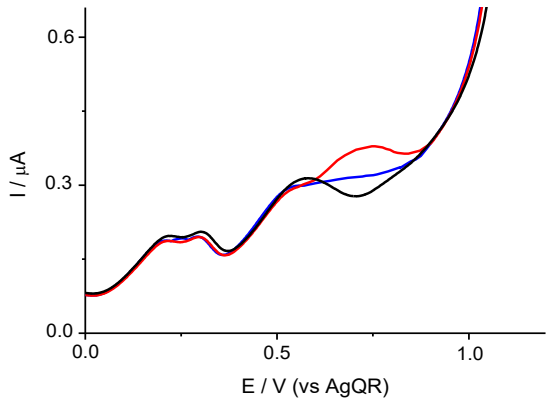

Fig 5.28 - DPVs recorded in plasma/acetonitrile mixture containing 0.05 M of $TBAPF_6$ and 0.73 mM of $Na_2B_4O_7$ with 0 (black line), 2 (blue line), 5 (red line) µM of CPT-11HCl.

5.1.5.1 Detection of CPT-11 after purification/extraction from solid phase extraction (SPE) columns

CPT-11 extraction from plasma samples was performed by using commercially available SPE columns (StrataXL). Strata XL type columns were chosen because, according to the indications provided by the manufacturer, they are suitable to absorb neutral compounds containing aromatic rings, which display relatively low solubility in aqueous or very polar solvents [68, 69]. This situation fits the case of CPT-11, whose un-protonated form is known to display low solubility in very polar media [70]. In the development of the analytical procedure, the following aspects were considered:

- eliminating, with a suitable mixture of solvents, organic substances with polar characteristics (for example endogenous acids, and co-drugs), while keeping CPT-11 adsorbed within the column;
- eluting with acetonitrile the drug of interest, sufficiently free from major interferents;
- use of small volumes of both plasma and eluents; the latter conditions is required because of the limited amounts of real samples available and to avoid excessive dilution of CPT-11 in the final solution in which voltammetric measurements are performed. To achieve these goals, a multi-steps extraction procedure was set up, as summarized in **Scheme 5.3**.

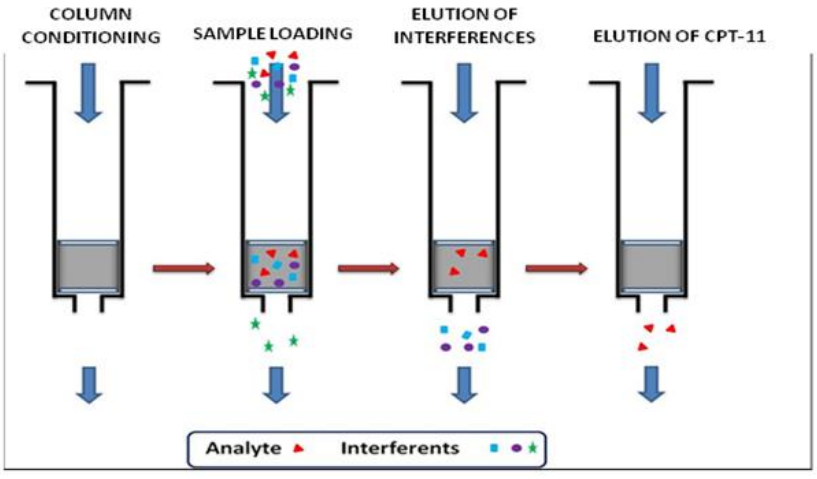

Scheme 5.3: Scheme of the procedure used to extract CPT-11 from plasma samples.

Initially, the column was conditioned with 1 mL of MeOH and then with 1 mL of milli-Q water to wet the stationary phase. The column was afterward loaded with 125 µL of plasma and 75 µL of PBS (pH 7.4); the latter buffer was used to keep plasma samples at their physiological values. Two aliquots (600 µL each) of a 90% Milli-Q water and 10% MeOH mixture were forced (by a N_2 stream) to pass through the column to eliminate polar substance of the sample. CPT-11 from the column was then eluted using 475 µL of pure CH_3CN (forced to pass through the column by

a pure N_2 stream). Prior to electrochemical analysis, 25 μL of a CH_3CN-borate buffer solution was added to achieve the final solution composition for the voltammetric analysis (i.e., 0.05 M $TBAPF_6$ and 0.73 mM of $Na_2B_4O_7$) It must be highlighted that although the above procedure involves many steps, it requires about 4 minutes to be completed.

The validity of the above procedure for eliminating interferences was assessed by its application to plasma samples spiked with 12 μM 5-FU and 10 μM FA. **Fig 5.29** (blue lines) shows typical CVs and DPVs obtained in the final extracts fortified with only supporting electrolyte and borate buffer; for comparison relevant voltammograms recorded directly in the plasma samples diluted in CH_3CN-borate buffer solution (un-spiked with CPT-11), and in the solutions containing the pure co-drugs (i.e., **Fig 5.26B** and **Fig 5.26 B**) are included. In **Fig. 5.29**, in any case, no peak was recorded up to about 1.5 V, thus confirming the successful elimination of the above interferents.

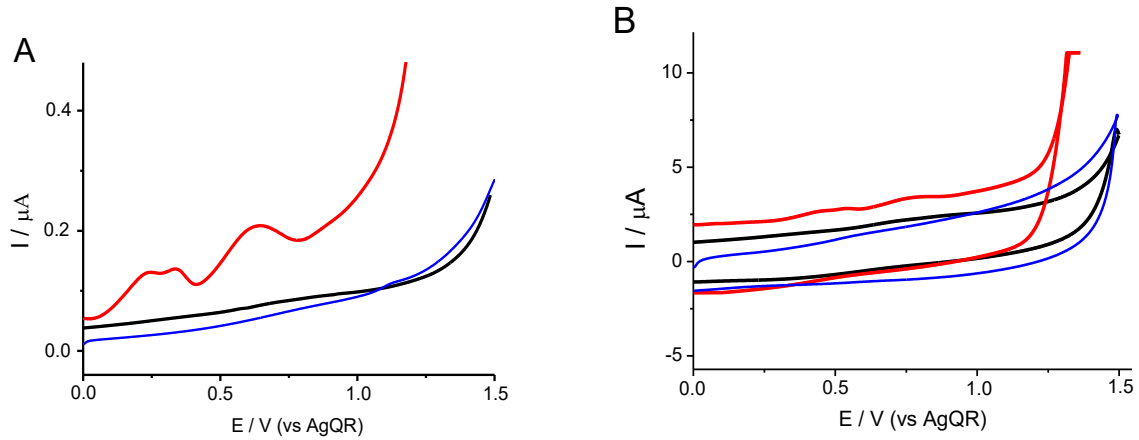

Fig 5.29: DPVs (**A**) and CVs (**B**) of the anodic region of a plasma/acetonitrile mixture (red lines), of the anodic region of a column extract (black lines) and of the anodic region of a column extract from plasma sample that was spiked with 12 μM 5-FU and 10 μM FA (blue lines). CVs were recorded at 100 mVs^{-1}.

To further support that the purification procedure was successful, CVs obtained in the synthetic acetonitrile solution (blue lines) and in the plasma extracts (red lines) spiked with 0.25 mM CPT-11HCl, in either neutral or basified (with $Na_2B_4O_7$) solutions, were compared (**Fig. 5.30**). In both cases almost overlapped responses were obtained.

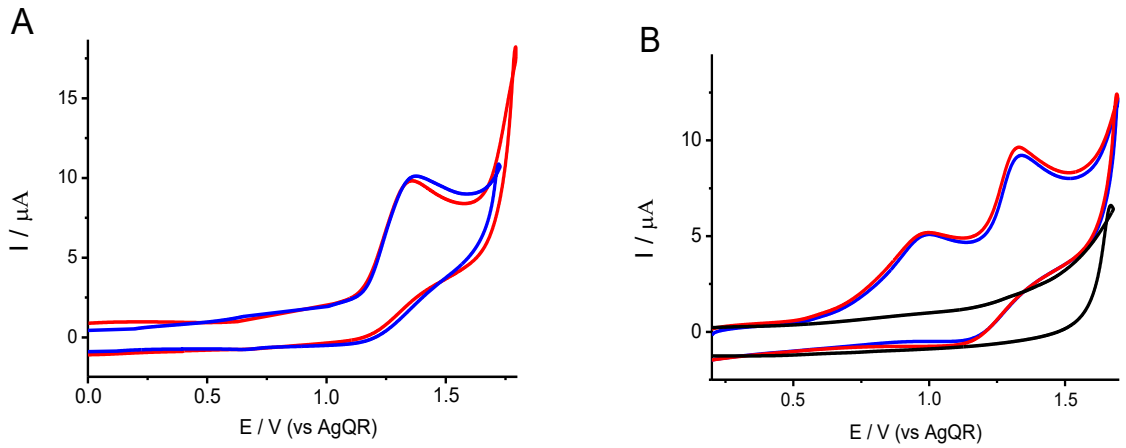

Fig. 5.30 - (A) Cyclic voltammograms of 0.25 mM CPT-11HCl recorded in CH_3CN, 0.05 M $TBAPF_6$ solution (blue line) and of 0.25 mM CPT-11 HCl spiked in the column extracts (red line). **(B)** Cyclic voltammograms of 0.25 mM CPT-11HCl recorded in CH_3CN, 0.05 M $TBAPF_6$ solution, amended with $Na_2B_4O_7$ (blue line) and of 0.25 mM CPT-11HCl spiked in the extract amended with $Na_2B_4O_7$ (red line). Scan rate: 100 mVs^{-1}.

Calibration plots performed by using the extracts as media were also constructed over the same dynamic range employed in section 5.1.3 using DPV. Typical voltammetric responses obtained along with the calibration plot are shown in **Fig 5.31**. **Table 5.3** compares the equations obtained by linear regression analysis of the experimental data. As is evident the analytical characteristics, including detection limits, obtained from the two types of calibration plots, compare well.

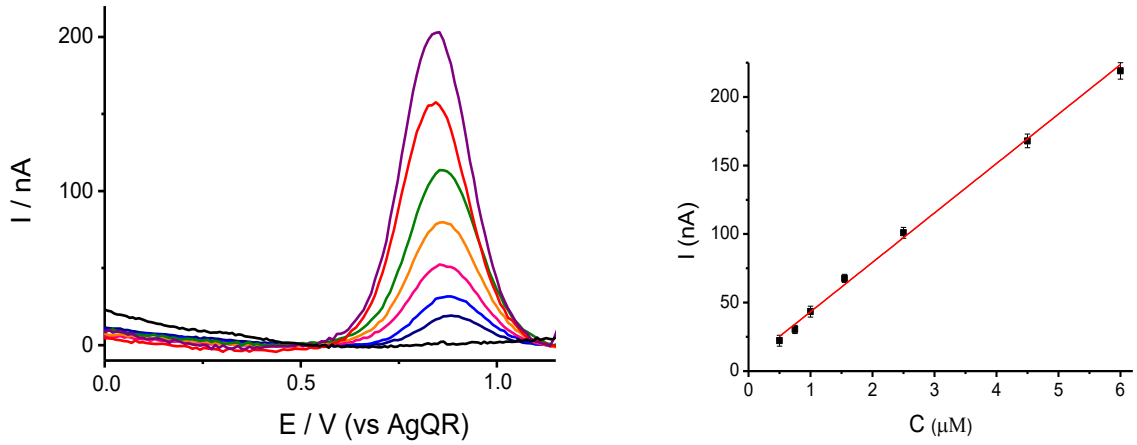

Fig 5.31 (A): DP voltammograms of CPT-11 HCl spiked in plasma extracts, which were amended with 0.1 M of $TBAPF_6$ and 0.73 mM of $Na_2B_4O_7$; **(B)**: relevant calibration plot (error bars refer to ± 2 SD form three replicates).

Table 5.3 Linear regression parameters obtained by DPV for the detection of CPT-11HCl recorded in Synthetic (0.1 M $TBAPF_6/CH_3CN$ solutions amended with $Na_2B_4O_7$), spiked (SX columns plasma extracts (see section 4.4.2) amended with$TBAPF_6$ and $Na_2B_4O_7$, in which CPT-11HCl is added after extraction) and extracted (SX columns plasma extracts amended with$TBAPF_6$ and $Na_2B_4O_7$, in which CPT-11HCl was added to plasma and then extracted).

Medium	Dynamic Range in mol L^{-1}	Linear regression equation $I\ (\mu A) = m\ C\ (\mu M) + b$	R^2	LOD(*A) (mol L^{-1})	LOQ(*B) (mol L^{-1})
Synthetic	$2.5 \times 10^{-7} - 9 \times 10^{-6}$	*I = 0.0326C +0.006*	0.994	$1.10\ 10^{-7}$	$3.74\ 10^{-7}$
Extract Spiked with CPT-11HCl	$0.5 \times 10^{-7} - 6 \times 10^{-6}$	*I = 0.0334C +0.008*	0.992	$1.28\ 10^{-7}$	$4.26\ 10^{-7}$
Plasma samples spiked with CPT-11HCl and examined in the extracts	$0.5 \times 10^{-7} - 6 \times 10^{-6}$	*I = 0.0332C +0.003*	0.987	$1.28\ 10^{-7}$	$4.26\ 10^{-7}$

(A*) $LOD = \frac{3\ SD_{background}}{m}$ where *m* is the slope of linear regression equation.

(B*) $LOQ = \frac{10\ SD_{background}}{m}$

5.1.5.2 Recovery of CPT-11 from plasma samples spiked before the extraction procedure

Recovery tests were also performed by subjecting a series of plasma samples, spiked with different amounts of CPT-11HCl or with CPT-11HCl and 5-FU and FA, to the extraction procedure. The quantification of CPT-11 in the extracts was achieved by using the standard addition method. **Fig. 5.32** shows examples of DPVs recorded in either the extracts (black lines) or after the standard addition. **Table 5.4** summarizes the CPT-11 concentrations expected and those found. The latter refer to the average values obtained from three replicates.

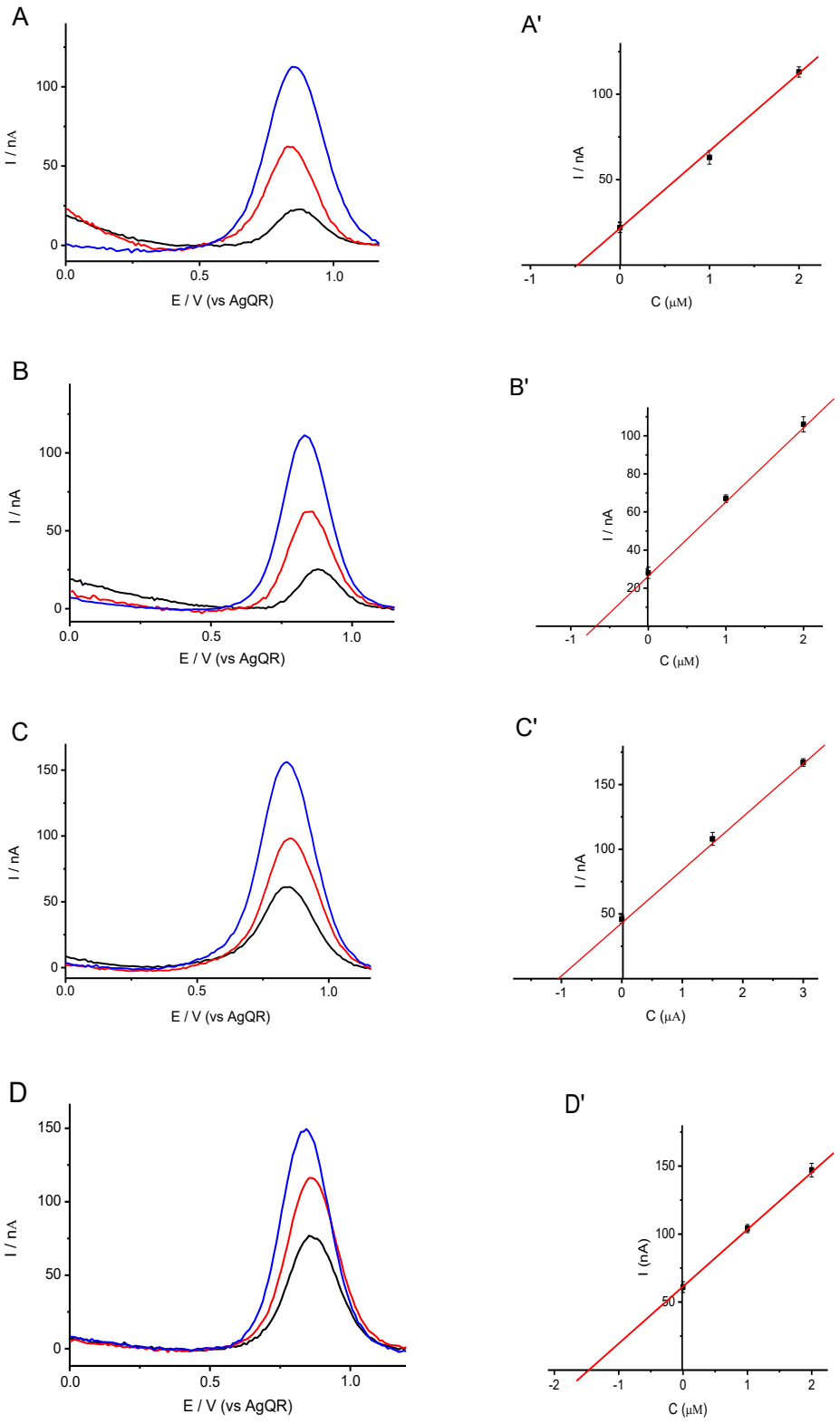

Fig 5.32 - DPVs of four different concentrations of CPT-11 extracted from plasma (black lines): A, B, C, D correspond to concentrations of 0.5, 0.75, 1, 1.5 µM, respectively. Red and blue lines are standard additions to the extracts. A', B', C', D' correspond to standard additions regression lines.

Table 5.4 - CPT-11 recovered from CPT-11HCl spiked in plasma and then extracted.

$C_{expected}$ (µM)	C_{found} (2SD[(A)])/ µM	Recovery[(B)] % (2RSD %)
0.50	0.52 (0.06)	104 (10)
0.75	0.71 (0.06)	95 (8)
1.00	1.02 (0.09)	102 (9)
1.50	1.45 (0.10)	97 (7)
2.50	2.44 (0.12)	97 (5)
4.50	4.60 (0.17)	102 (4)
6.00	5.85 (0.18)	97 (3)

(A): standard deviation ($SD = \sqrt{\frac{(C_i - C_M)^2}{N}}$) was obtained from three replicates.

(B): Recovery % = $\frac{C_{expected}}{C_{found}}$ %

Peak currents of the DPVs were also plotted against the CPT-11 concentrations found in the extracts (**Fig 5.33**) and regression analysis of the experimental data provided the equation included in **Table 5.3**. The latter compare well with that obtained in the extracts of plasma which was subsequently spiked CPT-11HCl. This further confirms the suitability of the extraction procedure for recovery CPT-11 and eliminating interferents.

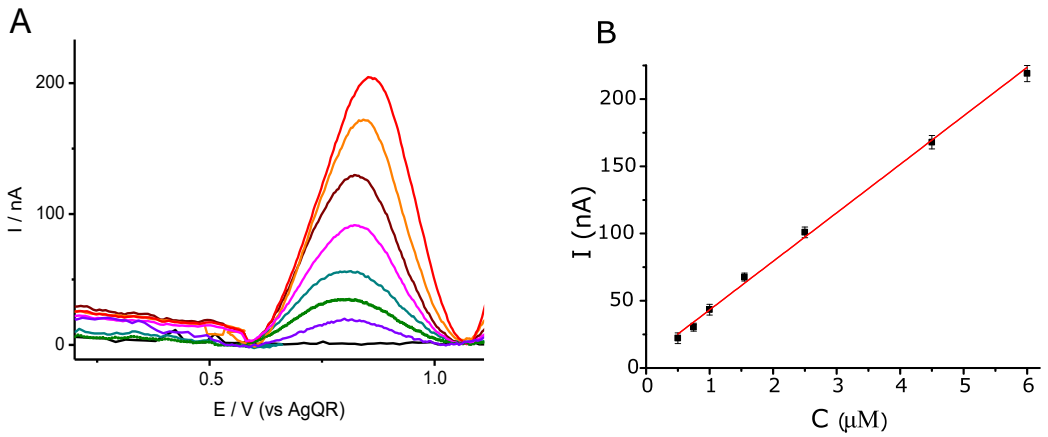

Fig 5.33- (A) DPVs of different concentrations of CPT-11 that was spiked in plasma and then extracted and analyzed. (**B**) Relevant calibration plot.

Finally, **Fig. 5.34** compares two series of DPVs obtained in the extracts of plasma samples spiked with only CPT-11HCl (2.5 and 6 µM) and those spiked with CPT-11HCl and 12 µM 5-FU and 10 µM of FA. As is evident, in all cases, the voltammetric responses are almost identical,

thus further confirming the usefulness of the extraction procedure to eliminate the interference due to the co-drugs.

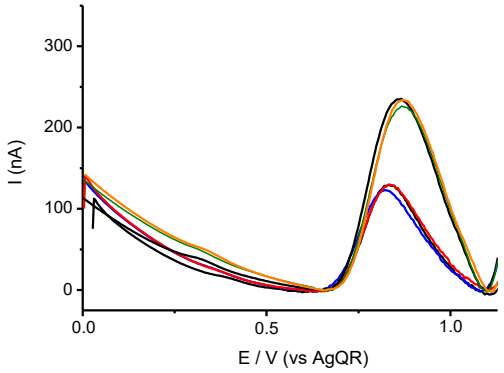

Fig 5.34 DPVs of 2.5 and 6 µM CPT-11 HCl that were spiked in human plasma and then extracted without (black lines) and with (colored lines, replicates) 12 µM 5-FU and 10 µM of FA.

With respect to the evaluation of method reliability, robustness and stability experiments were performed.

Firstly, the stability of CPT-11HCl in the analysis environment was verified. In **Fig 5.35** DPVs of CPT-11 recorded at different times after extraction are displayed.

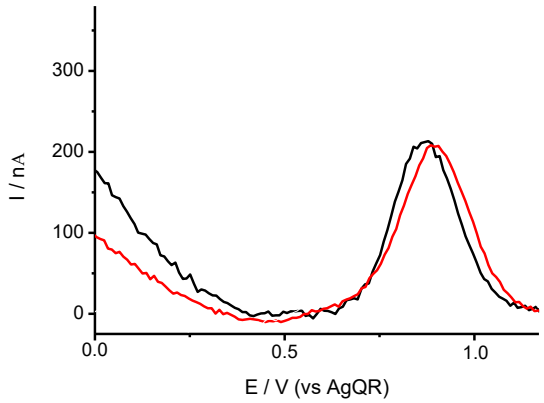

Fig 5.35 – DPVs of 5 µM of CPT-11HCl recorded in plasma extracts after 1 min (red line) and 60 min (black line) after extraction.

From **Fig 5.35** it is clear that the signal doesn't undergoes variations up to 1 h. After this time it starts to decrease slightly.

Inter-day, inter-day and inter-week variability, determined on plasma samples which were amended with 4 µM of CPT-11HCl, was always less than 10%, expressed in terms of RSD% of three replicates.

5.1.6 Role played by chloride ions of CPT-11HCl in the SPE steps

In the previous sections, no mention was made on the fate of chloride ions of CPT-11HCl when plasma samples, spiked with the latter compound, undergo the separation/extraction steps. In this section, the latter aspect is examined in detail, because Cl^- ions play an important role in the partition of CPT-11 within the SX columns during the cleaning steps performed with the 90% H_2O/10% CH_3OH mixture.

Fig 5.36 shows two series of DPVs recorded in the CH_3CN extracts without (**Fig 5.36A**) and with added borate buffer (**Fig 5.36B**). As it is evident, a single peak, due to chloride ion, or two distinct peaks, due to the tertiary amine and chloride ion (see previous sections), are recorded in the un-basified or basified medium, respectively. Moreover, a rough estimate of the current intensities of the two peaks at about 1.3 V provide similar values. This result suggests that Cl^- ions are not washed out from the SX columns during the cleaning procedure, and that their amounts in the final extracts are close to the tertiary ammine of CPT-11. To explain the reason why Cl^- ions, which are soluble in water media, remain trapped within the stationary phase, it was hypothesized that CPT-11H^+Cl^- forms an ionic couple, which partitions, by hydrophobic interaction, within the stationary phase. It is afterward eluted in the uncharged form during the CH_3CN extraction step.

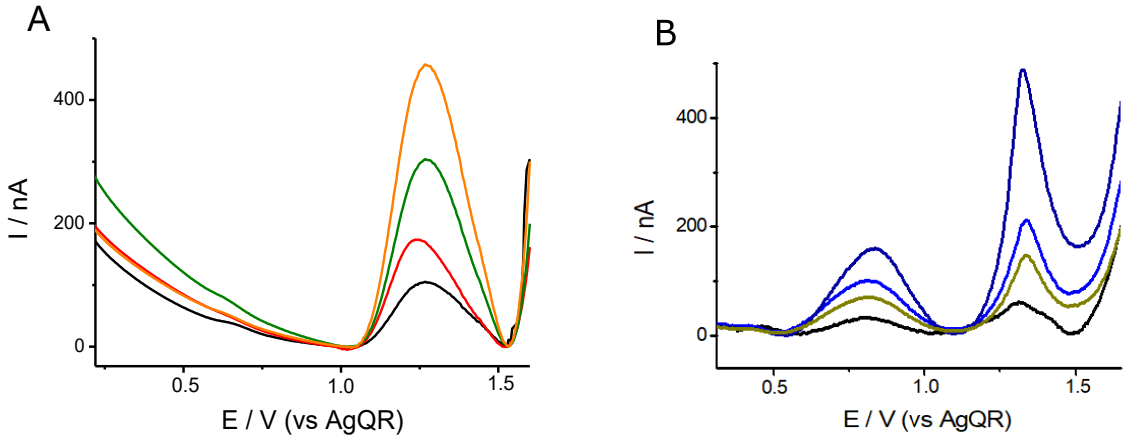

Fig 5.36 DPVs recorded in the CH3CN extracts of plasma sample spiked with CPT-11HCl (1.5, 3, 6, 9 µM) CPT-11HCl without (**A**) and with (**B**) 0.73 mM $Na_2B_4O_7$.

To confirm the above hypothesis, the following experiments were performed.

First, 200 µL of an aqueous sample containing 4µM CPT-11HCl and phosphate buffer pH 7.4 (i.e., close to the plasma pH) was loaded in the SX column and then subjected to the separation extraction procedure described in **Scheme 5.2**. DPVs performed in the extract provided a single

broad peak at about 1.3 V (**Fig 5.37,** black line), conceivably due to the Cl^- oxidation process. The latter peak increased by adding CPT-11HCl in the medium (**Fig 5.37** green and blue lines), thus confirming the presence of Cl^- ions in the extract.

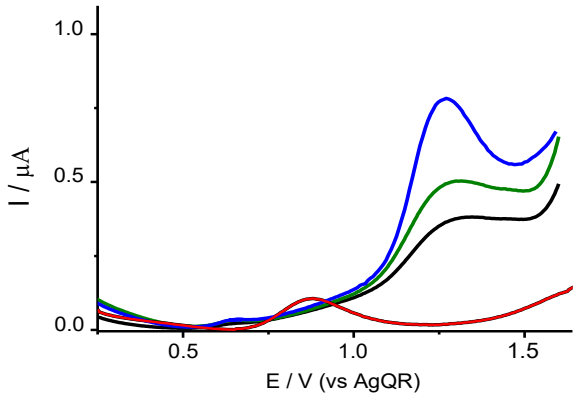

Fig 5.37 - Black line: DPV of 4 µM of CPT-11HCl extracted from an aqueous sample, employing the procedure described in **Scheme 5.2**. Standard additions of 4 µM (green) and 12 µM (blue) of CPT-11HCl. Red line: DPV of 4 µM of CPT-11HCl extracted adding $Na_2B_4O_7$ to the washing step.

In a second extraction/separation experiment, the 4 µM CPT-11HCl water sample, once loaded in the SX column, was cleaned with the H_2O/CH_3OH mixture containing also borate buffer. Under these condition CPT-11 is in its base form; Cl^- is not able to form the ionic couple and in fact, after the SX column was further treated with CH_3CN, the extract investigated by DPV provided the response shown in **Fig. 5.37** (red line), in which only the peak due to the tertiary ammine is evident.

To confirm the formation of an ionic couple between CPT-$11H^+$ and Cl^-, a voltammetric investigation was performed in CH_3CN without and with $TBAPF_6$ as supporting electrolyte, using a platinum microelectrode.

It is well known that with microelectrodes, voltammetry can be performed even in the absence of supporting electrolyte because the responses are negligibly affected by ohmic drop [71, *Daniele et al*]. However, in the absence of a suitable excess of electrolyte, the mass transport of a charged specie is affected by both diffusion and migration [72, 73]. Consequently, depending on the charge of the reagent and reaction products, the steady state current may vary sensibly with respect to the diffusion controlled processes.

At the Pt microdisk the following reaction processes could in principle occur:

$$2Cl^- \rightarrow Cl_2 + 2e^- \quad \text{(anodic process, following a fast chemical reaction)} \qquad (1)$$

$$2\text{CPT-}11H^+ + 2e^- \rightarrow 2\ \text{CPT-}11 + H_2 \ \text{(cathodic process)} \qquad (2)$$

Moreover reactions (*1*) and (*2*), at the electrode surface, can be preceded by the fast chemical reaction:

$$CPT\text{-}11H^+Cl^- \rightarrow CPT\text{-}11H^+ + Cl^- \qquad (3)$$

Both reactions (*1*) and (*2*) involve a singly charged species forming a neutral product. In these cases, theory predicts that the steady-state current is given by

$$i_m/i_d = n+1+2\rho-2[\rho(n+\rho)]^{1/2} \qquad (eq.\ 1)$$

where i_m and i_d are the current recorded with low and excess of supporting electrolyte, respectively; $\rho = C_{SE}/C_E$ (C_{SE} and C_E are the concentration of the supporting electrolyte and the electroactive specie, respectively) is the support excess; n is the charge of the electroactive species. Assuming, as is the case, $\rho = 0$ and $n = 1$, $i_m/i_d = 2$. If reaction (*3*) is coupled to reaction (*1*) or (*2*) and it occurs rapidly at the electrode surface, equation (4) provides $i_m/i_d = 1$, regardless of ρ, $CPT\text{-}11H^+Cl^-$ being neutral (i.e. $n = 0$).

Fig 5.38 shows steady-state voltammograms of CPT-11HCl recorded in CH_3CN solutions with (black lines) and without (red lines) 0.1 M of supporting electrolyte in either the positive (**Fig 5.38A**) or negative (**Fig 5.38B**) potential zone. As is evident in both cases almost overlapped waves, whose half-wave potential is located at about 1.35 V, are obtained. Actually, the plateau currents in the absence of electrolyte are slightly higher than those recorded in excess of electrolyte. These results therefore are congruent with the formation of a ion pair between the protonated tertiary amine and Cl^- ion.

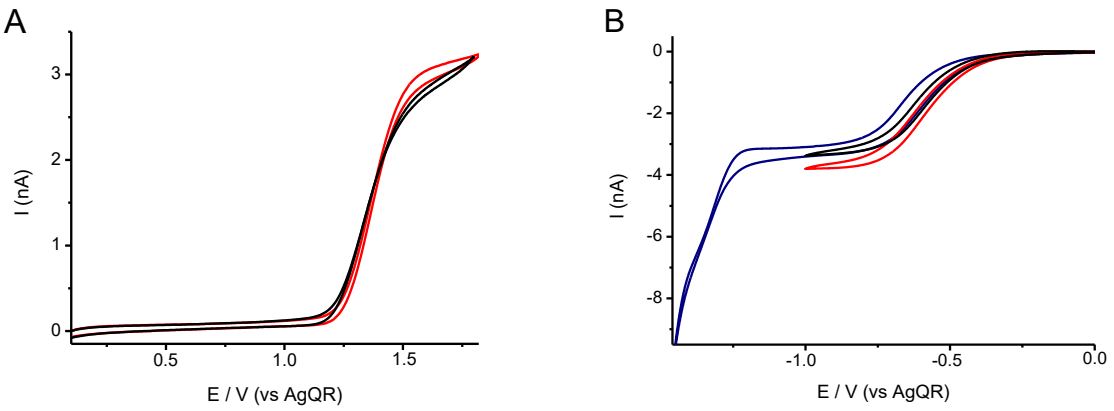

Fig 5.38 (A) - CVs of 0.5 mM CPT-11HCl recorded at a Pt microelectrode (Ø = 25µm) in CH_3CN solutions without (red) and with (black) 0.1 M of $TBAPF_6$. **(B)** CVs of 0.5 mM CPT-11HCl recorded at Pt microelectrode in CH_3CN solutions without (red) and with (black and blue) 0.1 M of $TBAPF_6$. $v = 10\ mVs^{-1}$.

Further CVs experiments were performed using the model compound TrEAHCl and TEACl, which should behave as CPT-11HCl and as a strong electrolyte, respectively. **Fig 5.39** shows typical CVs recorded in 0.5 mM CH_3CN solutions of the two compounds without (black line) and with (red line) 0.1 M $TBAPF_6$. As is evident, a dramatic behavioral difference exist between the two compounds, as is also shown in **Table 5.6**, where i_m/i_d values for the different investigated species are summarized. In the case of TEACl, i_m/i_d is almost equal to 2, as predicted by *eq. 1*, indicating that reaction (*1*) is likely to be operative. In other cases, i_m/i_d values close to 1 (or slightly higher) indicate that a neutral species is involved in the mass transport towards the electrode surface.

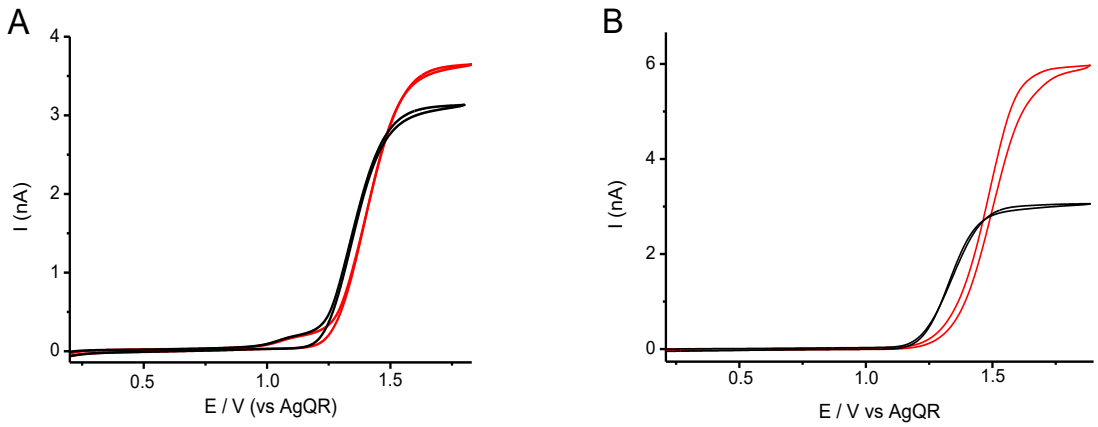

Fig 5.39- (A) CVs of 0.5 mM of TrEAHCl recorded at a Pt microelectrode (Ø = 25µm) in CH_3CN solutions without (red) and with (black) 0.1 M of $TBAPF_6$. **(B)** CVs of 0.5 mM of TEACl recorded at a Pt microelectrode in CH_3CN solutions without (red) and with (black) 0.1 M of $TBAPF_6$. $v = 10\ mVs^{-1}$

Overall, the above results corroborate the hypothesis of the formation of the ion pair $CPT\text{-}11H^+$ and Cl^-.

Table 5.5: ratios between the limiting currents recorded at a Pt microelectrode with and without supporting electrolyte.

Compound	i_m/i_d
CPT-11HCl (anodic)	1.07
CPT-11HCl (cathodic)	1.11
TrEAHCl (anodic)	1.21
TEACl (anodic)	1.96

5.1.7 Detection of CPT-11 in plasma samples collected from oncologic patient

The validity of the analytical protocol described above was applied to two plasma samples collected from a patient affected by colorectal cancer, undergoing the FOLFIRI chemotherapeutic treatment. The samples were collected at 30 min and 180 min from administration. DPVs recorded in SXL plasma extracts, are shown in **Fig 5.40A-B** (red lines), along with the addition of known amounts of CPT-11HCl (**Fig 5.40A-B,** green and blue lines**)** to evaluate the drug concentration using the standard addition method (**Fig 5.40 A'-B'**). As is evident clean DPVs at about 0.85 V are recorded (i.e., due to the oxidation of the tertiary amine), indicating the validity of the extraction/separation protocol optimized above. Average (from three replicates) CPT-11 concentration found, after considering the dilution of the drug due to the extraction step, are shown in **Table 5.6** Reproducibility was within 8% (RSD).

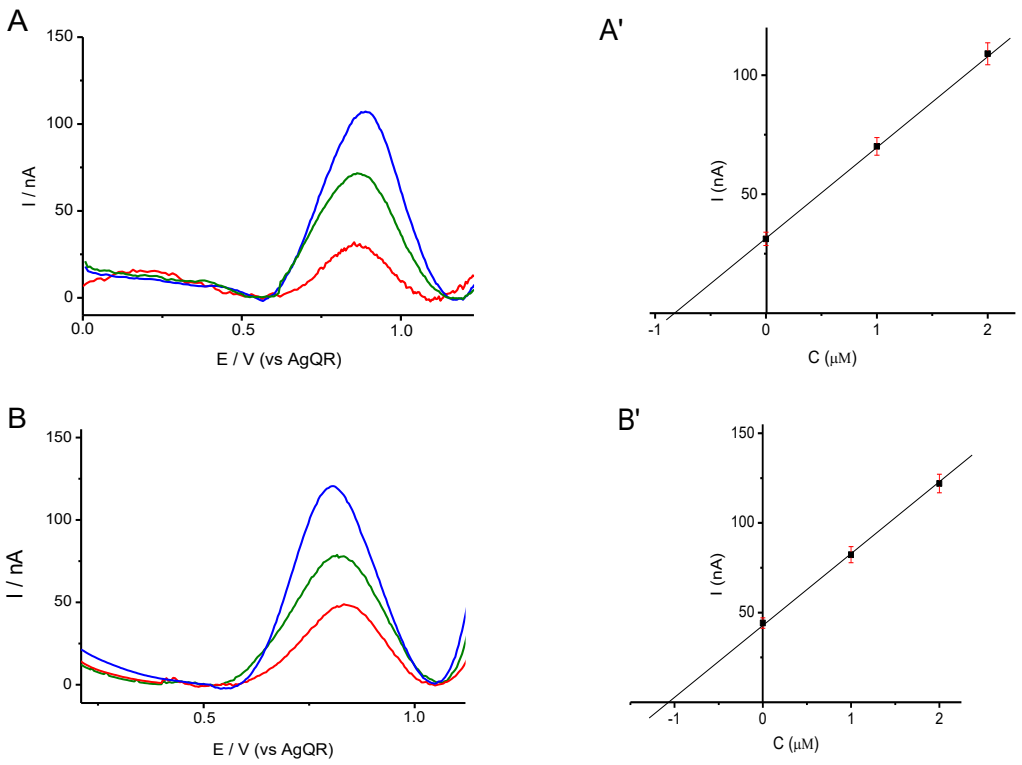

-Fig 5.40 (A-B) - DPVs recorded in plasma extracts obtained from plasma samples of a patient undergoing chemotherapeutic treatment. (**A'-B'**) – Relevant calibration plots . Measurements were run from 0 V to +1.1 V *vs.* AgQR. Red line: original measurement; green and blue line: standard additions of 0.25 μM each of CPT-11.

Table 5.6: comparison between the SPE-DPV method with a validated method: C_{ref} are the concentrations obtained with the reference method (HPLC-MS method, [17]) and C_{DPV} thus obtained with the electrochemical method. Sampling time is the time passed between drug administration and sample collection.

Sampling time (min)	**C_{ref} (2RSD%) µM**	**C_{DPV} (2RSD%)(*)µM**	**RE (%)**
30	3.59 (<10)	3.21 (3)	11.8
180	4.06 (<10)	4.70 (8)	20.7

(*)From 3 replicates RE % = $\frac{Err}{T}$ %; $Err = |O - T|$, where O is the concentration value obtained by DPV, T is the reference value

References

[1] N. Masuda, S. Kudoh, M. Fukuoka, Critical Reviews of Oncology/Hematology 24 (1996) 3-26.

[2] H. Hurwitz, L. Fehrenbacher, W. Novotny, T. Cartwright, J. Hainsworth, W. Heim, J. Berlin, A. Baron, S. Griffing, E. Holmgren, N. Ferrara, G. Fyfe, B. Rogers, R. Ross, F. Kabbinavar, The new England Journal of Medicine 350 (2004) 2335-2342.

[3] R. B. Ewesuedo, M. J. Ratain, The Oncologist 2 (1997) 359-364.

[4] J. Weekes, A. K. Lam, S. Sebesan, Y. H. Ho, World JournalGastroenterol 29 (2009) 3597-3602.

[5] C. Fuchs, E. P. Mitchell, P. M. Hoff, Cancer Treatment Reviews 32 (2006) 491-453.

[6] M. Ramesh, P. Ahlawat, N. R. Srinivas, Biomedical Chromatography 24 (2010) 104-123.

[7] R.H.J.Mathijssen, R. J. van Alphen, J. Verweii, W. J. Loos, K. Nooter, G. Storer, A. Sparreboom,Clinical Cancer Research 7 (2001) 2182-2194.

[8] J. G. Slatter, L. J. Schaaf, J. P. Sams, K. L. Feenstra, M. G. Johnson, P. Bombardt, K. S. Cathcart, M. T. Verburg, L. K. Pearson, L. D. Compton, L. L. Miller, D. S. Baker, C. V. Peshek, R. S. Lord, Drug Metabolism and Disposition 28 (2000) 423-433.

[9] M.E. Wall, M.C. Wani, C.E. Cook, K.H. Palmer, A.T. McPhail, G.A. Sim, Journal of American Chemical Society 88 (1966) 3888-3890.

[10] A. Falcone, S. Ricci, I. Brunetti, E. Pfanner, G. Allegrini, C. Barbara, L. Crinò, Journal of Clinical Oncology 25 (2007) 1670–76.

[11] A.J. Ordieres, A.J. Miranda, M.J. Garcia Gutierrez, A. Costa Garcia, P.T. Blanco, Analyst 112 (1987) 443-6.

[12] K. Freudenberger,U. Hilbig, G.Gauglitz,Trends in Analytical Chemistry 79 (2016) 257-268.

[13] L. A. Serrano, Y. Yang, E. Salvati, F. Stellacci, S. Krol, S. Guldin, Chemical Communications 54 (2018) 1485-1488.

[14] P. de Bruijn, J. Verweij, W. J. Loos, K. Nooter, G. Stoter, A. Sparreboom, Journal of Chromatography B 698 (1997) 277-285.

[15] E. Gravel, P. Bourget, L.Mercier, A.Paci Journal of Pharmaceutical and Biomedical Analysis 39 (2005) 581-586.

[16] S. Poujol, F. Pinguet, F. Malosse, C. Astre, M. Ychou, S. Culine, F. Bressolle, ClinicalChemistry 49 (2003) 1900-1908.

[17] E. Marangon, B. Posocco, E. Mazzega, G. Toffoli, PLOS one 10 (2015) 2-18.

[18] T. S. Owens, H.Dodds, K.Fricke, S. K.Hanna, K. R.Crews, Journal of Chromatography B1 (2003) 65-74.

[19] R. Z. Hahn, P. C. Arnhold, N. B. Andriguetti, A. Schneider, H. M. Kluck, S. L. Dos Reis, M. F. Bastiani, I. Kael, A. C. C. da Silva, G. Schwartsmann, M. V. Antunes, R. Linden, Journal of Pharmaceutical and Biomedical Analysis 150 (2018) 51-58.

[20] T. Bansal, A. Awashti, M. Jaggi, R. K. Khar, S. Talegaonkar, Talanta 76 (2008) 1015-1021.

[21] G. McMahon, R. O' Connor, Bioanalysis 1 (2009) 507-511.

[22] D. W. Kimmel, G. LeBlanc, M. E. Meschievitz,D. E. Cliffel**,** Analytical Chemistry 84 (2012) 685-707.

[23] B. J. Sanghavi, O.S.Wolfbeis, T. Hirsch, N. S. Swami, Microchimica Acta 182 (2015) 1-41.

[24] J. Liu, Y. Zhang, M. Jiang, L. Tian, S. Sun, N. Zhao, F. Zhao, Y. Li, Biosensors and Bioelectronics 91 (2017) 714-720.

[25] E. Salvati, F. Stellacci,S. Krol, Nanomedicine 10 (2015) 3495-3512.

[26] D.P. Valencia, L.M.F. Dantas, A. Lara, J. García, Z. Rivera, J. Rosas, M. Bertotti

Journal of Electroanalytical Chemistry 770 (2016) 50-55.

[27] M. D. Alvau, S. Tartaggia, A. Meneghello, B. Casetta, G. Calia, P. A. Serra, F. Polo, G. Toffoli, Analytical Chemistry 90 (2018) 6012-6019.

[28] P. Norouzi, M. Qomi, A. Nemati, M. R. Ganjali, International Journal of Electrochemical Science, 4 (2009) 1248-1261.

[29] Y. M. Temerk, H. S. M. Ibrahim, Journal of the Brazilean Chemical Society 24 (2013) n.10.

[30] N. Karadas, S. Sanli, B. Akmese, B. Dogan-Topal, A. Can, S. A. Ozkan, Talanta 115 (2013) 911-919.

[31] Y. M. Temerk, H. S. M. Ibrahim, W. Schumann,Electroanalysis 28 (2016) 372-379.

[32] G. Zotti, A. Berlin, B. Vercelli, Electrochimica Acta 231 (2017) 336-343.

[33] H.C. Pitot, R. M. Goldberg, J.M. Reid, J. A. Sloan, P. Atherton-Skaff, C. Erlichman, J. Rubin, P. A. Burch, A.A. Adjei, S. A. Alberts, L.J. Schaaf, G. Elfring, L.L. Miller, Clinical Cancer Research 6 (2000) 2236-2244.

[34] A. Paci, G. Veal, C. Bardin, D. Levêque, N. Widmer, J. Beijnen, A. Astier, E. Chatelut, European Journal of Cancer 50 (2009) 2010-19.

[35] J. M. Campbell, M. D. Stephenson, E. Bateman, M. D. J. Peters, D. M. Keefe, J. M. Bowen, The Pharmacogenomics Journal 17 (2017) 21-28.

[36] J. Wang, Journal of Pharmaceutical and Biomedical Analysis, 19 (1999) 47–53.

[37] G.D. Beretta, F. Petrelli, S. Stinco, M. Cabiddu, M. Ghilardi, M. Squadroni, K. Borgonovo, S. Barni, Medical Oncology 30 (2013) 486-99.

[38] O. Combes, J. Barré, J. Duchè, L. Vernillet, Y. Archimbaud, M. P. Marietta, J. Tillement, S. Urien,Investigational New Drugs 18 (2000) 1-5.

[39] R. D. Webster, A.M. Bond, R.G. Compton, Journal of Physical Chemistry 100 (1996) 10288-10297.

[40] L. Mattiello, L. Rampazzo, Journal of Electroanalytical Chemistry 507 (2001) 118-123.

[41] A. Shah, V. C. Diculescu, R. Qureshi, A. M. Oliveira-Brett, Bioelectrochemistry 79 (2010) 173-178.

[42] L.L. Okumura, N.R. Stradiotto, Electroanalysis 19 (2007) 709-716.

[43] S. Daniele, P. Ugo, G. Mazzocchin. G. Bontempelli, Analytica Chimica Acta 173 (1985) 141-148.

[44] S. Daniele, I. Lavagnini, M.A. Baldo, F. Magno, Journal of Electroanalytical Chemistry 404 (1996) 105-111.

[45] S.E. Treimer, D. H. Evans, Journal of Electroanalytical Chemistry 449 (1998) 39-48.

[46] S.E. Treimer, D. H. Evans, Journal of Electroanalytical Chemistry 455 (1998) 19-28.

[47] B. D. McCarthy, D. J. Martin, E. S. Rountree, A. C. Ullmann, J. L. Dempsey, Inorganic Chemistry 53 (2014) 8350-8361.

[48] V. Fourmond, P-A. Jacques, M. Fontecave, V. Artero, Inorganic Chemistry 49 (2010) 10338-10347.

[49] R. Sereno, V. A. Macagno, M.C. Giordano, Journal of Electroanalytical Chemistry 76 (1977) 199-216.

[50] A.J. Bard, L.R. Faulkner, Electrochemical Methods. Fundamental and Applications, Wiley, New York, 1980.

[51] H. Ikeuchi, K. Naganuma, M Ichikawa, H. Ozawa, T. Ino, M. Sato, H. Yonezawa,·S. Mukaida, A. Yamamoto,·T. Hashimoto, Journal SolutionChemistry 36 (2007) 1243–1259.

[52] C.K. Mann, K.K. Barnes, Electrochemical Reactions in Nonaqueous Systems, Marcel Dekker, New York, 1970.

[53] C.K. Mann, Analytical Chemistry 36 (1964) 2424-2426.

[54] A. Adenier, M. M. Chehimi, I. Gallardo, J. Pinson, N. Vilà, Langmuir 20 (2004) 8243-8253.

[55] M. Czaja, M. Makowski, L. Chmurzynski, Journal of ChemicalThermodynamics 38 (2006) 599-605.

[56] M. Czaja, M. Makowski, L. Chmurzynski, Journal of Chemical Thermodynamics 38 (2006) 606-610.

[57] R. Sokolová,J. E. Nycz, S. Ramešová, J. Fiedler, I. Degano, M. Szala, V. Kolivoška, M. Gál, Journal of Physical Chemistry B 119 (2015) 6074-6080.

[58] X. Hua, X. Hou, X. Gong, G. Shen Analytical Methods 5 (2013) 2470-2476.

[59] M. Mori, H. Hatta, S. Nishimoto Journal of Organic Chemistry 65 (2000) 4641-4647.

[60] S.D. Bukkitgar, N.P. Shetti, Journal of Analytical Science and Technology 7 (2016) 1-5.

[61] B. B. Prasad, S. Srivastava, K. Tiwari, P.S. Sharma, Sensors and Materials 21 (2009)291-306.

[62] M. Arvand, A. Pourhabib, M. Giahi, Journal of Pharmaceutical Analysis 7 (2017) 110-117.

[63] H. Yang, B. Lu, B. Qi, L. Guo, Journal of Electroanalytical Chemistry 660 (2011) 2-7.

[64] H.X. Guo, Y.Q. Li, L.F. Fan, X.Q. Wu, M.D. Guo, Electrochimica Acta 51 (2006) 6230-6237.

[65] S. Wei, F. Zhao, Z. Xu, B. Zeng, Microchimica Acta 152 (2006) 285-290.

[66] W. Szczepaniak, M. Ren, Electroanalysis 6 (1994) 505-507.

[67] G. Bonazza, F. Polo, S. Tartaggia, G. Toffoli, S. Daniele, Electrochimica Acta 289 (2018) 283-293.

[68] M.J. Hilton, K.V. Thomas, Journal of Chromatography A 1015 (2003) 129-41.

[69] M. Caban, Journal of Chemistry (2015) 1-9.

[70] S. Sawada, T. Yokokura, T. Miyasaka, Current Pharmaceutical Design 1 (1995) 113-132.

[71] S. Daniele, M.A. Baldo, C. Bragato, G. Denuault, M.E. Abdelsalam, Analytical Chemistry, 71 (1999) 811-18.

[72] S. R. Belding, J. G. Limon-Petersen, E. J. F. Dickinson, R. G. Compton, Angewante Chemie 122 (2010) 9428 –31

[73] M. Cizkowska, Z. Stojek, S.E. Morris, J.G. Osteryoung, Analytical Chemistry 64 (1992) 2372-77.

5.2 Imatinib and its detection in plasma samples

5.2.1 Imatinib: a milestone for cancer care

Imatinib (**scheme 5.4**) is an anti-leukemic drug mainly used for first-line treatment of: Philadephia chromosome-positive chronic myeloid leukemia (CML), acute lymphoblastic leukemia (ALL) and some types of gastrointestinal stromal tumors (GISTs) [1-3]. Imatinib has significant importance in the history of fight against cancer, being one of the first molecules belonging to the category of targeted drugs (see chapter 1, section 1.2.2). As mentioned previously, targeted cancer therapies are based on drugs or other substances, which block the growth and spread of cancer cells by interfering with specific molecules (so called molecular targets), which are involved in cancer progression mechanisms [4, 5]. Imatinib' molecular target is, specifically, the enzyme Bcr-Abl tyrosine kinase, which is involved in several phases of tumor development and progression [6]. Imatinib is primarily metabolized by CYP3A4 and CYP3A5 (cytochrome P450 3A4 and cytochrome P450 3A4, respectively) mainly to the active metabolite, N-des-methyl imatinib (des-imatinib, **scheme 5.4 B**), whose maximum concentration in the bloodstream is usually no higher than about 10% of its precursor [7-10]. In clinical regimen, imatinib is administered as imatinib mesylate (**scheme 5.4**), which is an acidic species [8].

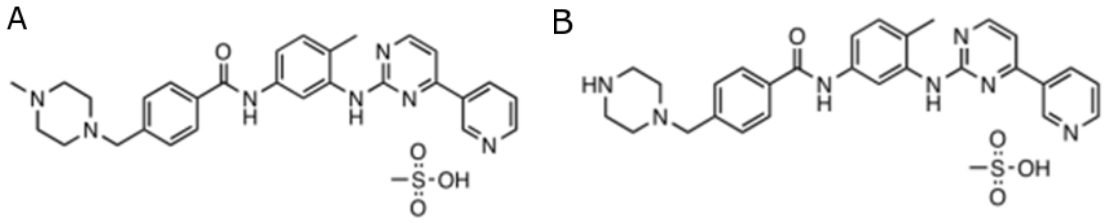

Scheme 5.4 -Structural formulas of imatinib (**A**) and of its main metabolite N-des-methyl imatinib (**B**) (des-imatinib).

5.2.2 TDM of Imatinib

The pharmacological treatments with imatinib, despite their impressive clinical efficacy [11-13], are not free of toxic effects. Commonly, the latter manifest through oedema, nausea, vomiting, muscle cramps and bone pain, so patients should be monitored periodically to adjust the dose of the drug, if necessary [13-17]. Imatinib has also a narrow therapeutic window. It is reported that the drug concentration in plasma should be above 1000 ng/mL (2.02 μM) to maintain treatment

effectiveness [15-18], but below 3000 ng/mL (6.06 μM) to avoid drug toxicity. Therefore, the use of TDM is particular suited for imanitib, and the development of cheap, fast and reliable analytical protocols for its detection are urgently required [16-18].

Most of the proposed procedures for TDM of Imatinib in biological matrices are based on a variety of hyphenated HPLC-MS, HPLC/MS-MS, LC-MS/MS [19-22], LC-UV methods [23-25] or Surface Enhanced Raman Spectrometry [26]. Again, no suitable electroanalytical approach is available for the detection of imatinib in plasma, though voltammetric studies on imatinib and their applications for quantitative evaluation of the drug have been reported in literature [27-35]. In particular, a DPV method on anodically pretreated boron doped diamond electrode (BDDE) [29] and a SWV method at screen-printed carbon electrodes [32], have been employed for the detection of imatinib in spiked urine; an application has also been reported in serum samples [35]. The latter, however, used a HDME (Hanging Mercury Drop Electrode) as working electrode, which is toxic and not suited for TDM devices. The measurements were performed in aqueous media, often exploiting the adsorption of the drug or of its electrode reaction products onto the electrode surface. This circumstance was useful, as sensitivity could be highly improved, while the detection limits were found to be very low (down to nM levels) [27-29, 32, 35]. However, in all the above articles, the issue of the drug interaction with proteins was not addressed. It is known that imatinib is strongly bound to plasma proteins (up to 98%) and consequently, for its full recovery from real plasma samples, an efficient extraction/denaturation step was required [36-39]. This could be performed by using extraction columns and suitable organic solvents, in whose extracts voltammetry of imatinib can be carried out. It must be remarked that, to the best of our knowledge, no electrochemical study on imatinib exists in non-aqueous media. Therefore, in the first part of this section the voltammetric behaviour of imatinib in EtOAc is presented. The latter solvent was chosen for the following reasons: it revealed best performance in terms of reproducibility of the voltammetric responses with respect to other solvent, such as CH_3CN (verified by screening experiments not reported here); it is a well-known denaturing agent [36]; SLE columns that fit with EtOAc as eluent are commercially available (see Chapter 4, section 4.1); it is relatively less toxic than other organic solvents (i.e., benzene and dichloromethane) suggested as eluents for SLE columns. Moreover, it must be considered that these latter SLE columns have recently been employed in pre-analytical procedures used prior detection of imatinib by chromatography [39]. The electrochemical investigations were performed using GCE, as the working electrode.

5.2.3 Voltammetric behaviour of Imatinib and its detection in EtOAc solutions

Preliminary, the voltammetric behavior of imatinib was studied in EtOAc and 0.025 M $TBAPF_6$ as supporting electrolyte. The investigation was limited to the anodic region, which allows, eventually, to establish fast and simple quantification procedures free from interference due to oxygen. **Fig 5.41** shows a typical cyclic voltammogram recorded in a 20 µM imatinib EtOAc solution over the potential window 0 - 1.2 V *vs*. AgQR. Under these conditions an irreversible oxidation peak at about +1.05 V was obtained.

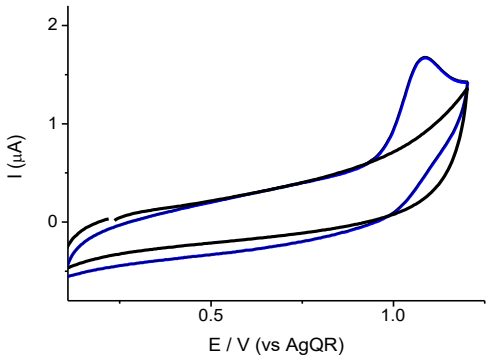

Fig 5.41: Cyclic voltammogram recorded in 20 µM imatinib in 0.025 mM $TBAPF_6$EtOAc solution (blue line); background (black line). Scan rate 100 mV s^{-1}.

The effect of scan rate was investigated over the range 10 - 150 mV s^{-1} (**Fig 5.42A**). It was found that peak current depended linearly with the square root of scan rate (**Fig 5.42B**); E_p-$E_{p/2}$ was 60 mV regardless of scan rate, while peak potential shifted slightly (overall about 30 mV) towards more positive potentials. These data are congruent with the occurrence of a diffusion controlled, one electron reversible process (heterogeneous reaction), followed by a very fast chemical reaction [33].

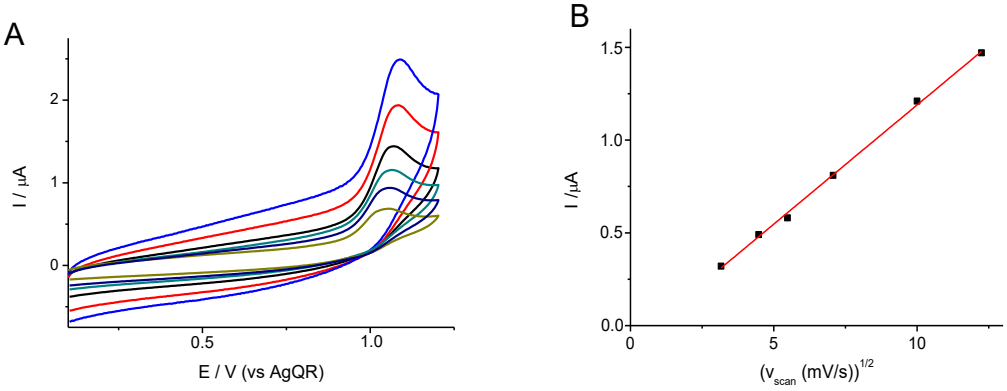

Fig 5.42- (A) Cyclic voltammograms recorded on a 20 µM of imatinib in EtOAc, 0.025 M $TBAPF_6$ solution at different scan rates (from 10 to 150 mVs^{-1}). (**B**) plot of the peak current *vs*. square root of scan rate.

The possibility to perform quantitative analysis of imatinib exploiting the above process over the therapeutic window was investigated by DPV. **Fig 5.43** shows typical DPVs obtained along with the relevant calibration plot. As is evident, although well distinguishable peaks (from the background) could be recorded down to 1 µM levels, linearity of the responses as function of concentration as well as reproducibility was rather poor.

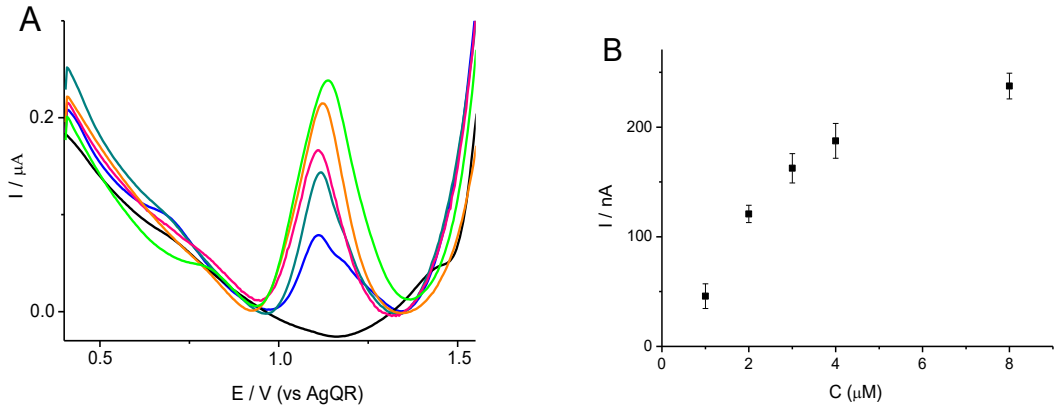

Fig 5.43 – (A) DPVs recorded in 0.025 mM $TBAPF_6$ EtOAc solution containing different concentrations of imatinib. (**B**) relevant calibration plot (error bars refer to 3 reprlicates).

Since in acidified aqueous media, more reproducible oxidation peaks for imatinib have been reported [27-32], a series of measurements were performed in EtOAc/water mixtures, aimed at verifying whether the advantages offered by the organic solvent (i.e., for denaturing plasma, while extracting the drug) and water (for obtaining reproducible and more sensitive responses) could be combined. Water, however, can be dissolved in EtOAc up to 3.2 (v/v) % at 25 °C [40]. Therefore, preliminary, CVs were performed in an optimized acidified EtOAc acidified mixture (EtOAc-AM) prepared as detailed in Experimental (see section 4.2), to which 0.025 M $TBAPF_6$ was added as supporting electrolyte. A typical CV obtained in 20 µM imatinib in EtOAc-AM is shown **Fig. 5.44**. As is evident, in the forward scan, a peak at about 0.95 V (peak 1), followed by a second less defined one at 1.1 V were recorded. In the reverse scan, essentially, a bell shaped reduction peak at 0.45 V (peak 2), suggesting the occurrence of a surface process was obtained. This picture, apart from the specific peak locations, close resembles that obtained in acidified water media [27-29, 32]. In the latter works, it was hypothesized that the oxidation of imatinib occurs in two steps, the first of which involves the nitrogen atom of the piperazine ring to provide a radical cation; the latter, in turn, in a the second step after the removal of a proton and one electron converts into a quaternary Schiff base [32]. This product, therefore, could be responsible for the reduction process observed in the backward scan. In order to shed more light

on the above processes and to confirm that the similarity of the voltammetric behavior in EtOAc-AM and acidified water fully applies, further series of CVs experiments were performed.

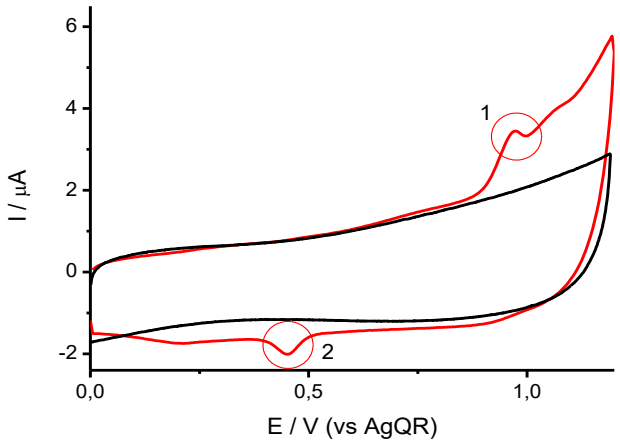

Fig 5.44- Cyclic voltammogram recorded in 20 µM imatinib,0.025 M $TBAPF_6$ EtOAc-AM solution (red line); background (black line). Scan rate: 100 mV s^{-1}.

Firstly, the origin of the cathodic peak at 0.45 V was ascertained by inverting the scan direction at different upper potentials, and specifically at 0.8 V and 1.1 V, which corresponded to a potential before and after the occurrence of the main oxidation peak of imatinib at 0.95 V. As is evident from **Fig 5.45**, no cathodic peak or change in the current potential profile was observed upon reversal the potential from 0.8 V (**Fig 5.45**, red line) or 1.1 V (**Fig 5.45**, black line), respectively, thus confirming that the appearance of the peak at 0.45 V is a consequence of the process at 0.95 V.

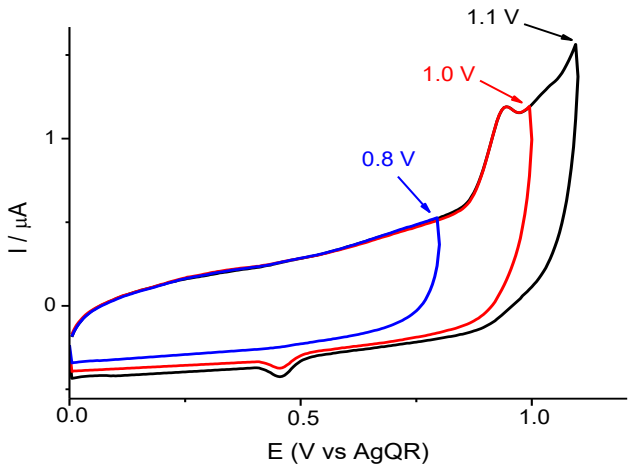

Fig 5.45-CVs recorded in a 20 µM imatinib, 0.025 M $TBAPF_6$ EtOAc-AM solution at different inversion potentials, at 20 mVs^{-1}.

The nature of the oxidation and reduction processes was also examined by performing CVs at different scan rates over the range 30 – 250 mV s^{-1}. **Fig 5.46** shows typical voltammograms obtained, while **Fig 5.47 A-B** shows the analysis of peak current as a function of scan rate. As is evident, current of peak 1 depended linearly on square root of scan rate ($R^2 > 0.99$), while for peak 2, current was proportional to the scan rate ($R^2 > 0.99$). These results indicate that peak 1 is under diffusion control, while peak 2 is a surface process.

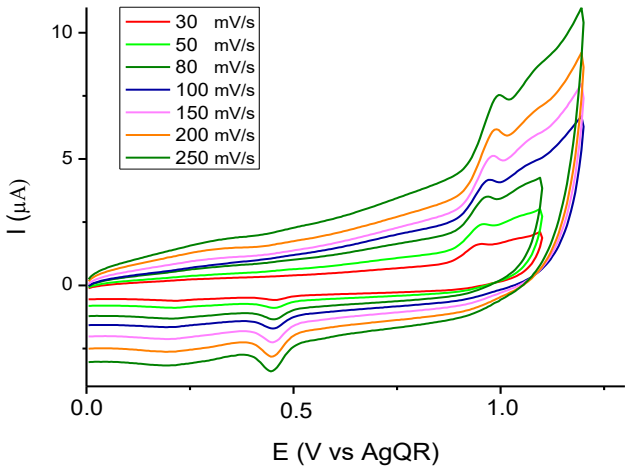

Fig 5.46-Cyclic voltammograms recorded a 20 µM imatinib,0.025 M $TBAPF_6$ EtOAc-AM solution at different scan rates (see inset).

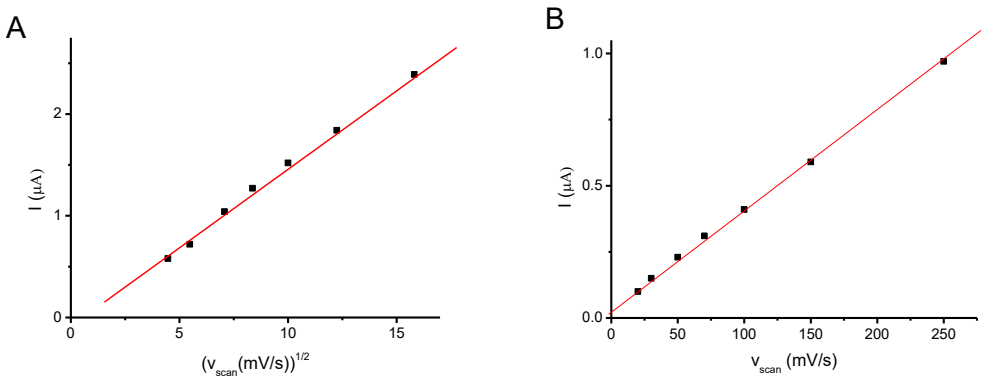

Fig 5.47-Peak currents against scan rate: (**A**) peak 1; (**B**) peak 2.

The analysis of peak potential (E_{p1}) and E_p- $E_{p/2}$ for peak 1 indicated that E_{p1} shifted slightly towards more positive potentials (about 20 mV per decade, upon varying the scan rate between 20 and 200 mV/s), while E_p- $E_{p/2}$ was 30 (±2) mV, regardless of scan rate. These data are congruent with a reversible (heterogeneous electron transfer) two-electrons process [40], followed by a fast chemical reaction; in fact the observed peak potential shift was reasonably due to a small ohmic drop. As for peak 2, $\Delta E_{p/2}$ was 60 (±2) mV, regardless of scan rate, indicating

the occurrence of a two-electrons reversible process [40]. These results are in line with those reported in the literature for imatinib in aqueous media [27-35].

In order to verify whether the species adsorbed onto the electrode surface was released upon reduction, a three-segments waveform as that displayed **Fig 5.48** was employed, and a typical voltammogram obtained is displayed in **Fig 5.48B**. As is evident in the second forward scan, a new bell-shaped peak (peak 3) at 0.45 V, of similar current intensity as that of peak 2, appeared, suggesting also for it the occurrence of a surface process. This was supported by the analysis of the voltammetric responses obtained at different scan rates (**Fig. 5.49A**). In fact, as is displayed in (**Fig. 5.49B**), current of peak 3 varied linearly with scan rate, almost overlapping the trend recorded for peak 2.

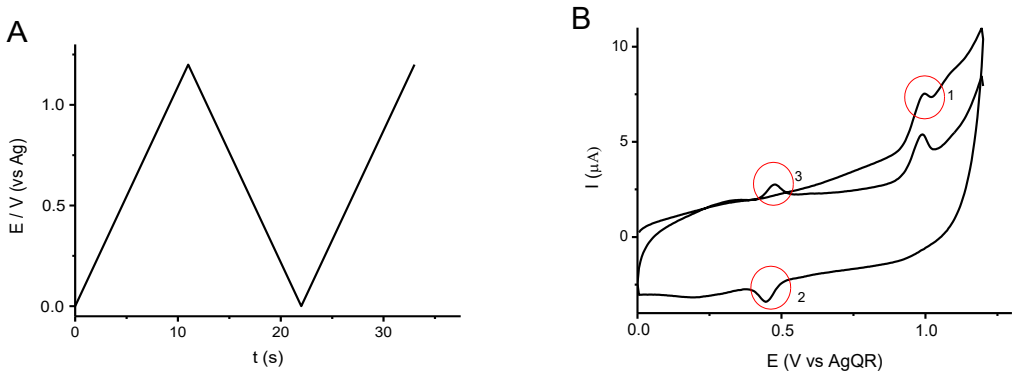

Fig 5.48- (**A**) Waveform used for experiments, (**B)** voltammogram recorded in a 20 µM imatinib, 0.025 M $TBAPF_6$ EtOAc-AM solution using the waveform displayed in **Fig 5.48 A**.

Peak potential difference (E_{p3}- E_{p2}) was only 9 (±2) mV (at 250 mV/s), indicating the occurrence of a reversible process [40].

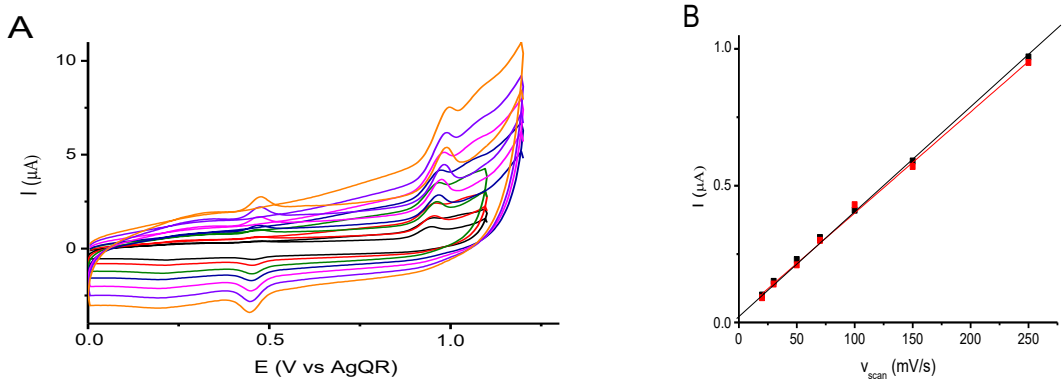

Fig 5.49 (A) -Voltammograms recorded in a 20 µM imatinib, 0.025 M $TBAPF_6$ EtOAc-AM solution at 30 (black), 50 (red), 80 (green), 100 (blue), 150 (magenta), 200 (violet), 250 (orange) mVs^{-1}. **(B)**- Comparison between peak current vs scan rate of peak 2 (black) and peak 3 (red).

The occurrence of the surface processes (2) and (3) could actually be exploited to accumulate the oxidation products of imatinib onto the electrode surface, which, in principle, could lead to the increase of the sensitivity in the measurements. The effect of accumulation of the oxidation products was preliminary investigated in a 20 µM imatinib EtOAc-AM solution at different scan rates (over the range 20-200 mVs^{-1}) to assess whether, the accumulation step could induce modification on the general voltammetric behavior or could produce saturation of the electrode surface. **Fig 5.50** shows a series of CVs performed in the latter solution, using 30 s accumulation at 1.1 V. As is evident, the general shape of the three processes remain, essentially, unaffected; the analysis of peak current as a function of scan rate provided results as those reported above for peaks 2 and 3 (**Fig 5.50B)**, in accordance with the occurrence of surface processes. On the contrary for peak 1, peak current was not proportional to the square root of scan rate or scan rate itself (**Fig 5.50B)**, this suggests that a different mechanism (or even a different species [27, 28]) might be involved in the oxidation process.

For the above concentration level, current responses were proportional to the accumulation time (t_{acc}) at 1.1 V, provided that it was ≤ 30s.

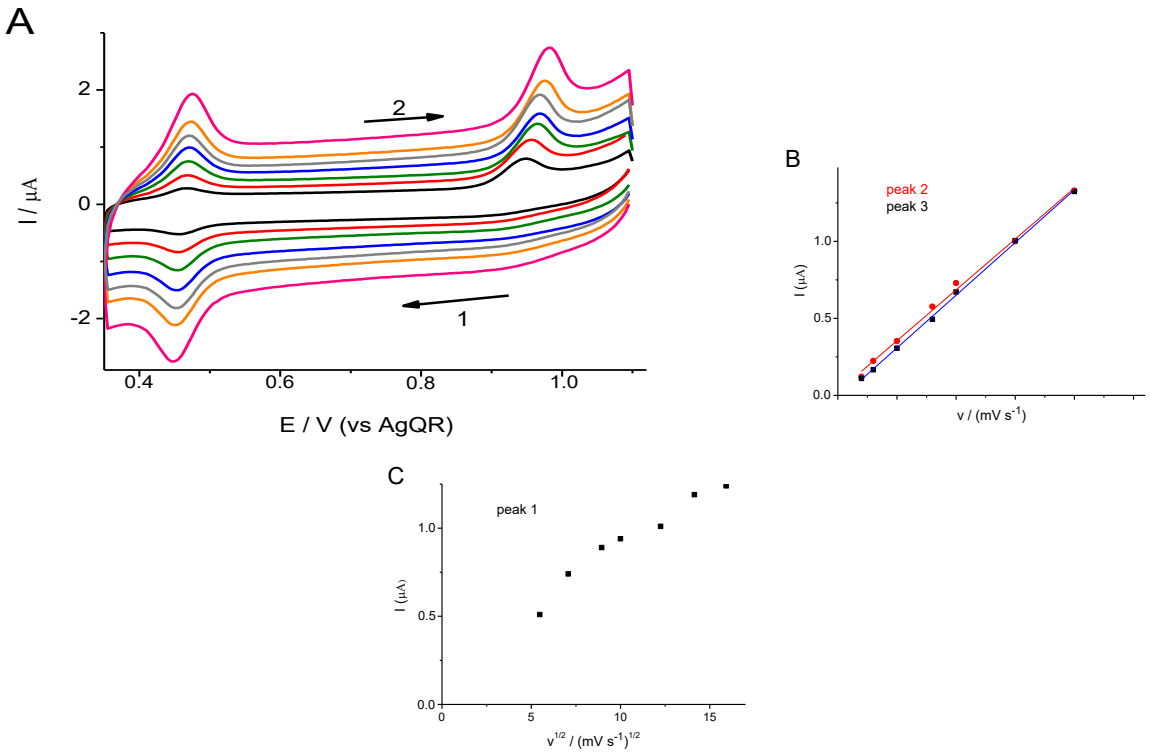

Fig 5.50 (A) - Voltammograms recorded in a 20 µM imatinib, 0.025 M $TBAPF_6$ EtOAc-AM solution at 30 (black), 50 (red), 80 (green), 100 (blue), 150 (grey), 200 (orange), 250 (pink) mVs^{-1}. (**B)** - Comparison between peak current *vs.* scan rate of peak 2 (red) and peak 3 (black). (**C**) - Peak current of peak 1 *vs.* square root of scan rate.

The effect of concentration was examined by using the waveform displayed in **Fig 5.51A**, which can be regarded as an adsorptive stripping voltammetry (AdSV) technique; the response obtained for 1 µM imatinib, with accumulation potential (E_{acc}) 1.1 V, t_{acc} = 30 s and scan rate 100 mVs^{-1}, is displayed in **Fig 5.51B**. These conditions provided the best results in terms of both reproducibility and sensitivity.

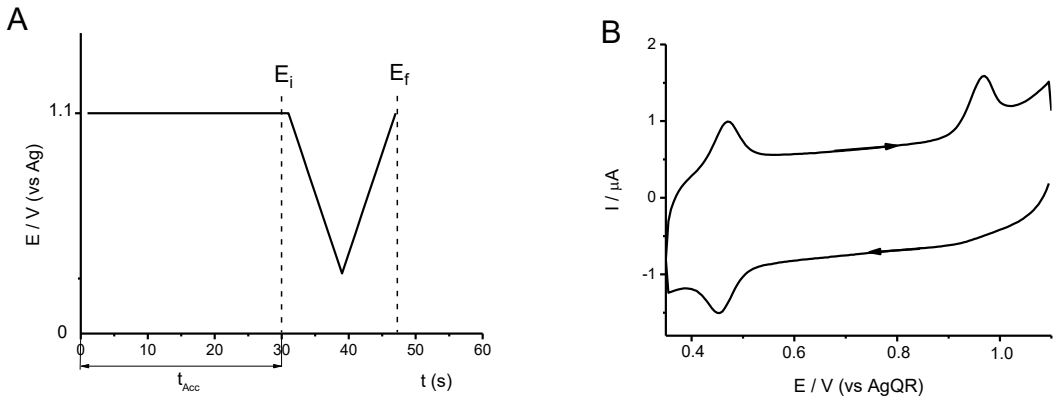

Fig 5.51- (A) waveform used for experiments. (**B**) AdSV recorded in a1 µM imatinib, 0.025 M $TBAPF_6$ EtOAc-AM solution using the wavefrom displayed in **Fig 5.51A.**

5.2.5 Calibration plots obtained by adsorptive stripping voltammetry

AdSV was chosen for quantitative analysis, using the above optimized parameters also for imatinib concentrations less than 1 µM. **Fig 5.52** shows a series of AdSVs recorded over the concentration range 40 – 900 nM.

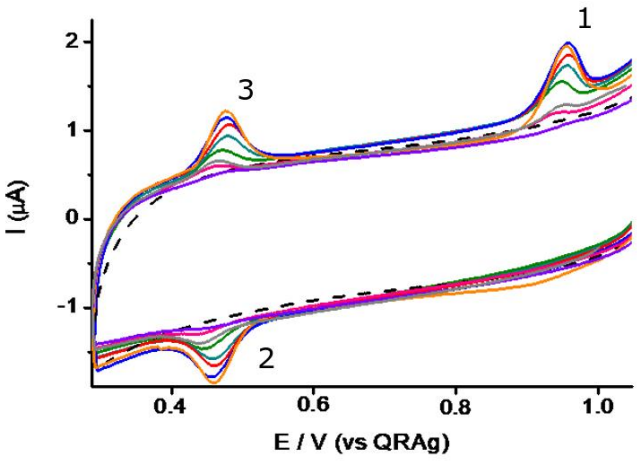

Fig 5.52- AdSVs recorded in EtOAcAM with 0.025 M $TBAPF_6$ solution with different concentrations of imatinib (40 – 900 nM) at a GCE, using the waveform displayed in **Fig 5.51A**.

Calibration plots were constructed by using current values for all the three peaks, and for peaks 2 and 3. These parameters were evaluated after subtraction of the background current. Typical AdSVs, background corrected, are shown in **Fig 5.53 A,B,C**. The corresponding calibration plots that provided higher correlation coefficients and sensitivity are also included in **Fig 5.53 A',B',C'**. **Table 5.7** summarizes dynamic ranges and linear regression equations obtained from the experimental data.

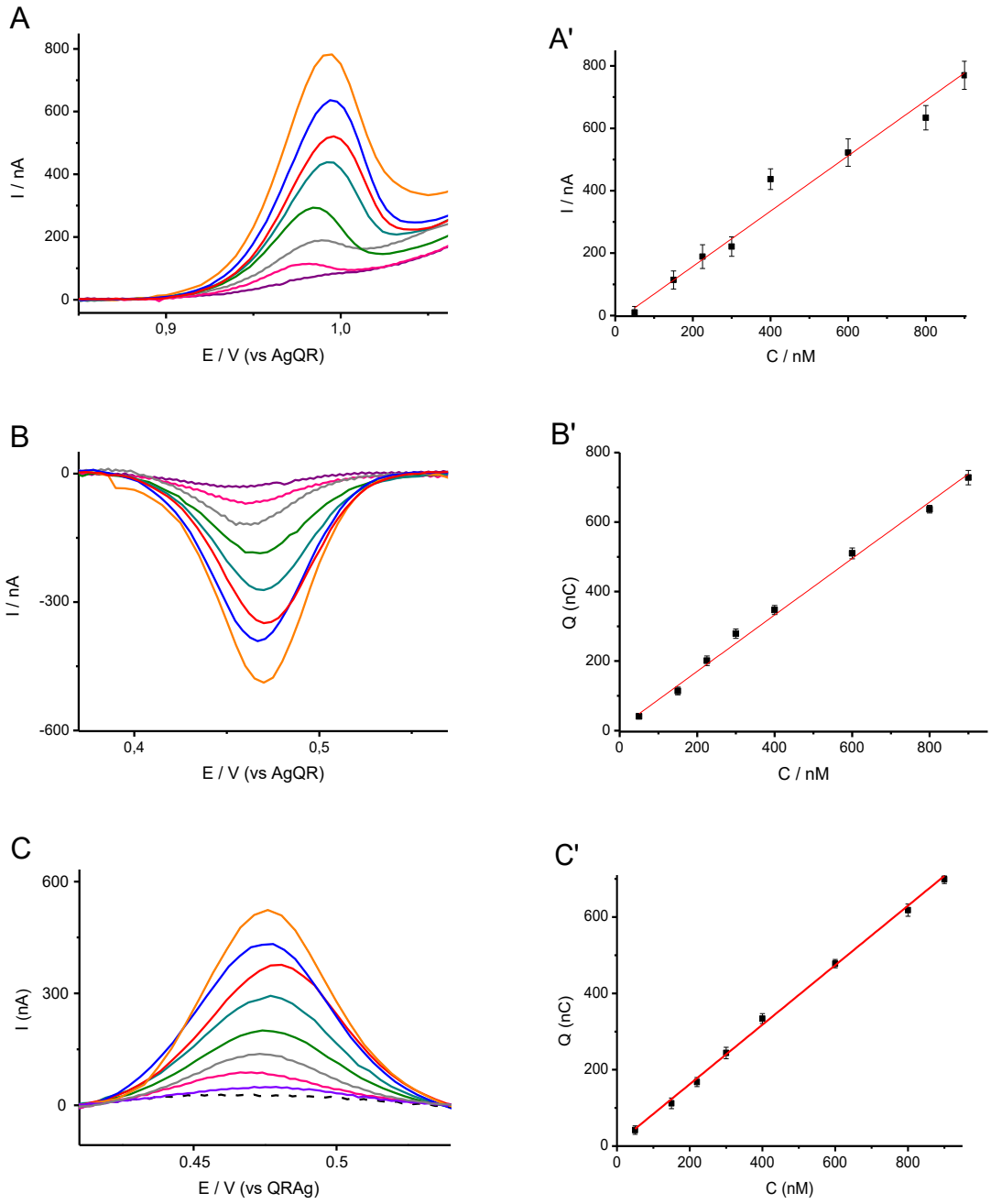

Fig 5.53- baseline subtracted AdSVs and relevant calibration plots obtained from **Fig 5.52 A,A'**: peak 1; Fig **B,B'**: peak 2; Fig **C,C'**: peak 3. Error bars refer to 3 replicates.

Table 5.7 - Linear regression parameters obtained from calibration plots obtained by AdSVs recorded in EtOAcAM and 0.025 mM $TBAPF_6$for the different peaks and processes (peak current: *Ip* , charge: *Q*).

Process	Dynamic Range (mol/L)	Linear regression equation *I (nA) = mC (nM) + b*	Linear regression equation *Q (nC) = mC (nM) + b*	R^2	LOD (mol/L)	LOQ (mol/L)
I_{p1}	$9.0 \times 10^{-8} - 1 \times 10^{-6}$	*I = 0.744C +17*	\	0.952	2.2×10^{-8}	7.3×10^{-8}
I_{p2}	$7.0 \times 10^{-8} - 1 \times 10^{-6}$	*I = 0.492C - 10*	\	0.987	1.6×10^{-8}	5.3×10^{-8}
I_{p3}	$7.0 \times 10^{-8} - 1 \times 10^{-6}$	*I = 0.475C +12*	\	0.983	1.4×10^{-8}	4.6×10^{-8}
Q_{p2}	$4.0 \times 10^{-8} - 1 \times 10^{-6}$	\	*Q = 0.832C + 6*	0.992	8.2×10^{-9}	2.7×10^{-8}
Q_{p3}	$4.0 \times 10^{-8} - 1 \times 10^{-6}$	\	*Q = 0.846C + 11*	0.991	8.4×10^{-9}	2.9×10^{-8}

From **Table 5.7,** it is evident that the charges associated to processes 2 and 3 are the most suitable for quantification.

5.2.4.2 - Voltammetric behavior of Des-IMA

In **Scheme 5.4**, the chemical structure of the main imatinib's metabolite, N-desmethyl-imatinib (des-imatinib) is shown. It is evident that, apart from the $-CH_3$ moiety on the piperidine ring, des-imatinib structure is equivalent to that of imatinib. This could conceivably imply that their voltammetric behaviors are very similar. This aspect was ascertained by performing cyclic voltammetric measurements in the same medium as that used for imatinib. **Fig 5.54** shows a typical CV obtained in 20 µM of des-imatinib and, for comparison, that of imatinib at the same concentration. The two CVs completely overlap indicating that no way exists to differentiate by voltammetry the two analyte. This needs to be taken into account in the analytical protocol for the detection of imatinib in the real samples.

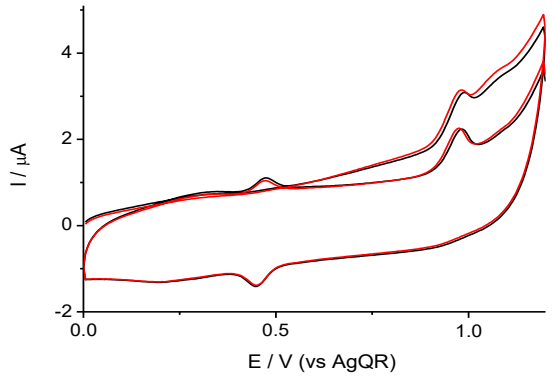

Fig 5.54- Cyclic voltammograms of 20 µM each imatinib (black line) and des-imatinib (red line) recorded in 0.025 M $TBAPF_6$ EtOAc-AM solutions. 100 mV/s.

5.2.5 Elution of plasma samples trough SLE columns to eliminate interferences

As discussed in **Chapter 5.1** for irinotecan, the detection of imatinib directly in the plasma samples, even after denaturing proteins of the real matrix with EtOAc, was prevented due to the endogenous compounds (such as ascorbic or uric acid), which interfered with the process due to imanitib. Therefore, also for this analyte, the electroanalytical method set up in the previous sections was applied to EtOAc extracts from plasma samples. The procedure for the extraction is described in detail below, and illustrated in **Scheme 5.5**. The procedure, however, was initially applied to un-spiked plasma samples to address the problems related to interferences.

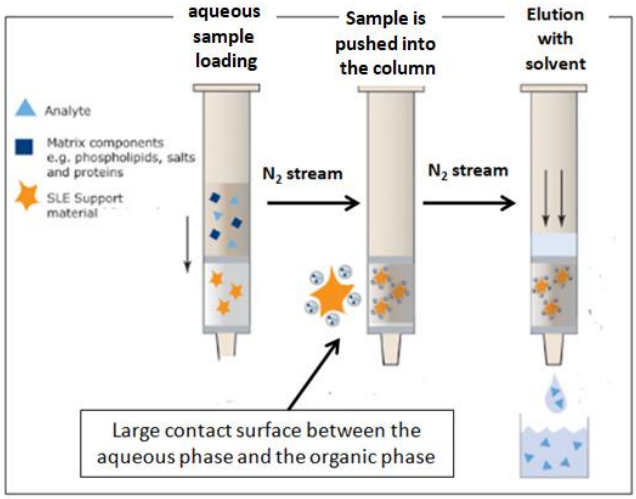

Scheme 5.5: Extraction procedure of imatinib from plasma samples by using SLE columns.

Initially, the column was loaded with 50 µL of plasma and 50 µL of MilliQ-water, which were pushed into the column with a N_2 stream. In this case the hydrophilic species remained entrapped within the aqueous phase in the SLE column. Afterwards, 500 µL of EtOAc were pushed in the column with a N_2 stream. This step was repeated two times, so that the final volume of eluted EtOAc is 1 mL. This solution was then amended with 0.025 M of $TBAPF_6$ along with the suitable amounts of H_3PO_4 and CH_3COOH to achieve the EtOAc-AM composition. This medium was then examined by AdSV.

Fig 5.55 compares the AdSVs obtained in a synthetic EtOAc-AM solution (red line) and those obtained from four plasma extracts (black lines). As is evident, in the extracts the AdSVs differ from that recorded in the EtOAc-AM, because of a higher background current and a small feature that appears at 0.45 V. The latter may actually interfere with process 2 of the AdSV of imatinib. This was actually assessed by performing a series of voltammetric measurements in

plasma extracts and subsequently spiked with imatinib at different concentrations in the range 40 - 500 nM (**Fig 5.56**).

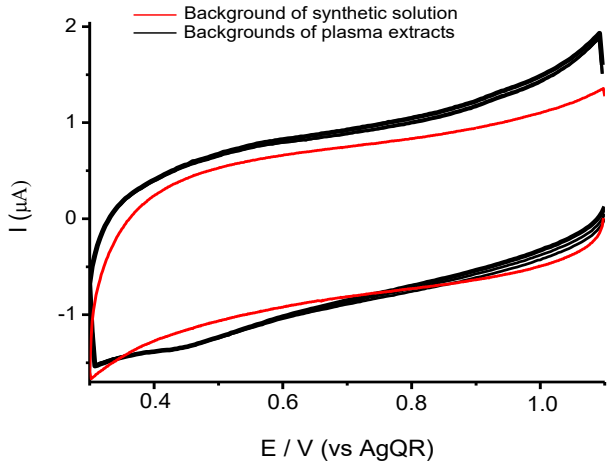

Fig 5.55- AdSVs recorded in 0.025 M $TBAPF_6$ EtOAc-AM solution (red line) and in 4 un-spiked plasma extracts (black lines). The latter refer to four replicates of the whole extraction procedure. Scan rate: 100 mV s^{-1}.

Fig 5.56A shows series of AdSVs thus recorded, after addition of the supporting electrolyte and the suitable acids. It is evident that all three peaks increase with concentration; however, calibration plots, obtained by using the charges involved in peaks 2 and 3 (see **Fig 5.56 B-C**, **Fig 5.56 B'-C'**) indicated that linearity (i.e., correlation coefficient) and reproducibility was higher if data of peak 3 were considered, this conceivably due to the lack of interferences due to the plasma matrix.

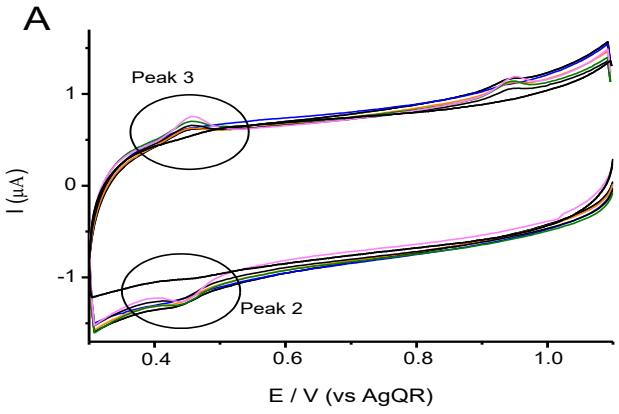

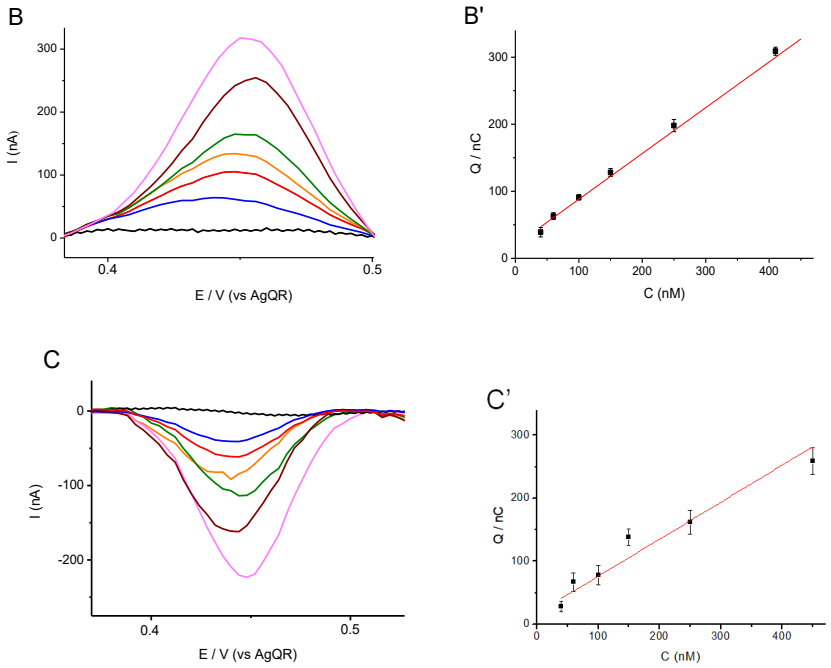

Fig 5.56- (**A**) AdSVs recorded in plasma extracts spiked with different imatinib concentrations, as indicated in the figures. Background (black lines). (**B)** and **(C)** AdSVs baseline-corrected for peak 2 and 3, respectively; **B'-C'**: calibration plots using charges obtained from peaks 2 and 3, respectively. Scan rate: 100 mV/s.

Table 5.7 summarizes regression parameters obtained for the AdSVs displayed in **Fig 5.56**.

Table 5.7–regression parameters of the calibration plots obtained by AdSV extracts of plasma samples spiked with imatinib.

Process	Dynamic Range (mol/L)	Linear regression equation *Q (nC) = mC (nM) + b*	R^2	LOD (mol/L)	LOQ (mol/L)
Q_{p2}	$4.0 \times 10^{-8} – 5 \times 10^{-7}$	*Q = 0.698C + 21*	0.944	1.4×10^{-8}	4.5×10^{-8}
Q_{p3}	$4.0 \times 10^{-8} – 5 \times 10^{-7}$	*Q = 0.822C + 70*	0.993	1.1×10^{-8}	3.4×10^{-8}

5.2.5.1 Optimization of imatinib extraction procedure and recovery tests

The above procedure (here indicated as **Procedure 1**) applied to plasma samples revealed to be effective in eliminating interferences due to endogenous compounds. Tests were then performed to establish its effectiveness for the recovery of imatinib from plasma samples. To this purpose, a series of measurements was performed in plasma spiked with 3 µM of imatinib and, after eluting with EtOAc, AdSV measurements were performed in the extracts.

Quantification was done using the multiple standard addition method along with the charge of peak 3, which provided the best results in terms of sensitivity and reproducibility. **Fig 5.57** shows typical AdSVs recorded in plasma extracts and **Table 5.8** summarizes the linear

regression parameters of the calibration plot and the % of recovery. It must be considered that the amount determined is diluted due to the extraction step.

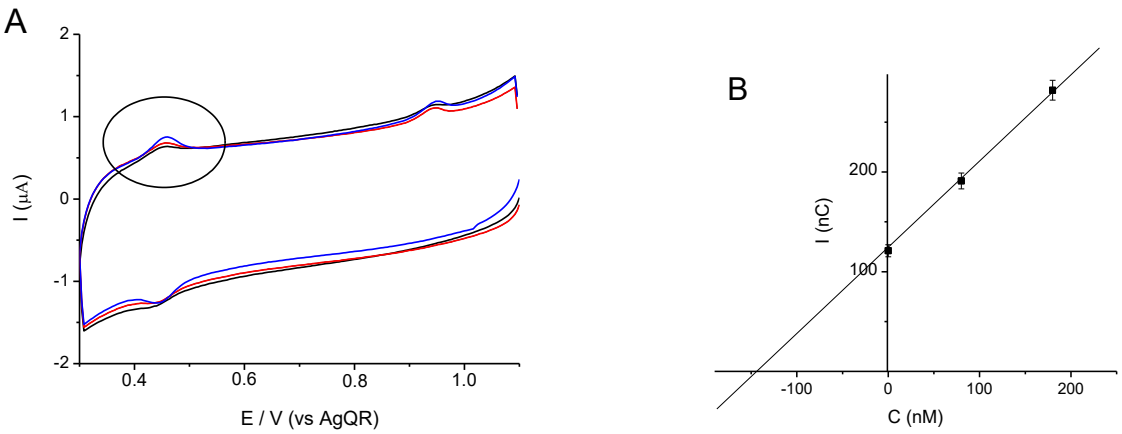

Fig 5.57(**A**) - AdSVs recorded in a plasma extract, which was amended with 3 µM of imatinib and was extracted using **procedure 1** (see **Table 5.8**). Black line is the voltammogram recorded in the extract. Red and blue lines are standard additions. (**B**)-calibration plot relevant to peak 3 (marked with a circle). 100 mVs^{-1}.

From **Table 5.8**, it is evident that, with **procedure 1**, the recovery is around 58%, with low reproducibility. Further extraction steps with EtOAc led to an increase of the amount of imatinib recovered, but dilutionof the analyte in the overall extract of the sample was too high. This circumstance suggested that the low recovery could be due to a not fully denaturation of the proteins in plasma, so that a high amount of the drug remained trapped within the column. To overcame this drawback, **Procedure 1** was modified in two ways as described in detail below (i.e., **Procedure 2** and **Procedure 3**), and the changes made essentially involved the solvent employed in loading step.

Table 5.8 – Recoveries obtained from 3 µM of imatinib that was spiked in plasma and then extracted.

Procedure	Linear regression equation [A] *Q (nC) = mC (nM) + b*	R^2	C_{det} (2SD [B]) /nM	C_{rec} (2SD[C]) /µM	Recovery% (2RSD%)
1	*Q = 0.811C + 21*	0.991	87 (14)	1.74 (0.26)	58 (16)
3	*Q = 0.822C + 7*	0.993	137 (8)	2.73 (0.16)	90 (6)

(A) obtained from multiple standard addition method .
(B) obtained from 3 replicates.
(C) concentration values recalculated (from C_{det}) taking into account dilution of the sample.

In **Procedure 2**, 50 µL of imatinib-spiked plasma were loaded with 25 µL of water and 25 µL of methanol. The latter solvent was added to make the denaturation process more effective. The EtOAc extracts were then examined by AdSVs and typical responses recorded are displayed in **Fig 5.58**. As is evident broad peaks, likely associated to electroactive compounds naturally present in plasma (ascorbic acid, uric acid, etc.), were obtained and they strongly overlapped those due to imatinib.

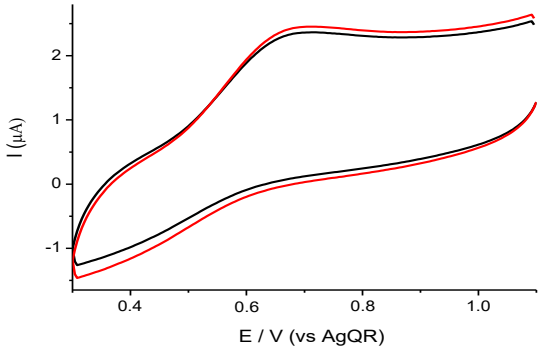

Fig 5.58- AdSVs recorded in a plasma extract, which was amended with 3 µM of imatinib and was extracted using **procedure 2** (black line). Plasma extract without imatinib (red line). Scan rate: 100 mVs^{-1}.

In **procedure 3**, 50 µL of imatinib-spiked plasma were loaded with 50 mL of water basified with ammonia (0.16 % Vol). The latter was used to neutralize the proton level of the drug, which is administered as imatinib mesylate (see above). Under these conditions, imatinib in its neutral form [41] could be better extracted with EtOAc. This procedure, outlined in **Scheme 5.6**, provided the best results in terms of both recovery and reproducibility. Typical AdSVs obtained directly in the extract and those recorded after addition of the known amounts of imatinib are shown in **Fig. 5.59A**. Data illustrating the analytical performance of the latter procedure are shown in either **Fig 5.59B** or **Table 5.8**. In this case, a satisfactory recovery of about 90% was obtained. To explain the lower than expected amount of imatinib recovered, it must be considered that of the overall volume of EtOAc (i.e., 1 mL) used to elute the analyte from the SLE column, generally 830 (± 10) µL were collected. Therefore, a fraction of imatinib can be still trapped within the column with EtOAc.

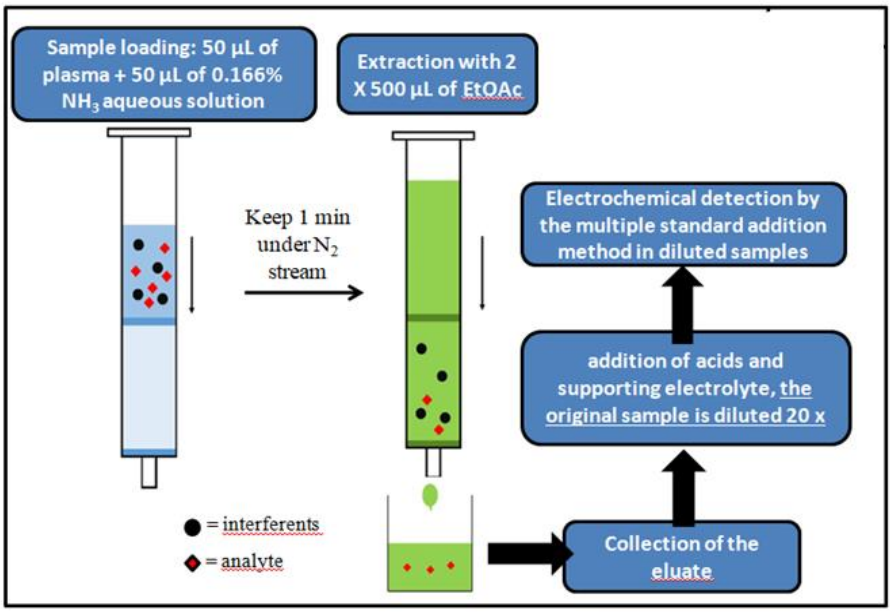

Scheme 5.6- schematic of the procedure for imatinib detection.

Considering the previous results, **Procedure 3** seemed the most suitable for both eliminating interference and recovery the analyte from plasma samples. This approach was then applied to a series of plasma samples to which different concentrations of the drug was added to cover the full therapeutic range (i.e., between 1.5 – 9 µM). **Fig 5.59** shows AdSVs and relevant plots recorded in the quantification procedure. **Table 5.9** summarizes relevant linear regression parameters, % of recovery and relative standard deviation.

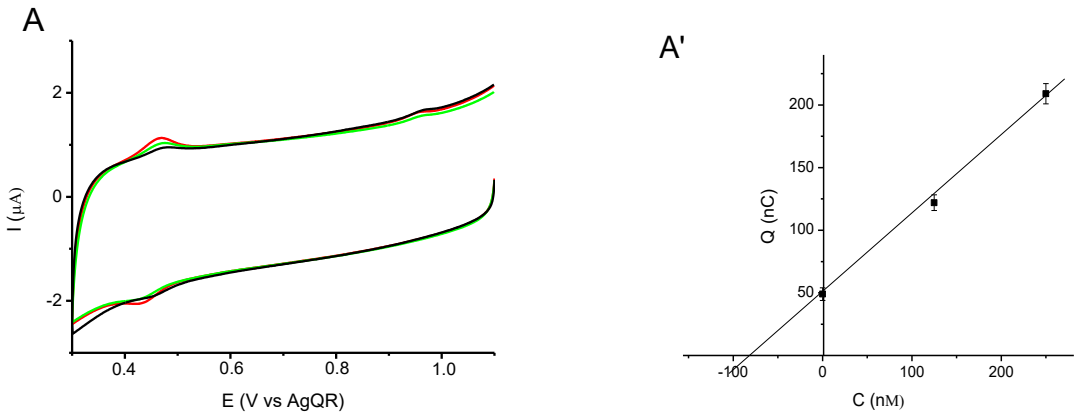

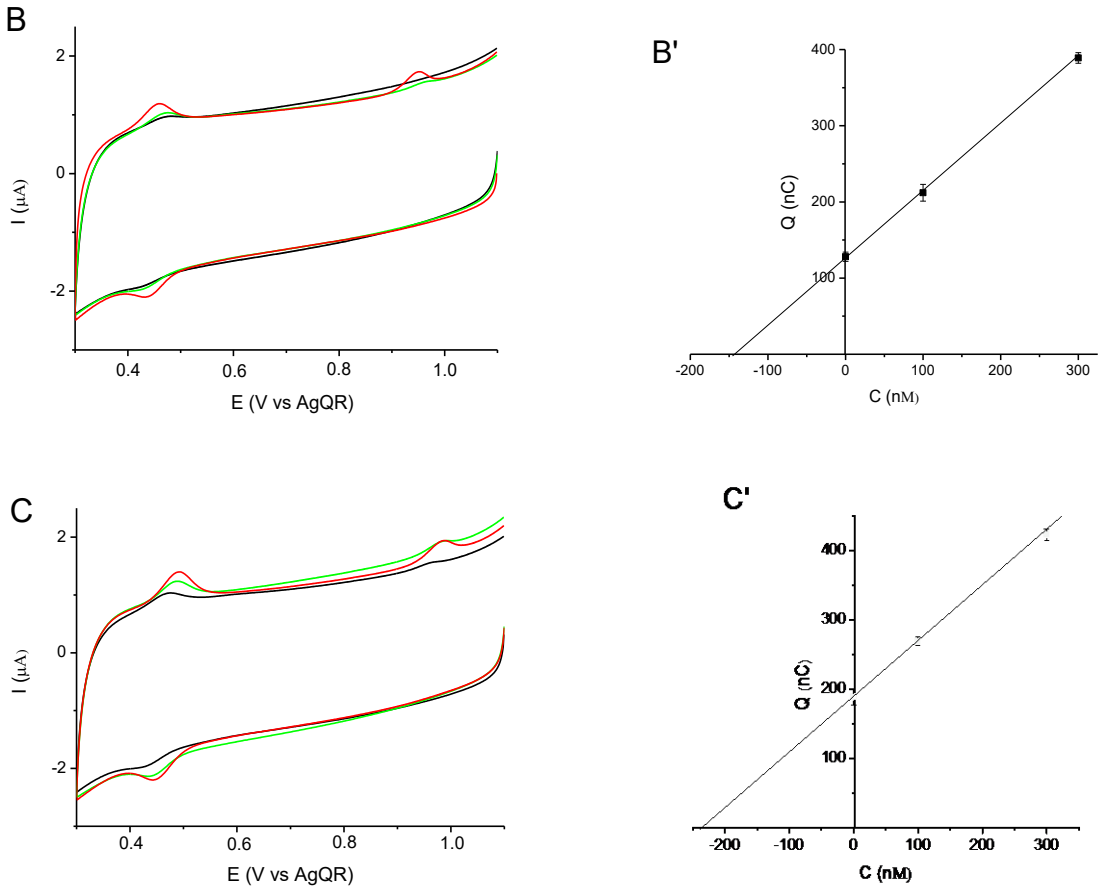

Fig 5.59- AdSVs of different concentrations of imatinib extracted from plasma (black lines): **A-A'**, **B-B'**, **C-C'** correspond to spiked concentrations of 70, 150, 250 nM respectively. Standard additions of imatinib: green and red lines.

Table 5.9- Analytical performance of the calibration obtained applying **procedure 3** to the determination of imatinib in spiked plasma samples at different concentrations. C_{plasma} are concentrations of imatinib spiked in plasma, C_{det} are concentrations determined in the extracts. C_{rec} are concentration values recalculated (from C_{det}) taking into account dilution of the sample.

C_{plasma} /µM	linear regression equation [A] Q (nC) = mC(nM) + b	C_{det} (2SD [B]) / nM	C_{rec} (2SD [C]) / µM	Recovery% (2RSD%)
1.50	*Q = 0.816C + 2*	70 (7)	1.40 (0.14)	92 (10)
2.00	*Q = 0.823C + 2*	90 (7)	1.80 (0.14)	90 (8)
3.00	*Q = 0.832C + 7*	137 (8)	2.74 (0.16)	91 (6)
5.00	*Q = 0.815C + 9*	228 (10)	4.56 (0.20)	91 (4)
9.00	*Q = 0.838C + 5*	419 (15)	8.38 (0.30)	93 (4)

(A) obtained from multiple standard addition method .

(B) obtained from 3 replicates.

(C) concentration values recalculated (from C_{det}) taking into account dilution of the sample.

As is evident, the performance of the overall analytical procedure for the detection of imatinib is satisfactory for all concentration levels of interest. Also, in any case, recovery slightly higher than 90% was obtained. However, considering that the amount of EtOAc collected from the column was, on average, 830 µL, after correction for this effect, a recovery of 110 (± 3) % can be calculated.

Finally, using the AdSVs obtained in the extracts (**Fig 5.60A**) and the concentration obtained from the standard addition method, a calibration plot was obtained and evaluated (**Fig 5.60B**) and relevant parameters of the linear regression analysis were compared with those obtained in synthetic EtOAc-AM and in plasma sample eluted from the SLE column (corrected with the supporting electrolyte and acids (**Table 5.10**). Sensitivity, LODs and LOQs compare well, which corroborate the validity of the procedure set up.

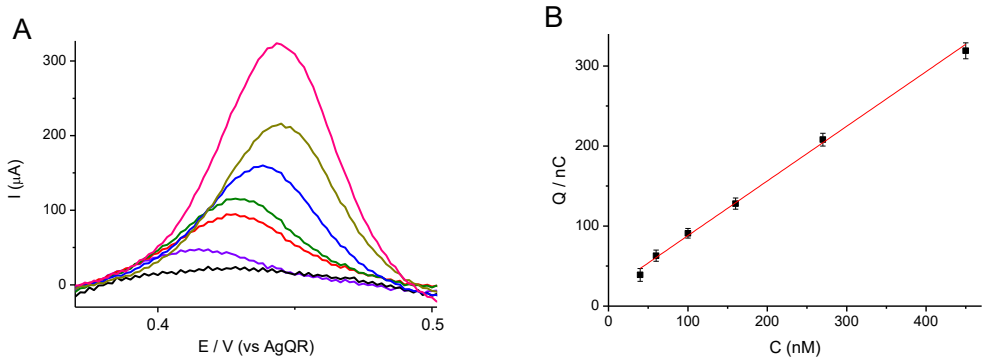

Fig 5.60- (**A**) AdSVs (peak 3, detail) of different concentrations of imatinib spiked in plasma and then extracted and analyzed.(**B**) Relevant calibration plot. Regression analysis parameters are in **Table 5.10**.

Table 5.10- comparison of linear regression parameters of peak 3 obtained in EtOAc-AM (synthetic), plasma extracts in which imatinib was spiked after the extraction (spiked), plasma a extracts in which imatinib was spiked in plasma then extracted and analyzed (extracted).

Medium	Dynamic Range(mol L^{-1})	Linear regression equation $Q\ (nC) = m\ C\ (nM) + b$	R^2	LOD (mol L^{-1})	LOQ (molL^{-1})
Synthetic	4 x 10^{-8}– 1 x10^{-6}	*Q = 0.846C + 11*	0.991	8.4 x 10^{-9}	2.9 x 10^{-8}
Spiked	5 x 10^{-8}– 6 x10^{-7}	*Q = 0.822C + 7*	0.993	1.03 10^{-8}	3.4 x 10^{-8}
Extracted	5 x 10^{-8}– 6 x10^{-7}	*Q = 0.819C + 8*	0.989	1.11 10^{-8}	3.6 x 10^{-8}

5.2.6 Detection of imatinib in plasma samples collected from patients undergoing chemotherapeutic treatment.

The SLE-AdSV procedure optimized above was applied to plasma samples collected from patients undergoing the chemotherapeutic treatment for CML, after 24 from administration. The samples, provided by the Research Centre of Oncology of Aviano (PN), were stored at -80°C and once de-frosted and equilibrated at room temperature, were examined as described above. **Fig 5.61** shows AdSVs and calibration plots obtained from the standard addition method. The concentration values are shown in **Table 5.11**. As is evident the concentrations of imatinib obtained for two patients fall within the therapeutic window, while for the third sub-therapeutic concentrations were detected. The differences found from one patient to the other are related to the inter-individual variation in drug disposition [43].

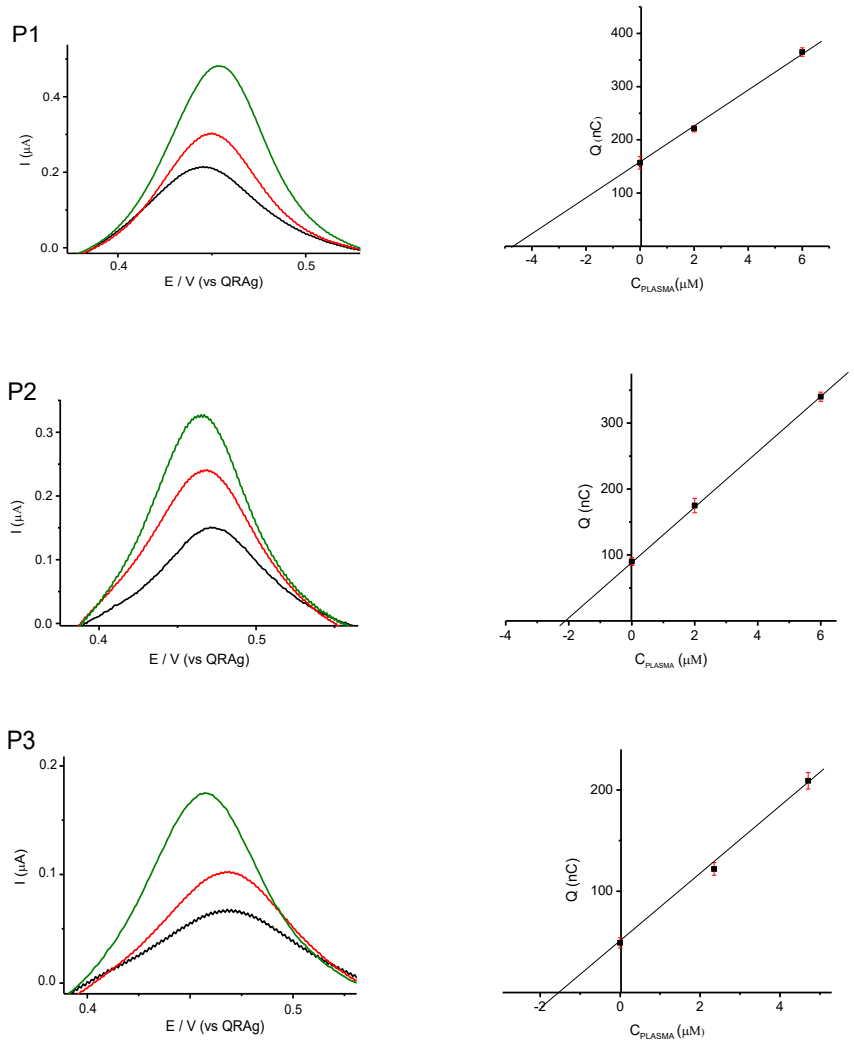

Fig 5.61–detail of peak 3 took from AdSVs recorded in plasma extracts from three different patients (P1, P2, P3) undergoing chemotherapeutic treatment. Black line is the original sample, colored lines are standard additions. On the right of each voltammogram there are relevant calibration plots.

The accuracy of the procedure was assessed by comparison of AdSVs values with those obtained with a validated HPLC-MS method (RSD % ≤ 10%) [44], which are included in **Table 5.11**.

Table 5.11- comparison between the concentrations found with HPLC-MS and SLE-AdSV methods. C_{ref} are the concentrations obtained with the reference method (HPLC-MS method) and C_{AdSV} those obtained with the electrochemical method.

SAMPLE	C_{AdSV} (RSD %)*/µM	$C_{HPLC/MS}$ (RSD %) /µM	RE %
Patient 1	4.73 (4)	4.64 (≤ 10)	1.9 %
Patient 2	2.04 (6)	2.20 (≤ 10)	6.4 %
Patient 3	1.69 (6)	1.29 (≤ 10)	31 %

*From 3 replicates. RE % = $\frac{Err}{T}$ %; $Err = |O - T|$, where O is the concentration value obtained by AdSV, T is the reference value.

References

[1] M.D. Moen, K. McKeage, G.L.Plosker, M.A. Siddiqui, Drugs 62 (2007) 299-320.

[2] Y. Zhu, S. Qian, OncoTargets Therapy 7 (2014) 395-404.

[3] S. Patel, Cancer Chemotherapy and Pharmacology 72 (2013) 277-86.

[4] V.T. DeVita, J. Chu, E. Chu, Cancer Research 68 (2008) 8643-53.

[5] K.W. Kim, J.K. Roh, H.J. Wee, C. Kim, Cancer Drug Discovery (2016) 175-238.

[6] M.K. Paul, A.K. Mukhopadhyay, International Journal of Medical Sciences 1 (2004) 101-15.

[7] H.P. Gschwind, U. Pfaar, F. Waldmeier, M. Zollinger, C. Sayer, P. Zbinden, M. Hayes, R. Pokorny, M. Seiberling, M. Ben-Am, B. Peng, G. Gross, Drug Metabolism and Disposition, 33 (2005) 1503-1512.

[8] B. Peng, P. Lloyd, H. Schran, Clinical Pharmacokinetics 44 (2005) 879-894.

[9] D. Friedecky, Journal of Chromatography A, 1409 (2015) 173–181.

[10] C. Delbaldo, E. Chatelut, M. Ré, A. Deroussent, S. Séronie, A. Jambu, P. Berthaud, A. Le Cesne, J. Blay, G. Vassal, Clinical Cancer Research, 12 (2006) 6073-6080.

[11] N. Iqbal, N. Iqbal, Chemotherapy research and Practice (2014) 1-9.

[12] E.A. Hahn, G.A. Glendenning, M.V. Sorensen, Journal of Clinical Oncology 21 (2003) 2138–2146.

[13] H.Y. Kim , J.H. Martin, A.J. Mclachlan, A.V. Boddy, Translational Cancer Research 6 (2017) 1500-1511.

[14] A. J. Galpin, W. E. Evans Clinical Chemistry 39 (1993) 2419-2430.

[15] M. Miura, Biological and Pharmaceutical Bullettin 38 (2015) 645-654.

[16] T.I. Mughal, A. Schrieber, Biologics: Targets and Therapies 4 (2015) 315-323.

[17] J.F. Teng, V.H. Mabasa, M.H. Ensom, Therapeutic Drug Monitoring 34 (2012) 85-97.

[18] S. Bouchet et al, European Journal of Cancer, 57 (2016) 31-38.

[19] W. Zhuang, J. Xie, Z. Zhou, Y. Zhou, X. Sun, X. Yuan, M. Huang, S. Liu, S. Xin, Q. Su, H. Qiu, X. Wang, Cancer Medicine 7 (2018) 317-324.

[20] V.M. Rezende, A.J. Rivellis, M.M. Gomes, F.A. Dorr, M.M.Y. Novaes, L. Nardinelli, A.L. Costa, D.F. Chamone, I. Bendit, Brasilian Association of Hematology and Hemotherapy, 35 (2013) 103-108.

[21] R.A. Parise, R.K. Ramanathan, M.J. Hayes, M.J. Egorin, Journal of Chromatography B 791 (2003) 39 –44.

[22] I. Solassol, F. Bressolle, L. Philibert, V. Charasson, C. Astre, F. Pinguet, Journal of Liquid Chromatography & Related Technologies 29 (2006) 2957–2974.

[23] B. Rochat, A. Fayet, N. Widmer, S.L. Lahrichi, B. Pesse, L.A. De´costerd, Journal of Mass Spectrometry 43 (2008) 736–752.

[24] R.L. Oostendorp, J.H. Beijnen, J.H.M Schellens, O.V. Tellingen, Biomedical Chromatography 21 (2007) 747-54.

[25] A. Davies, A.K. Hayes, K. Knight, S.J. Watmough, M. Pirmohamed, R.E. Clark, Leukemia Research 34 (2010) 702–07.

[26] S. Fornasaro, A. Bonifacio, E. Marangon, M. Buzzo, G. Toffoli, T. Rindzevicius, M.S. Schmidt, V. Sergo, Analytical Chemistry 90 (2018) 12670-12677.

[27] V. C. Diculescu, M. Vivan, A. M. Oliveira Brett, Electroanalysis 18 (2006) 1808-1814.

[28] V. C. Diculescu, M. Vivan, A. M. Oliveira Brett, Electroanalysis 18 (2006) 1800-1807.

[29] M. Brycht, K. Kaczmarska, B. Uslu, S. A. Ozkan, S. Skrzypek, Diamond and Related Materials 68 (2016) 13-22.

[30] J. Rodriguez, J.J. Berzas, G. Castaneda, N. Rodriguez, Talanta 66 (2005) 202-09.

[31] M.Popa, V. C. Diculescu, Electrochimica Acta, 112 (2013) 486-492.

[32] J. Rodríguez, G. Castañeda, I. Lizcano,Electrochimica Acta, 269 (2018) 668-675.

[33] S.C.B. Oliveira, A.M. Oliveira-Brett, Combinatorial Chemistry and High Throughput Screening 13 (2010) 628-640.

[34] V.C. Diculescu, T.A. Enache,Analytica Chimica Acta 845 (2014) 23-29.

[35] E. Hammam, H.S. El-Desoky, A. Tawfik, M.M. Ghoneim, Canadian Journal of Chemistry 82 (2004) 1203-1209.

[36] C. E. de Kogel, J.H.M. Schellens, The Oncologist 12 (2007) 1390-94.

[37] M.P. Juhascik, A.J. Jenkins, Journal of Chromatographic Science, 47 (2009) 553-557.

[38] J. Wieling, Data Handling in Science and Technology 19 (1996) 265-307.

[39] J. Zeng, H. Cai, Z. Yang, Q. Wang, Y. Zhu, P. Xu, X. Zhao, Journal of Pharmaceutical Analysis 7 (2017) 374-380.

[40] A. Reis, A. Rudnitskaya, G.J. Blackburn, N.M. Fauzi, A.R. Pitt, C. M. Spickett, Journal of Lipid Research 54 (2013) 1812-1824.

[41] A.J. Bard, L.R. Faulkner, Electrochemical Methods, Wiley, New York (2001).

[42] J.A. Winger, O. Hantschel, Superti-Furga,J. Kuriyan, BMC Structural Biology 9 (2009) 1-12.

[43] D.D. Breimer, Clinical Pharmacokinetics 8 (1983) 371-377.

[44] E. Marangon, M. Citterio, F. Sala, E. Barisone, A.A. Lippi, C. Rizzari, A. Biondi, M. D'Incalci, M. Zucchetti, Cancer Chemotheraphy and Phamacology, 63 (2009) 563-566.

Chapter 6 – Miniaturized electrochemical sensors

6.1-Inkjet printed electrochemical probes

6.1.1 Inkjet printing technologies

Inkjet printing is a non-contact printing technique and represents one of the fastest emerging techniques for direct patterning of solution based materials, called the precursor or ink [1-6]. The area of printing continues to flourish from printed text on paper to printed electronics on numerous materials such as textiles and polymer foils [1]. The stunning advantage of inkjet printing is that masks are not needed for designing patterns and that, with proper motion control of the print head, print over irregular substrates is possible. Two types of high resolution inkjet printers are shown in **Fig. 6.1,** the second of which is, probably, the most employed for printing electronic circuits.

Fig 6.1: two types of high-resolution inkjet printers; left: CERADROP 3000. Right: Dimatix Fujifilm, DMP 2831.

Inkjet printers can be divided in two families: Continuous jet (CIJ) and Drop On Demand (DOD) (**Scheme 6.1**). The latter type, in particular, has the possibility to jet the drops only when required and to regulate the jetting, allowing great versatility in the design of print patterns.

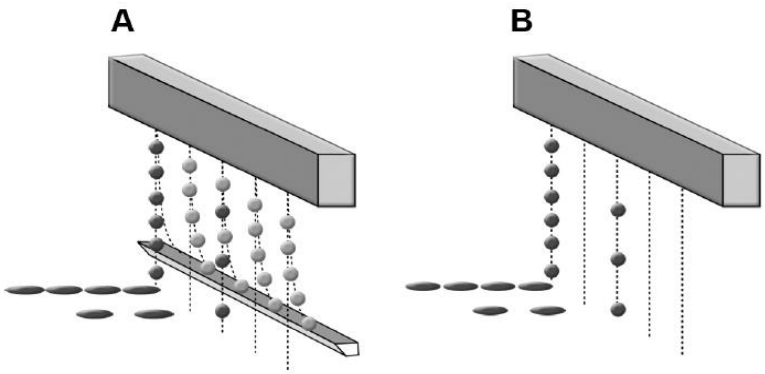

Scheme 6.1: continous inkjet print-head (**A**), Drop on demand print-head (**B**)

DOP printers have been employed for the preparation of the electrode systems investigated in this thesis, and the specific method used to generate the drops defines some primary subcategories within DOD printers [2, 8]:

- Thermal inkjet. With this approach, drops are formed by heating a resistive element in a small chamber containing the ink. The rising temperature of the resistive element causes the vaporization of a thin film of ink, which rapidly converts in a bubble, thus generating a pressure pulse that forces a drop of ink through the nozzle (**Fig 6.2a**).
- Piezoelectric inkjet. A piezo crystal undergoes distortion when an electric field is applied; this distortion is used to mechanically create a pressure pulse that makes the drop to be ejected from the nozzle (**Fig 6.2b**).
- Electrostatic inkjet. In this case, drops are drawn from an orifice under the influence of an electrostatic field. The field, generated between the orifice and an electrode, attracts charged particles within a conducting ink, bringing them to the ink surface. In such a way a drop is produced, provided that the electrostatic pull exceeds the surface tension of the ink (**Fig 6.2c**).

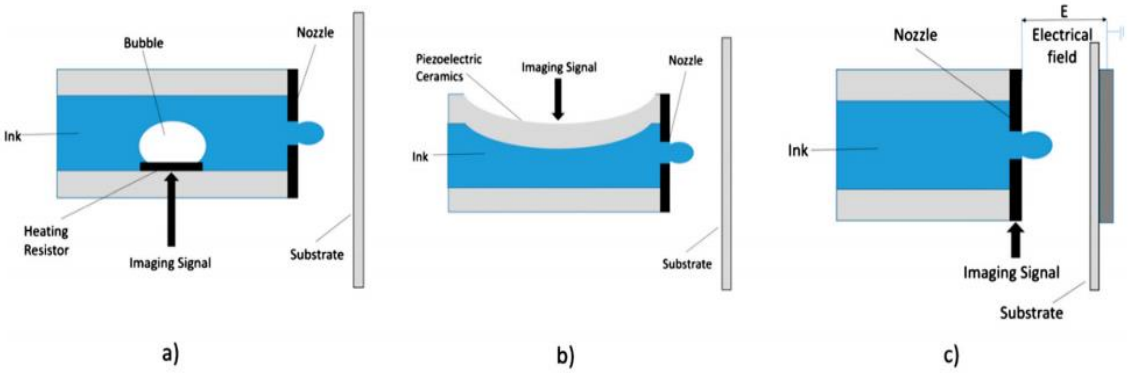

Fig 6.2 –Schematic of: **a**) thermal, **b**) piezoelectric, **c**) electrostatic inkjet printing. From [8]

There exists DOD printers, which combines two of the modes for drop generation [1,2,7].

For many emerging applications, piezoelectric printers are preferred, because they allow high versatility in the choice of inks [2].

As for inks and substrate, the most common conducting materials used in inkjet printing are based on silver [9], gold [10], carbon nanomaterials (such as grapheme or carbon nanotubes) [11, 12], and conducting polymers (such as polyaniline (PANI) [13, 14]. The dielectric materials used to protect conducting tracks and to define the active areas are, usually, solvent based or UV-curable inks [15]. Inkjet printing is most commonly performed on flexible substrates [11, 14], such as polyethylene naphtalate (PEN), polyethylene therephtalate (PET), polyimide and paper. However, it can also be applied to rigid substrates such as glass or silicon [16]. Ink and substrates need a careful choice, this to avoid print defects or clogging of the nozzles [1, 2]. Moreover, for each type of ink a specific optimization of the printing tool is needed.

Over recent years, a number of inject printing approaches have been employed for low cost fabrication of chemical and electrochemical sensors on flexible substrates [17-26]. These systems could be used in TDM applications, provided that the experimental conditions (i.e., matrices, solvent, etc.) employed are compatible with the manufacturing materials. In general, inject-printed sensors are employed with aqueous media, because of the low stability of inks and substrates in most organic solvents. As a matter of fact, to the best of our knowledge, no work exists in the literature reporting on the use of inkjet printed electrochemical sensors in organic solvents. Considering the two drugs of interest in this thesis, the possibility of using inject printed probes for their TDM, with the procedures set up in the previous chapters, would require verifying the stability of the inkjet printing systems in organic solvents. In this chapter, therefore, inkjet printed electrodes, fabricated as described in detail in Chapter 4 (see also **Fig. 6.3**), were tested in MeOH/H_2O, CH_3CN, EtOAc and DMSO, i.e., the solvents involved in the various steps of the overall analytical procedures for the detection of either irinotecan and imatinib (see chapter 5). For comparison, some test CVs in aqueous media were performed.

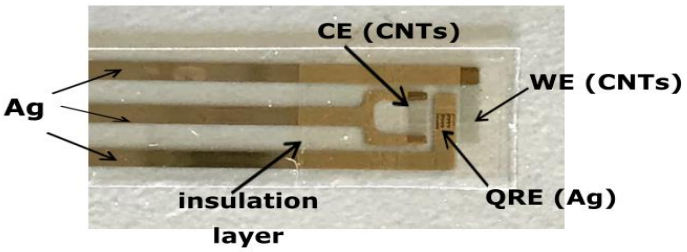

Fig 6.3 – Optical image of an inkjet printed sensor. WE, Working electrode; CE counter electrode (CE) QRE quasi-reference electrode. From [25].

6.1.2 Preliminary experiments on the stability of the materials used to construct the electrode systems.

The stability of the substrate (PET) and of the conducting CNT-based and AgNPs-based inks was evaluated by cyclic voltammetry by dipping inkjet printed working electrodes (without any insulation layer, **Fig 6.4A**) in the solvents containing 1 mM FcMeOH and 0.1 M $TBAPF_6$ as supporting electrolyte. For $MeOH/H_2O$ and H_2O, 0.1 M NaCl was used as supporting electrolyte. To roughly control the geometric surface area of the WE, a kapton (polyimide) tape was employed (**Fig 6.4A**). This material is known to be very stable in numerous organic solvents [27]. CVs obtained in the different media are shown in **Fig 6.4B**. Well-shaped voltammetric responses were in any case obtained, as expected for a reversible electrode process, as it applies for the electroactive species investigated. Moreover, CVs obtained in the organic media, apart from peak currents and positions, compare well with those recorded in the aqueous medium. Peak currents were different because of the different surface area left discovered by kapton tape. Replicate CVs or long time measurements, performed with the same printed electrode, immersed in the solutions for at least 1 h, provided reproducible (within 5% RSD) responses. These results indicated that PET and CNTs-ink did not suffer from degradation problems when in contact with the above media.

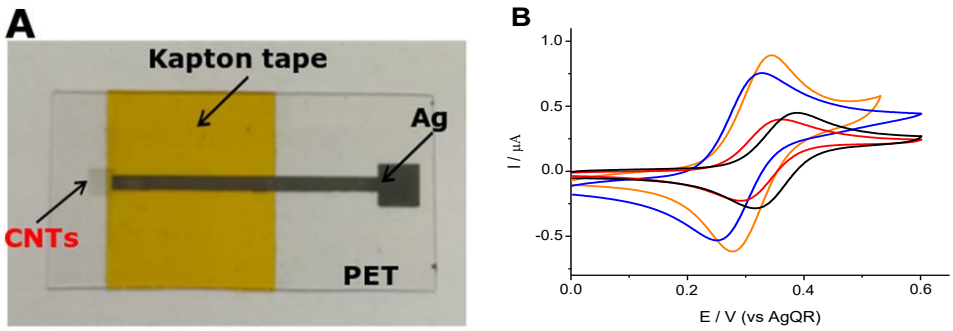

Fig 6.4 – (**A**) optical image of an inkjet printed electrode. (**B**) CVs recorded with the inject printed electrodes in 1 mM FcMeOH solution of EtOAc (black line); CH_3CN (red line); DMSO (blue line); CH_3OH/H_2O (orange line); H_2O (green line). Scan rate 50 mV s^{-1}.

Stability tests in the various solvents were also performed on the insulating layer, which represents the most critical factor on the stability of the inject printed electrodes. As reported in experimental, the insulating layer was obtained with the UV-curable EMD-6415 ink. For the purpose of the work presented in the thesis, the latter ink was chosen, because after UV-curing, it leads to hard and non-porous surfaces [28]. This circumstance could, in principle, also impart higher stability to the material, when it comes into contact with organic solvents.

CV tests were performed using electrodes, printed without any insulating layer, onto which EMD-6415 was drop casted and then subjected to UV-curing for about 30 minutes (it became completely solid). Its thickness was about 80 (± 20) µm (**Fig 6.5A**).

Typical CVs recorded with the so obtained electrode system in FcMeOH solutions are shown in **Fig 6.6**.

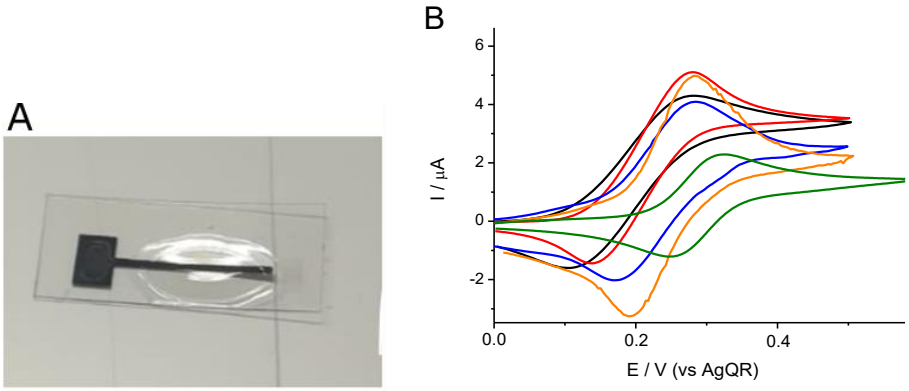

Fig 6.6 – (**A**) Optical image of an inkjet printed electrode in which the insulating layer is drop-casted with EMD 6415. **(B)** Cyclic voltammograms recorded at IJPE drop casted with EMD 6415 in 1 mM FcMeOH solutions in various solvents. Black line: ethyl acetate. Red line: acetonitrile. Orange line: water-methanol solution. Blue line: dimethylsulfoxide. Green line: water.

From **Fig 6.4**, it is evident that the CVs, other than from peak height and position, ad apart from those recorded in water, display peak potential separations larger than those expected for a one-electron reversible electrode process (i.e., about 60 mV [29]); it increased up to about 180 mV for EtOAc and CH_3CN. Instead, in water solutions, the expected CV parameters were found. Reproducibility and log-time stability was also assessed. These characteristics were, actually, linked each other, as is shown in **Table 6.1** (second entry), which summarizes time intervals within which the electrode was stable. These were established by considering those CVs for which the forward and backward peak currents changed no more than 10% (RSD, from at least 3 replicates). From the table, it appears that CH_3CN is the worst solvent for the investigated insulating layer. In EtOAc measurements could be performed within about 20 min, while in other organic solvents, and in particular in DMSO, the stability characteristics were similar to those in water.

Table 6.1- stability of drop-casted and inkjet printed insulating material (EMD-6415) in the investigated solvents.

SOLVENT	STABILITY *DROP CASTED* EMD-6415	STABILITY *INKJET PRINTED* EMD-6415	OBSERVATIONS
ETHYL ACETATE	10-20 min	3-10 min	de-adhesion, some cracks
ACETONITRILE	3-4 min	0.5-2 min	de-adhesion, cracks
DIMETHYLSULFOXIDE	>60 min	60-180 min	de-adhesion
WATER/METHANOL (34%/66%)	>60 min	>60 min	
WATER	>60 min	>60 min	

6.1.3 Tests on the inkjet printed working electrodes in the organic solvents

An investigation similar to that reported in **Section 6.1.2** was performed on working electrodes prepared by using the inkjet printing procedure in all steps, i.e., including that needed for the fabrication of the insulating layer. In this way, the active surface area exposed to the solutions could be controlled with accuracy (i.e., a square of 1 mm^2), while the insulating layer formed was thinner than that obtained by drop casting (about 8 (± 1) µm) **(Fig 6.6A**). Typical CVs recorded with the latter electrodes are shown in **Fig 6.6B**. As is evident, the thus fabricated electrode systems, apart from water, provide quite distorted and irreproducible responses in all solvents. In particular, those recorded in CH_3CN (red line, **Fig 6.6B**), are affected by high ohmic drop, while the current intensity is much larger than that expected on the basis of the printed surface area.

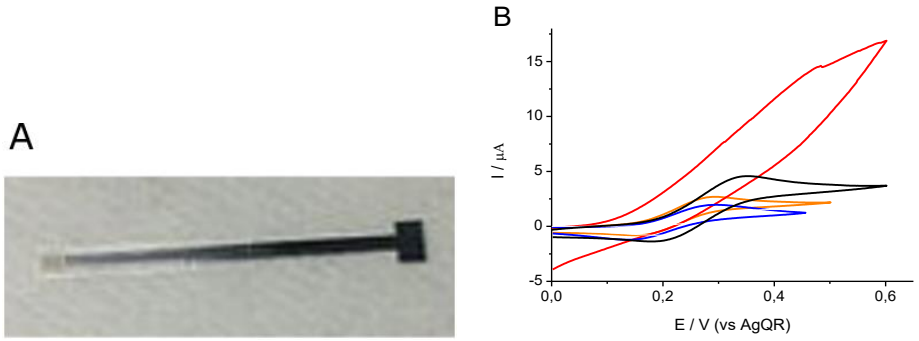

Fig 6.6- (A) Optical image of a fully inkjet printed electrode, in which the insulating layer is EMD 6415. (**B**) cyclic voltammograms recorded at IJPE in 1 mM FcMeOH solutions in various solvents. Black line: ethyl acetate. Red line: acetonitrile. Orange line: water-methanol solution. Blue line: dimethylsulfoxide.

These results suggested that the stability of the insulating material in the organic solvents was in general poor. In fact, cracks, through which the solvent could penetrate, were formed during the

measurements, a phenomenon clearly observed by examining the inject printed electrodes under at a laser scanning microscope. **Figs 6.7** – **6.8** show series of images thus obtained at different immersion times in EtOAc, CH_3CN and DMSO. Cracks, indicated as red arrows, form mainly at the border between the UV-curable ink and the CNTs; once again this degradation phenomenon occurred faster in CH_3CN (i.e., less than a minute) (**Fig 6.7A**).

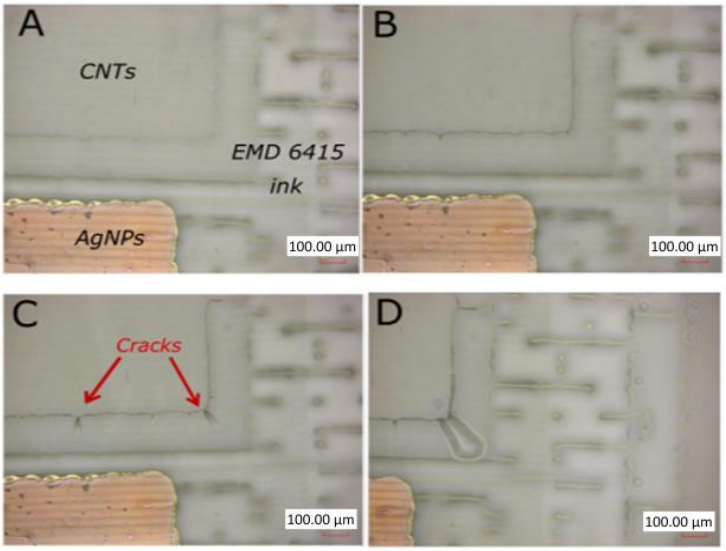

Fig 6.7- Microscope images of an IJPE that was immersed in EtOAc-AM for 0.5, 1, 3, 5 min (corresponding to A, B, C, D respectively).

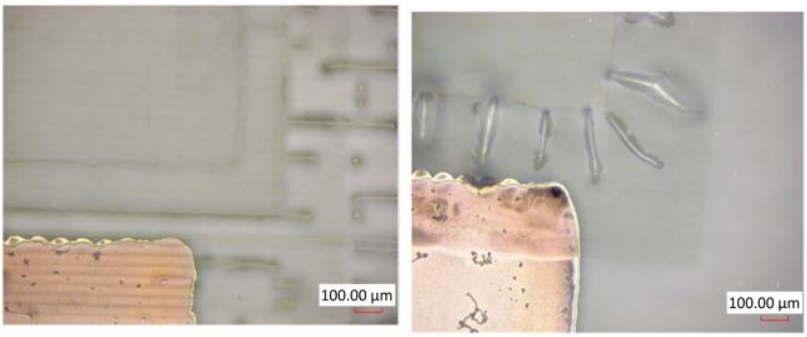

Fig 6.8- Microscope images of IJPEs before (left) and after (right) 5 min immersion in CH_3CN.

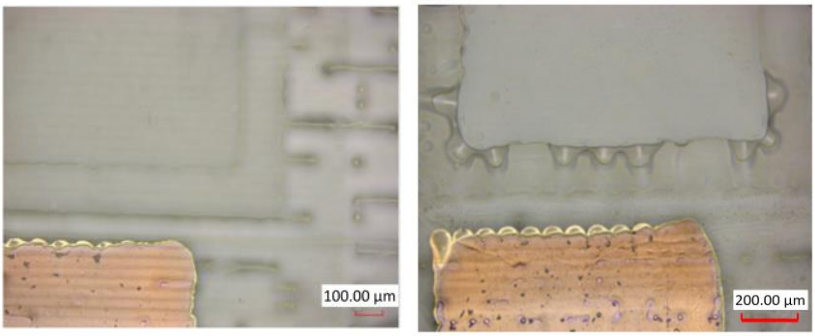

Fig 6.9- Microscope images of IJPEs before (left) and after (right) 180 min immersion in DMSO.

6.1.4 "Tripodal-Inkjet printed" electrodes (T-IJPEs)

In order to minimize the above inconvenience, a different printing pattern was adopted. In particular, the 1 mm^2 CNTs, forming the surface area of the working electrode, was connected to the conducting AgNPs band through three thinner CNTs bands, each 0.15 mm width and 1 mm long (**Fig 6.10**). The insulating ink was applied to the upper part of the three CNTs and the AgNPs bands (**Fig 6.10**). In this way, the contact between the CNTs and the insulating material was minimized with respect to the previous scheme. The working electrodes in the new configuration, from now on, will be named "**T-IJPEs**".

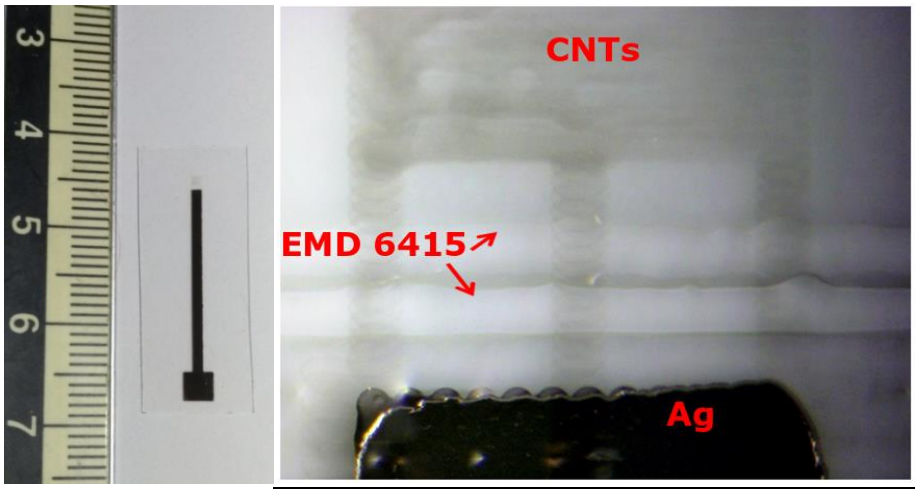

Fig 6.10 – Right: an electrode printed with the new shape (**T-IJPE**). **Left**: detail of the electrode.

The performance of the latter types of working electrodes was investigated in the various solvents containing FcMeOH and typical CVs are displayed in **Fig 6.11**. As is evident, better defined CV patterns are obtained for all solvents, apart from CH_3CN.

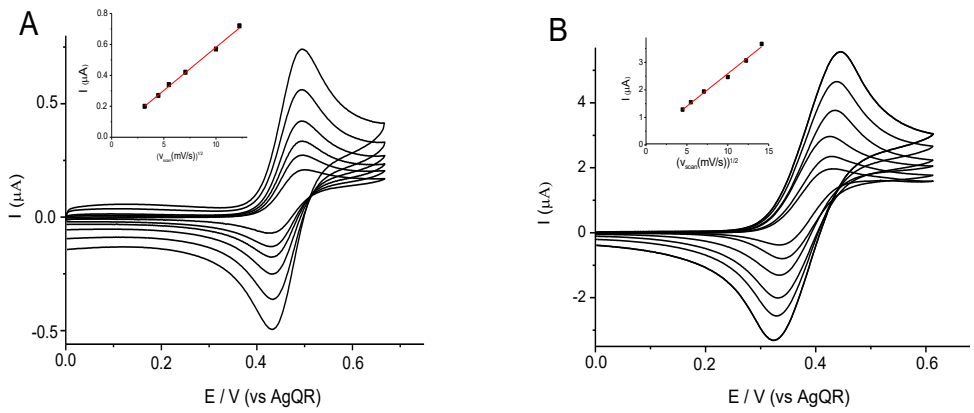

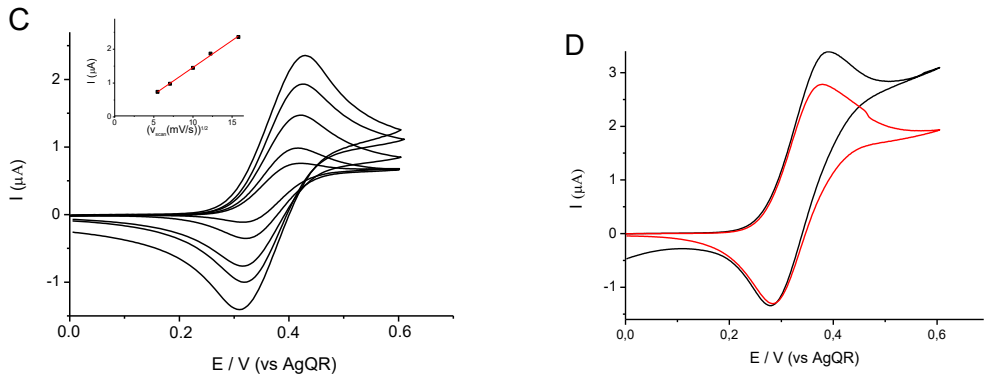

Fig 6.11- Cyclic voltammograms recorded at different scan rate using 1 mM FcMeOH in: (**A**) 0.1 M $TBAPF_6$, DMSO; (**B**) 0.1 M $TBAPF_6$; EtOAc; (**C**) 0.1 M NaCl, H_2O : MeOH (33.3 : 66.6 % (V/V)). Different scan rates from 10 to 100 mVs^{-1}. (**D**) 0.1 M $TBAPF_6$ CH_3CN (CVs recorded at 50 mV s^{-1} after 0 and 1 min from the immersion of the electrode in the solution). Insets: peak currents against square root of scan rate.

The analysis of peak currents against the square root of scan rate was linear, indicting that the oxidation process of FcMeOH was controlled by diffusion (see insets in **Fig 6.11**) in DMSO, EtOAc and MeOH/H_2O (**Fig 6.11A,B,C**). In CH_3CN, the shape of the changed with time as displayed in **Fig 6.11D**. For the solvents in which the **T-IJPEs** were enough stable (i.e., at least for 20 min), the analysis of cathodic to anodic peak current ratios (*Ip,c/Ip,a*) and peak potential separations (*Ep,a –Ep,c*) were evaluated and shown in **Fig 6.12**. *Ip,c/Ip,a* were close to 1, regardless the scan rate in all solvents. (*Ep,a –Ep,c*) was about 60 mV in DMSO and changed only slightly with the scan rate, in agreement with the occurrence of a reversible electrode process. In the other solvents, peak potential separations were in general larger than the expected 59 mV, and increased with scan rate. These results indicate that the process is affected by ohmic drop.

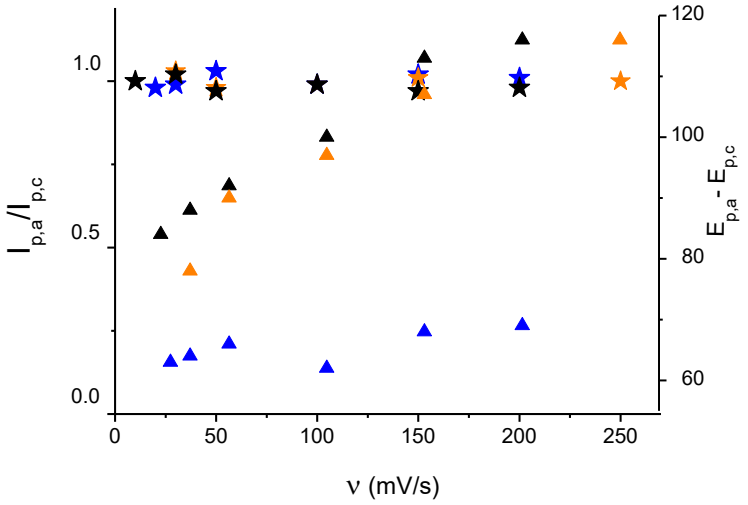

Fig 6.12- $I_{p,a}/I_{p,c}$ ratios (stars) and $E_{p,a}$-$E_{p,c}$ (triangles) obtained from the voltammograms reported in **Fig 6.12**. Blue: DMSO. Orange: H_2O/MeOH. Black: EtOAc.

Optical observations of the electrodes by a laser scanning microscope,indicated, however that, apart from CH_3CN, also in EtOAc and DMSO, the electrodes were somewhat damaged. For instance **Fig 6.13** shows optical images recorded for a working electrode after 30 min immersion in EtOAc.

De-adhesion of the insulating ink from CNT surface was the main cause of damage (see t30 min).

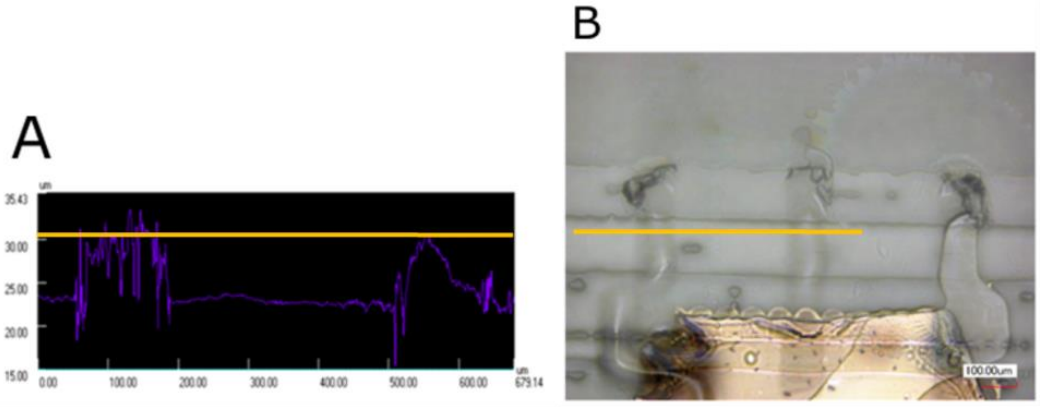

Fig 6.13- (**A**) laser scanning microscope topographic image of a T-IJPE that was dipped in acidified EtOAc for 30 min. (**B**) Microscope image of a T-IJPE (as the one shown in **Fig**) after 30 min dipping in acidified EtOAc.

De-adhesion of the insulator from CNTs was, however, not equally dramatic for all the solvents investigated. **Table 6.1** includes stability recorded in the various solvents. On the basis of the latter stability values, it was considered that T-IJPE could be used for one – shot measurements,

in view of the fact that the production of these electrodes by the inkjet printing approach can be very cheap.

6.1.5 Detection of imatinib at T-IJPE

The performance of T-JPE in the EtOAc-AM, for the detection of imatinib was preliminarily investigated, using the CV and AdSV optimized in chapter 5.2.

Typical CV and AdSV obtained in 20 µM imatinib in EtOAcM are shown in **Fig 6.14**. The shape is same as those recorded at GCE. The difference of peak potentials are due to the different reference electrode employed.

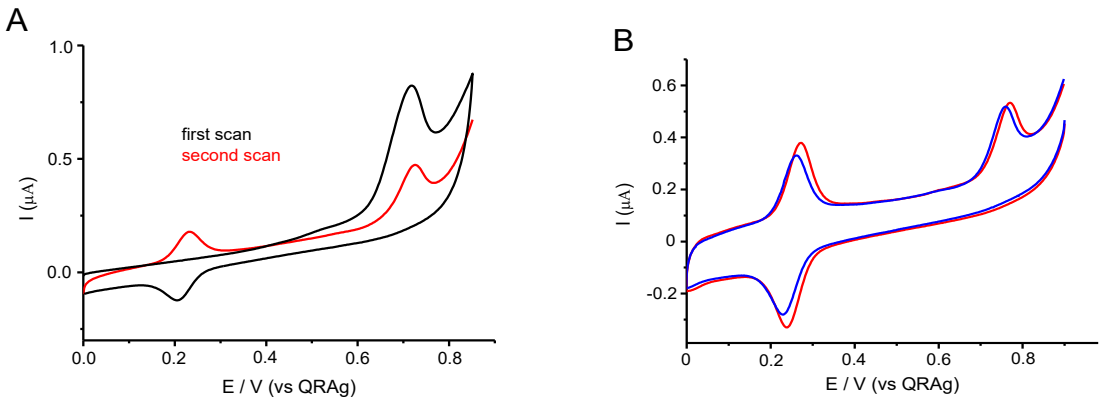

Fig 6.14 - cyclic voltammograms (**A**) and AdSVs (**B**) of 20 µM of imatinib recorded at IJPE that were drop casted with EMD-6415 in 0.025 M $TBAPF_6$ EtOAcM.

Fig 6.15A shows a series of AdSVs obtained in EtOAc-AM containing imatinib at different concentrations over the range 60-400 nM (only the peak used for imatinib quantification is displayed); **Fig 6.15B** shows relevant calibration plot. It can be noted that linearity of the responses as function of concentration as well as reproducibility was poor. This is probably because each measurement was carried out with a different printed electrode, due to the instability of the latter. The de-adhesion of the insulating layer does not occur exactly the same for all the electrodes. As a consequence, their degree of damage and their voltammetric response presents substantial differences.

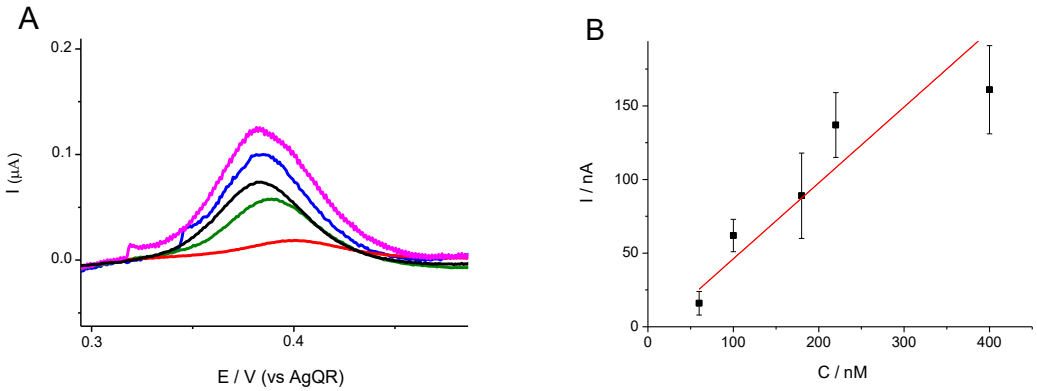

Fig 6.15 - (**A**) AdSVs of different imatinib concentrations recorded at T-IJPEs in 0.025 M $TBAPF_6$ EtOAc-AM. (**B**) Relevant calibration plot. Error bars are from 2 replicates.

References

[1] N.C. Raut, K. Al Shamery, Journal of Materials Chemistry C 6 (2018) 1618-1641.

[2] S. Magdassi, The chemistry of inkjet printing, World Scientific Publishing (2010).

[3] F. Ely, Synthetic Metals 161 (2011) 2129–2134.

[4] J. U. Park, Nature Materials 6 (2007) 782–789.

[5] E. Alarousu, A. AlSaggaf, G. E. Jabbour, Nature Scientific Reports 3 (2013) Art. ID 1562.

[6] M. Pudas, J. Hagberg, S. Leppävuori, Progress in Organic Coating 49 (2004)324–335.

[7] R. Wong, M. L. Hair, M. D. Croucher, Journal of Imaging Science and Technology 14 (1988) 129–131.

[8] H.W. Tan, T. Tran, C. K. Chua, Virtual and Physical Prototyping 11 (2016) 271-288.

[9] M. Jovic, F. Cortés-Salazar, A. Lesch, V. Amstutz, H. Bi, H.H. Girault, Journal of Electroanalytical Chemistry 756 (2015) 171–178 .

[10] F.J. Pavinatto, C.W. Paschoal, A.C. Arias Biosensors and Bioelectronics 67 (2015) 553–559.

[11] A. Lesch, F. Cortes-Salazar, V. Amstutz, P. Tacchini, H.H. Girault Analytical Chemistry 87 (2015) 1026–1033.

[12] S.R. Das, Q. Nian, A.A. Cargill, J.A. Hondred, S. Ding, M. Saei, G.J. Cheng, J.C. Claussen, Nanoscale 8 (2016) 15870–15879.

[13] P. Sjöberg, A. Määttänen, U. Vanamo, M. Novell, P. Ihalainen, A.J. Andrade, J. Bobacka, J. Peltonen Sensors and Actuators B 224 (2016) 325–332.

[14] P. Teengam, W. Siangproh, A. Tuantranont, C.S. Henry, T. Vilaivan, O. Chailapakul, Analytica Chimica Acta 952 (2017) 32–40 .

[15] Z. Xu, Q. Dong, B. Otieno, Y. Liu, I. Williams, D. Cai, Y. Li, Y. Lei, B. Li Sensors and Actuators, B 237 (2016) 1108–1119.

[16] C. Hu, X. Bai, Y. Wang, W. Jin, X. Zhang, S. Hu, Analytical Chemistry 84 (2012) 3745–3750.

[17] Paul Calvert, Chemistry of Materials 13 (2001) 3299-3305.

[18] H. R. Kang, Journal of Imaging Science and Technology (1991) 179–188.

[19] S. Khan, L. Lorenzelli, R. S. Dahiya, IEEE Sensors Journal 15 (2015)

[20] X. Nie, H. Wang, J. Zou Applied Surface Science 261 (2012) 554-560.

[21] A. Lesch, F. Cortés-Salazar, V. C. Bassetto, V. Amstutz, H. H. Girault, Chimia 69 (2015) 284-89.

[22] A. Moya, G. Gabriel, R. Villa, F. Javier del Campo, Current Opinion in Electrochemistry 3 (2017) 29-39.

[23] G. Cummins, M.P.Y. Desmulliez, Circuit World 38 (2012) 193–213.

[24] A. Lesch, F. Cortés-Salazar, V. Amstutz, P. Tacchini, H. Girault, Anaytical Chemistry 87 (2015) 1026-33.

[25] A. Lesch, M. Jovic, M. Baudoz, Y. Zhu, P. Tacchini, F. Gumy, H. Girault, ECS Transactions 77 (2017) 73-81.

[26] P. Zhuang, M.N. Blackburn, C.B. Peterson, Journal of Biological Chemistry 271 (1996) 14323-14332.

[27] Y. Strunskus, M. Grunze (1994) Polyimides—fundamentals and applications. In: Crosh M, Mittal K, editors. New York: Marcel Dekker, 187–205.

[28] Y.Y. Lim, Y.M. Goh, C. Liu, D. Hutt, Surface and Coatings Technology, 266 (2015) 93-104.

[29] A.J. Bard, L.R. Faulkner, Electrochemical Methods, Wiley, New York (2001).

6.2 Headspace Sensing of Volatile Aldehydes at Room Temperature Ionic Liquid Modified Electrochemical Microprobe

6.2.1 Analysis of short chain aldehydes

Measurement of volatile aldehydes (VAs) is of great interest in many fields, including food industry and medical diagnosis [1-7]. The interest in this latter field, arises from the fact that a relation between these compounds and oxidative stress is well established [5, 6] (see section 1.2.2). VAs are produced by biological cells, during peroxidation of lipids in cellular membranes and are insoluble in blood, so they pass quickly into breath and are excreted within minutes from their formation. As today, gas chromatographic or hyphenated gas chromatographic/mass spectrometry analysis coupled with several extraction and enrichment procedures are the mostly employed analytical methods for the detection of these organic compounds [1-7]. Albeit they are highly sensitive and provide the most detailed information on sample composition, the above methods require expensive instrumentation, limiting their widespread applications. Electrochemical systems, which possess several attractive advantages over the above techniques, have been relatively less employed for the detection of VAs. This consideration particularly applies for dynamic electroanalytical methods such as those based on voltammetry and amperometry.

In general, the detection of gaseous species, directly in atmospheres by dynamic electroanalytical techniques, requires suitable electrodes and/or electrochemical assemblies. For this purpose, different devices have been proposed in earlier and more recent literature reports (see for instance [8-28]). Among others sensor systems, those incorporating room temperature ionic liquids (RTILs) as electrolytes, have recently received special interest [11-21, 22-28]. This is due to the unique properties of RTILs, such as negligible vapour pressure, high thermal and chemical stability, low melting point and acceptable ionic conductivity [24]. High viscosity represents a major drawback of RTILs in voltammetric/amperometric applications, as diffusion coefficients of the electroactive species are typically slow, at least one order of magnitude slower than in molecular solvents [25, 26]. Nevertheless, simple and/or miniaturized membrane-free amperometric sensors based on RTILs, have been proposed for the detection of a variety of gaseous species, mainly inorganic in nature (for example, O_2, O_3, H_2S, CO, CO_2, NH_3, SO_2, NO_2, NO, Cl_2) [11-21].

Focusing on VAs, a literature survey provided only a few articles in which voltammetric/amperometric RTILs-based sensors have been used for the detection of acetaldehyde [18, 27] and benzaldehyde [28] For these purposes, aprotic ionic RTILs have been employed, as they are able to keep the level of the water in the system at trace levels [18,27]. However, it was demonstrated that the presence of water in the media favors the electrooxidation process of the aldehydes when platinum materials are employed as working electrodes [18,27]. Under such conditions, the electrooxidation process of the aldehydes seems to proceed through similar pathways as in water electrolytes [18, 27].

In acid aqueous electrolytes, the electrooxidation of aldehydes at platinum electrodes involves, along with the dissociative chemisorption of the compounds, the formation of poisoning intermediates (such as CO), which however, at high enough positive potentials provide CO_2 or the corresponding carboxylic acids [29, 30]. In aqueous alkaline electrolytes, the formyl group of the aldehydes converts into a geminal-diol anion [30-33], which, after adsorption onto metal electrode surfaces, such as gold [33] and platinum [31], proceeds favourably towards the formation of the corresponding carboxylate anion. The formation of carboxylate anion has also been suggested to be one of the final products in the electrooxidation of n-butanol in NaOH electrolyte, in which the corresponding aldehyde is formed as an intermediate [34]. From an analytical point of view, it has been found that in aqueous alkaline media, the electrooxidation process provides more sensible current responses [30, 32]. Thus, on the basis of the above considerations, one could expect that similar benefits could be achieved if voltammetric/amperometric detection of VAs is performed in basic RTILs.

In this work, for the first time, it is reported the use of RTILs as media to perform electrooxidation of typical aldehydes that can be originated as a consequence of deterioration phenomena, technological treatments, or peroxidative stress. In particular, propanaldehyde (PA) and hexanaldehyde (HA) are considered as target analytes, and their voltammetric behaviour is investigated in three 1-butyl-3-methylimidazolium ([BMIM]) based ionic liquid shaving neutral, acid and basic characters. A platinum microelectrode is employed in the measurements to exploit, from one side, the catalytic activity of the electrode material towards the oxidation of the aldehydes [29-31]; from the other, the properties of microelectrodes, which are well suited for carrying out measurements in viscous media [35-37]. Since the intent is to develop a sensor to be employed in real world conditions, the RTILs are used with the water content they absorb from air moisture under ambient conditions.

The results here reported show that in 1-butyl-3-methylimidazolium hydroxide ([BMIM][OH]) (i.e., a basic RTIL), a clear oxidation process for both PA and HA can be recorded and that it can

be exploited for monitoring the above aldehydes in headspace. This is achieved using an electrochemical microprobe (EMP) incorporating [BMIM][OH] as electrolyte. The usefulness of the EMP assembly proposed here for real world applications is assessed for measurements of HA in the headspace of squalene samples spiked with known amounts of the aldehyde.

The electrochemical microprobe (EMP) was employed both for bulk and headspace measurements. In the latter cases, the EMP was coated with a film of [BMIM][OH] by dip-coating [14], thus ensuring the electrolyte contact between the two platinum electrodes. The RTIL film had a thickness of 138 (± 18) μm, as estimated by weighing the microprobe before and after dip-coating.

Both in batch and headspace measurements were performed in a 2 mL glass vial, provided with suitably pierced PTFE–silicon screw caps to insert either the microprobe or the desired sample investigated. Typically, 0.2 mL of the ionic liquid (without or spiked with known amounts of PA) or HA, or pure aldehydes, or squalene samples spiked with known amounts of HA were placed on the bottom of the vial. For bulk measurements, the EMP was dipped directly in the RTILs solutions and kept at ambient temperature, 23 (±1)°C. Headspace measurements were performed in static atmospheres, at different temperatures, after allowing the achievement of the equilibrium of the analyte between the liquid and gas phase. The background gas was in all cases air. The measurements taken at 40°C, 50°C and 60°C were performed by dipping the vial in a thermostatic water bath equipped with a suitable temperature control system (IKA Werke, Staufen, Germany) (see **Scheme 6.2**).

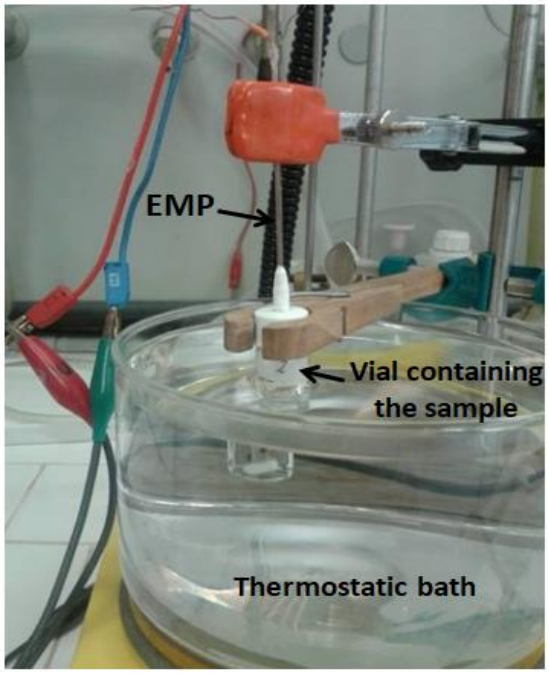

Scheme 6.2 – Picture of the experimental setup.

The water content in the RTILs was determined by Karl Fischer (Mettler Toledo DL 32) titrations and, unless otherwise stated, under ambient conditions. The relative humidity level (RH) in the laboratory, where the measurements were performed, was on average of 60 (±10%) RH. Under these condition, the average water contents in the various RTILs were found to be 0.25 (±0.05)% wt/wt, 1.1 (±0.2)% wt/wt and 5 (±1)% wt/wt for [BMIM][NTF_2], [BMIM][HSO_4] and [BMIM][OH], respectively. Dynamic viscosity of RTILs was measured using a Contraves LS 40 cone-plate stress rheometer (Mettler-Toledo, Greifensee, Switzerland). These measurements were performed at 20, 40 and 50°C on RTILs as received and with the water content found under ambient conditions. Obtained viscosity values are shown in **Table 6.2**.

Table 6.2 Viscosity of RTILs obtained under ambient conditions at 20 °C, 40 °C and 60°C.

Name	**Formula**	**η (mPa s)**		
		20°C	40°C	50°C
[BMIM][OH]	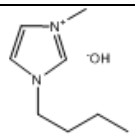	629.1 ± 0.4*	131.3 ± 0.2*	71.8 ± 0.1*
[BMIM][HSO_4]	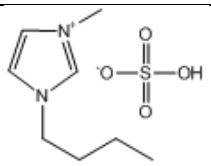	352 ± 0.4*	85.0 ± 0.8*	50.6 ± 0.3*
[BMIM][NTF_2]	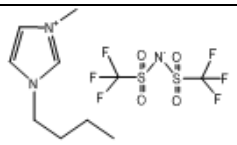	59.8 ± 0.2*	27.7 ± 0.1*	20.7 ± 0.1*

**obtained from three replicates*

6.2.2 Anodic behavior of the RTILs at the Pt microelectrode without and with PA and HA

Three 1-butyl-3-methylimidazolium based ionic liquids, namely [BMIM][HSO_4], [BMIM][NTF_2] and [BMIM][OH], were investigated as media for the electrooxidation of PA and HA. Preliminarily, the cyclic voltammetric behaviour of the aldehyde-free RTILs was examined atthe Pt microelectrode, and **Fig 6.16** shows a series of CVs recorded at 20 mVs^{-1} in the potential range 0 – 1.8 V. As is evident, in the anodic scan in both [BMIM][HSO_4] and

[BMIM][NTF_2] small features over the potential range 1.1 – 1.8 V are observed (see details in inset **Fig 6.16**), while an oxidation wave reaching a quasi-plateau at about 1.3 V was recorded in [BMIM][OH].

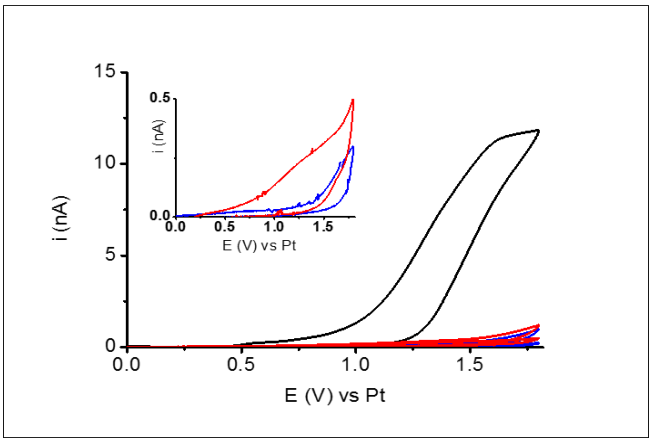

Fig 6.16- Cyclic voltammograms recorded with a Pt microdisk 12.5 µm radius in the aldehydes-free RTILs, under ambient conditions. [BMIM][NTF_2] (blue lines), [BMIM][HSO_4] (red lines), [BMIM][OH] (black lines). Inset: enlargement of the CVs recorded in [BMIM][NTF_2] and [BMIM][HSO_4]. Scan rate: 20 mV s^{-1}.

The observed waves are conceivably related to the oxidation of water present in the medium. In fact, their magnitudes correlate well with the water content and the hydrophobicity or hydrophilicity character of each RTIL [20, 40]. Moreover, similar measurements performed in the vacuum dried RTILs displayed cyclic voltammograms with much less background currents, and this was particularly evident for [BMIM][OH] (**Fig 6.17** dashed line), which is the most hydrophilic RTIL among those investigated here. The uptake of moisture in the latter medium was remarkably rapid as is displayed in inset of **Fig 6.17**, where backgrounds CVs were monitored for about 30 min. The background current reached an almost constant value of 12.5 (± 1.2) nA (**Fig 6.17**, full line) after about six hours.

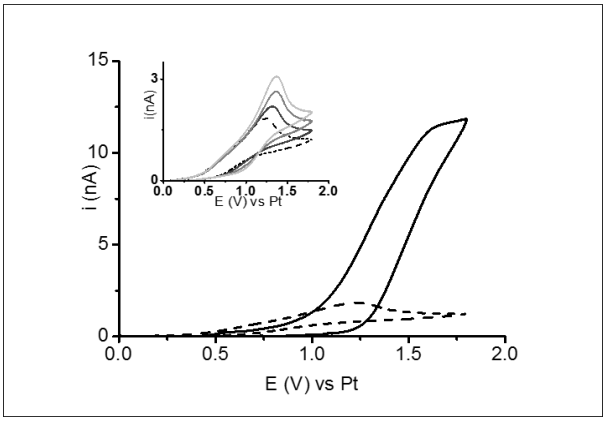

Fig 6.17- Cyclic voltammograms recorded with a Pt microdisk 12.5 µm radius in the aldehydes-free [BMIM][OH] under: ambient conditions, containing 5% wt/wt H_2O (full line); vacuum dried, containing 0.5% wt/wt H_2O (dashed line). Inset: effect of water uptake on the CVs recorded in [BMIM][OH] exposed to the atmospheric humidity (about 55% RH) for 0 min (dashed line), 10 min (dark gray), 20 min (grey) and 30 min (light grey). Scan rate 20 mV s^{-1}.

Another feature worth to be noted is the potential onset of the wave attributed to water, which for the protic [BMIM][OH] and [BMIM][HSO_4] occurred at lesser positive potentials than that of the aprotic [BMIM][NTF_2] (**Fig 6.16**). This shift also agrees with the circumstance that the water oxidation at Pt materials, actually leads to the formation of Pt oxides even in RTILs [18, 23, 41] and, as happens in aqueous electrolytes, their formation is favoured in basic media [42].

The addition of PA (**Fig 6.18a**) and HA (**Fig 6.18b**) to the not vacuum-dried RTILs resulted in only minor changes in the CVs recorded in [BMIM][HSO_4] and [BMIM][NTF_2], where the current, just before the onset of the water oxidation process, increased to a relatively small extent (see details in insets in **Fig 6.18** with full lines), indicating low efficiency of these media in promoting the electrooxidation of the two aldehydes. Conversely, in [BMIM][OH], an oxidation process, whose onset occurred at less positive potentials and in part overlapping with that attributed to water, was recorded (**Fig 6.18**, main pictures with black full lines). Upon incremental addition of the aldehydes to the RTILs, only in [BMIM][OH] a corresponding significant current increase of the waves was observed (results not shown). This result supports the circumstance that the basic medium favours the electrooxidation process of the aldehydes, similarly to what happens in aqueous electrolytes [30-34].

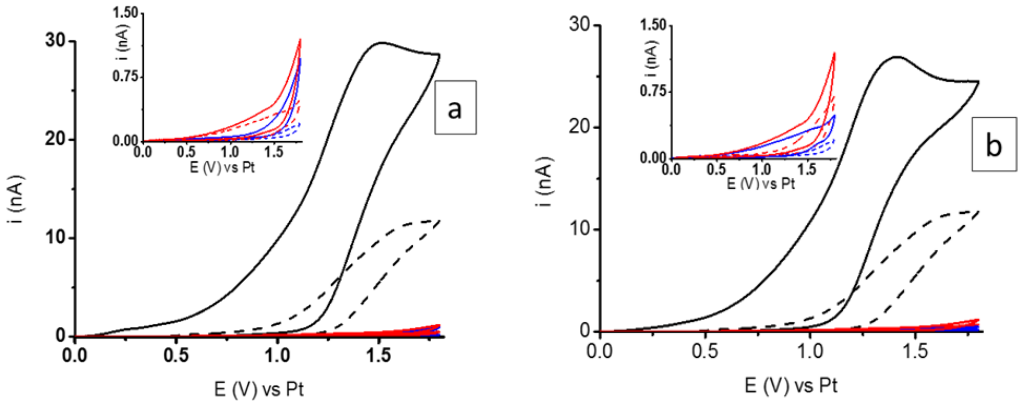

Fig 6.18. Cyclic voltammograms recorded with a Pt microdisk 12.5 µm radius in the RTILs, under ambient conditions, containing **(a)** 200 mM PA and **(b)** 300 mM HA (CVs with full lines); backgrounds are also included as dashed lines. [BMIM][NTF_2] (blue lines), [BMIM][HSO_4] (red lines), [BMIM][OH] (black lines). Insets, enlargements of the CVs recorded in [BMIM][NTF_2] and [BMIM][HSO_4] with and without aldehydes. Scan rate 20 mV s^{-1}.

It must be considered that, because of the higher content of water in [BMIM][OH], the aldehyde electrooxidation process could also be promoted by water itself. To shed light on this matter, measurements were performed in the RTILs, containing PA and HA and different water content.

Fig 6.19a shows CVs recorded in vacuum dried [BMIM][OH] (water content about 0.2% wt/wt) and 200 mM PA (i.e., same as in **Fig 6.18a**). As is evident, under these conditions, a wave smaller than that recorded with excess of water (i.e. about six times less), is obtained. This indicates that water plays an important role in the overall electrooxidation process of the aldehyde. However, CVs performed in [BMIM][HSO_4] and [BMIM][NTF_2], with intentionally added water (up to 5% wt/wt), did not lead to any significant change (**Fig 6.19b**, full lines) with respect to those recorded above with much less water content (**Fig 6.19b** dashed lines for comparison). This suggests that also OH^- ions are needed for an efficient electrooxidation of the aldehyde. Similar results were obtained using HA.

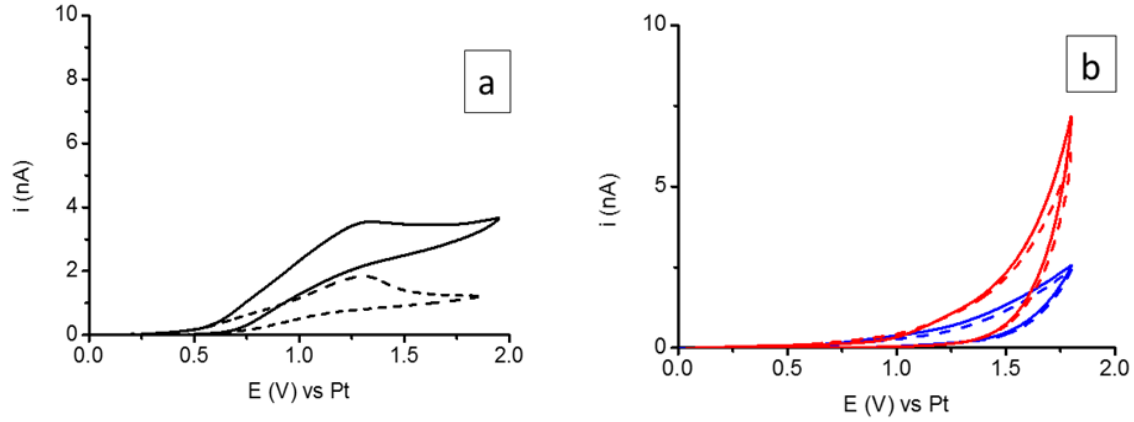

Fig 6.19. Cyclic voltammograms recorded with a Pt microdisk 12.5 µm radius in the RTILs, containing 200 mM PA. **(a)** [BMIM][OH] vacuum-dried; **(b)** [BMIM][NTF_2] (blue lines), [BMIM][HSO_4] (red lines) with added 5% wt/wt H_2O. CVs with dashed lines refer to the background. Scan rate 20 mV s^{-1}.

Although at this stage we are unable to propose a clear reaction mechanism (this was beyond the aim of the present work), the overall electrode processes probably involve Pt oxides, as it was also reported for the electrooxidation of acetaldehyde [18] and other organic molecules, such as methanol [41] and ethylene [23] in other RTILs. It is also likely that, because of the basic medium, the formyl moiety of the aldehydes converts in the bulk medium to a geminal-diol anion [30-34] which, after adsorption onto the electrode surface evolves towards the formation of the corresponding carboxylate anion [30, 31-34].

Based on the above results, [BMIM][OH] under ambient conditions seemed the best solvent where to perform sensible detection of aldehydes. Therefore, in the following sections, the discussion refers only to the results obtained using the latter RTIL with the water content it usually absorbs in ambient conditions (i.e., about 5% wt/wt, see above in Experimental).

6.2.2.1 Stability of the current signal with time, recorded in the bulk media

The stability of the current response due to the electrooxidation process of the aldehydes at a fixed potential was assessed by chronoamperometry. The measurements were performed in bulk [BMIM][OH] spiked with known amounts of the aldehydes, and stepping the potential from 0 V to 1.5 V. **Fig 6.20** shows a series of current potential profiles recorded for 400 s in the medium containing PA; the background current response is also included. From the figure it is evident that after the typical and expected sudden current decrease, the currents decline slowly. More stable signals were obtained by applying an electrochemical cleaning step to refresh the electrode surface. The overall waveform used is described in **Fig 6.20**. The potential from 0 V was stepped up to 2 V, kept for 5 s, and then turned back to 0 V and kept for 10 s (cleaning step); for the monitoring step, the potential was suddenly raised again at 1.5 V and kept for 150 s. Current against time plots recorded for 150 s with the two different wave forms (i.e., without and with the cleaning step) are contrasted in **Fig 6.20**, and, as is evident, the triple pulse step provides a better current stability at longer times.

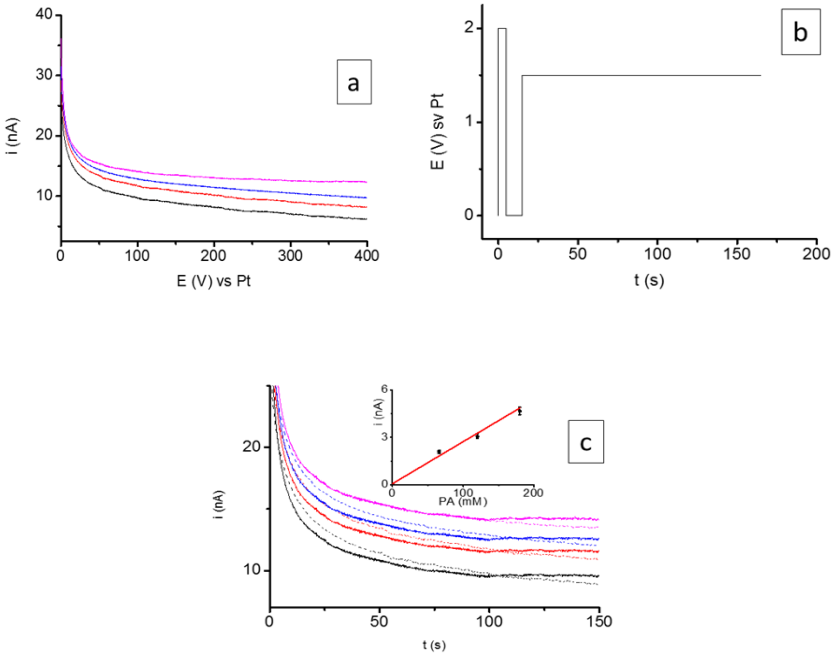

Fig 6.20- Chronoamperometric measurements performed at a Pt microdisk 12.5 µm radius in [BMIM][OH], under ambient condition, spiked with: 0 mM (black), 61 mM (red), 122 mM (blue), 183 mM (magenta) of PA. **(a)** Single pulse from 0 V to 1.5 V *vs.* Pt. **(b)** Triple pulse waveform for the cleaning and monitoring steps. **(c)** Comparison of the chronoamperometric profiles recorded for 150 s, using the single potential step (as described in **a**) and the triple potential steps (as described in **b**); inset: background-corrected current against PA concentration.

Current values, averaged over the range 100-150 s, plotted against PA concentration, provided a linear trend as displayed in the inset of **Fig 6.20c**. Similar results were obtained by using HA (not shown). Reproducibility of the average current obtained from three replicates was within 5% (RDS).

6.2.3 Headspace sensing of PA and HA by the electrochemical microprobes

Headspace measurements of the investigated aldehydes were performed by using the EMP coated with a layer of [BMIM][OH]. Initially, the RTIL-integrated sensor was exposed to the aldehyde vapours produced at ambient temperature by 0.2 mL of the pure aldehydes placed on the bottom of the 2 mL vial. PA and HA are characterised by rather different vapour pressures, which, at 25 °C, are 42.5 kPa [33] and 1.517 kPa [34], respectively. CVs recorded under these conditions are displayed in **Fig 6.21** for different exposure times. It is evident that, in both cases, the wave heights increase with time up to achieve a constant value after about 10 and 20 minutes for PA and HA, respectively (see insets in **Fig 6.21**), indicating, conceivably, the achievement of the partition equilibrium of the aldehydes between the gas and the RTIL phase. The current due to HA increased to a smaller extent, in agreement with its lower vapour pressure at ambient temperature. For the latter aldehyde, therefore, voltammetric measurements in the headspace were also performed at higher temperatures, over the range 40 – 60 °C. **Fig 6.22** (full lines) shows a series of CVs recorded with the [BMIM][OH]-coated EMP exposed to the HA vapours for about 5 min, and as is evident the overall wave increases, as the temperature (T) increases. Control measurementswere also performed with the microprobe exposed to HA-free atmospheric gas (inset in **Fig 6.22**), this to exclude that the current increment observed upon varying T were due to the background (i.e., to the process assigned to water oxidation). It was observed that the background current also increased with temperature, however, to a much lower extent (**Fig 6.22**, insert dashed lines). Background-corrected current (i_c) against temperature increased (inset in **Fig 6.22**), clearly indicating the involvement of the HA in the electrooxidation process. The current increment as the temperature increases, can be due, other than to the higher vapour pressure of the aldehydes, to other factors and, particularly, to the decrease of the medium viscosity (**Table 6.2**), which reflects on an increase of the diffusion coefficient of the electroactive species, as is predicted by the Stokes-Einstein equation [43].

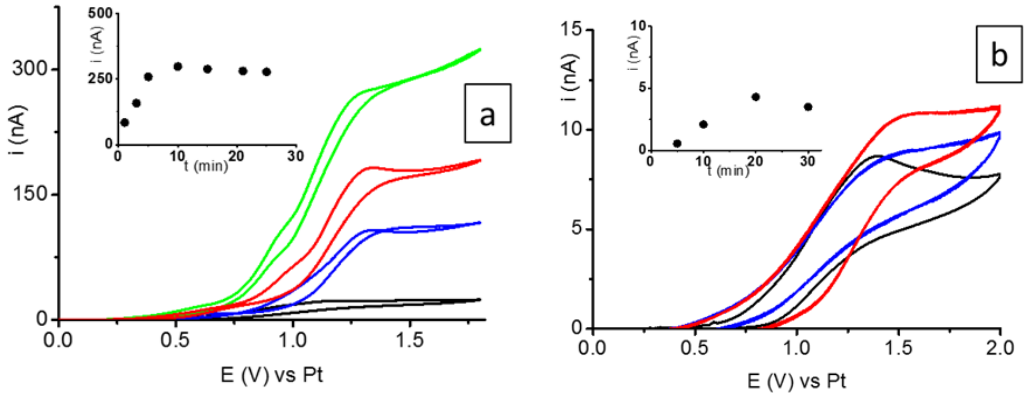

Fig 6.21 Cyclic voltammograms recorded with the [BMIM][OH]-coated MPE exposed to the aldehydes vapors of **(a)** PA for 0 min (black line), 1 min (blue line), 3 min (red line), 5 min (green line); **(b)** HA for 0 min (black line), 5 min (blue line), 10 min (red line). Insets background-corrected current against exposure time. Scan rate 20 mV s^{-1}.

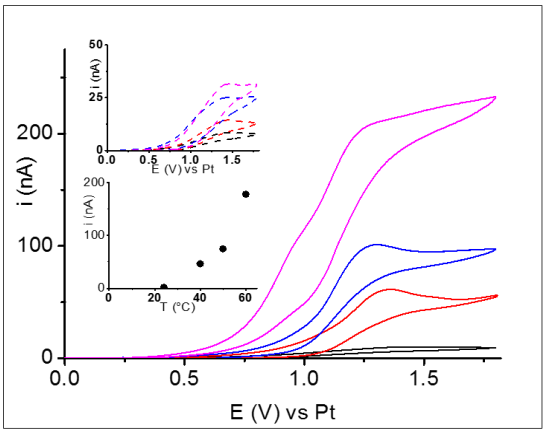

Fig 6.22 Cyclic voltammograms recorded with the [BMIM][OH]-coated EMP exposed to HA vapors at different temperatures: 23 °C (black), 40 °C (red), 50 °C (blue), 60 °C (magenta). Insets: temperature effect on the background CVs (colors refer same temperature as above) and background-corrected current against temperature. Scan rate 20 mV s^{-1}.

6.2.3.1 Recovery and reproducibility of the EMPs in headspace measurements

To verify the possibility to reuse the same RTIL-coated EMP for several measurements, recovery of the thin RTIL layer to the original conditions was investigatedby exposing the RTIL-coated EMP, loaded with the aldehydesto the ambient atmosphere, while performing CVs at different times (not shown). It was found that recovery of the RTIL film at its initial background signals required about 4 and 6 min for PA and HA, respectively. However, this loading-recovery procedure could be repeated for no more than 6-8 cycles, to keep the reproducibility of the current responses (evaluated at the wave/peak maxima) within 5% (RSD). Afterwards, the current responses started to decrease, probably due to poisoning of the electrode surface as well as for building-up of the electrooxidation products in the liquid film. As it is described later on in Section 6.2.4.2, this drawback could be overcome by using a suitable triple potential step.

6.2.4 Headspace detection of HA in a lipidic simulant matrix

The usefulness of the EMP for practical applications was assessed by detecting HA in the headspace of squalene solutions containing known amounts of the aldehyde. Squalene is a solvent frequently employed to simulate lipids matrices [44, 45], while HA was chosen as target analyte as it is frequently used as a marker of lipid oxidation processes [46, 47]. The measurements were conducted by exposing the [BMIM][OH]-coated EMP in the headspace for 5 min at 40 °C, 50 °C and 60 °C.

Typical CVs recorded at 40 °C are shown in **Fig 6.23a**; the corresponding calibration plot, obtained using current maxima against aldehyde concentration, is displayed in **Fig 6.23b**. Similar results were obtained at 50 °C and 60 °C (not shown). **Table 6.3** summarizes the regression equations of the calibration curves (correlation coefficients were higher than 0.992), dynamic ranges and detection limits evaluated for a signal-to-noise ratio of 3. Reproducibility of the average current obtained from three replicated was within 5% (RDS).

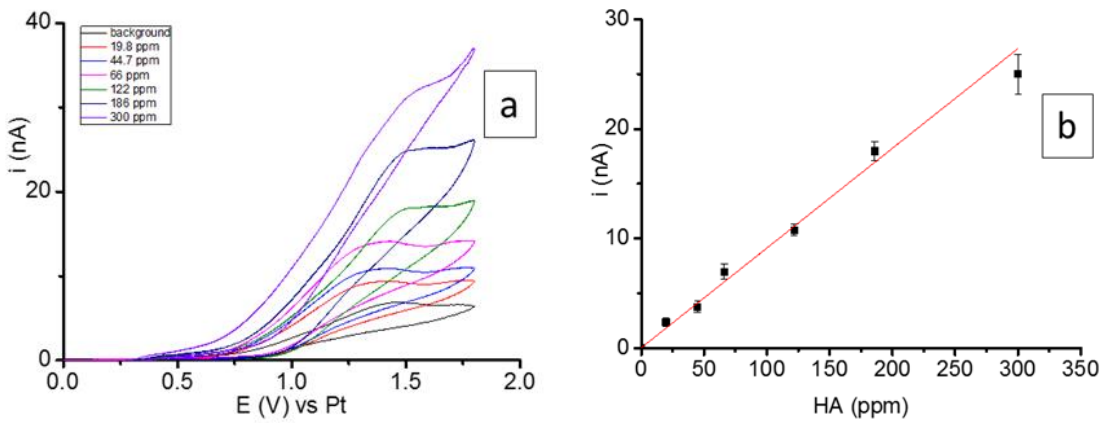

Fig 6.23 (a) Cyclic voltammograms recorded at 40 °C with the [BMIM][OH]-coated EMP in the head space of squalene solutions spiked with different amounts of HA; scan rate 20 mV s^{-1}. **(b)** Calibration plot obtained from background-corrected current against HA concentration; symbols refer to mean values from at least three replicates.

Table 6.3 Analytical parameters (regression equations, dynamic ranges and detection limits) for the headspace detection of hexanaldehyde in squalene using the [BMIM][OH]-coated EMP and voltammetry.

Item	**Temperature**		
	40°C	50°C	60°C
Regression equation [a]	y=9.1E-11 x+ 3.1E-11	y=1.5E-10 x+ 4.1E-11	y=2.2E-10 x+ 3.5E-11
Dynamic range (ppm)	3 - 300	3- 300	3- 300
Detection limit (ppm)	1.7	1.6	1.0

[a] y is in nA; x is in ppm.

Chronoamperometry was also used to construct calibration plots in the headspace of squalene samples spiked with different amounts of HA. In these experiments, to ensure good stability and repeatability of the current with time, the triple-pulse waveform displayed in **Fig 6.24a** was employed. It differs from that displayed in **Fig 6.20b** for two aspects: the monitoring step was shorter (3 s) and the triple pulse was repeatedly applied for the full length of the experiment. This was done for removing, by forced oxidation, HA-oxidation products, which could accumulate in the RTIL layer. The applied potential and the measurement length where chosen so as to optimize both repeatability and sensitivity in the measurements. **Fig 6.24b** shows a series of typical current-time responses recorded at 40°C with the above waveform, in the headspace of HA–spiked squalenesamples. From the figure, it is evident that the current responses are quite stable starting from t > about 50 s. The calibration plots were obtained using the average currents acquired during the 100- 150 s time interval and plotted against HA concentration.

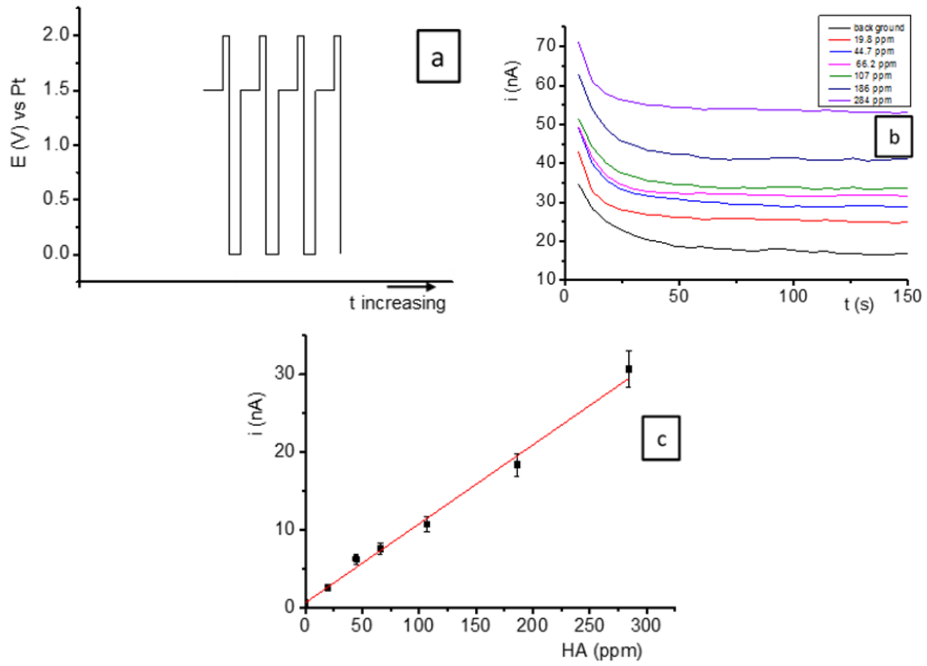

Fig 6.24 Chronoamperometric measurements performed at 40 °C with the [BMIM][OH]-coated EMP in the head space of squalene solutions spiked with different amounts of HA. **(a)** Applied potential/time waveform. **(b)** Current against time profile obtained at different concentration. **(c)** Calibration plot obtained from background-corrected current against HA concentration; symbols refer to mean values from at least three replicates.

Table 6.4 summarizes the regression equations of the calibration curves (correlation coefficients were higher than 0.993), dynamic ranges and detection limits evaluated for a signal-to-noise ratio of 3. Reproducibility of the average current obtained from three replicated of the above wave form was within 5% (RSD).

Table 6.4 Analytical parameters (regression equations, dynamic ranges and detection limits) for the headspace detection of hexanaldehyde in squalene using [BMIM][OH]-coated EMP and amperometry.

Item	**Temperature**		
	40 °C	50 °C	60 °C
Regression equation [a]	y =1.1E-10 x+ 7.1E-10	y =1.6E-10 x+ 4.1E-10	y =2.4E-10 x+ 3.5E-10
Dynamic range (ppm)	3 - 300	3 - 300	3 - 300
Detection limit (ppm)	1.2	1.0	0.9

[a] y is in nA; x is in ppm.

The above results indicate that both voltammetry and amperometry can be employed for the detection of aldehydes in headspace by the proposed [BMIM][OH]-coated EMP. It is also worth emphasizing that dynamic ranges, detection limits and reproducibility are suitable for the determination of aldehydes as marker of oxidative processes in food or medical analysis (e.g. detection of aldheydes in human breath) [52, 53].

References

[1] L. Sghaier, J. Vial, P. Sassiat, D. Thiebaut, M.Watiez, S. Breton, C.B. Cordella, European Journal of Lipid Science and Technology 118 (2016) 1853- 1879.

[2] S. Pastorelli, S.Valzacchi, A. Rodriguez, C. Simoneau, Food Additives and Contaminants 23 (2006) 1236-1241.

[3] S. Pastorelli. L. Torri, A. Rodriguez, S. Valzacchi, S. Limbo, V. Simoneau, Food Additives and Contaminants 24 (2007) 1219-1225.

[4] W. Cao, Y. Duan, Analytical Chemistry 37 (2007) 3-13.

[5] K. Pors, J.S Moreb, Drug Discovery Today 19 (2014) 1953-1963.

[6] V. Shestivska, A. V. Rutter, J. Sulé-Suso, D. Smith, P. Španěl, Rapid Communications in Mass Spectrometry 31 (2017) 1344–1352.

[7] G. Cao, D. Ruan, Z. Chen, Y. Hong, Z. Cai, Trends in Analytical Chemistry 96 (2017) 201-211.

[8] T. D. Rapson, H. Dacres, Trends in Analytical Chemistry 54 (2014) 65–74.

[9] S. K. Pandey, K.-H. Kim, K.-T. Tang, Trends in Analytical Chemistry 32 (2012) 87-99.

[10] L. Rassaei, M. Amiri, C. Mihai, M. Sillanpaa, F. Marken, M. Sillanpaa, Trends in Analytical Chemistry 30 (2011) 87-99.

[11] L. Xiong, R.G. Compton, International Journal of Electrochemical Science 9 (2014) 7152-7181.

[12] R. Toniolo, N. Dossi, A. Pizzariello, A. Casagrande, G. Bontempelli, Analytical and Bioanalytical Chemistry 405 (2013) 3571-3577.

[13] R.Toniolo,A.Pizzariello, N. Dossi, S. Lorenzon, O. Abollino, G. Bontempelli, Analytical Chemistry 85 (2013) 7241-7247.

[14] R. Toniolo, R. Bortolomeazzi, R. Svigelj, N. Dossi, I.G. Casella, C. Bragato, S. Daniele, Sensors and Actuators B240 (2017) 239-247.

[15] A. Rehman, X. Zeng, Accounts of Chemical Research 45 (2010) 1667-1677.

[16] M.C. Buzzeo, C. Hardacre, R.G. Compton, Analytical Chemistry 76 (2004) 4583-4588.

[17] L. Spinelle, M. Gerboles, G. Kok, S. Persijn, T. Sauerwald, Sensors 17 (2017) 1520.

[18] X. Chi, Y. Tang, X. Zeng**,** Electrochimica Acta 216 (2016) 171-180.

[19] Y-L Liu, M-C Tseng, Y-Ho Chu, Chemistry Communications 49 (2013) 2560-2562.

[20] D.S. Silvester, Analyst 136 (2011) 4871–4882.

[21] K. Murugappan, D. W. M. Arrigan, D. S. Silvester, Journal of Physical Chemistry C 119 (2015) 23572−23579.

[22] E. Menart, V. Jovanovski, S.B. Hočevar, Sensors and Actuators B 238 (2017) 71-75.

[23] M.A. G. Zevenbergen, D. Wouters, V.-A T. Dam, S. H. Brongersma, M. Crego-Calama, Analytical Chemistry 83 (2011) 6300–6307.

[24] N. Yao, H.B. Wang, Y.L. Hu, Mini-Reviews in Organic Chemistry 14 (2017) 237-254.

[25] L.E. Barrosse, A. M Bond, R.G. Compton, A. M. O'Mahony, E.I. Rogers,D. S. Silvester, Chemistry. An Asian Journal 5 (2010) 202-230.

[26] A Molina, E. Laborda , E.I. Rogers, F. Martínez-Ortiz, C. Serna, J.G. Limon-Petersen, N. V. Rees, R.G. Compton, Journal of Electroanalytical Chemistry 634 (2009) 73-81.

[27] H. Wana, H. Yina, L. Linb, X. Zeng, A. J. Mason, Sensors and Actuators B 255 (2018) 638–646.

[28] J. Gębicki, A. Kloskowski, Metrology and Measurement Systems 4 (2010) 637–650.

[29] L.W.H. Leung, M. J. Weaver, Langmuir 6(1990) 323–333.

[30] O.A. Khazova, Yu.B. Vasil'ev, V.S. Bagotskii, Izvestiya Akademii Nauk SSSR (Eng. Translation) 10 (1965) 1778-1787.

[31] S. Sibille, J. Moiroux, J. -C. Marot, S. Deycard, Journal of Electroanalytical Chemistry 88 (1978) 105-121.

[32] M.S. Baymak, W.J. Bover, H. Celik, P. Zuman, Electrochimica Acta 50 (2005) 1347-1359.

[33] R.W. Yan, B.K. Jin, Chinese Chemical Letters 24 (2013) 159–162.

[34] P. Mukherjee, S. Kumar Bhattacharya, Journal of Applied Electrochemistry 44 (2014) 857–866.

[35] M. A. Baldo, P. Oliveri, R. Simonetti, S. Daniele, Journal of Electroanalytical Chemistry 731(2014) 43-48.

[36] M.A. Baldo, P. Oliveri, R. Simonetti, S. Daniele, Talanta 161 (2016) 881-887.

[37] P. Oliveri, M. A. Baldo, S. Daniele, M. Forina, Analytical and Bioanalytical Chemistry 395 (2009) 1135-1143.

[38] B.C. Ranu, S. Banerjee, Organic Letters 7 (2005) 3049-3052.

[39] R. M. Souto, Y. Gonzlez-Garca, D. Battistel, S. Daniele, Chemistry - A European Journal 18 (2012) 230 – 236.

[40] A. M. O'Mahony, D.S. Silvester, L. Aldous, C. Hardacre, R.G. Compton, Journal of Chemical and Engineering Data 53 (2008) 2884–2891.

[41]A. Ejigu, L. Johnson, P. Licence, D. A. Walsh, Electrochemistry Communications 23 (2012) 122-124.

[42] S. Cherevko, A. R. Zeradjanin, G. P. Keeley, K. J. J. Mayrhofer, Journal of The Electrochemical Society 161 (2014) H822-H830.

[43] J. O. Bockris, A. K. N. Reddy, Modern Electrochemistry, vol. 1, Plenum, New York, 1970.

[44] R. Toniolo, S. Susmel, N.Dossi, A. Pizzariello, M. Martinis, G. Bontempelli, Electroanalysis 22 (2010) 645–652.

[45] Kim Se-Kwon; KaradenizFatih, Chapter 14: Biological importance and applications of squalene and squalane, in: Kim Se-Kwon (Ed.), Advances in Food and Nutrition Research, vol., 65: Marine medicinal foods: implications and applications - animals and microbes, Academic Press, USA, 2012, pp. 223-233.

[46] Y. Xiuzhu, L. Mengjun, C. Jia, W. Xingguo, International Journal of Food Properties 20 (2018) S3 S2926-S2938.

[47] H. J. Henryk, M. Obuchowska, R. Zawirska-Wojtasiak, E. Wąsowicz, Journal of Agricultural and Food Chemistry 48 (2000), 2360-2367.

[48] I. G. Casella, M. Contursi, Electrochimica Acta 52 (2006) 649–657

[49] J. Wang, P. V. A. Pamidi, G. Cepria', Analytica Chimica Acta 330 (1996) 151-158.

[50] B. C. Ranu, J. Ranjan Jana, European Journal of Organic Chemistry (2006) 3767–3770.

[51] E. N. Frankel, Lipid Oxidation, Second Edition, The Oily Press, Bridgwater, England, 2005.

[52] P. Fuchs, C. Loeseken, J.K. Schubert, W. Miekisch, International Journal of Cancer, 126 2663-2670.

[53] J. Obermeier, P. Trefz, K. Wex, B. Sabel , J.K. Schubert, W. Miekisch, Journal of Breath Research, 9 (2015) 1-10.

Chapter 7 – SECM and small molecules sensing

7.1 A SECM approach for establishing the interaction between CPT-11HCl and immobilized peptides

7.1.1 Cyclic peptides for molecular recognition of CPT-11

Sensing systems, based on molecular recognition, are increasingly employed for the selective detection of an analyte in complex matrices [1]. The preferential recognition of an analyte (guest), by a receptor (host), is exploited to induce changes in the physical-chemical properties of the sensing system [1]. To this purposes, several classes of synthetic "host" moleculesfor the recognition of large (such proteins) or small molecules and ionshave been developed in the past. Examples included crown ethers [2], pillararenes [2], porphyrins [3], cyclodextrins [4], calixarenes [5]. A relatively new class of receptors is represented by cyclic peptides. These compounds consist in short aminoacid chains taking a ring structure. The ring structure can be formed by linking two ends of the peptide through an amide bond, or other chemically stable bonds such as lactone, ether, thioether or disulfide [6]. Cyclic peptides aremainly usedas therapeutic agents [6-8]. For instance, tyrocidineand gramicidin (**Scheme 7.1A,B**) have bactericidal activity; Cyclo-RGD peptide EMD 66203 (**Scheme 7.1C**) is a potent inhibitor of cell adhesion.

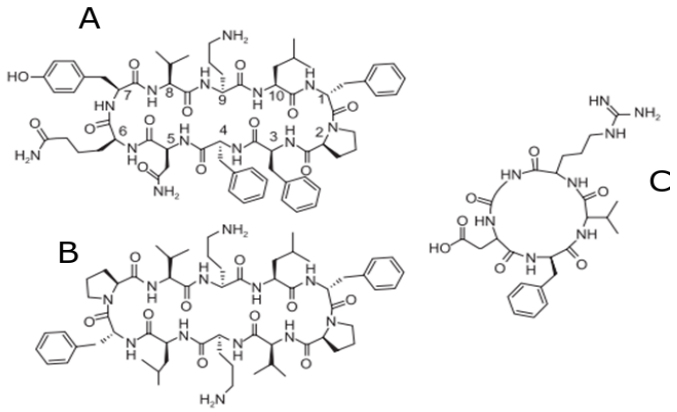

Scheme 7.1-Structural formulas of cyclic peptides employed for therapeutic use. **A**: Tyrocidine A. **B**: Gramicidin S.**C:** Cyclo-RGD Peptide EMD 66203. From [6].

Cyclic peptides have many advantages with respect to other receptors, including high stability, standard synthetic protocols, and easy chemical modification. In particular, peptides with short chains of amino acids generally have good chemical and conformational stability [9]. For this reason, they are promising candidates,as alternatives to proteins, as receptors in the fabrication of biosensors. Peptide-based molecular biosensors have been developed for convenient, fast detection of various analytes including antibodies, DNA, metallic ions and a variety of small organic molecules [9-13].

Recently, it has been reported a theoretical investigation to design cyclic peptides able to specifically bind CPT-11 in water and methanol media (**Scheme 7.2**). The method was based on an algorithm in which the geometries of the ligand–peptide complexes were generated by molecular dynamics [14, 15]. The binding affinity of CPT-11 with some of the optimized structures in methanol was proved by Surface Plasmon Resonance and fluorescence spectroscopy. It resulted to be at micromolar levels, i.e. similar to the LOD achieved by the electrochemical approach for the detection of irinotecan and described in Chapter 5.1. Therefore, it appeared useful to investigate one of these cyclic peptides as suitable receptor for the selective quantification of irinotecan in acetonitrile. The cyclic peptide, here designated as HK, was synthesized on purpose and its exact sequence is given in the experimental section.

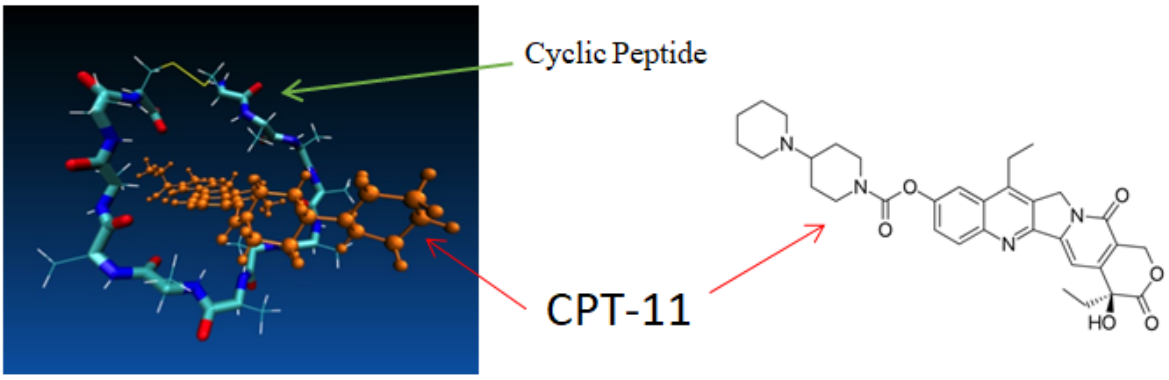

Scheme7.2- CPT-11 and the cyclic oligo-peptide HK, designed for its specific recognition. [From 14].

In many practical sensor devices, the host molecules are often immobilized onto a surface by electrostatic or covalent bonds [16-18]. This strategy would allow employing the platforms as transducers for the analyte detection. Alternatively, such types of platforms could be employed for rapid screening of the content of an analyte, provided that external and suitable probes exist able to respond to the amount of analyte under investigation. SECM is a powerful tool for the latter purposes; in fact, it was employed to measure enzyme activities after their covalent

immobilization over various substrates [19, 20] or, more in general, as a read-out system for immunosensors [21].

This section of the thesis deals with a study devoted to the preparation of a platform, containing the HK cyclic peptide immobilized on its surface, which is then used to evaluate by a SECM strategy the ability of the peptide to bind irinotecan in acetonitrile (i.e., the denaturing environment employed in Chapter 5.1).

7.1.1.1 Scheme for the construction of the platform

The procedure for the immobilization of the cyclic peptide on a gold substrate is shown in **Scheme 7.3** and it is described in detail in Chapter 4 (section 4.5-4.6).

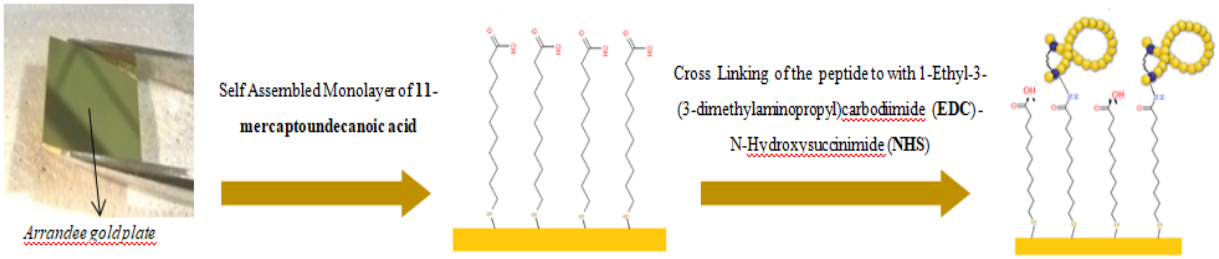

Scheme 7.3- Scheme of the procedure employed for the immobilization of cyclic peptides over the gold plate.

Firstly, the procedure involves the formation of a self assembled monolayer (SAM) of 11-mercaptoundecanoic acid (MUA) onto the surface of Au(111) gold plate. Secondly, the cyclic peptide HK is covalently immobilized to the SAM by means of an amide bond, formed between the $–NH_2$ group of the lysine moiety of the peptide and the carboxylic moiety of the MUA. The latter reaction was performed in the presence of EDC and NHS, which are used as activating agents for carboxylic acids [22].

The different steps of the above procedure were monitored by using voltammetry and SECM, as detailed in the following subsections.

7.1.2 Characterization of the substrate by voltammetry

MUA-SAMs formed on gold (Au 111) plates were characterized using cyclic voltammetry and **Fig 7.1** shows typical voltammograms recorded in 1 mM $[Ru(NH_3)_6]Cl_3$, 0.1 M KCl solutions at the bare gold plate (black line) and at MUA-SAM modified electrodes (blue lines).As is evident, at the bare gold surface, the CV is that expected for a reversible electrode process; at the SAM

modified electrode, essentially, background current was recorded (see enlargement in **Fig. 7.1**). This clearly indicates that SAM was successfully formed and almost blocks the electrode surface. The small features recoded by amplification of the current axis are conceivably due to small defects or pinholes [23-25]. Similar results were reported in the literature for MUA close-packed SAMs, formed over Au (111) substrates [24, 26].

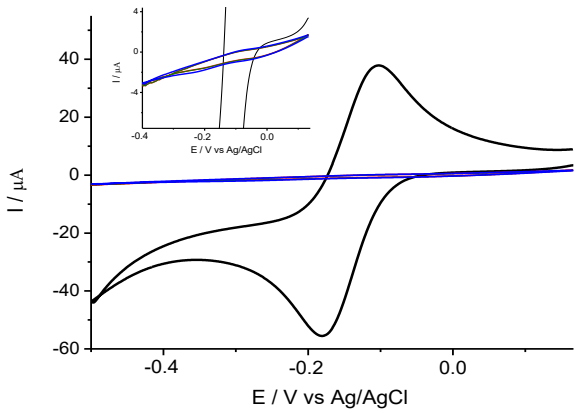

Fig 7.1- Cyclic Voltammograms recorded in 1 mM $[Ru(NH_3)_6]Cl_3$ 0.1 M KCl aqueous solution at a bare gold plate (black) and at a MUA SAM modified gold plate (blue, green and red lines). Inset is a magnification of voltammograms recorded at the MUA SAM modified gold plate. Scan rate: 50 mV/s.

To further support that the electrode surface was completely coated with a sufficiently uniform MUA- SAM layer, the reductive desorption of the thiolate was performed [27-29]. This process, occurring at very negative potential in basified water media, involves a one-electron reductive path described by the following reaction:

$$AuS(CH_2)_{10}COOH + e^- \rightarrow Au(0) + {}^-S(CH_2)_{10}COOH \qquad (1)$$

Fig 7.2 shows typical responses obtained on two different substrates coated with the same MUA-SAM. The feature of the CVs agreeswith those widely reported in literature [23, 27-29].

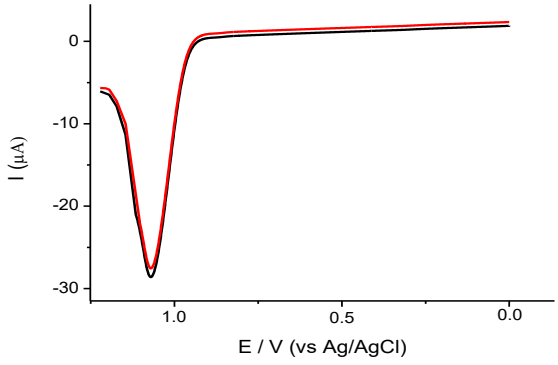

Fig 7.2- Voltammograms recorded at MUA-SAM modified gold plate in 0.5 M NaOH at 100 mV/s.

The charge (Q),associated to the reductive desorption peak, allowed determining the SAM surface coverage (Γ_c), by using the following relationship:

$$\Gamma_c = \frac{Q}{nFA} \qquad (2)$$

where A is the geometrical surface area and other symbols have their usual meanings. Average $Q$was 38.8 (± 3.5) µC cm^{-2} (from three replicates), which corresponds to a surface coverage of 4.02 (±0.30) x 10^{-10} mol/cm^2 of MUA-SAM. This value compares well with those reported in literature for the same compound (over the range between 4.0 x 10^{-10} and 8.9x 10^{-10} mol/cm^2 [23, 29, 30]).

The occurrence of the reaction between MUA-SAM and the cyclic peptide could not be investigated directly, as the latter was not electroactive. An indirect proof on the fact that the immobilization process of peptide could take place was obtained by attaching dopamine (DOPA, electroactive species), which possesses the -NH_2 group and therefore able to bind to the –COOH end of the SAM [31]. The procedure employed followed the **Scheme 7.2** apart from the immobilized molecule**.**

Fig 7.3 shows a typical CV recorded at the DOPA-modified MUA-SAM in an aqueous solution containing 0.1 M KNO_3. As is evident, a couple of broad peaks, having characteristics of surface processes, are obtained. In fact, the analysis of peak current against scan rate was linear. The broad peaks also suggest that the process is somewhat hindered, conceivably due to the long alkyl chain of MUA. These results are in line with data available in the literature for similar SAM-coated electrodes.

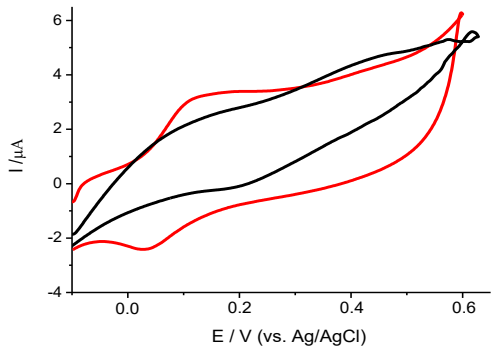

Fig 7.3 – Cyclic voltammogram of MUA SAM at which dopamine was covalently attached using the procedure described in **Scheme 7.2**, recorded in a 0.1 M KNO_3 solution. Black line is background. Scan rate: 50 mVs^{-1}.

The stability of the MUA-SAMs was also investigated in acetonitrile, which is the solvent of interest to study the interaction between the cyclic peptide and irinotecan. In this case, the electroactive species employed was ferrocene (0.5 mM solutions). **Fig 7.4** shows CVs recorded in at the bare gold substrate (black line) and the corresponding MUA-SAM (red line). It is evident that, after modification, the gold surface appeared blocked. Repetitive CVs recorded at the MUA-SAM did not display significant changes up to six hours. The small features, which can be observed by amplification of the current axis, are probably due to small pinholes in the coating [23, 30-35].

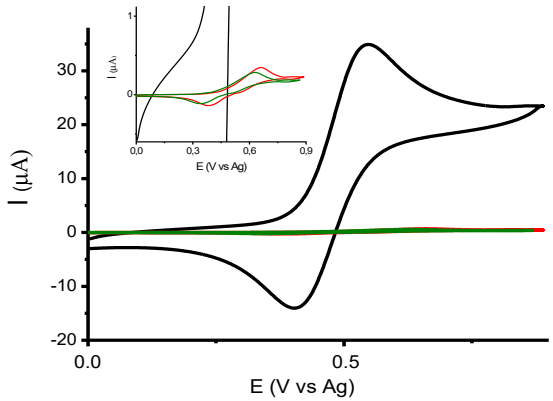

Fig 7.4 -Cyclic Voltammograms recorded in 0.5 mM Fc, 0.1 M $TBAPF_6$,CH_3CN solution at a bare gold plate (black line) at a MUA modified gold plate (red line) and at a MUA + peptide-modified gold plate (green line). Scan rate 50 mV s^{-1}.

The MUA-SAM substrate after modification with the cyclic peptide provided CVs as that shown in **Fig. 7.4** (green line). No substantial difference with respect to the previous voltammograms was observed.

Further insights on spatially resolved characteristics of the system were obtained by SECM, as is illustrated in the next section.

7.1.3 Characterization of the substrate by SECM

SECM was used to characterize the substrate in acetonitrile solutions; ferrocene (Fc) was used as redox mediator and Pt microelectrodes with radii of 12.5 µm (RG = 5) and 300 nm (RG = 10) were employed as SECM probes.

Fig 7.5 shows families of approach curves recorded above different zones of the gold substrate modified by either MUA-SAM (**Fig 7.5A**) or MUA-SAM-cyclic peptide (**Fig 7.5B**). In all measurements the Pt 12.5 µm radius was posed at +0.7 V *vs.* Ag, at which Fc is oxidized to Fc^+

at diffusion-controlled rate (**Fig 4.5** in Chapter 4). As is evident, apart from the case of the bare gold, negative feedback responses, fitting theoretical approach curves, are obtained. These results are consistent with those found by CV, indicating that the electron transfer process of the redox mediator with the underlying gold substrate was essentially blocked by the thin coating layers. The positive feedback observed at the bare unbiased gold substrate (**Fig. 7.5A**, magenta line) is the consequence of the lateral electron transfer, which takes place when the substrate surface is much larger than that of the microtip [32].

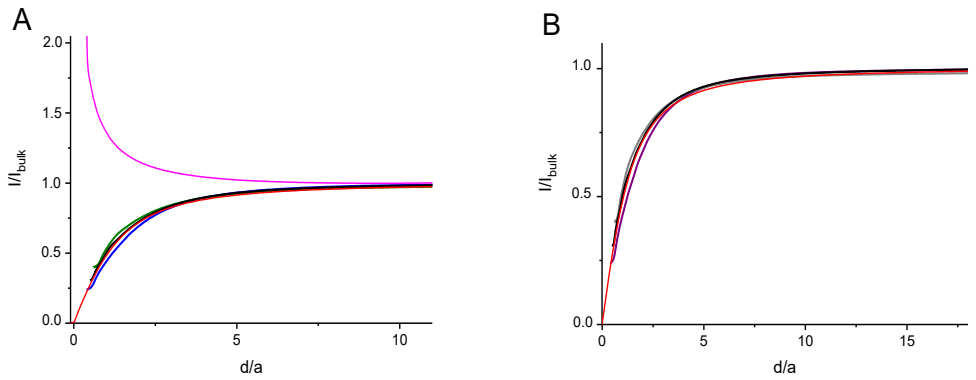

Fig 7.5 (A)- Approach curves recorded at a Pt microlelectrode held at +0.7 V *vs.* Ag over: gold, unbiased, substrate (magenta line), different zones of the MUA SAM unbiased substrate (black, blue and green lines) in 1 mM Fc, 0.1 M $TBAPF_6$ acetonitrile solution. **(B)**Approach curves recorded over different zones ofthe peptides-modified unbiased substratein 1 mM Fc, 0.1 M $TBAPF_6$ acetonitrile solution (purple, black and gray lines).Red lines are theoretical negative feedback curve.

To verify whether electron transfer processes could occur by direct tunneling through the MUA-SAM or MUA-SAM-cyclic peptides, or pinhole defects, SECM measurements were performed in the classical feedback mode, specifically, by applying +0.7 V *vs.* AgQR at the SECM tip and 0 V at the substrate, at which the redox mediator can be fully recycled. **Fig 7.6** shows typical approach curves thus obtained. They would resemble the theoretical profiles for pure negative feedback (**Fig. 7.6** red dashed lines). However, a closer inspection reveals that a slight, yet measurable feedback current is obtained, implying that the regeneration of Fc through direct electron tunneling or through the pinholes cannot be neglected.

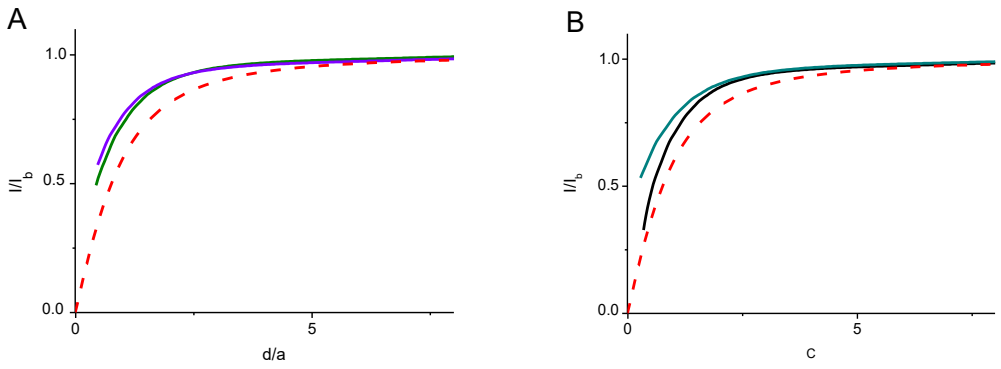

Fig 7.6- Typical approach curves recorded at a Pt microelectrode held at + 0.7 V *vs.* AgQR over different zones of MUA SAM modified substrate **(A)** and peptides-modified substrate (**B**) in 1 mM Fc, 0.1 M $TBAPF_6$ acetonitrile solution. The substrates were biased at + 0.0 V *vs.* AgQR. Red lines: theoretical negative feedback curve.

To support the above view, series of measurements, similar to those discussed above, were performed at the various substrates, using so called "competition mode". Under these conditions, both tip and substrate are biased at +0.7 V vs. AgQR. This implies that the oxidation of Fc to Fc^+ could occur not only at the tip, but also at the substrate, provided that the electron transfer could occur through either direct electron tunneling or pinholes [23, 36-38]. **Fig 7.7** shows families of approach curves thus recorded at either MUA-SAM (**Fig 7.7A**) or MUA-SAM-cyclic peptide (**Fig 7.7B**) substrates.

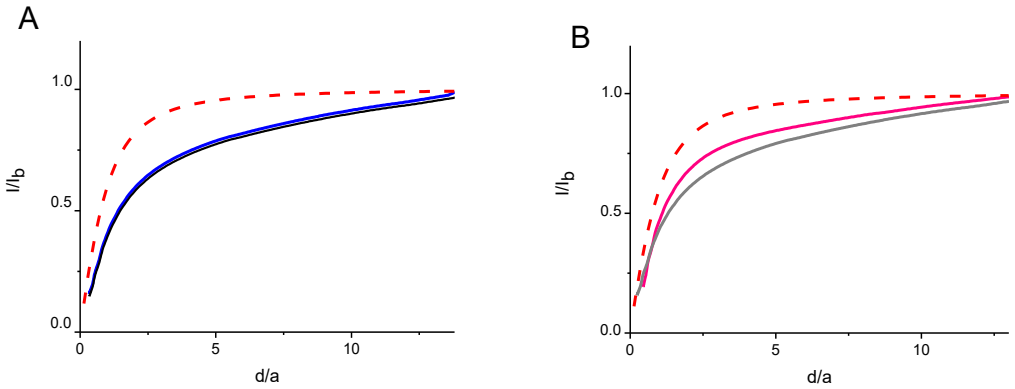

Fig 7.7-Typical approach curves recorded at a Pt microelectrode held at + 0.7 V *vs.* AgQR over different zones of MUA SAM modified substrate **(A)** and peptides-modified substrate (**B**) in 1 mM Fc, 0.1 M $TBAPF_6$ acetonitrile solution. The substrates were biased at + 0.7 V *vs.* AgQR. Red lines: theoretical negative feedback curve.

It is evident that current against distance profiles fall well below the theoretical curves expected for negative feedback. Moreover, current starts decreasing at distance relatively far away from the substrate (even at *d/a*> 10). These results clearly suggest that the redox mediator, within the

tip to substrate gap, is depleted not only because of the hindered mass transport, but also for its consumption at the substrate.

The various substrates were also investigated using a Pt nanoelectrode, which allowed improving the spatial resolution. Typical approach curves obtained are shown in **Figs 7.8- 7.9** for both types of substrates, i.e., coated with MUA-SAM (**Fig 7.8**) or MUA-SAM-cyclic peptide (**Fig 7.9**), while operating in pure feedback (**Figs 7.8A - 7.9A**) or competition (**Figs 7.8B – 7.9B**) modes.

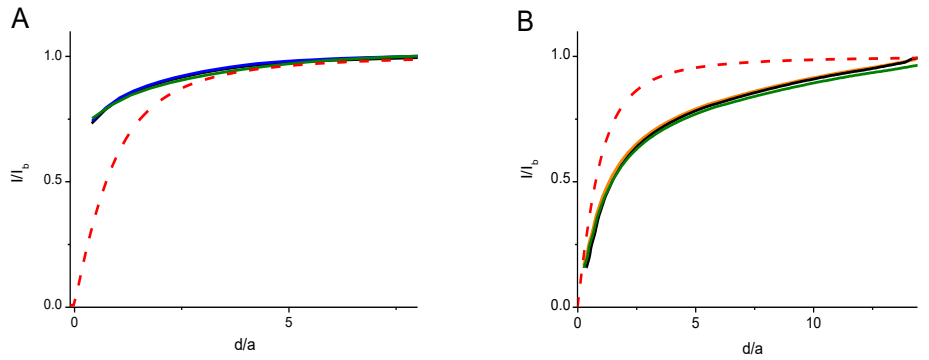

Fig 7.8- (**A**) Approach curves recorded at a Pt nanoelectrode (a = 290 nm)over different zones of the MUA SAM biased at +0.0 V *vs.* AgQR (blue, green and black lines). (**B**) Approach curves recorded at a Pt nanoelectrode (a = 290 nm) over different zones ofthe MUA SAM biased at +0.7 V *vs.* AgQR (green, yellow and black lines). Measurements were performed in a 1 mM Fc, 0.1 M $TBAPF_6$ acetonitrile solution. Red lines are theoretical negative feedback curve.

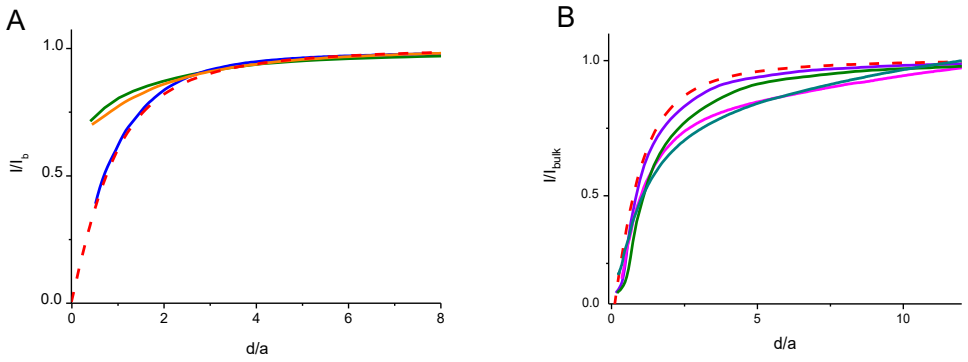

Fig 7.9- (**A**) Approach curves recorded at a Pt nanoelectrode over different zones ofthe peptides-modified substrate biased at +0.0 V *vs.* AgQR (blue and green lines). Orange line is a typical approach curve recorded over MUA SAM modified substrate. (**B**) Approach curves recorded over peptides-modified substrate biased at + 0.7 V *vs.* AgQR (purple, magenta and green lines). Cyan line is a typical approach curve recorded over MUA SAM modified substrate.

From **Figs 7.8A- 7.9A**, it appears that recycling of the redox mediator occurred to some extent, but the phenomenon depended on the specific location for the MUA-SAM-cyclic peptide

substrate (green and purple lines in **Fig 7.9**). This would suggest that the presence of the peptide in the coating layer, from one side, blocks more efficiently the electron transfer process; from the other makes the substrate surface less homogeneous, probably due to regions in which the MUA-SAM has not cyclic peptide bound to its structure. This different behavior of the two types of substrates also emerges from **Figs 7.8B– 7.9B**,where approach curves were recorded in competition. In fact, while the current against distance profiles recorded above the MUA-SAM are essentially independent on locations (**Fig 7.8B** black, magenta and red full lines), those recorded on MUA-SAM modified with cyclic peptides differ from one location to the other, due to the above mentioned surface heterogeneity (**Fig 7.9B**). In addition, it is worth noting that at the substrate unmodified with the cyclic peptide, the current decreases faster, suggesting the occurrence of a more efficient direct tunneling (or pinholes induced) electron transfer process.

The above phenomena were also imaged by performing both line and two-dimensional scans, using micro (**Fig 7.10 A,B**) and nano-electrodes (**Fig 7.11**). As shown in **Fig 7.10**, using the microelectrode biased at 0.7 V and the substrate unbiased, currents, as expected, are higher at the bare gold and decrease passing to the MUA-SAM and MUA-SAM-cyclic peptide substrate, congruently with the trend obtained by the approach curves. The surfaces in all cases seemed quite homogeneous, small differences are conceivably due to the substrate topography or tilting. SECM images that agree with the trends obtained above with the approach curves were obtained by posing the substrate at 0 or + 0.7 V (data not shown).

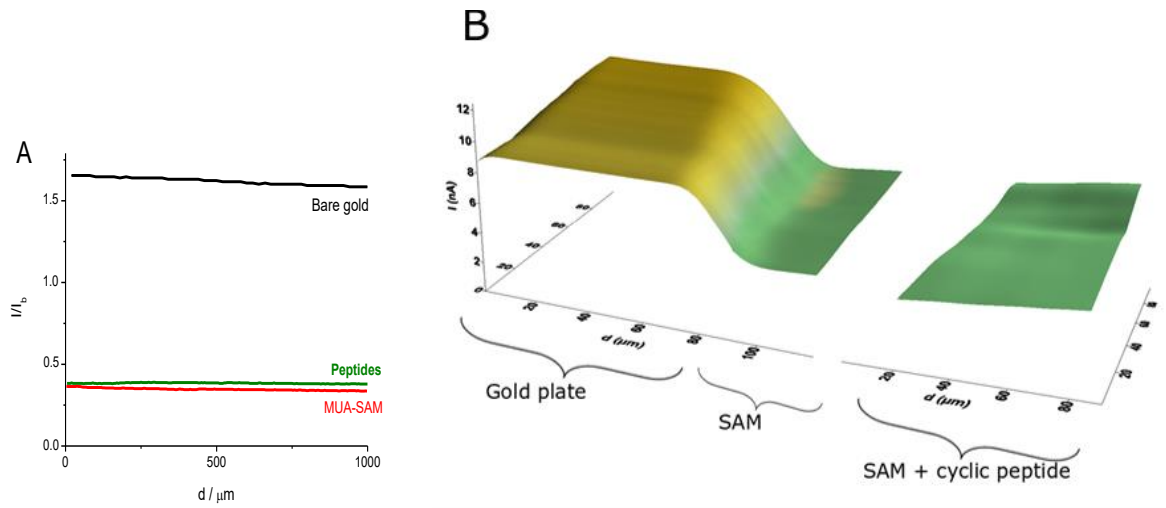

Fig 7.10 (A) - Linear scans recorded in a 1 mM Fc, 0.1 M $TBAPF_6$ acetonitrile solution at Pt microelectrode (a =12.5 µm) over bare gold (black line), SAM modified substrate (red line), peptides modified substrate (green line). The substrates were biased at +0.0 V *vs.* AgQR. **(B) -** 2D scans recorded over (from left to right) bare gold plate, SAM modified gold plate, SAM + cyclic peptide modified gold plate.

Fig 7.11 shows line scans and images obtained by using the nano-electrodes, which was in all cases biased at 0.7 V. The MUA-SAM and MUA-SAM-Cyclic peptide substrates where either unbiased or biased at 0 V (i.e., in classical feedback mode). Because of the higher spatial resolution achieved, clear differences appear depending on the two different conditions employed. The MUA-SAM substrate provided essentially homogeneous surfaces (the current changes were rather small) (**Fig 7.12 A'-A''**), again, in agreement with the information gathered from the approach curves. The peptide modified substrate (**Fig 7.12 B'-B''**) gave rise to much more marked current differences, depending on specific zones, confirming the un-homogeneity of the distribution of the cyclic peptide across the surface, as also discussed above describing the shapes of the approach curves.

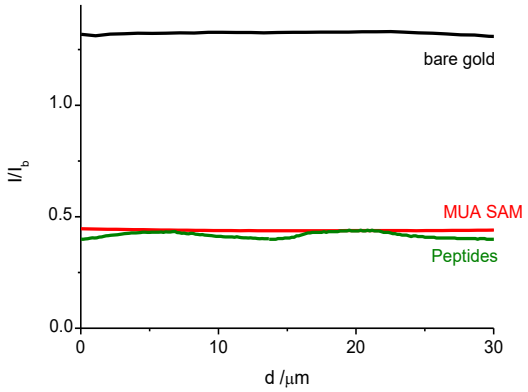

Fig 7.11- Linear scans recorded in a 1 mM Fc, 0.1 M TBAPF6 acetonitrile solution at Pt nanoelectrode (a =12.5 μm) over bare gold (black line), SAM modified substrate (red line), peptides modified substrate (green line). The substrates were biased at 0.0 V *vs* Ag.

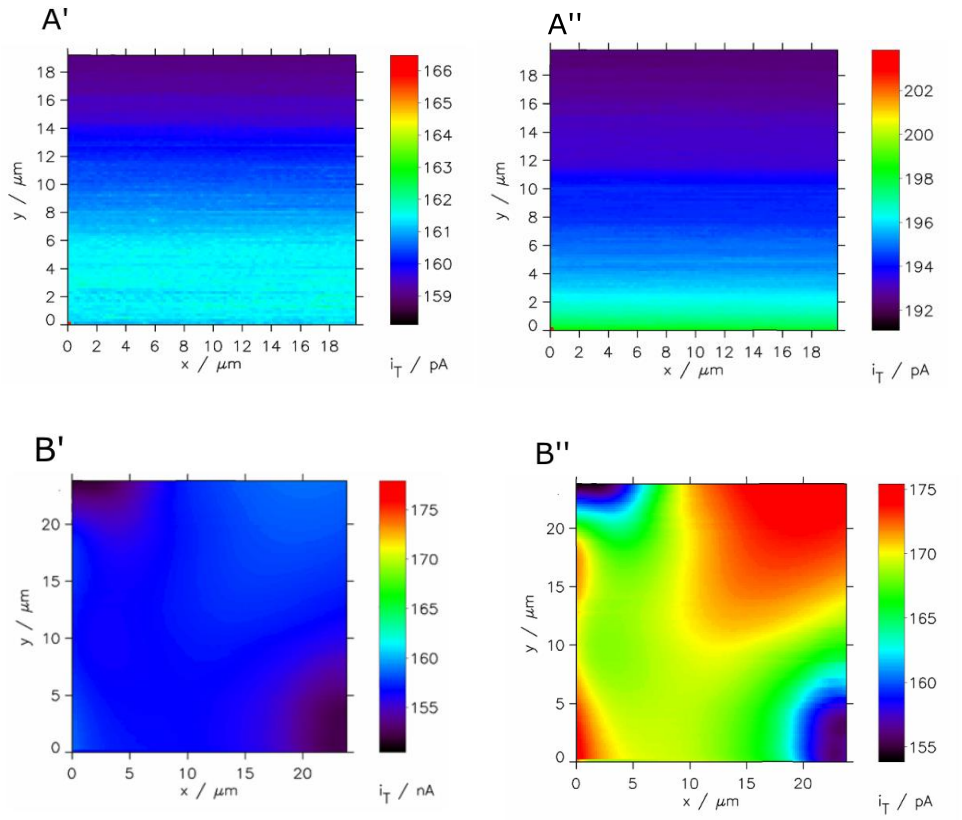

Fig 7.12-(**A**) Map recorded over MUA SAM modified substrate unbiased (**A'**) and biased at 0.0 V *vs.* Ag (**A''**) in 2 mM Fc, 0.1 M $TBAPF_6$ acetonitrile solution. (**B**) Maps recorded over the same zone of MUA SAM modified with cyclic peptides recorded at Pt nanoelectrtode at unbiased substrate (**B'**) and substrate biased at +0.0 V *vs.* Ag (**B''**).

7.1.4 Interaction between CPT-11HCl and peptides-modified substrate

The interaction between the immobilized cyclic peptide and CPT-11 in CH_3CN was investigated by using CPT-11HCl as redox mediator and exploiting its oxidation process at the Pt 12.5 µM electrode in the presence of 0.1 M $TBAPF_6$ (see also Section 5.1.6). Typical CVs recoded at low scan rates for a range of concentrations from 0.2 to 1.2 mM, are displayed in **Fig. 7.13**. The process, as discussed previously, is due to the oxidation of Cl^-, which forms an ionic couple with the protonated tertiary amine end of CPT-11. The process therefore occurs through a CE scheme (i.e., chemical reaction preceding the heterogeneous electron transfer); nevertheless, the current plateau depends linearly on concentration of CPT-11HCl (inset in **Fig. 7.13**).

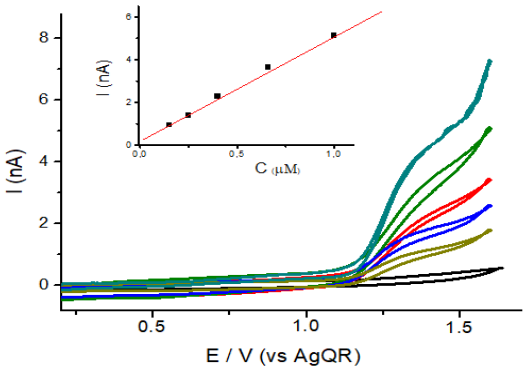

Fig 7.13– CV recorded at a Pt microelectrode (Ø =25 µm), at different concentration of CPT-11HCl in 0.1 M $TBAPF_6/CH_3CN$ solutions. Black line is background Scan rate: 20 mVs^{-1}.

Fig. 7.14 shows typical approach curves recorded above the MUA-SAM-cyclic peptide and, for comparison, those obtained at the bare gold and MUA-SAM substrates. The microdisk tip was biased at +1.45 V *vs.* AgQR, where the oxidation process is diffusion controlled. As is evident, above the peptide modified substrate, at various locations (**Fig 7.14A,** colored lines), the approach curves, at short tip-to substrate distance (i.e., about 10 µm), change from negative to positive feedback, and differ substantially from the others (**Fig 7.14B,** colored lines). The latter almost fit the theoretical curve for pure negative feedback (black dashed line). The current increase recorded above the peptides-modified substrate can be explained assuming that the concentration of the redox mediator (i.e., CPT-11HCl) at the substrate solution interface is much larger than that of bulk solution. This would be congruent with an accumulation of irinotecan onto the substrate. In order to support this hypothesis several control experiments were performed.

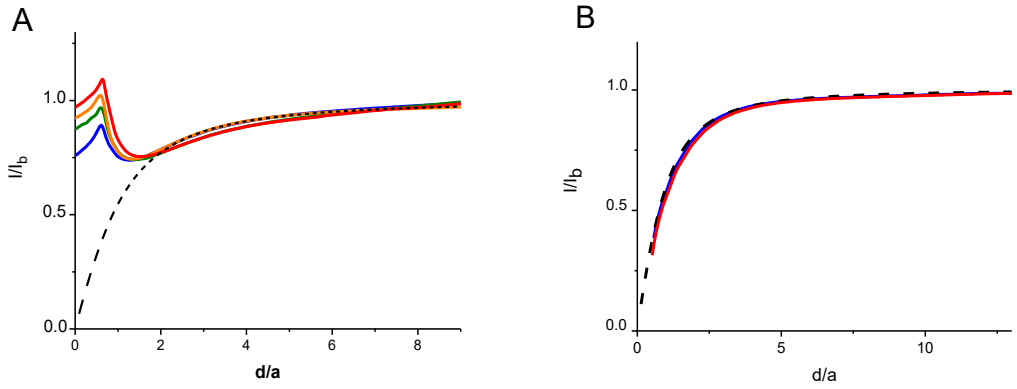

Fig 7.14-(**A**) Approach curves recorded over different zones of the peptides-modified substrate in 0.5 mM CPT-11HCl 0.1 M $TBAPF_6$ CH_3CN solution. **(B)** approach curves recorded over bare gold substrate (blue line) and over MUA modified substrate (red line) in 0.5 mM CPT-11HCl 0.1 M $TBAPF_6$ CH_3CN solution. Theoretical negative feedback approach curves (black dashed line) are displayed for comparison.

Firstly, a point by point approach curve was constructed, by recording steady-state voltammograms at various tip-to-substrate distances and plotting the plateau current (current measured at 1.45 V *vs.* Ag was considered) against distance. This allowed to directly visualize the oxidation process of CPT-11HCl and to exclude possible occurrence of artifacts. **Fig 7.15** shows steady-state voltammograms (**Fig 7.15A)** and the relevant approach curve (**Fig 7.15B,** blue symbols) thus obtained. As is evident the approach curve has same shape as that recorded by scanning the SECM tip towards the substrate (**Fig 7.15B**, dashed line).

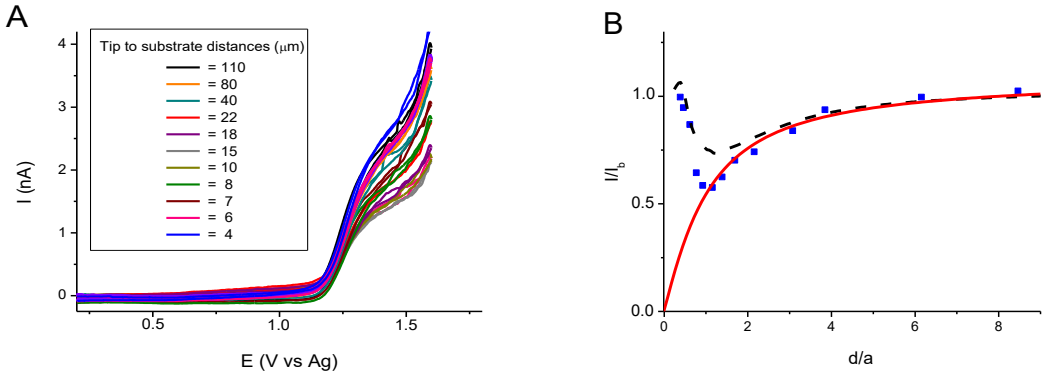

Fig 7.15 – (**A**) CVs recorded at different tip to substrate (Peptides modified) distance in 0.5 mM CPT-11HCl 0.1 M $TBAPF_6$ CH_3CN solution. Scan rate: 20 mV/s. (**B**) Normalized currents from CVs at + 1.45 V *vs.* Ag in function of tip to substrate distance. Dashed line is an approach curve recorded as those of **Fig 7.14A**. Red line is a theoretical negative feedback curve.

Performing similar measurements above a MUA SAM substrate provided steady-state voltammograms (**Fig 7.16A**) and point by point approach curves (**Fig 7.16B**), which are consistent with a pure negative feedback phenomenon.

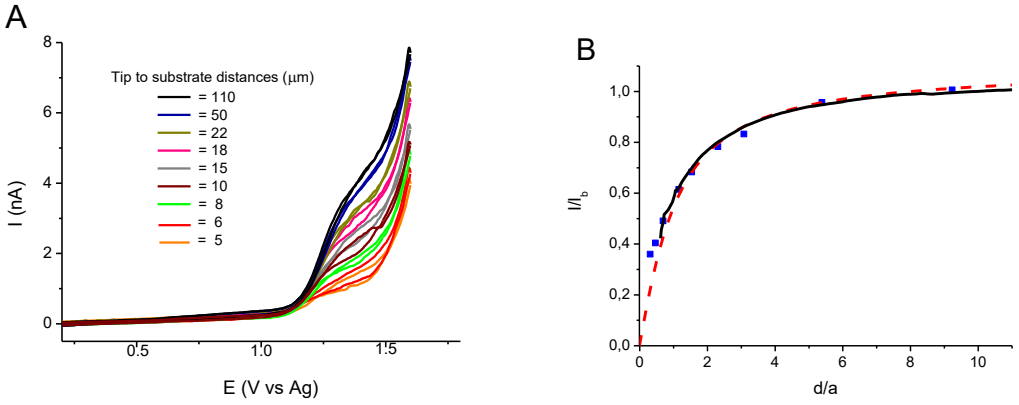

Fig 7.16 –(**A**) CVs recorded at different tip to substrate (MUA modified) distance in 0.66 mM CPT-11HCl 0.1 M $TBAPF_6$ CH_3CN solution. (**B**) Currents measured from CVs at + 1.45 V *vs.* Ag plotted in function of tip to substrate distance (blue dots), experimental approach curve over MUA-modified substrate (black line), theoretical negative feedback curve (red line).

Furthermore, to exclude that the oxidation process was due to CPT-11HCl ionic couple and not to other specie containing Cl^- ions, control experiments were performed also using TrEAHCl as redox mediator, which as CPT-11HCl forms a ionic couple in CH_3CN and provide an oxidation process at almost same potential of CPT-11HCl (see discussion in Section 5.1.6); it however should not interact with the cyclic peptide. **Fig 7.17** compares the approach curves recorded with and CPT-11HCl (green line) and TrEAHCl (blue line), the latter providing a curve that fits theory for pure negative feedback (black dashed line). This result corroborates the involvement of CPT-11HCl in the approach curves recorded in close proximity of the substrate solution interface.

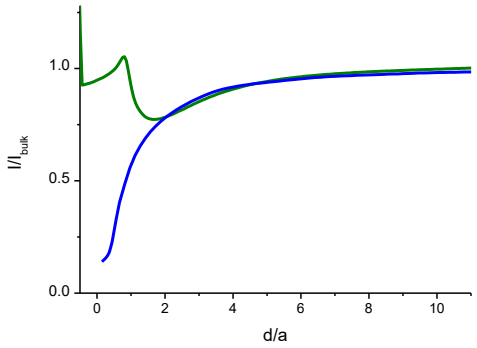

Fig 7.17 - Approach curves recorded over a peptide-modified substrate in 0.5 mM TrEACl (blue line) and 0.5 mM CPT-11HCl (green line) 0.1 M $TBAPF_6$ acetonitrile solution.

Other series of SECM measurements were performed for establishing, with higher accuracy, the tip to substrate distance at which the current increase, due to the accumulation of CPT-11HCl at the interface, occurred. This was done by using Fc as an "external" redox mediator, which was added to the CPT-11HCl solutions. The lack of interaction between Fc and CPT-11HCl in the solution was primarily ascertained by steady-state voltammetry, and **Fig 7.18** shows typical current potential profiles recorded in the CH_3CN solutions containing CPT-11HCl without (**Fig 7.18** black line) and with Fc (**Fig 7.18** red line). As is evident the two processes are well separated and the overall current, at the second plateau, reflects exactly the sum of the steady state currents applying when each of the two species is alone in the medium. This is shown in **Fig 7.18** (with the blue dashed line), where the steady state voltammogram of CPT-11 was translated above the plateau current of Fc. This result clearly indicates that no interaction exists between the two redox systems.

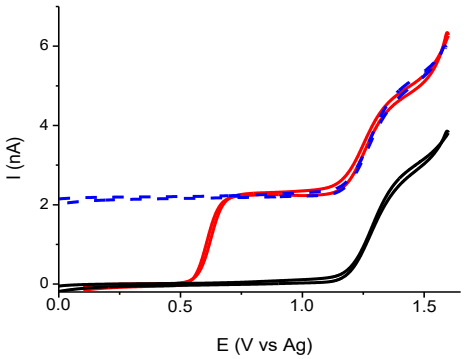

Fig 7.18- (A) Voltammograms of 0.66 mM CPT-11HCl recorded in 0.1 M $TBAPF_6$ CH_3CN solution without (black line) and with (red line) 0.5 mM of Fc. Blue dashed line is the CPT-11HCl voltammogram translated. Scan rate: 20 mVs^{-1}.

Point by point approach curves were constructed by using either the steady-state current of Fc, at 0.8 V, or the overall current, of both Fc and CPT-11HCl at 1.45 V, obtained upon changing the tip to substrate distance. The family of the steady-state voltammograms and relevant approach curves obtained are shown in **Fig. 7.19A**, and **7.19B**, respectively. It is evident that the current against distance obtained at the Fc plateau fits theory for pure negative feedback (**Fig. 7.19B**, black symbols), whereas that obtained from the overall plateau (**Fig. 7.19B**, blue symbols) deviates towards positive feedback when the normalized distance becomes smaller than about 0.9 (i.e., at less than 11 µm from the substrate). A similar behavior was obtained by plotting the current due to only CPT-11HCl (i.e., by subtracting from the overall current that due to Fc) against distance (**Fig. 7.19B**, red symbols). These results are fully consistent with those discussed above, corroborating the hypothesis of the lack of interaction between the cyclic peptide with CPT-11HCl.

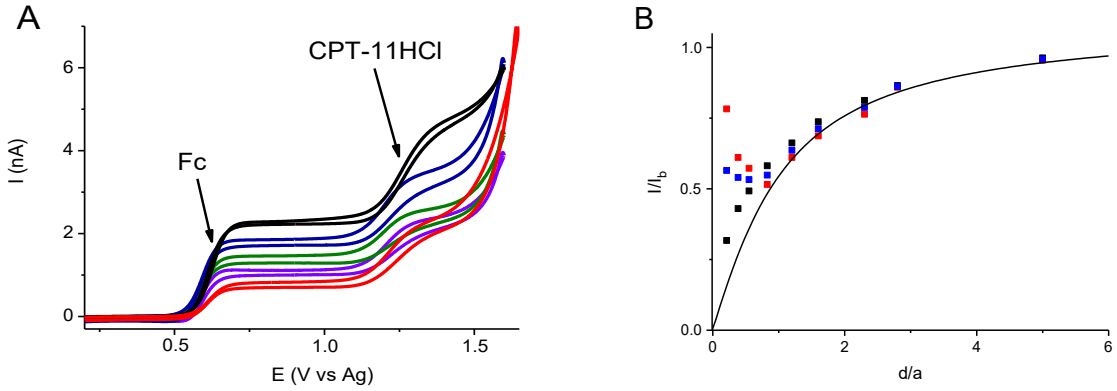

Fig 7.19- (A) CVs recorded, at 20 mVs^{-1}, in a 0.66 mM CPT-11HCl, 0.5 mM Fc CH_3CN solution over a gold substrate modified with peptides, at different tip to substrate distances. **(B)** normalized currents recorded in 0.1 M $TBAPF_6$ acetronitrile solution for 0.5 mM Fc (black dots) and 0.66 mM CPT-11HCl (red dots) at different tip to substrate distance.

The interaction between irinotecan and the immobilized cyclic peptide was investigated at lower concentration, over the range 20 - 300 µM. In this case DPV was employed as the voltammetric technique, so as to increase the sensitivity. This investigation was performed by using SECM in proximity mode. In these experiments the probe was firstly positioned above the substrate at 3 µm distance, by using Fc as redox mediator. Then, the bulk solution was spiked with increasing amounts of CPT-11HCl and voltammetric measurements were performed over the potential window 0 – 1.6 V, such that both the oxidation of Fc and CPT-11HCl could take place. **Fig. 7.20** shows a series of DPVs thus obtained above the MUA-SAM-cyclic peptide (**Fig. 7.20A**) and, for comparison, MUA-SAM (**Fig. 7.20B**).

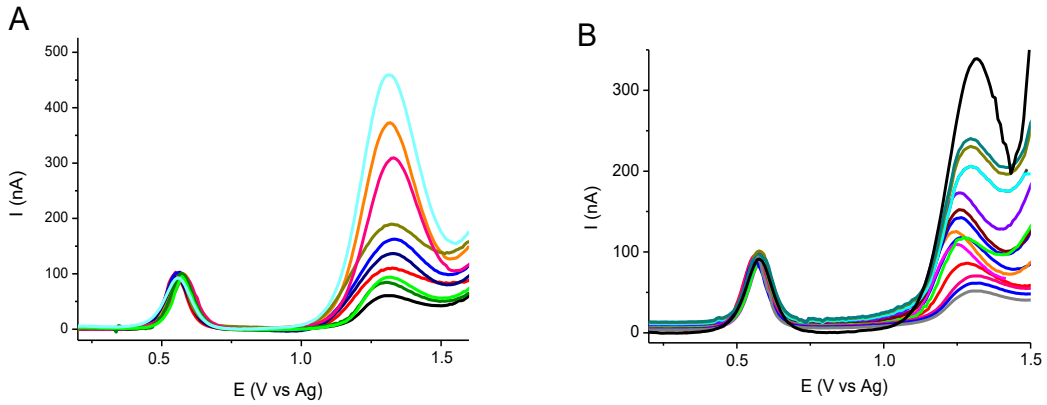

Fig 7.20 - DPVs recorded at 3 µm from peptide-modified substrate (**A**) and peptide-unmodified substrate (**B**) using 0.1 mM of Fc and different concentrations of CPT-11 in CH_3CN - 0.1 M $TBAPF_6$ solutions. DPV parameters were the same used for CPT-11 detection in plasma (see section 5.1).

As is evident, while the Fc peak remained constant throughout the entire series of measurements (because the constant both concentration and tip-to substrate distance), the CPT-11HCl peak increased by increasing its concentration. However, plotting peak current against concentration, different linear trends were observed for the two substrates (**Fig. 7.21**). In particular, above the MUA-SAM-cyclic peptide, higher currents were recorded for CPT-11HCl concentrations ≥ 50 µM, which is congruent with a high CPT-11 concentration at the substrate/solution interface. On the other hand, at lower concentrations, apparently no difference exists on the ability of the two substrate to interact with irinotecan. This could be due to the fact that CPT-11H^+ Cl^- ionic couple is more dissociated, so that only free Cl^- ions are involved in the process; alternatively, it might also suggest that CPT-11HCl interaction with the cyclic peptide is slower at low concentration. In order to prove that this was the case, approach curves as those illustrated above at higher concentrations were constructed.

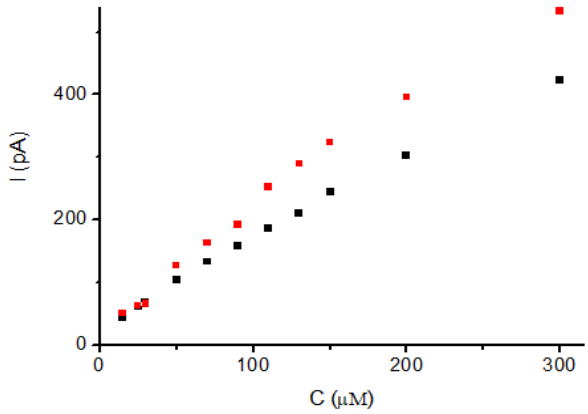

Fig 7.21-Peak currents of different concentrations (from 20 to 300 µM) of CPT-11HCl recorded at a tip to substrate distance of 3 µm. MUA-SAM-cyclic peptide (red dots); MUA-SAM (black dots).

(**Fig 7.22A**) displays DPVs recorded at different tip to substrate distances, and (**Fig 7.22B**) the corresponding approach curve (red symbols). As is evident, under the latter conditions, the approach curve recorded using CPT-11HCl fits the theoretical prediction for pure negative feedback and overlap with that obtained with Fc at all distances. This confirms the lack of accumulation of CPT-11 at the substrate/solution interface.

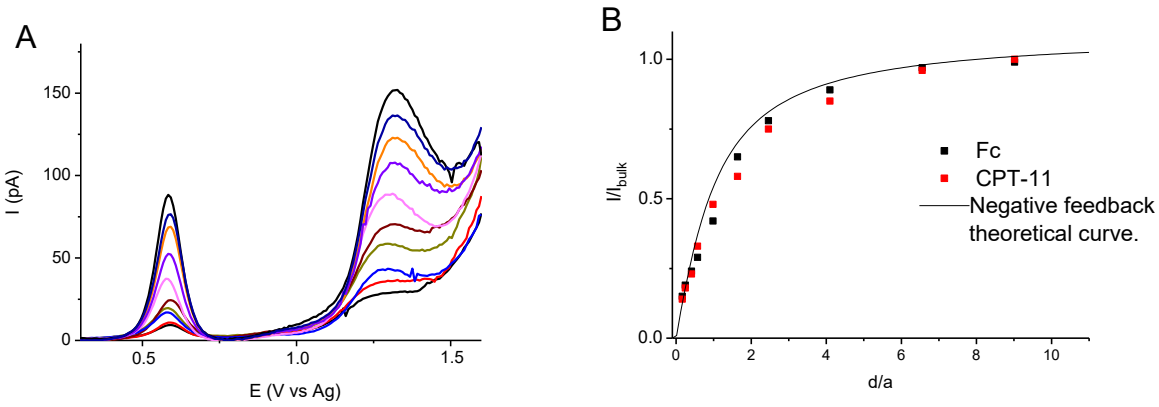

Fig 7.22–(A) DPVs recorded in a 0.03 mM CPT-11HCl, 0.02 mM Fc CH_3CN solution over a peptide modified gold substrate, at different tip to substrate distances.

Fig 7.23 A shows the ratio of peak currents recorded over MUA SAM modified and unmodified with peptides. I_P are the peak currents recorded at 3 µm from substrates containing peptides, I_S are peak currents recorded at 3 µm from substrates not containing peptides.

In order to highlight the effect of concentration on CPT-11HCl accumulation at the MUA-SAM-Cyclic peptide substrate, current data shown from **Fig 7.23** were elaborated in a different

fashion. In particular, as is displayed in **Fig 7.23**, the ratio of peak current at the peptide modified MUA-SAM (*Is*) to that at the unmodified MUA-SAM (*Ip*) are plotted against CPT-11HCl concentration. The experimental points were fitted with a polynomial function (from Origin 8.0), and from it an estimate of the affinity binding in terms of dissociation constant (K_D) of 70 µM was evaluated. To verify the reliability of the latter value, comparative measurements were performed by a classical approach, and in particular using fluorescence spectroscopy. The experiments were performed in a water/acetonitrile solution (i.e., that used to denaturing plasma samples [39]) at a fixed concentration of CPT-11, at which increasing amounts of cyclic peptide were added. Plotting the fluorescence quenching of CPT-11 due to the cyclic peptide against peptide concentration a curve as that displayed in **Fig 7.22**. An affinity constant ($K_{D,}$, i.e., the ligand concentration producing 50% saturation [40]) of 40 µM was found. This values is lower than that found by the SECM approach, yet comparable in terms of order of magnitude. The affinity binding values, found here by SECM and fluorescence spectroscopy compare with those recently reported in the literature for a series of cyclic peptides designed on purpose for irinotecan in aqueous or methanol media (i.e., over the range 20 – 50 µM) [15].

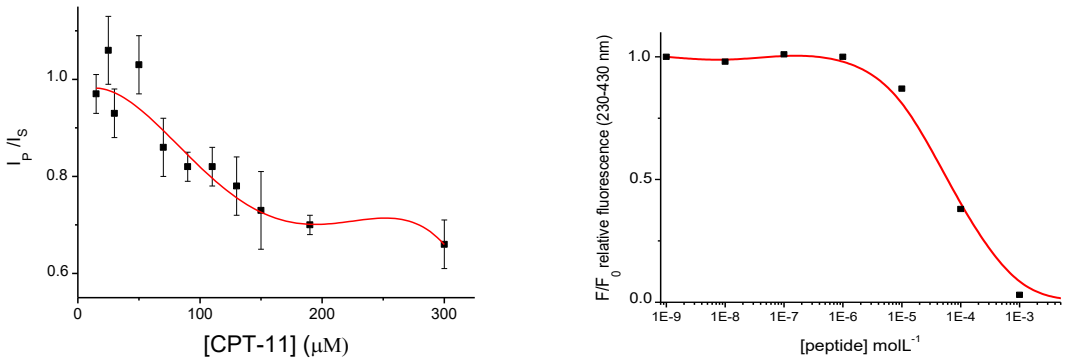

Fig 7.23 – (A) Ratio of the peak currents from DPVs reported in **Fig 7.20** in function of CPT-11HCl concentration. I_P are peak currents measured at the microelectrode put at a distance of 3 µm from the substrate over MUA SAM, at different concentrations of CPT-11HCl. I_S are peak current measured, in identical conditions, over peptides-modified substrate. Error bars refer to 3 replicates. (**B**) – Measurements of fluorescence quenching of 1 µM of CPT-11HCl performed in a CH_3CN/water mixture at increasing concentrations of HK peptide.

Overall, the above SECM results indicate that the affinity of the cyclic peptide employed towards irinotecan is relatively low. This precludes its use, as receptor, for constructing sensors in TDM applications. In fact, the upper limit of the therapeutic window for CPT-11 is about 8 µM. On the other hand, the novel SECM approach presented here can be used to investigate the interaction between other guests and receptors immobilized onto solid (either conducting or

insulating) substrates. The latter types of platforms can be employed for one-shot solid state sensors for the detection of a variety of analytes.

References

[1] Z. Iskierko, K. Noworyta, P.S. Sharma, Biosensors and Bioelectronics 109 (2018) 50–62.

[2] S. van Dun, C. Ottmann, L. Milroy, L. Brunsveld, Journal of the American Chemical Society 139 (2017) 13960-13968.

[3] C. Lee, M. Maestre-Reyna, K. Hsu, H. Wang, C. Liu, W. Jeng, L. Lin, R. Wood, C.C. Chou, J.M. Yang, A.H.J. Wang, Angewandte Chemie, Int. Ed. 53 (2014) 13054.

[4] D. Zheng, D.Y. Fu, Y. Wu,Y.L. Sun, L.L. Tan, T. Zhou, S.Q. Ma, X. Zha, Y.W. Yang, Chemistry communications 50 (2014) 3201.

[5] P.B. Crowley, P. Ganji, H. Ibrahim, ChemBioChem 9 (2008) 1029.

[6] S.H. Joo, Biomolecules and Therapeutics 20 (2012) 19-26.

[7] A. Ulman, Chemistry Reviews 96 (1996) 1533.

[8] P. K. Ferrigno Essays In Biochemistry 60, (2016) 19–25.

[9] Q. Liu, J. Wang, B. J. Boyd, Talanta 136 (2015) 114–127.

[10] K.Y. Tomizaki, H. Mihara, J. Mater. Chem. 15 (2005) 2732–2740.

[11] H. Lankinen, T. Heiskanen, L. Kaikkonen, A.A. Alitalo, K. Hedman, S. Meri, Journal of Peptide Sciences 10 (2004) 251-261.

[12] B. Claro, M. Bastos, R. Garcia-Fandino, Peptide Applications in Biomedicine, Biotechnology and Bioengineering 1 (2018) 87-129.

[13] C. Li, X. Chen, F. Zhang, X. He, G. Fang, J. Liu, S. Wang, Analytical Chemistry 89 (2017), 10431–10438.

[14] I. Gladich, A. Rodriguez, R.P.H. Enriquez, F. Guida, F. Berti, A. Laio, The Journal of Physical Chemistry B 8 (2015) 12963-12969.

[15] F. Guida, A. Battisti, I . Gladich, M. Buzzo, E. Marangon, L. Giodini, G. Toffoli, A. Laio, F. Berti Biosensors and Bioelectronics 100 (2018) 298-303.

[16] D. Samanta, A. Sarkar, Chemical Society Reviews 40 (2011) 2567-2592.

[17] P.S. Banerjee, P. Ostapchuk, P. Hearing, I. Carrico, Journal of the American Chemical Society 132 (2010) 13615–13617.

[18] E. Reimhult, F. Höök, Sensors 15 (2015) 1635-1675.

[19] D. Zigah, M. Pellissier, B. Fabre, F. Barriere, P. Hapiot, Journal of Electroanalytical Chemistry 628 (2009) 144−147.

[20] S. Evans, K. Brakha, M. Billon, P. Mailley, G. Denuault, Electrochemistry Communications 7 (2005) 135-140.

[21] W. Song, Z. Yan, K.Hu, Biosensors and Bioelectronics, 38 (2012) 425-429.

[22] M.J. Fischer, Methods in Molecular Biology 627 (2010) 55-73.

[23] J.C. Love, L.A. Estroff, J.K. Kriebel, R.G. Nuzzo, G.M. Whitesides, Chemistry Reviews 105 (2005) 1103-1169.

[24] F. Cecchet, M. Marcaccio, M. Margotti, F. Paolucci, S. Rapino, P. Rudolf, Journal of Physical Chemistry B 110 (2006) 2241-2248.

[25] C. Cannes, F. Kanoufi, A.J. Bard, Langmuir 18 (2002), 8134-8141.

[26] S. Campuzano, R. Galvez, M. Pedrero, F.J.M. de Villena, J.M. Pingarro´n, Journal of Electroanalytical Chemistry 526 (2002) 92-98.

[27] M.M. Walczak, D.D. Popenoe, R.S. Deinhammer, B. D. Lamp, C. Chung, M. D. Porter, Langmuir 11 (1991) 2687-2693.

[28] X. Xiao, H. Li, M. Wang, K. Zhang, P. Si, Analyst 139 (2014) 488-494.

[29] M.R. Anderson, R. Baltzersen, Journal of Colloid and Interface Sciences 263 (2003) 516-521.

[30] A.H. Suroviec, The Chemical Educator 17 (2012) 83-85.

[31] N. Xia, Y. Xing, G. Wang, Q. Feng, Q. Cheng, H. Feng, X. Sun, L. Liu, International Journal of Electrochemical Sciences 8 (2013) 2459-2467.

[32] A.J. Bard, M.V. Mirkin, Scanning Electrochemical Microscopy, M. Dekker, New York, (2001).

[33] K.A. Groat, S.E. Creager, Langmuir 9 (1993) 3668–3675.

[34] S. Casalini, C.A. Bortolotti, F. Leonardi, F. Biscarini, Chemical Society Reviews 46 (2017) 41-70.

[35] M.R. Anderson, M.N. Evaniak, M. Zhang, Langmuir 12 (1996) 2327-2331.

[36] B. Liu, A.J. Bard, M.V. Mirkin, S.E. Creager, Journal of American Chemical Society 126 (204) 1485-1492.

[37] K. Slowinski, R.V. Chamberlain, C.J. Miller, M. Majda, Journal of American Chemical Society 119 (1997) 11910.

[38] M.V. Mirkin, A.J. Bard, Journal of Anaytical Chemistry 64 (1992) 2293-2998.

[39] M.J. Hilton, K.V. Thomas, Journal of Chromatography A 1015 (2003) 129-41.

[40] J. P. Landry, Y. Ke, G. Yu, X.D. Zhu, Journal of Immunological Methods 417 (2015) 86-96.

7.2 Dual soft probes for simultaneous sensing of two chemical properties with Scanning Electrochemical Microscopy

7.2.1 Soft probes applications in SECM

The most common probes used in SECM, as already mentioned in previous chapters and sections, are amperometric microelectrodes, produced, typically, by sealing metal wires of micrometer or sub-micrometer diameters in glass capillaries and, subsequently, exposing the cross-section, which include both active surface and surrounding insulator, by grinding and polishing [1-5]. These kinds of probes allows, monitoring one chemical characteristic, often buried within or mixed with topographic characteristics of the surface under investigation. Complementary information on topography and local reactivity could be obtained by combining SECM with other scanning probes techniques, such as AFM [6-10]. Also, simultaneous information on different substrate properties can be gathered using multiple SECM probes, in which one electrode is used for the determination of tip-to substrate distance (and then the surface topography) and the others for monitoring chemical properties [11]. Other examples include vertical tip-position modulation, in which the probe can be vertically vibrated; vibration is damped in close proximity to the sample surface, thus allowing to control the probe-substrate distance [12]. Non-electrochemical distance information can also be obtained by shear-force measurements [13].

Recently, soft microelectrodes for SECM applications were introduced. These work in a peculiar contact mode, sliding on the target substrate, thus allowing discriminating between electrochemical signal variations, due to topographic or feedback effects [14-22]. Soft probes are extremely suited for investigating large and irregular samples (e.g. curved or soft surfaces). In this context, they were employed to investigate biological samples, such as tissues and cells, as diagnostic tools for a variety of illnesses [16-18].

Local pH changes and reactive nitrogen species (RNS) such as nitric oxide (NO), nitrite ion (NO_2^-), peroxynitrite (ONO_2) play an important role in cancer [23-25]. The development of a sensor for their simultaneous detection would therefore be of great interest. This section reports the results concerning the development of a dual soft probe, made of two parallel, individually addressable microelectrodes, able to detect, at substrate/solution interfaces, both pH and RNS simultaneously with high spatial resolution. Although double probes for SECM measurements have been reported in the literature (see for instance [26-29]), those developed herein have the

advantage, in addition of being soft constant distance mode tools for tissues, of being easily constructed, easy to use and the procedure for their preparation allows the integration of different electrode materials. The presented approach uses UV curable dielectric inks to embed and fix metal wires and carbon fibresto the flexible soft probe support.

7.2.2 Preparation and voltammetric characterization of dual soft probes

The soft probes fabricated here follow a novel procedure, which, at variance of the previous already available approaches, allows obtaining multiple, independently connected probes made of different materials. The fabrication procedure is outlined in **Scheme 7.4A**. Two fibers of the desired metals (here, fibers of Pt and Au, 25 µm and C, 8 µm diameter) are placed on the surface of a PET foil (5 cm long x 1 cm wide, 180 µm thick) and fixed at one side by adhesive tape. They were then rinsed with isopropanol and left to dry at room temperature for about 10 min. 2-4 µL of UV curable dielectric ink EMD-6200 (SunChemical) was dropped on the wires. This was followed by placing temporarily a PET cover foil gently on top, resulting in the adsorption of the PET foil with the UV curable ink spreading over the PET surface to cover an almost rectangular surface area of about 1 cm^2. The ink was then cured for 5 min under a UV lamp. Afterward, the PET protection foil was removed, leaving the fibers embedded in the insulating ink. Its thickness, determined by a digital micrometer, typically ranged between 25 and 35 µm and depended to the volume of ink placed initially on the PET foil. External electric connections were made by silver epoxy, which was cured in oven at 80°C for about 3 hours. The cross section was exposed by a razor blade cutting, thus defining the two disk shaped active areas. The optical image of a Pt-Au dual soft probe thus fabricated is shown in **Scheme 7.4B**, while a laser scanning microscope image of the cross section, displaying the Pt and Au microdisks, is shown in **Scheme 7.4C**.

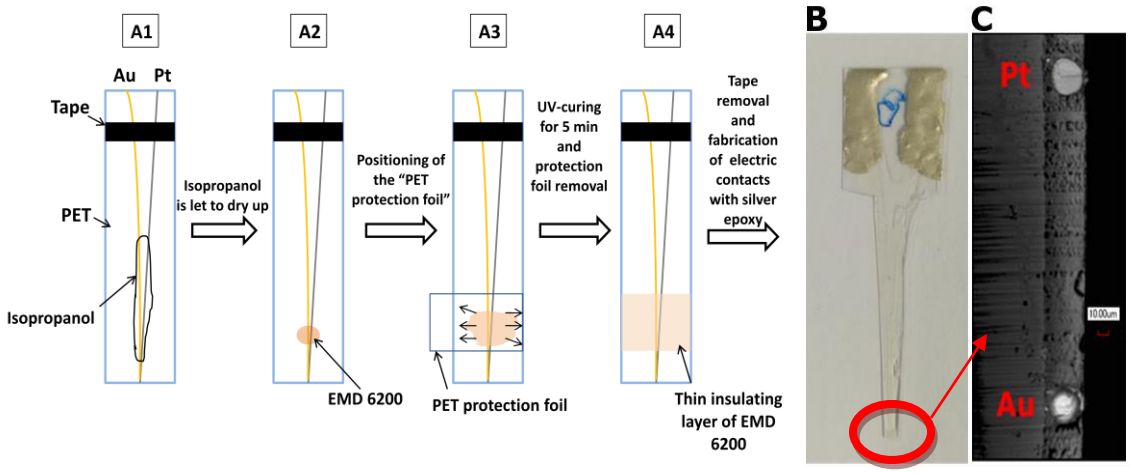

Scheme 7.4- (**A1-A4**) Manufacturing of a soft Au-Pt double probe. (**B**) picture of the soft probe. (**C**) Cross section of the soft probe.

The quality of the cross section was evaluated to a greater detail for a variety of dual probes, prepared as described above, to optimize the various steps, including the amount of ink, the way how to expose the cross section. The latter is a critical step, as it could damage the active surface area or make very irregular the cross-section size. **Fig 7.24** shows the laser scanning microscope image of a good cut, where the microdisks are well defined. It was verified that good cuts occurred when the razor blade impacted the PET sheet first; this avoided damage of the EMD-6200 insulation. In adverse situations, the insulating ink surrounding the metal fibers could form cracks (not shown).

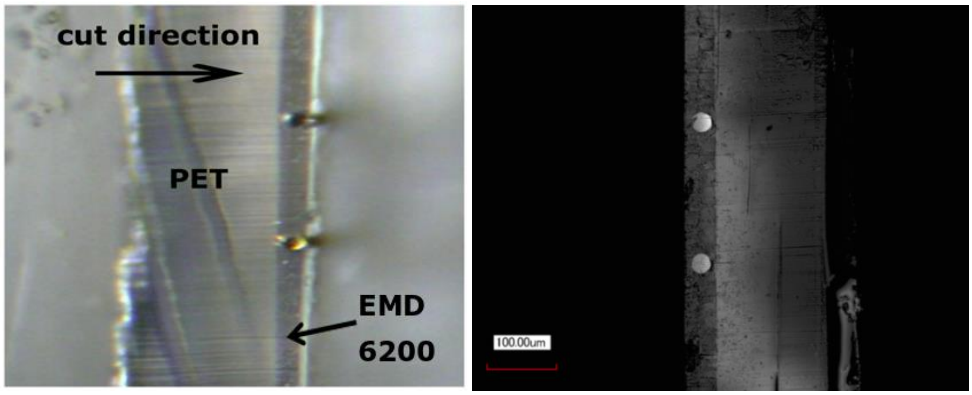

Fig 7.24–Laser scanning microscope images of the cross sections of dual soft probesafter the razor blade-cut: (**left**) Pt-Au optical micrograph ; (**right**) Pt-Pt laser micrograph.

Fig 7.25 shows top views and cross sections of a well constructed dual Pt-Au soft probe.

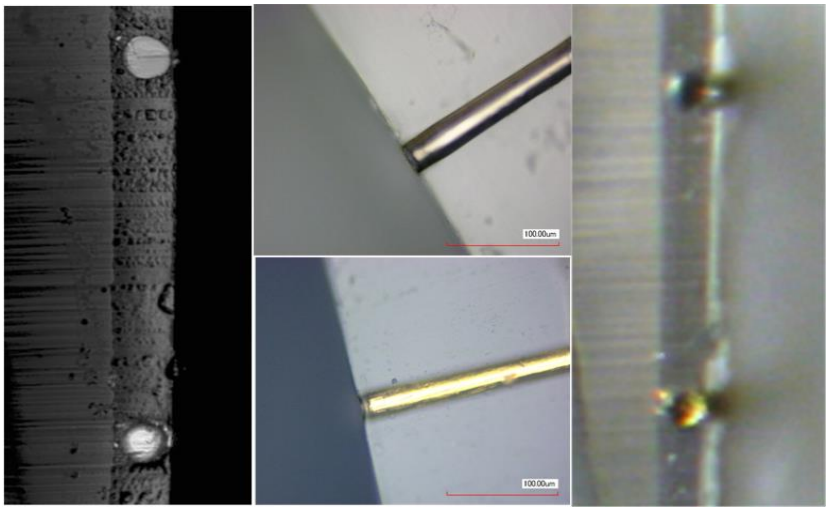

Fig 7.25-other microscope images of a dual Au-Pt electrode. Wires have Ø = 25 µm.

The thickness of the insulation layer could be modified by changing the volume of the ink droplet placed on PET; examples of probes having different insulating thicknesses are shown in

Fig 7.26. It was verified that, when the thicknesses of the insulating layer were was between 20 and 35 µm, they appeared quite well defined, flat and homogeneous. As for the electrodes inter-distance, it typically varied between 180 and 250 µm. This avoided overlapping of diffusion layers of the two-electrode system [31].

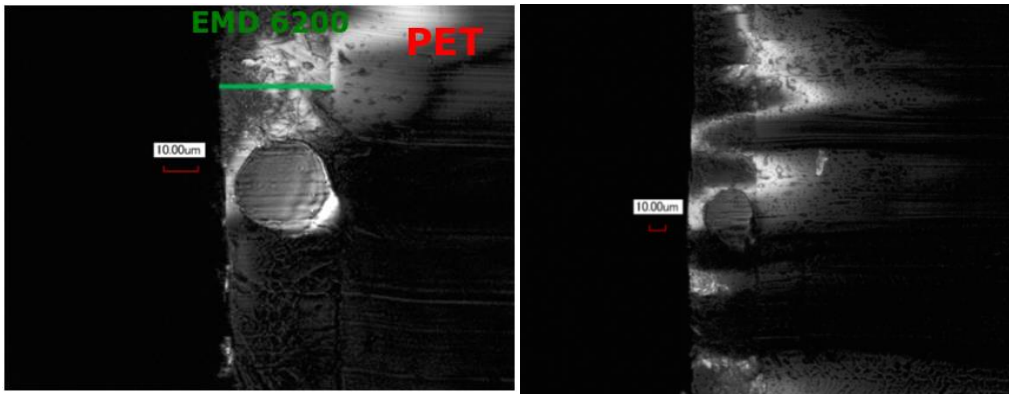

Fig 7.26-Two platinum electrodes having insulation layers of EMD 6200 thicknesses of 27 (left) and 35 (right) µm.

The dual probes, once prepared, were characterized by steady-state voltammetry in an aqueous solution containing 1 mM FcMeOH and 0.1 M KNO_3, as supporting electrolyte, as well as by optical observations. **Figs. 7.27 -7.29** show typical CVs at low scan rate (**Figs. 7.27A -7.29A**) and optical images of relevant soft the probes employed (**Figs. 7.27B -7.29B**).

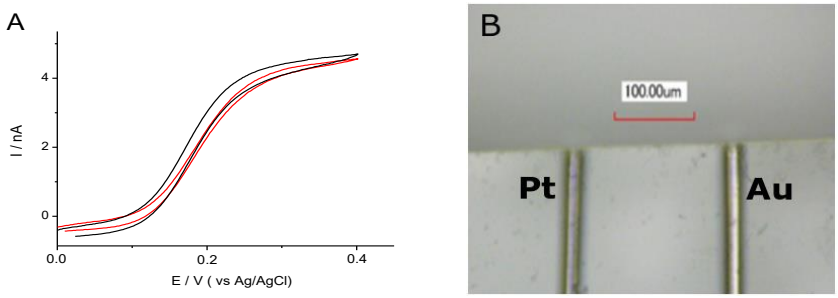

Fig 7.27- (A) CVs recorded at a Pt (black line)-Au (red line) dual probe in 1 mM FcMeOH, 0.1 M KNO_3 aqueous solution, at 20 mV/s. **(B):** top view of the probe.

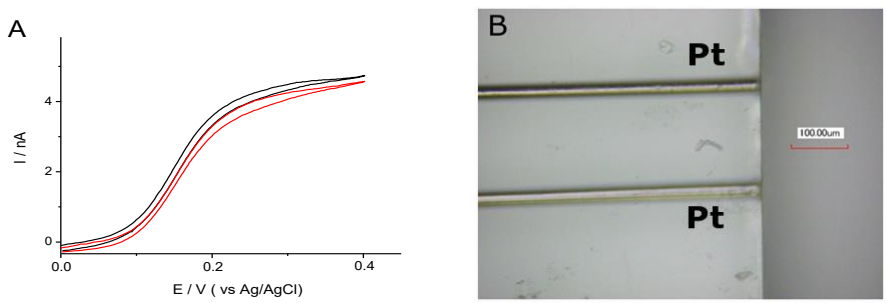

Fig 7.28- (A) CVs recorded at a Pt-Pt dual probe in 1 mM FcMeOH, 0.1 M KNO_3 aqueous solution, at 20 mV/s. (**B):** top view of the probe.

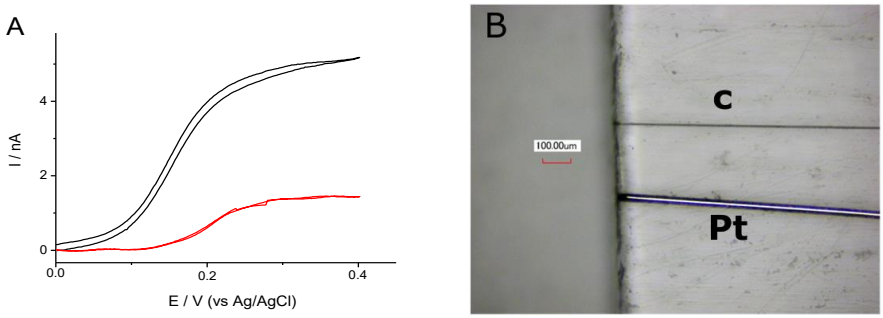

Fig 7.29- (A) CVs recorded at a dual Pt (black line)–C (red line) soft probe in 1 mM FcMeOH, 0.1 M KNO_3 aqueous solution, at 20 mV/s. (**B):** top view of the probe.

The voltammetric parameters, steady-state limiting current (I_{exp}) and Tomes parameter ($E_{3/4} - E_{1/4}$, see section 3.2) for the various dual-soft probes prepared are summarized in **Table 7.1**. Theoretical values, expected for diffusion limiting current at an inlaid microdisk embedded in an infinite insulating plane (i.e., those predicted by *eq16* , Chapter 3), are also included. From the table it is evident that, in general, experimental current values are larger than expected. This is due to the thin insulation sheath around half the microdisk geometry, which induces diffusion from behind the plane of the electrode, thus enhancing the flux (and consequently the current) to the inlaid disk [32, 33]. Instead, the Tomes parameter, for all the investigated soft probes, compares well with 56.3 mV, theoretical value expected for a reversible one-electron process at 25°C for either thin or thick insulating sheaths [32, 33].

Table 7.1- Steady state currents recorded at soft probe microelectrodes having different thicknesses of insulating layer. Pt and Au electrodes had a = 12.5 µm, graphite (C) electrodes had a = 4 µm.

Electrode material	Thickness of insulating layer (µm)	I_t (nA) (1)	I_{exp} (nA)(2)	I_{exp}/I_t	$(E_{3/4} - E_{1/4})$(3)(mV)
Pt	27	3.46	4.11	1.19	59
Au	27	3.46	4.05	1.17	58
C	27	1.11	1.22	1.05	61
Pt	29	3.46	3.88	1.13	57
Au	29	3.46	3.97	1.15	58
C	29	1.11	1.13	1.02	59
Pt	35	3.46	3.57	1.03	60
Au	35	3.46	3.54	1.02	59
C	35	1.11	1.09	0.99	62

(1) Theoretical current expected for an inlaid disk microdisk

(2) Experimental values.

(3) Experimental Tomes parameter. Theoretical value at 25 °C = 56 mV.

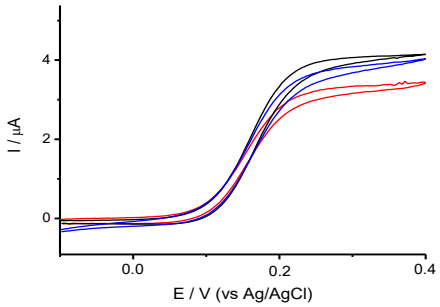

Fig 7.30- steady state voltammograms recorded in 1 mM FcMeOH solution at soft microelectrodes with different insulation layer thickness (determined with optical microscope). Black = 27 µm. Blue = 29 µm. Red = 35 µm.

7.2.3 Characterization of the dual soft probes by SECM

The dual soft probes above fabricated were also tested by using SECM. Primarily, approach curves over either insulating or conducting surfaces were recorded. To this purpose, the probes were fixed in a home-made holder (**Scheme 7.5A** and **Fig 7.31A**), with a variable inclination angle between the probe and the surface normal of the substrate (**Scheme 7.5** and **Fig 7.31**). This to pre-setting the bending direction of the probe, which was an important aspect for ensuring a good current contrast during SECM imaging in contact mode (**Scheme 7.5B** and **Fig 7.31B**). For SECM imaging, a lift-off routine was applied to retract the probe into the bulk solution during reverse scanning, in order to avoid probe over-bending and strong mechanical forces to the probe, as well as to the sample.

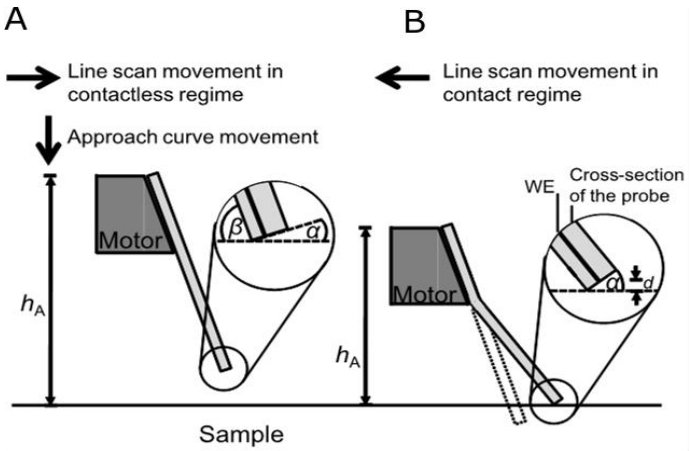

Scheme 7.5- scheme of typical working mode of soft probes: (**A**) while approaching the surface; (**B**) while scanning across the surface. Schematic adapted from [22].

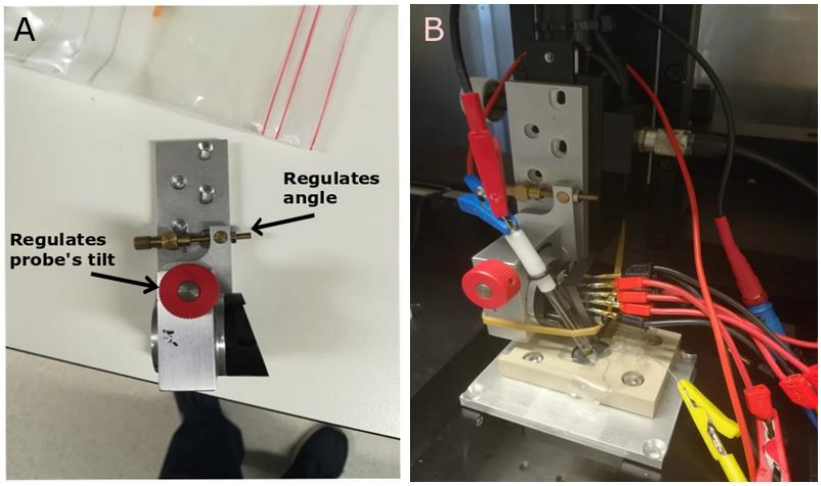

Fig 7.31-SECM apparatus details: **(A**) holder for soft probes; (**B**) setup of electrochemical cell used to perform measurements.

Typical approach curves recorded with a Pt-Au (both microdisks were 25 µm in diameter) dual probe are shown in **Fig 7.32**. For comparison, theoretical approach curves for microdisk tips, RG = 2, are also included. As it can be seen, approach curves obtained with the two types of probes differ to a substantially extent. In particular, with the soft probe, currents flatten upon the probe starts touching the substrate. Also, maximum or minimum currents and slopes of the ascending or descending parts of the positive and negative feedback approach curves, respectively, are different. These reflect the different recycling or hindering mass transport conditions that apply to the dual probes geometry. In fact, both recycling and blocking effects of the redox mediator towards the electrode surface are less effective. It must be considered that no theory was developed for these kinds of probes, this because too many geometrical variables are involved (e.g. tilt angle, asymmetries in the insulation layer), which makes theory difficult to include in simple relationships.

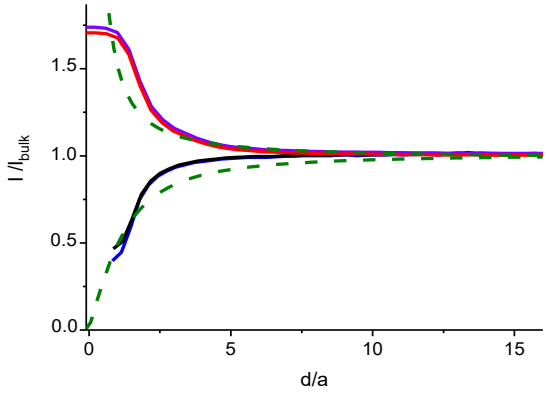

Fig 7.32 Typical approach curves over a glass slide (black and blue lines) and over a glassy carbon electrode (red and violet lines) recorded at a Pt-Au dual probe in 1 mM FcMeOH, 0.1 M KNO_3 solution. The probes were held at +0.3 V vs Ag/AgCl. Green dashed lines are theoretical approach curves for a microdisk electrode having RG = 2.

The thickness of the insulation layer proved to have a role both in the steady state current measured at the electrodes (see above) and in the shape of the approach curves. In **Fig 7.33** approach curves recorded either over insulating (**Fig 7.33A**) or conducting (**Fig 7.33B**) substrates, recorded at electrodes having different thicknesses of insulating layer, are displayed. As is evident, the smaller the thickness the lower is the feedback. This is, again, expected, due to the partial thin shield diffusion effect [32-34].

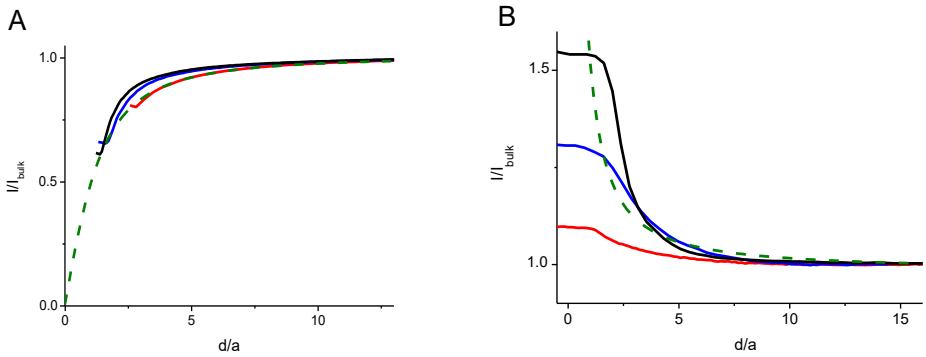

Fig 7.33- Approach curves recorded over a glass slide (**A**) and over a Glassy Carbon Electrode (**B**) with a Pt-Au soft probe with different insulating thickness (Black = 27 µm. Blue = 29 µm. Red = 35 µm) in 1 mM FcMeOH, 0.1 M KNO_3 solution. The probes were held at +0.3 V *vs.* Ag/AgCl. Green dashed lines: theoretical for an inlaid microdisk with RG = 2.

7.2.3.1 Dual soft probes for imaging

The performance of the soft probes for imaging was tested above different arrays of mixed conducting/insulating samples (each conducting spot of size hundreds of microns) prepared by the inkjet-printing approach onto a PET surface as described previously (Section 5.4). SECM

images were recorded in 0.1 M KNO_3 aqueous solutions and using FcMeOH as redox mediator. A typical SECM image, obtained with a Pt-Pt soft probe over an inkjet printed CNTs electrode, is displayed in **Fig 7.34A**. This image is contrasted with that obtained by a laser scanning microscope (**Fig 7.34B**). As is evident, SECM image is able to better define the CNTs and AgNPs conducting zones.

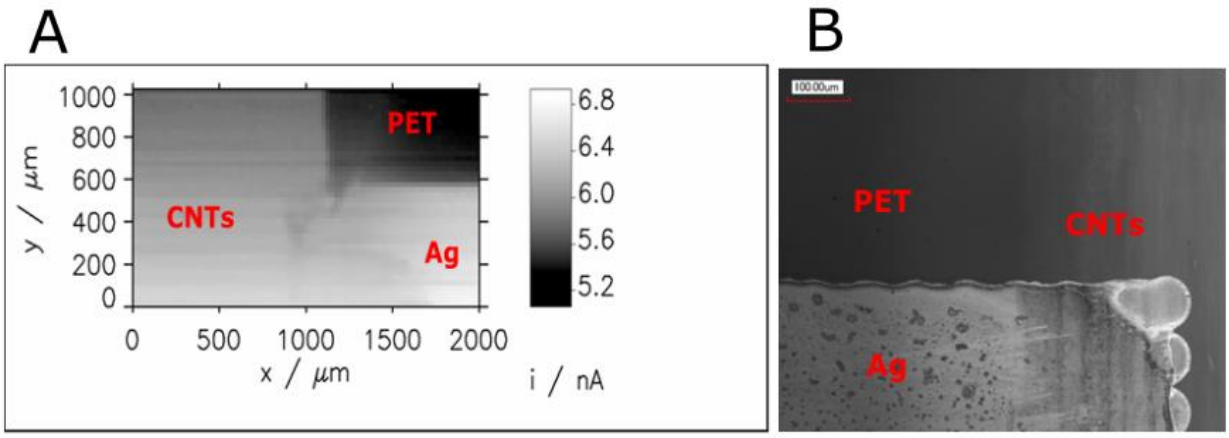

Fig 7.34- (**A**) Map recorded over an inkjet printed electrode (see section 5.3) with a Pt soft probe in 1 mM FcMeOH, 0.1 M KNO_3 solution. The probe was held at +0.3 V vs Ag/AgCl. Substrate was unbiased. Scan recorded at 200 μms^{-1}. (**B**) Microscope image of the analyzed area of an inkjet printed electrode.

The dual Pt-Au soft probe was employed to image, by both linear and two dimensional scans, silver micro-bands patterned on a PET substrate. **Fig 7.35** shows the laser scanning microscope image (**Fig 7.35A**) and line scans (**Fig 7.35B**) obtained with the two microelectrodes included in soft probe. **Fig 7.36** shows the corresponding 2D image.

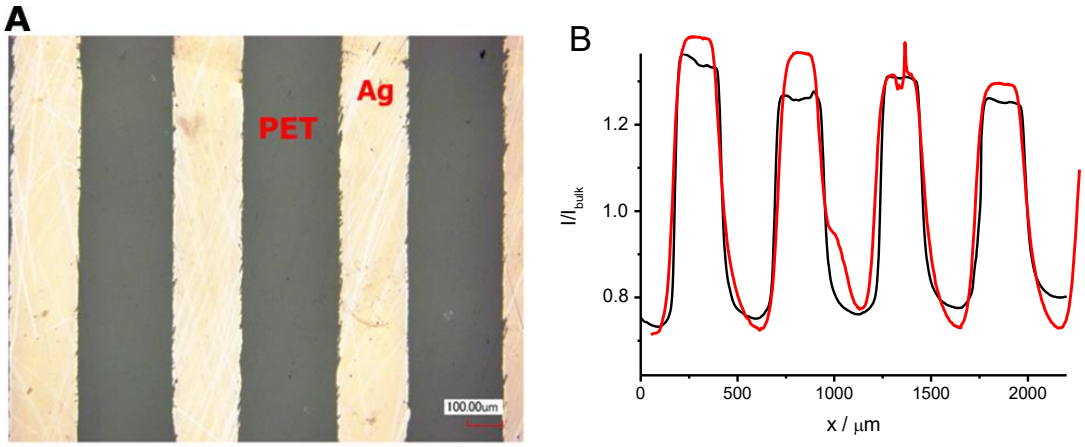

Fig 7.35-(**A**) microscope image of ink-printed silver line pattern. (**B**) Linear scans recorded over the pattern in 1 mM FcMeOH 0.1 M KNO_3 solution.

The size of the silver bands are clearly affordable with the SECM probes. Moreover, inhomogeneous conducting zones can be clearly revealed by the latter imaging approach. Small

differences in the current values obtained at the two microdisks can be due to either small irregularities of the insulating layer or the tilting of the probe with respect to the substrate.

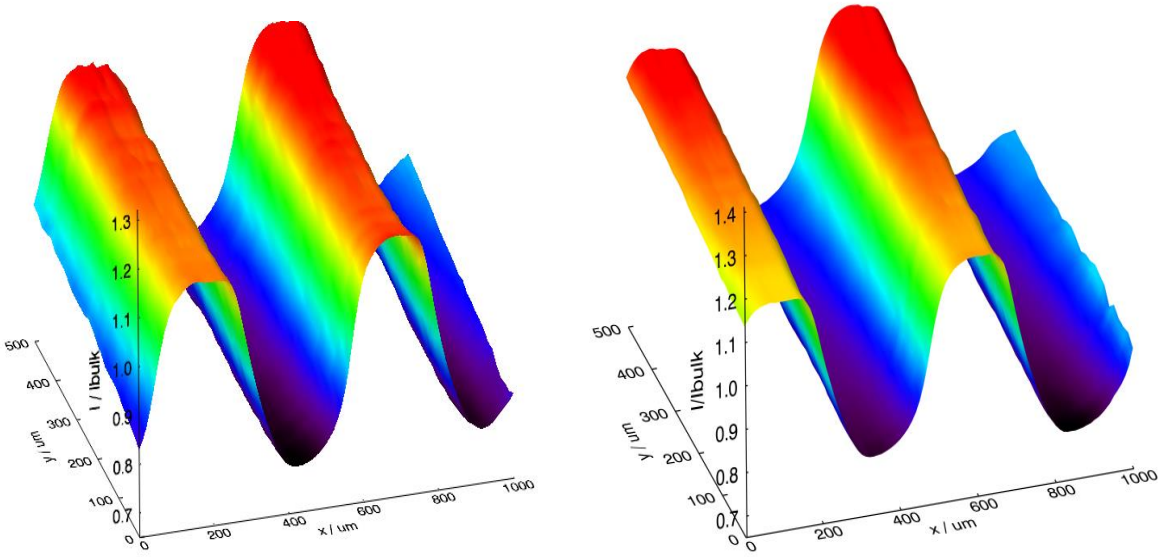

Fig 7.36 –2D scans recorded over silver lines pattern in a 1 mM FcMeOH, 0.1 M KNO_3solution, using a dual Au-Pt soft probe.

The Pt-Au soft probe was further employed to image arrays of disk-shaped Ag micro-patterns produced by inkjet printing. Drying of inkjet printed spots often leads to the well-known coffee ring effect, which originates from the different evaporation rates of the solvent across the drop [35]. This phenomenon leads solute, within a solution, to move towards the boarder, thus depleting the center of drop. Because of this, the conductivity in the center of the printed Ag spots can be lower, due to a critical Ag layer thickness.

Fig 7.37 shows the laser scanning microscope image, while **Fig 7.38** shows the corresponding 2D images obtained with the two microelectrodes.

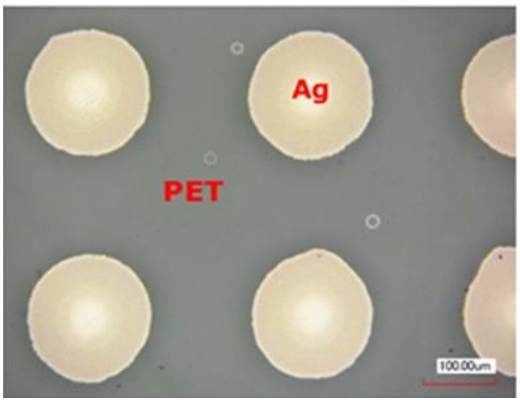

Fig 7.37-microscope image of ink-printed silver dot pattern.

The current decrease at the center of each droplet can be clearly seen in 2D scans (**Fig 7.38**).

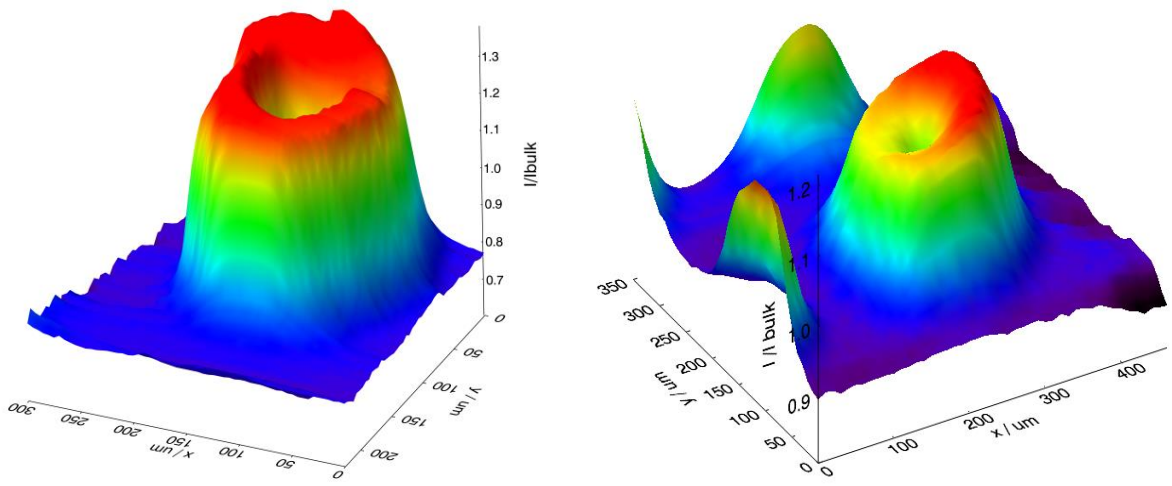

Fig 7.38 – SECM images recorded over silver dots pattern in a 1 mM FcMeOH, 0.1 M KNO_3 solution, using a dual Au-Pt soft probe.

7.2.4 Dual soft probes as potentiometric-amperometric sensor

The dual soft probes employed in this section integrate two microelectrodes of Pt and Au. The platinum microdisk was coated with a layer of platinum black for the amperometric detection of RNS; the gold microdisk was coated with iridium oxides for the potentiometric monitoring of pH. This configuration, combining amperometric and potentiometric detection approaches, avoids mutual perturbation of the local chemical environment, as the potentiometric part acts as a passive probe [2].

The Pt microelectrode was coated with a layer of Pt-black to increase its catalytic activity towards RNS [36-38].

The Au microdisk was coated with IrOx to exploit their sensitivity towards pH changes. In fact, the potential of the Ir(IV)/Ir(III) system peaks (see experimental) depended on pH due to the following redox process that governs the potentiometric response of the IrO_x electrode [39, 40]:

$$2[IrO_2(OH)_{2-x}(2+x)H_2O]^{(2-x)-} + (3-2x)H^+ + 2e^- \rightleftharpoons [Ir_2O_3(OH)_{3-x}(3+x)H_2O]^{(3-x)-} + 2H_2O \qquad \textbf{1}$$

Because of this complex dependence of the redox potential on H^+ concentration, the IrO_x sensor may display a super-Nernstian pH response, with slopes varying from -59 to -90 mV per pH unity, at room temperature [41]. The dependence of the IrOx prepared here was preliminary assessed by measuring potential values at open circuit (OCP) in 0.1 $molL^{-1}$ $HPO_4^{2-}/H_2PO_4^-$ solutions at different pH values in the range 3 to 7, adjusted by addition of HNO_3 or NaOH solutions. Typical OCP responses obtained as a function of time are shown in **Fig 7.39**. The

calibration plot (**Fig 7.39B**) provided a slope of 61 mV/-logH^+. This value is within the range of other reported IrOx electrodes [29, 42, 43].

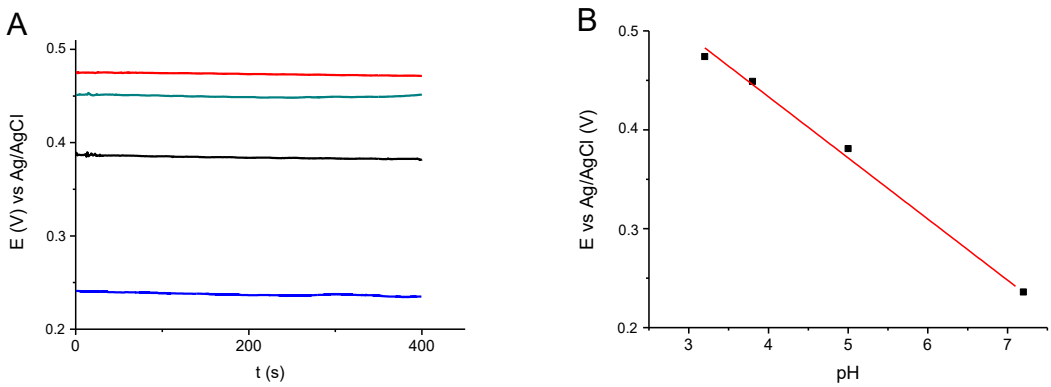

Fig 7.39 – (A) OCP vs time recorded at different HNO_3 concentrations (from 0 to 5 x 10^{-4} M), in 0.1 M KNO_3 solutions. (**B**) OCP vs pH diagrams, related to values of **Fig 7.39A**.

7.2.4.1 Monitoring silver corrosion products using dual potentiometric-amperometric soft probe

As a proof of concept, the simultaneous SECM monitoring of NO and pH was established above an Ag inkjet printed line (about 250 µm wide), printed on PET, submerged in a diluted HNO_3 solution (0.2 mM), left to corrode spontaneously, following the overall process [44, 45]:

$$3\,Ag + 4HNO_3 \rightarrow 3AgNO_3 + 2H_2O + NO \qquad \textbf{2}$$

In the presence of oxygen, other RNS species can be formed according to the following reaction pathways [46]:

$$NO + O_2 \rightleftharpoons ONOO^{\cdot} \qquad \textbf{3}$$

$$ONOO^{\cdot} + NO^{\cdot} \rightarrow ONOONO \qquad \textbf{4}$$

$$ONOONO \rightarrow 2NO_2^{\cdot} \qquad \textbf{5}$$

$$NO_2^{\cdot} + NO^{\cdot} \rightarrow N_2O_3 \qquad \textbf{6}$$

$$N_2O_3 + H_2O \rightarrow 2NO_2^- + 2H^+ \qquad \textbf{7}$$

Reactions ***4-6*** are very fast and provide species whose lifetime is very short [46]. Therefore, the specie which can be detected with the approach and resolution time of the technique employed here are $ONOO^-$, NO, NO_2^-. For the latter, $E_{/2}$ values (*vs.* Ag/AgCl) are available in the literature, corresponding to -0.12 V, 0.2 V and 0.68 V for $ONOO^-$, NO, NO_2^-, respectively [47]. Therefore,

at 0.85 V, i.e., the potentials employed in the experiments described below, performed under aerated solutions, all the above sufficiently stable species can be oxidized.

The overall spontaneous Ag corrosion (as described by reactions ***2-7***) involves therefore a change of both pH and of RNS, which can be monitored by SECM across the Ag band surface (**Fig 7.40**).

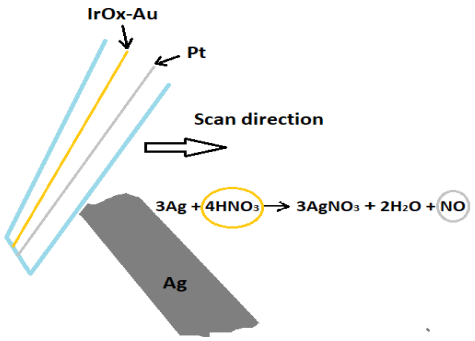

Fig 7.40- Scheme of the method used for simultaneous local measurement of pH and RNS oxidation current over the Ag pattern during its corrosion in presence of HNO_3.

In the measurements, a bipotentiostat was employed. The Pt microelectrode was kept at +0.85 V vs. Ag/AgCl, at which RNS oxidation occurs at diffusion controlled rate [38], while the IrO_x-modified microelectrode was kept at open circuit and reflected the change of H^+ activity. The suitability of the above potential value for the detection of RNS was verified in preliminary tests made on the silver band immersed in the dilute HNO_3 solution. The potential applied to the Pt-black was varied from 0.6 to 0.85 V and line scans were performed. As is shown in **Fig 7.41A**, at 0.6 V only background current was recorded; above the latter potential, currents increased and at 0.85 V levelled off. Correspondingly, the OCP at the IrOx-Au changed sensibly (from 0.458 (± 0.005) to 0.374 (± 0.005) V, see **Fig 7.41B**), indicating a simultaneous decrease of H^+ activity (about 1.3 pH unit), in agreement with the occurrence of reaction ***2***.

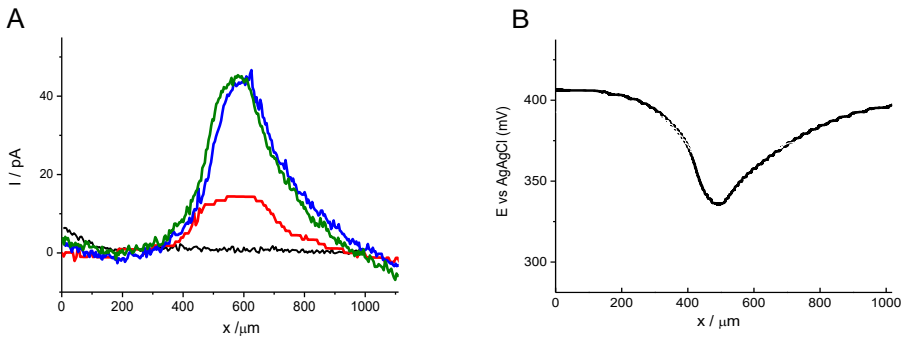

Fig 7.41 (A)-Line scans (baseline subtracted) over the Ag line pattern recorded at platinized Pt electrode at which potentials of +0.6 V (black line), +0.7 V (red line), +0.8 V (blue line), + 0.85 V (green line) *vs.* Ag/AgCl were applied. (**B**)- Line scans recorded at the same time at IrOx-Au electrode. Probe translation speed: 5 μms^{-1}.

Control experiments were performed with the Ag band immersed in the neutral 0.1 M KNO_3 electrolyte, where corrosion of Ag should be negligible or proceed to a much slower extent. **Fig 7.42** shows current and OCP changes observed under the latter conditions, while the soft probe was linearly scanned on the Ag surface. As is evident, only background current was recorded at the Pt-black, while a small, yet significant OCP variation (corresponding to about 0.2 pH unit) was observed. This is conceivably due to a slow corrosion of the Ag, such that the RNS amount generated is below the detection limit of Pt-black sensor. Instead, the IrOx-Au sensor possessed a higher sensitivity towards pH changes.

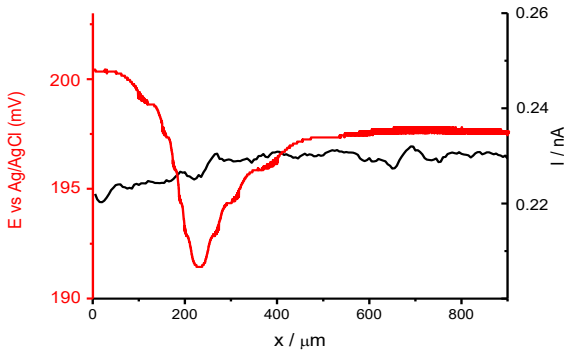

Fig 7.42- Potentiometric (red) and amperometric (black) responses recorded performing a line scan over Ag pattern at the dual (Au-IrOx)-Pt probe in a 0.1 M KNO_3 aqueous solution. Probe translation speed: 5 μms^{-1}.

The simultaneous monitoring of RNS and pH was then tested in the 0.2 mM of nitric acid and **Fig 7.43** shows the simultaneous current and OCP changes recorded. Current and OCP vary, as expected, giving minimum and maximum values almost in the same location.

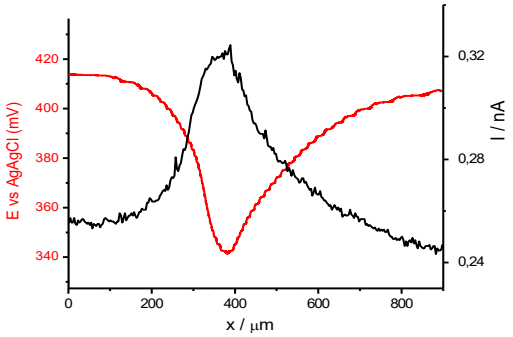

Fig 7.43- Potentiometric (red) and amperometric (black) responses recorded performing a line scan over Ag pattern at the dual (Au-IrOx)-Pt probe in a 2×10^{-4} M HNO_3, 0.1 M KNO_3 solution. Probe translation speed: 5 μms^{-1}.

OCP values, interpolated in the pH calibration curve, provided data displayed in **Fig 7.44**, where they are contrasted with current data of the Pt-black electrode.

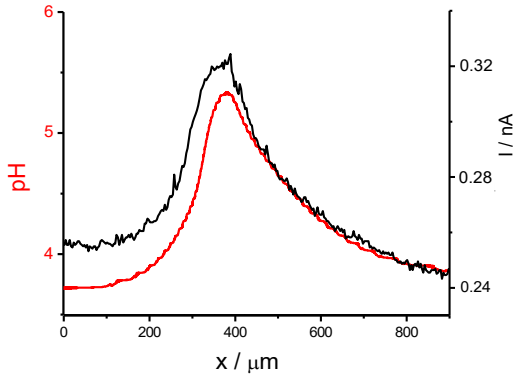

Fig 7.44- pH (red) and amperometric (black) responses obtained at the dual (Au-IrOx)-Pt probe in a 2×10^{-4} M HNO_3 , 0.1 M KNO_3 solution.

Finally, a full 2D image for the simultaneous RNS and pH monitoring was acquired as is displayed in **Fig 7.45**, which further highlights the good performance of the soft probe proposed here.

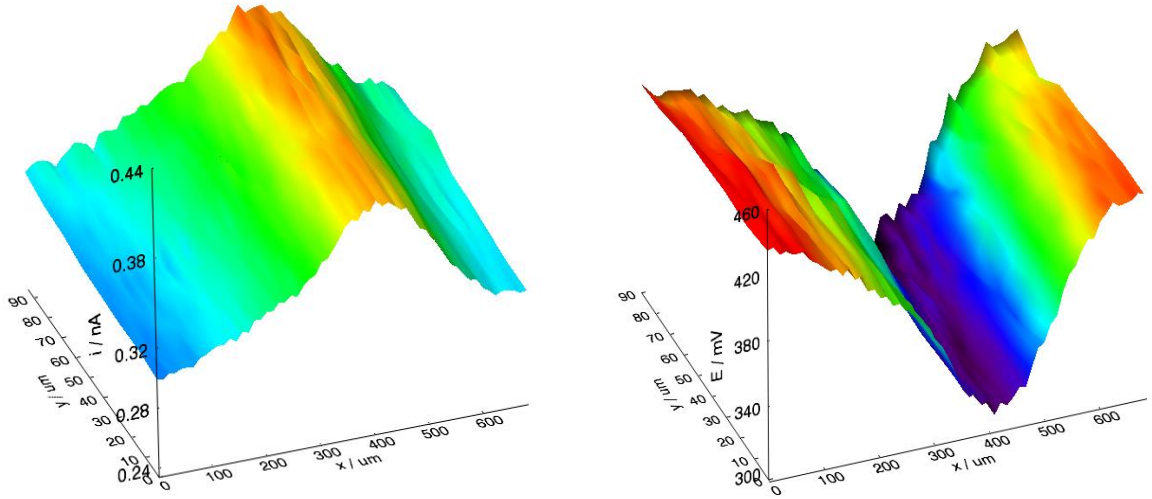

Fig 7.45- SECM Images of current (**left**) and OCP *vs.* Ag/AgCl (**right**) of an Ag band left to corrode in a 0.2 mM HNO_3 aqueous solution. Probe translation speed: 5 μms^{-1}.

References

[1] P. Sun, F.O. Laforge, M.V. Mirkin, Physical Chemistry Chemical Physics 9 (2007) 802−823.

[2] A.J. Bard, M.V. Mirkin, Scanning Electrochemical Microscopy, M. Dekker, NewYork, (2001).

[3] D. Polcari, P. Dauphin-Ducharme, Janine Mauzeroll Chemical Reviews 116 (2016) 13234−13278.

[4] S. Kuss, D. Trinh, J. Mauzeroll, *Analytical Chemistry* 87(16) (2015) 8102–8106.

[5] C.S. Santos, A.J. Kowaltowski, M. Bertotti, Nature Scientific Reports 7 (2017) n.11428.

[6] C. Kranz, G. Friedbacher, B. Mizaikofft, A. Lugstein, J. Smoliner, E. Bertagnolli, Analytical Chemistry 73 (2001) 2491-2500.

[7] A. Davoodi, J. Pan, C. Leygraf, S. Norgren, Electrochimica Acta 52 (2007) 52, 7697-7705.

[8] A. Ueda, O. Niwa, K. Maruyama, Y. Shindo, K. Oka, K. Suzuki, AngewandteChemie, Int. Ed. 46 (2007) 8238-8241.

[9] T.H. Treutler, G. Wittstock, Electrochimica Acta 48 (2003) 48, 2923-2932.

[10] P.S. Dobson, J.M.R. Weaver, M.N. Holder, P.R. Unwin, J.V. Macpherson, Analytical Chemistry 77 (2005) 424-434.

[11] C. Wei, A.J. Bard, G. Nagy, K. Toth, Analytical Chemistry 67 (1995) 1346-1356.

[12] M.A. Edwards, A.L. Whitworth, P.R. Unwin, Analytical Chemistry 83 (2011) 1977−1984.

[13] Y. Lee, A.J. Bard, Analytical Chemistry 74 (2002) 3626-3633.

[14] A. Lesch, F. Cortés-Salazar, M. Prudent, J. Delobel, S. Lion, N. Tissot, J. Tacchini, H. Girault, Journal of Electroanalytical Chemistry 717-718 (2014) 717–718, 61–68.

[15] F. Cortes-Salazar, M. Trauble, F. Li, J.M. Busnel, A.L. Gassner, M. Hojeij, G. Wittstock, H.H. Girault, Analytical Chemistry 81 (2009) 6889− 6896.

[16] T.E. Lin, Y. Lu, C. Sun, H. Pick, J. Chen, A. Lesch, Angewandte Chemie 56 (2017) 16498-16502.

[17] T.E. Lin, F. Cortés-Salazar, A. Lesch, L. Qiao, A. Bondarenko, H.H. Girault, Electrochimica Acta 179 (2015) 57-64.

[18] T.E. Lin, Y. Lu, C. Sun, J. Chen, A. Lesch, H.H. Girault, ECS Transactions 77 (2018) 85-90.

[19] F. Cortès-Salazar, D. Momotenko, H.H. Girault, A. Lesch, G. Wittstock, Analytical Chemistry 83 (2011) 1493–1499.

[20] F. Cortès-Salazar, D. Momotenko, G. Wittstock, A. Lesch, H.H. Girault, Analytical Chemistry 82 (2010) 10037–10044.

[21] A. Lesch, P. Chen, F. Roelfs, C. Dosche, D. Momotenko, F. Cortes-Salazar, H.H. Girault, G. Wittstock, Analytical Chemistry 86 (2014) 713−720.

[22] A. Lesch, D. Momotenko, F. Cortés-Salazar, I. Wirth, U.M. Tefashe,F. Meiners, B. Vaske, H.H. Girault, G. Wittstock, Journal of Electroanalytical Chemistry 666 (2012) 52-61.

[23] L.L. Thomson, F.G. Lawton, R.G. Knowles, J.E. Basley, V. Riversomoreno, S. Moncada, Cancer Research 54 (1994) 1352–1354.

[24] G. Sciutto, S. Prati, R. Mazzeo, M. Zangheri, A. Roda, L. Bardini, G. Valenti, S. Rapino, M. Marcaccio, Analytica Chimica Acta 831 (2014) 31−37.

[25] S. Isik, W. Schuhmann, Angewandte Chemie, 45(44) (2006) 7451-7454.

[26] A.L. Barker, P.R. Unwin, J.W. Gardner, H. Rieley, Electrochemistry Communications 6 (2004) 91–97

[27] M. Etienne, P. Dierkes, T. Erichsen, W. Schuhmann, I. Fritsch, Electroanalysis (2007) 318–323.

[28] B.M. Fernandez-Pèrez, J. Izquierdo, S. Gonzalez, R. M. Souto, Journal of Solid State Electrochemistry 2014, 1–10.

[29] B.P. Nadappuram, K. McKelvey, R. Al Botros, A.W. Colburn, P.R. Unwin, Analytical Chemistry 85 (2013) 8070-8074.

[30] K. Štulik, C. Amatore, K. Holub, V. Maracek, W. Kutner, Pure and Applied Chemistry 72 (2000) 1483-1492.

[31] M.P. Longinotti, H.R. Corti, Electrochemistry Communications 9 (2007) 1444–1450.

[32] I. Ciani, S. Daniele, Analytical Chemistry 76 (2004) 6575-81.

[33] S. Daniele, C. Bragato, M.A. Baldo, I. Ciani, Talanta 77 (2008) 235-240.

[34] S. Daniele, I. Ciani, D. Battistel, Analytical Chemistry 80 (2008) 253-259.

[35] D. Soltman, V. Subramanian, Langmuir 24 (2008) 2224-2231.

[36] W.H. Reinmuth, Analytical Chemistry 32 (1960) 1509-1512.

[37] A. Kicela, S. Daniele, Talanta 68 (2006) 1632-1639.

[38] B.J. Privett, J. H. Shin, M.H. Schoenfisch, Chemical Society Reviews 39 (2010) 1925-1935.

[39] I.G. Casella, M. Contursi, R. Toniolo, Journal of Electroanalytical Chemistry 736 (2015) 147– 152.

[40] J.E. Baur, T.W. Spaine, Journal of Electroanalytical Chemistry 443 (1998) 208– 216.

[41] H.A. Elsen, C.F. Monson, M. Majda, Journal of Electrochemical Society 156 (2009) F1.

[42] K. Yamanaka, Japanese Journal of Applied Physics 28 (1989) 632– 637.

[43] C.S. Santos, A.S. Lima, D. Battistel, S. Daniele, M. Bertotti, Electroanalysis 28 (2016) 1441-1447.

[44] B.D. Craig, D.S. Anderson, Handbook of Corrosion Data 2nd ed. ASM International, 1995.

[45] S. Elzey, V.H. Grassian, Journal of Nanoparticles Research 12 (2010) 1945-1958.

[46] S. Goldstein, G. Czapski Journal of American Chemical Society 117 (1995) 12078-12084.

[47] Y. Wang, J. Noel, J. Velmurugan, W. Nogala, M.V. Mirkin, C. Lu, M.G. Collignon, F. Lemaitre, C. Amatore, PNAS 109 (2012) 11534-11539.

Conclusions

In this thesis a series of studies, based on the use of various electroanalytical techniques and electrodes types, have been performed for the determination of molecules, ions and parameters, which are important in the field of cancer care or that reflect the presence of neoplasms in the human body.
The main achievements and relevant concluding remarks for each specific topic are summarised below for each chapter.

Chapter 5 – Irinotecan and Imatinib

In this chapter, the voltammetric behaviour of the drugs irinotecan (CPT-11) and imatinib has been examined in detail, using a GCE as working electrode, in acetonitrile and ethyl acetate, respectively. These solvents were chosen because they can profitably be used for plasma proteins denaturation (both drugs are strongly bound to proteins) and, simultaneously, as media in which voltammetric measurements can be performed straightforwardly. This to implement an easy therapeutic drug monitoring (TMD) procedure for a rapid detection of the drugs in the plasma samples.
CPT-11, which is typically administered to patients affected by colorectal cancer as CPT-11HCl, undergoes a rather complex metabolic pathway, activated by the enzyme liver-carboxylesterase. This leads to several compounds having similar chemical structures. For this reason, and in the lack of literature reports, a thorough voltammetric investigation of CPT, CPT-11HCl and its main metabolites in acetonitrile was necessary. The results have shown that all compounds displayed voltammetric features strongly resembling one another, especially in the negative potential region. In the anodic region, the piperidine group end of CPT-11 gave rise to an oxidation process at a potential essentially free from interference. The latter electrode process revealed therefore useful for the quantification of CPT-11. Since the injectable form of irinotecan is CPT-11HCl, and because the protonated tertiary amine is not electroactive over the positive potential range affordable in the medium, for the quantification of the drug, the neutralization of the proton level by a basic buffer was required. In the investigation concerns on interferences due to co-drugs, which are often administered concomitantly with irinotecan, have also been addressed. From the above investigation, it was concluded that a pre-treatment step, involving denaturation of proteins or extraction of irinotecan from the matrix, was required before performing the voltammetric analysis. To these purposes, commercially available SPE columns (StrataXL), which are suitable to absorb neutral compounds containing aromatic rings, were employed. A detailed protocol, including washing, to eliminate interferents also from

plasma matrix, and extraction to recover CPT-11 from plasma, was set up. The detection step was performed using differential pulse voltammetry (DPV) to enhance sensitivity. The analytical protocol revealed adequate in terms of LOD, LOQ, reproducibility and accuracy for monitoring CPT-11 in the upper region of the therapeutic window (i.e., around 8 µM). Even with the above limit, the proposed method could be particularly useful for monitoring CPT-11 concentrations immediately after or during the infusion. In fact, hepatic enzyme carboxylesterase starts immediately the conversion of CPT-11 in its metabolites. The conversion rate, during the infusion, could be an important diagnostic tool linked to drug tolerance and therefore to drug dosing decision.

An investigation similar to that described above was also performed for imatinib, using ethyl acetate (EtOAc) as solvent, in which no voltammetric report exists in the literature. In the body, imatinib is metabolized, primarily, by CYP3A4 and CYP3A5 mainly (i.e., 12-15%) to the active metabolite, N-des-methyl imatinib (des-imatinib), whose maximum concentration in the bloodstream is usually no higher than about 10% of its precursor. Thus, for this drug, analytical concerns are mainly related to its strong interaction with protein, and, to a much lower extent, to the circumstance that in clinical regimens, it is administered as imatinib mesylate. The voltammetric results have shown that imatinib provided an oxidation process leading to a product species, which are strongly adsorbed onto the GCE surface. The surface process revealed useful for the detection of the drug at very low concentration levels, down to tens of nM, exploiting an optimised adsorptive stripping voltammetric wave form, based on adsorptive stripping voltammetry (AdSV). Also for imatinib, to get rid from interferences due to plasma components, and extraction procedure was set-up, using SLE columns (Novum). A detailed protocol to eliminate interferents, and extraction to recover imatinib from plasma, was set up. The optimized analytical protocol revealed adequate in terms of LOD, LOQ, reproducibility and accuracy for monitoring imatinib over the entire range of the therapeutic window (i.e., 2 - 6 µM). It must be remarked that the sensitivity of the method is even lower than the therapeutic range. This fits well with the circumstance that in the extraction step, dilution of the analyte occurs.

Overall, it can be concluded that the analytical protocols developed here for the two drugs are simple and fast; for a single run measurement it is required about 4-5 min. Moreover, accuracy, checked against an HPLC-MS approach, currently used at the Centro di Riferimento Oncologico (CRO) in Aviano (PN), revealed suitable for their TDM applications.

Chapter 6 - Miniaturized electrochemical sensors

This chapter deals with the development of miniaturized electrodes or electrochemical cells for monitoring molecules and species related to cancer diseases. In fact, the advantages offered by the electroanalytical techniques can be expanded using printing technologies and microelectrodes. These enable, from one side, the large-scale production of low-cost and highly reproducible sensing devices with high potential for on-site monitoring; from the other to carry measurements in non-usual environments for dynamic electrochemical techniques, such as gaseous atmospheres.

Section 6.1 is devoted at the investigation of the stability in organic solvents of inkjet-printed electrodes, prepared with an ink, never employed before, which could in principle display higher resistance to the chemical attack of organic solvents. The ink had the function to insulate electrical connections and to define the active surface area of the electrodes. In particular, the insulating layer was obtained by the UV-curable EMD-6415 ink, which after UV-curing, it led to hard and non-porous surfaces. This circumstance could, actually imparted higher stability to the material, when it comes into contact with organic solvents. The electrode systems were investigated in acetonitrile and ethyl acetate, employed in for the detection of CPT-11 and imatinib, as well as in DMSO and in a water/methanol mixture, which are also used in several steps of the analytical protocols developed in Chapter 5. The probe molecule was FcMeOH, whose electrochemistry is well-known. From the investigation, it was found that the optimized - in terms of materials and procedure employed inkjet-printed electrodes were very unstable in acetonitrile, while they displayed increasing stability passing from ethyl acetate to DMSO. In the latter solvent, stability was almost same as in aqueous solutions, in which media inkjet- printed electrodes are typically employed. Since the stability of the inkjet-printed electrodes in ethyl acetate was relatively large (about 30 min), it was possible to obtain reliable AdSVs of imatinib for its quantification by these novel probes. This circumstance promises a new way for the preparation of disposable sensors for TDM applications in the organic solvent.

Section 6.2 is devoted to the development of a miniaturized sensor for gaseous analysis. It is made by double barrel platinum microelectrode system, whose tip end is coated with a thin layer of the room temperature ionic liquid (RTIL), 1-butyl-3-methylimidazolium hydroxide ([BMIM][OH]). The results presented in this section have shown that that [BMIM][OH] is a suitable medium/electrolyte to perform the electrooxidation of volatile aldehydes (VAs), which are often produced by biological cells, during peroxidation of lipids in cellular membranes, and used as biomarkers even for cancer disease. The investigation proved that the use of this simple

electrochemical microprobe, allowed headspace monitoring of the investigated aldehydes, namely, propionaldehyde and hexanaldehyde, under ambient conditions. Since the elctrooxidation of aldehydes at Pt electrode is favoured by basic media, [BMIM][OH] can successfully replace conventional bases, which suffer from high vapor pressure at ambient temperature. With this regard, it must be considered that the negligible vapor pressure of the RTIL prevents even thin films from evaporating, hence resulting in low-drift sensors. The developed sensor is able to detect aldehyde concentration down to a few ppm levels.

Chapter 7 - SECM and small molecule sensing

This chapter deals with the development of strategies able to characterize the interaction between specific molecules and receptors immobilized on a solid substrate, or to the construction of suitable probes to monitor small molecules and ionic species with high spatial resolution. To achieve the latter goals, scanning electrochemical microscopy (SECM) approaches have been used.

In section 7.1 SECM was employed to establish the interaction between CPT-11-HCl and a cyclic peptide, designed on purpose by molecular dynamics to bind specifically CPT-11 in given samples. Generally, these kinds of measurements are performed in bulk solutions, where energy involved in the interaction between the species of interest and receptor could be different from those acting when one of the species is bound to a different phase. Moreover, spatially resolved measurements can provide information at micrometer scale of the distribution of the receptor on the surface. The investigation was performed in acetonitrile with the cyclic peptide immobilized on a gold substrate trough a self-assembled monolayer. The binding ability of the cyclic peptide towards CPT-11HCl was assessed trough approach curves recoded using CPT-11HCl itself as redox mediator. It was found, in fact, that CPT-11HCl concentration increased to a considerable extent, as soon as the tip to substrate distance was less than about 10 µm. Moreover, using properly normalized current signals as a function of normalised tip-to-substrate distances, an affinity constant of about 70 µM was evaluated. This value indicates a relatively weak interaction, probably not useful to TDM applications for the investigated drug. Apart from this data, the investigation presented in this section represents a novel approach to better address chemical events occurring at interfaces.

In section 7.2, it is proposed a novel methodology for the construction of soft probes, able to detect electroactive species over a surface, including not-flat or soft matter surfaces (i.e., skin,

cell membrane and so on). Dual soft probes made of platinum, gold, carbon, or mixed microelectrodes (25 or 8 μM diameter) were fabricated and thoroughly characterized by using voltammetry, SECM and laser scanning microscopy. These probes revealed useful for recording simultaneously, by a SECM apparatus, two chemical properties. Moreover, because they work in contact mode with the surface, they do not need coupled systems to control tip to substrate-distance, contrary to what happens for SECM measurements based on classic rigid probes. A proof of concept of their usefulness in SECM imaging has been illustrated by using a Pt-Au soft probe for imaging simultaneously NO and pH changes above an Ag band immersed on a dilute HNO_3 solution. The platinum microdisk, modified with a thin film of platinum black, was employedfor the amperomentric detection of NO; the gold microdisk, coated with iridium oxides, was used for the potentiometric monitoring of pH. This configuration, combining amperometric and potentiometric detection approaches, avoids mutual perturbation of the local chemical environment, as the potentiometric part acts as a passive probe. The choice of NO and pH, as highlighted in introduction, is due to the fact that anomalous concentration of nitric oxide (NO) and of NO-related species have been detected in various types of cancer. On the other hand, NO formation is accompanied by an increase of H^+ concentration, whose flux in turn is related to enhanced activity of cancer cells.